

A FIELD STUDY OF THE PHYSICAL MECHANISMS
UNDER EXCHANGE AND UNIDIRECTIONAL
FLOW CONDITIONS INFLUENCING TRANSPORT
OF SEDIMENT THROUGH CAYUGA INLET
(ITHACA, NY, USA)

A Thesis

Presented to the Faculty of the Graduate School

of Cornell University

In Partial Fulfillment of the Requirements for the Degree of

Master of Science

by

Brianna Lynn Datti

May 2017

© 2017 Brianna Lynn Datti

ABSTRACT

Cayuga Lake serves as a drinking water source as well as a popular recreational lake. It is the second largest of the Finger Lakes (New York, USA), with a long narrow shape. Concerns exist regarding the lake's phosphorus and turbidity loadings, specifically on the southern shelf (also where three point sources discharge: two waste water treatment plants and Cornell's Lake Source Cooling Facility). Cayuga Inlet, along with Fall Creek, flow into the southern end and account for 40% of the total inflow to the entire lake. Studies indicate Cayuga Inlet and Fall Creek account for 87% of the bioavailable phosphorus load specifically entering in the southern shelf. A number of complex physical processes establish exchange and transport between the lake and the inlet. Understanding which mechanisms control transport of loadings is essential to evaluating the processes that govern water quality.

Using data collected over the summer and fall months in 2015 and 2016 along Cayuga Inlet, from the inflowing tributaries, through the inlet, and out to the southern lake, we examine various physical mechanisms and their influence on turbidity loads. Velocity profiles in Cayuga Inlet are captured with an acoustic Doppler current profiler (ADCP) and High Resolution (HR) acoustic Doppler Profiler (ADP), and turbulence measures with an acoustic Doppler velocimeter (ADV). Water quality sondes are used to monitor turbidity and temperature along with a widely-distributed set of thermistors to obtain a detailed description of temperature structures throughout the area of interest. Data from United States Geographical Survey (USGS) gage stations as well as local meteorological stations are utilized to more fully understand forcing mechanisms important to flow behavior in Cayuga Inlet.

Our results suggest flow through Cayuga Inlet is continuously influenced by barotropic seiches in Cayuga Lake while occasional large baroclinic events occur, the largest of which transport lake water into Cayuga Inlet. Over the stratified season exchange flows are typical and largely forced by

temperature differences between the tributaries and southern lake bounding the inlet. The predominant wind stress is along the axis of the lake and the inlet and sets up seiching behavior in the lake which influences flow behavior in the inlet. A strong wind stress also increases vertical mixing in the inlet. Minimal sediment resuspension occurs in the inlet and generally, the inlet is a conduit through which suspended sediment is advected. The tributaries carry significant turbidity loads into the inlet during runoff events, which in two layer flows under conditions of cooler tributary temperatures relative to the inlet and southern lake, typically appear in the lower layer. In the spring, when the southern lake is expected to be cooler than that observed over the summer and fall deployment periods analyzed here and tributary flows are expected to warm faster, significant turbidity loads may pass through the top layer of the inlet with more frequency. At times turbidity loads in the southern lake are transported by seiching back into the inlet and again in two layer flows typically appear in the appropriate stratified layer based on the southern lake temperature relative to the inlet and tributaries.

BIOGRAPHICAL SKETCH

Brianna Lynn Datti grew up in Durham, NH with her sister Sammy Datti and parents Ed Datti and Gail Goodspeed. Both her parents are collegiate women's gymnastics coaches and although she started out with gymnastics quickly found her passion for volleyball. Along with spending hours in the gym training, throughout middle school and high school Brianna enjoyed exploring and learning about environmental systems and processes that control so much of the world on which we depend. Summers were spent playing volleyball at every opportunity and on the particularly hot summer days going to her favorite beaches along the Maine and New Hampshire coast. Her love for math, the sciences, and the environment led her to pursue Environment Engineering at the University of Connecticut, where she also competed on the women's volleyball team as a libero. In her studies, she continued to develop her passion for protecting the environment and particularly water resources, which led her to pursue a master's degree focused on environmental fluid mechanics and hydrology at Cornell University.

ACKNOWLEDGEMENTS

First, I would like to thank my advisor, Todd Cowen, and my minor committee member, Todd Walter, for their support and guidance. I have learned so much and feel honored I had the privilege to work with you both.

I would like to thank the Cornell University Graduate School Fellowship and the Joseph H. DeFrees Fellowship for their financial support.

Throughout this research, I was fortunate to be aided by many. P.J. Rusello, thank you for jump starting this work and sharing your knowledge on the equipment used to collect our data. Allie King, thank you for all the advice, particularly in the beginning, and helping to motivate this work. Seth Schweitzer, thank you for showing me the ropes out on the lake. You were extremely helpful whenever I had any questions on setting up our data collection. Jack Powers, thank you for your help in the field and teaching me how to trailer and launch a boat. Paul Charles, Tim Brock, and Cameron Willkens, thank you for all the help maintaining equipment used in the field, including getting the work truck fixed when it refused to start. EFMH group members, thank you for creating such a great environment to work and learn in.

Lastly, Mom, Dad, and Sammy, thank you for continuing to support me in all my endeavors. I could not ask for a better family, that always has my back and pushes me to pursue my dreams.

TABLE OF CONTENTS

1. Motivation.....	1
1.1. Cayuga Lake Assessment	1
1.2. Cayuga Inlet Assessment	3
2. Characterization of Physical Mechanisms in Cayuga Lake and Inlet.....	7
2.1. Seasonal Stratification	7
2.2. Lake Seiches and Upwelling Events	10
2.3. Two-Layer Exchange Flow	14
2.4. Vertical Mixing	17
2.5. Bed Sediment Resuspension	18
3. Methods.....	21
3.1. Field Instruments	21
3.2. Summer/Fall 2015 Field Deployment Setup	24
3.3. Summer 2016 Field Deployment Setup	27
4. Data Validation Techniques.....	29
4.1. Quality Control Analysis of Velocity Data	30
4.1.1.ADCP	30
4.1.2.HR Profiler	42
4.1.3.Vector	44
4.2. Comparison of Velocity Data from Different Instruments	53
4.3. Model of Inlet Depth Average Flow	62
5. Results and Discussion.....	66
5.1. General Conditions in Cayuga Inlet	66
5.1.1.Temperature	66
5.1.2.Vertical Mixing	74
5.1.3.Turbidity	78
5.1.4.Flow Conditions	86
5.2. Froude Number Analysis	99
5.3. Influence of Physical Mechanisms on Turbidity Loads	114
5.3.1.Bed Sediment Resuspension	114
5.3.2.Flow Conditions and Vertical Mixing	129
5.3.3.Wind Stress	139
5.4. Specific Events	148
5.4.1.Maximum Tributary Flowrate	148
5.4.2.Inlet Top Layer Turbidity > Bottom Layer Turbidity	150
5.4.3.Precipitation Events	151
5.4.4.“Upwelling” Events	159
5.5. Conclusion	166
A Uncertainty Analysis.....	168
Bibliography.....	170

LIST OF FIGURES

- Figure 1.1: Subwatersheds of Cayuga Lake...**3**
- Figure 1.2: Map of the southern end of Cayuga Lake and Cayuga Inlet and Fall Creek inflows, as well as the three point sources which discharge into the southern end...**4**
- Figure 1.3: Visible suspended sediment load entering southern Cayuga Lake through Cayuga Inlet in April 2014...**4**
- Figure 2.1: Expected temperature profile in Cayuga Lake in the summer...**8**
- Figure 2.2: Vertical temperature profiles in Cayuga Lake from 1994 (Stearns & Wheler, 1997)...**9**
- Figure 2.3: Processes causing exchange flow in Cayuga Inlet starting with a southerly wind...**12**
- Figure 2.4: Froude number plane. The shaded region represents internally subcritical flow ($G < 1$) and the non-shaded region represents internally supercritical flow ($G > 1$) (Armi and Farmer, 1986)...**15**
- Figure 3.1: Deployment locations in Cayuga Inlet from Summer/Fall 2015 experiment and list of equipment at each location. Note Cayuga Inlet enters the lake at the top of this map...**24**
- Figure 3.2: Bottom frame setup deployed in the primary inlet location over Deployment 1. Holds the ADCP, ADCP battery case, HR Profiler, and 6600 Water Quality Sonde...**26**
- Figure 3.3: Deployment locations in Cayuga Inlet from Summer 2016 experiment and list of equipment at each location...**27**
- Figure 3.4: Bottom frame setup deployed in the primary inlet location. Holds the ADCP, ADCP battery case, Vector, Vector battery case, and 6600 Water Quality Sonde...**29**
- Figure 4.1: *Echo amplitudes* during Deployment 1 for each beam over all ensembles and bins.
- Figure 4.2: Histograms of ADCP *correlation* values for each beam...**31**
- Figure 4.3.1: ADCP beam velocities for different bins at burst 1000 before and after the AGW filter applied to Deployment 1...**32**
- Figure 4.3.2: ADCP beam velocities at burst 50 and beam 1 velocities at different bins at burst 50 before and after the AGW filter applied to Deployment 2...**33**
- Figure 4.4.1: Velocities in xyz coordinates from the ADCP for Deployment 1, over the ensemble number (time) and bin number (depth), where the lower bin numbers are at greater depths and highest bin number near water surface (scale set to $\pm 0.1m/s$, with few larger velocities: $-0.14m/s < u < 0.15m/s$; $-0.19m/s < v < 0.15m/s$; $-0.04m/s < w < 0.03m/s$)...**34**
- Figure 4.4.2: Velocities in xyz coordinates from the ADCP for Deployment 2, over the ensemble number (time) and bin number (depth), where the lower bin numbers are at greater depths and highest bin number near water surface (scale set to $\pm 0.1m/s$, with few larger velocities: $-0.33m/s < u < 0.14m/s$; $-0.23m/s < v < 0.30m/s$; $-0.03m/s < w < 0.12m/s$)...**35**
- Figure 4.5.1: Histogram of θ , angle between ADCP recorded u and dominant flow direction through the inlet for Deployment 1...**36**
- Figure 4.5.2: Histogram of θ , angle between ADCP recorded u and dominant flow direction through the inlet over Deployment 2...**37**
- Figure 4.6.1: Individual ADCP streamwise bin velocities, u_{sw} , over time over Deployment 1 (all bins: left; bins at approximately 0.5m, 1m, and 1.5m deep: right)...**37**
- Figure 4.6.2: Individual ADCP streamwise bin velocities, u_{sw} , over time over Deployment 2 (all bins: left; bins at approximately 0.5m, 1m, and 1.5m deep: right)...**38**

Figure 4.7.1: ADCP streamwise velocities, u_{sw} , (m/s) over the ensemble number (time) and bin number (depth) over Deployment 1...**38**

Figure 4.7.2: ADCP streamwise velocities, u_{sw} , (m/s) over the ensemble number (time) and depth, over Deployment 2...**38**

Figure 4.8: Various velocity profiles measured by ADCP interpolated and extrapolated using PCHIP. Measured data in red dots and interpolated and extrapolated data in blue lines...**40**

Figure 4.9.1: Depth average streamwise velocity (U) over Deployment 1, using extrapolated/interpolated ADCP velocity profiles...**40**

Figure 4.9.2: Depth average streamwise velocity (U) over Deployment 2, using extrapolated/interpolated ADCP velocity profiles...**41**

Figure 4.10.1: Depth average absolute velocity over Deployment 1, using extrapolated/interpolated ADCP velocity profiles...**41**

Figure 4.10.2: Depth average absolute velocity over Deployment 2, using extrapolated/interpolated ADCP velocity profiles...**42**

Figure 4.11: HR Profiler beam velocities for bins at burst 100 before and after applying AGW filter...**43**

Figure 4.12: Streamwise velocity along the inlet from the HR Profiler, over the ensemble number (time: August 27th, 2015 to September 7th, 2015) and bin number (depth), where lower bin numbers are at greater depths and highest bin number is at approximately 1m deep...**44**

Figure 4.13: Histograms of Vector *correlation* for each beam...**45**

Figure 4.14: Vector beam velocities at burst 10 before and after applying the AGW filter...**46**

Figure 4.15.1: Vector velocities in xyz coordinates over Deployment 2...**47**

Figure 4.15.2: Vector Velocities in xyz coordinates over Deployment 3...**47**

Figure 4.16.1: Streamwise velocity based on Vector data over Deployment 2, for flow out of the inlet towards the lake (+) and in to the inlet from the lake (-)...**48**

Figure 4.16.2: Streamwise velocity based on Vector data over Deployment 3, for flow out of the inlet towards the lake (+) and in to the inlet from the lake (-)...**48**

Figure 4.17: Power spectra of Vector beam velocities. Spectra were calculated for each ensemble, which was over the 2.5minute burst interval the instrument was recording. The above plots are averages of those spectra over 1day. Red line indicates the -5/3 slope that characterizes turbulence to compare to power spectra slope (analyzed averaged spectra at 5 day intervals over deployment, beginning→end: left, top→right, bottom)...**50**

Figure 4.18: Wind records (right) corresponding to select velocity spectra (left) from previous Figure. N/S indicates magnitude of wind along North/South axis, where North is positive and E/W indicates magnitude of wind along East/West axis, where East is positive...**52**

Figure 4.19: Power spectra for pressure corresponding to selected power spectra for beam velocities...**53**

Figure 4.20: Comparison of streamwise velocities measured by the ADCP versus the HR Profiler at depths of approximately 1.2 meters (left), 1.1 meters (middle), and 1.0 meters (right)...**54**

Figure 4.21: Comparison of Vector and ADCP streamwise velocities at approximately the same depth and time...**55**

Figure 4.22.1: Depth average velocities from the IAWWTP ADP (left) and velocity profiles recorded from the IAWWTP ADP (right) over Deployment 1' before and after filtering (top and bottom, respectively). Note dark blue values on bottom right plot are removed data and North refers to magnetic north...**57**

Figure 4.22.2: Depth average velocities from the IAWWTP ADP (left) and velocity profiles recorded from the IAWWTP ADP (right) over Deployment 2' before and after filtering (top and bottom,

respectively). Note dark blue values on bottom right plot are removed data and North refers to magnetic north...57

Figure 4.23.1: IAWWTP ADP cell end (left) and SNR (right) over Deployment 1', parameters used to set filters as described above...58

Figure 4.23.2: IAWWTP ADP cell end (left) and SNR (right) over Deployment 2', parameters used to set filters as described above...58

Figure 4.24.1: Comparison of depth average streamwise velocity determined by the Cornell ADCP versus the IAWWTP ADP over Deployment 1...59

Figure 4.24.2: Comparison of depth average streamwise velocity determined by the Cornell ADCP versus the IAWWTP ADP over Deployment 2...60

Figure 4.25: Streamwise velocity through the inlet recorded by the Vector compared to that recorded by bin 2 of IAWWTP ADP over Deployment 3...61

Figure 4.26.1: Measured and modeled depth average velocity in Cayuga Inlet using ADCP data and above mentioned model with best fit parameters over Deployment 1...63

Figure 4.26.2: Measured and modeled depth average velocity in Cayuga Inlet using ADCP data and above mentioned model with best fit parameters over Deployment 2. Top shows the entire time series while the rest are zoomed in on a few selected dates...63

Figure 4.26.3: Measured and modeled depth average velocity in Cayuga Inlet using IAWWTP ADCP data and previously described model with USGS gage data over Deployment 3 with best fit parameters of Deployment 2...65

Figure 4.26.4: Measured and modeled depth average velocity in Cayuga Inlet using IAWWTP ADCP data and previously described model with USGS gage data over Deployment 3 with new best fit parameters...66

Figure 5.1.1: Average temperatures of tributaries (Inlet Creek, Sixmile Creek, and Cascadilla Creek), southern Cayuga Lake, and Inlet over Deployment 1, based on 15-minute average...67

Figure 5.1.2: Average temperatures of tributaries (Inlet Creek, Sixmile Creek, and Cascadilla Creek), southern Cayuga Lake, and inlet over Deployment 2, based on 15-minute average...67

Figure 5.1.3: Average temperatures of tributaries (Inlet Creek, Sixmile Creek, and Cascadilla Creek), southern Cayuga Lake, and Inlet channel over Deployment 3, based on 15-minute average...68

Figure 5.2: Root mean square error (RMSE) between measured and predicted tributary temperatures from range of combinations with backward (T_{OFF}) and center (T_{AVG}) averaging intervals. Location of lowest RMSE indicated by red circle...69

Figure 5.3: Predicted tributary temperatures based on air temperature and best fit moving average...69

Figure 5.4: Average temperatures of inflowing tributaries (Inlet Creek, Sixmile Creek, and Cascadilla Creek), southern Cayuga Lake, and Inlet over periods of interest during Deployment 2...71

Figure 5.5: From left to right and top to bottom, water temperature profiles over Deployment 1 moving downstream Cayuga Inlet, into the southern lake. Approximate depths of thermistors the center of each bin plotted. White spaces indicate missing data...72

Figure 5.6: Locations of thermistor chains deployed in Cayuga Inlet for temperature profiles...73

Figure 5.7: Average horizontal temperature profile over Deployment 1, where horizontal distance of 0 indicates the main inlet location and positive values indicate moving out towards the lake...73

Figure 5.8.1: N^2 in the inlet over Deployment 1 at Treman Marine site...74

Figure 5.8.2: N^2 in the inlet over Deployment 2...75

Figure 5.8.3: N^2 in the inlet over Deployment 3...75

Figure 5.9.1: Comparison of vertical mixing and advective timescales in inlet over Deployment 1...77

Figure 5.9.2: Comparison of vertical mixing and advective timescales in inlet over Deployment 2...77

Figure 5.9.3: Comparison of vertical mixing and advective timescales calculated using IAWWTP ADCP data, for velocity profile and depth average velocity, over Deployment 3...77

Figure 5.10: Turbidity averaged over 15 minutes (top), 4 hours (middle), and 1 day (bottom). Bottom Inlet: turbidity ~1.5m deep at Cayuga Inlet location; Top Inlet: turbidity ~0.5m deep at Cayuga Inlet location; Top Inlet-Lake; turbidity ~0.5m deep downstream towards lake of Cayuga Inlet location; Top Lake: turbidity ~0.5m deep at piling cluster on southern shelf of lake...79

Figure 5.11: Raw inlet turbidity over Deployment 2...81

Figure 5.12: Distinguishing between real event based increases in turbidity (top) and spikes (bottom)...81

Figure 5.13.1: Inlet turbidity filtered by 2-hour periods over Deployment 2...83

Figure 5.13.2: Inlet turbidity filtered by every 100 measurements over Deployment 2...83

Figure 5.14.1: Turbidity in southern lake and inlet averaged onto 15-minute time axis over Deployment 1...84

Figure 5.14.2: Turbidity in southern lake and inlet averaged onto 15-minute time axis over Deployment 2. Range of low, medium, high, and extreme turbidity indicated...85

Figure 5.14.3: Turbidity in southern lake and inlet averaged onto 15-minute time axis over Deployment 3...85

Figure 5.15.1: U over short time intervals to observe period of oscillations (left→right: 6/28/16, 7/10/16, 7/18/16)...86

Figure 5.15.2: U on 7/25/16, when tributary flowrates reached maximum for Deployment 2...86

Figure 5.16.1: Vertical streamwise velocity profiles from ADCP at various times during Deployment 1, demonstrating an exchange flow (left) and unidirectional flows (middle and right)...87

Figure 5.16.2: Vertical streamwise velocity profiles from HR Profiler at various times during Deployment 1, demonstrating exchange flows and unidirectional flows in bottom meter of inlet...87

Figure 5.17: Distribution of $|U|$ (m/s) through inlet under different flow conditions. Top: Deployment 1; Middle: Deployment 2; Bottom: Deployment 3...92

Figure 5.18: Distribution of U_{abs} (m/s) through inlet under different flow conditions. Top: Deployment 1; Middle: Deployment 2; Bottom: Deployment 3...92

Figure 5.19: Distribution of N (1/s) in inlet under different flow conditions. Top: Deployment 1; Middle: Deployment 2; Bottom: Deployment 3...93

Figure 5.20: Distribution of $\frac{10\tau_z}{\tau_A}$ in the inlet under different flow conditions. When $\frac{10\tau_z}{\tau_A} < 1$, expect the inlet to be well-mixed. (Note: all timescale comparisons greater than 10, when advective timescale faster than vertical mixing timescale, placed into the 10 bin) Top: Deployment 1; Middle: Deployment 2; Bottom: Deployment 3...94

Figure 5.21: Distribution of southerly wind speed (m/s) over Cayuga Lake under different inlet flow conditions. Top: Deployment 1; Middle: Deployment 2; Bottom: Deployment 3...95

Figure 5.22.1: Distribution of KE_{trib} (top), KE_{wind} (middle), and PE (bottom) under different inlet flow conditions over Deployment 1...97

Figure 5.22.2: Distribution of KE_{trib} (top), KE_{wind} (middle), and PE (bottom) under different inlet flow conditions over Deployment 2...98

Figure 5.22.3: Distribution of KE_{trib} (top), KE_{wind} (middle), and PE (bottom) under different inlet flow conditions over Deployment 3...98

Figure 5.23.1: Depth average velocity, total depth and reduced gravity in inlet to calculate the bulk Froude number over Deployment 1...**100**

Figure 5.23.2: Depth average velocity, total depth and reduced gravity in inlet to calculate the bulk Froude number over Deployment 2...**100**

Figure 5.23.3: Depth average velocity, total depth and reduced gravity in inlet to calculate the bulk Froude number over Deployment 3...**101**

Figure 5.24.1: Layer velocities, heights and reduced gravity during exchange flows in inlet to calculate internal Froude numbers over Deployment 1 (1 represents the top layer and 2 represents the bottom layer in inlet)...**101**

Figure 5.24.2: Layer velocities, heights and reduced gravity during exchange flows in inlet to calculate internal Froude numbers over Deployment 2 (1 represents the top layer and 2 represents the bottom layer in inlet)...**102**

Figure 5.24.3: Layer velocities, heights and reduced gravity during exchange flows in inlet to calculate internal Froude numbers over Deployment 3 (1 represents the top layer and 2 represents the bottom layer in inlet)...**102**

Figure 5.25.1: Difference in layer velocities and reduced gravity during exchange flows in the inlet to calculate the shear Froude number over Deployment 1...**105**

Figure 5.25.2: Difference in layer velocities and reduced gravity during exchange flows in the inlet to calculate the shear Froude number over Deployment 2...**106**

Figure 5.25.3: Difference in layer velocities and reduced gravity during exchange flows in the inlet to calculate the shear Froude number over Deployment 3...**106**

Figure 5.26: Distribution of Fr_{bulk} in inlet under different flow conditions. Top: Deployment 1; Middle: Deployment 2; Bottom: Deployment 3...**107**

Figure 5.27: Distribution of F_{Δ} under different exchange flows in the inlet...**108**

Figure 5.28: Distribution of G under different exchange flows in the inlet...**108**

Figure 5.29: F_{Δ}^2 compared to inlet turbidities (left) and percent difference in turbidities in the inlet (right). Top: Deployment 1; Middle: Deployment 2; Bottom: Deployment 3...**109**

Figure 5.30: Ranges of bottom layer turbidities in the Froude Number plane. Top: Deployment 1; Middle: Deployment 2; Bottom: Deployment 3...**111**

Figure 5.31.1: Fr_{bulk} (left), F_1 (center), F_2 (right) compared to inlet turbidities over Deployment 1...**112**

Figure 5.31.2: Fr_{bulk} (left), F_1 (center), F_2 (right) compared to inlet turbidities over Deployment 2...**112**

Figure 5.31.3: Fr_{bulk} (left), F_1 (center), F_2 (right) compared to inlet turbidities over Deployment 3...**113**

Figure 5.32: G^2 compared to percent difference in layer turbidities within the inlet. Left: Deployment 1; Center: Deployment 2; Right: Deployment 3...**113**

Figure 5.33: Dotted blue line shows a velocity profile from HR Profiler and the solid line shows the log law fit to the profile 0.2m above the bed...**114**

Figure 5.34: Compare bed stress (blue dots) to critical bed stress (red line) at the inlet bed...**115**

Figure 5.35: Effect of $|u_*|$, based on HR Profiler, on bottom layer turbidity in the inlet...**115**

Figure 5.36. Shields curve for critical bed stress...**116**

Figure 5.37: Bed stress predicted by applying log law to ADCP data over Deployment 1...**117**

Figure 5.38: Bed stress predicted by applying log law to ADCP data compared to turbidities (left) and percent difference in turbidity (right) along inlet water column over Deployment 1...**118**

Figure 5.39: Streamwise velocity profiles from ADCP over Deployment 2 in blue dots and log law fits to 0.8m above the bed in red lines...**118**

Figure 5.40: u' and w' from Vector data over Deployment 2...119

Figure 5.41.1: u' (blue) and w' (black) for burst with maximum average u (top) and corresponding SNR (middle) and *Correlation* (bottom) for beam 1 (black), 2 (blue), and 3 (green)...120

Figure 5.41.2: u' (blue) and w' (black) for burst with maximum average w (top) and corresponding SNR (middle) and *Correlation* (bottom) for beam 1 (black), 2 (blue), and 3 (green)...120

Figure 5.41.3: u' (blue) and w' (black) for burst with maximum single u (top) and corresponding SNR (middle) and *Correlation* (bottom) for beam 1 (black), 2 (blue), and 3 (green)...121

Figure 5.41.4: u' (blue) and w' (black) for burst with maximum single w (top) and corresponding SNR (middle) and *Correlation* (bottom) for beam 1 (black), 2 (blue), and 3 (green)...121

Figure 5.41.5: u' (blue) and w' (black) for burst with peak u' (top) and corresponding SNR (middle) and *Correlation* (bottom) for beam 1 (black), 2 (blue), and 3 (green)...122

Figure 5.41.6: u' (blue) and w' (black) for burst with peak w' (top) and corresponding SNR (middle) and *Correlation* (bottom) for beam 1 (black), 2 (blue), and 3 (green)...122

Figure 5.42: Bed stress based on Reynolds stress (left) and log law (right) over Deployment 2...123

Figure 5.43: Bed stress based on log law (ADCP) vs Reynolds stress (Vector) over Deployment 2...123

Figure 5.44.1: Bed stress based on Reynolds stress after filtering out wave component over Deployment 2...124

Figure 5.44.2: Bed stress based on Reynolds stress after filtering out wave component, using a 15 second average, over Deployment 2...125

Figure 5.45: Method for finding $|\overline{W}_j|$ based on power spectra, S_{ww} (m^2/s). Blue line represents the least squares regression for spectra outside wave peak frequencies...126

Figure 5.46: Bed stress based on Reynolds stress after filtering by phase method to remove wave component over Deployment 2...126

Figure 5.47.1: Bed stress compared to inlet and southern lake turbidity over Deployment 2. (Left: bed stress based on log law and ADCP measurements; Right: bed stress based on Reynolds stress and Vector measurements—different averaging times due to frequency of measurements)...127

Figure 5.47.2: Bed stress compared to percent difference in turbidity in the top versus bottom layer of the inlet over Deployment 2. (Left: bed stress based on log law and ADCP measurements; Right: bed stress based on Reynolds stress and Vector measurements—different averaging times due to frequency of measurements)...127

Figure 5.48: u' and w' from Vector data over Deployment 3...128

Figure 5.49: Bed stress based on Reynolds stress after filtering out wave component, using a 15 second average, over Deployment 3...128

Figure 5.50: Bed stress compared to inlet and southern lake turbidity (left) and percent difference in turbidity in the top versus bottom layer of the inlet (right) over Deployment 3...129

Figure 5.51.1: Turbidities versus $|U|$ as measured by the ADCP and as determined by the model using USGS flowrates in the tributaries over Deployment 1...130

Figure 5.51.2: Turbidities versus $|U|$ as measured by the ADCP and as determined by the model using USGS flowrates in the tributaries over Deployment 2...131

Figure 5.51.3: Turbidities versus $|U|$ as measured by the ADCP and as determined by the model using USGS flowrates in the tributaries over Deployment 3...131

Figure 5.52: Distribution of bottom layer turbidity (NTU) in the inlet under different flow types. Top: Deployment 1; Middle: Deployment 2; Bottom: Deployment 3. (Note over Deployment 2, flow condition 2 missing outlier ~ 165.7 NTU)...133

Figure 5.53: Distribution of top layer turbidity (NTU) in the inlet under different flow types. Top: Deployment 1; Middle: Deployment 2; Bottom: Deployment 3...**133**

Figure 5.54: Distribution of top layer turbidity (NTU) in the inlet downstream from primary inlet location (where ADCP located) under different flow types over Deployment 1...**134**

Figure 5.55: Distribution of southern lake turbidity (NTU) under different inlet flow types. Top: Deployment 1; Middle: Deployment 2; Bottom: Deployment 3...**134**

Figure 5.56: Distribution of percent difference in layer turbidities in inlet under different flow types. Top: Deployment 1; Middle: Deployment 2; Bottom: Deployment 3...**135**

Figure 5.57.1: Turbidities versus N over Deployment 1...**136**

Figure 5.57.2: Turbidities versus N over Deployment 2...**137**

Figure 5.57.3: Turbidities versus N over Deployment 3...**137**

Figure 5.58.1: Distribution of turbidities when assume inlet is well mixed (i.e. $\tau_A > 10\tau_z$) (top) and all other times (bottom) over Deployment 1...**138**

Figure 5.58.2: Distribution of turbidities when assume inlet is well mixed (i.e. $\tau_A > 10\tau_z$) (top) and all other times (bottom) over Deployment 2...**138**

Figure 5.58.3: Distribution of turbidities when assume inlet is well mixed (i.e. $\tau_A > 10\tau_z$) (top) and all other times (bottom) over Deployment 3...**138**

Figure 5.59: Wind speeds at the piling cluster on the southern shelf of Cayuga Lake. N/S indicates along the North/South axis, (+) traveling to the North. E/W indicates along the East/West axis, (+) traveling to the East. Top: Deployment 1; Middle: Deployment 2; Bottom: Deployment 3...**139**

Figure 5.60.1: $|U|$ (top) and U_{abs} (bottom) compared to wind speeds to the North (left) and East (right) over Deployment 1...**140**

Figure 5.60.2: $|U|$ (top), U_{abs} (middle), and streamwise velocity measured by Vector (bottom) compared to wind speeds to the North (left) and East (right) over Deployment 2...**141**

Figure 5.60.3: $|U|$ (top), U_{abs} (middle), and streamwise velocity measured by Vector (bottom) compared to wind speeds to the North (left) and East (right) over Deployment 3...**141**

Figure 5.61: Wind stress over time (top) compared to N over the depth based on temperature profiles at indicated locations during Deployment 1...**142**

Figure 5.62: Wind stress compared to N (left) and percent difference of turbidity in the inlet (right). Top: Deployment 1; Middle: Deployment 2; Bottom: Deployment 3...**143**

Figure 5.63: Streamwise layer velocities measured by ADCP compared to u_*^{water} predicted from wind stress. Left to right and top to bottom layer depth decreases and corresponds to Table 5.3...**145**

Figure 5.64: Streamwise layer velocities measured by ADCP compared predicted streamwise layer velocities from above analysis based on wind stress. Left to right and top to bottom layer depth decreases and corresponds to Table 5.4...**147**

Figure 5.65: U (left) and U_{abs} (right) from ADCP measurements compared to from predicted velocity profile based on wind stress...**148**

Figure 5.66: Daily precipitation (top) and flowrates from tributaries entering Cayuga Inlet (bottom)...**148**

Figure 5.67: Conditions from 9/27/2015 through 10/4/2015...**150**

Figure 5.68: Distribution of wind speeds to the north and east when top layer turbidity was greater than bottom layer turbidity (top) and all other times (bottom)...**151**

Figure 5.69: Distribution of N in the inlet when top layer turbidity was greater than bottom layer turbidity (left) and all other times (right)...**151**

Figure 5.70: Turbidities in the inlet and southern lake and daily precipitation over Deployment 2...	153
Figure 5.71: Tributary flowrates measured by USGS gage stations over Deployment 2...	154
Figure 5.72.1: Conditions from 7/24/2016 through 7/28/2016...	155
Figure 5.72.2: Conditions from 7/16/2016 through 7/20/2016...	156
Figure 5.72.3: Conditions from 7/08/2016 through 7/13/2016...	157
Figure 5.73: Daily precipitation (left) and Cayuga Inlet Creek (CI), Sixmile Creek (SC), and Cascadilla Creek (CC) flowrates based on USGS gage stations (right) over Deployment 3...	158
Figure 5.74: Conditions from 8/10/2016 through 8/15/2016...	159
Figure 5.75: Conditions from 9/5/2015 through 9/11/2015...	160
Figure 5.76: Three significant periods of increased degree of stratification in inlet starting around 6/27/2016, 7/5/2016, and 7/14/2016...	161
Figure 5.77.1: Conditions from 6/24/2016 through 6/30/2016...	162
Figure 5.77.2: Conditions from 7/04/2016 through 7/08/2016...	163
Figure 5.77.3: Conditions from 7/13/2016 through 7/17/2016...	164
Figure 5.78: Conditions from 8/19/2016 through 8/23/2016...	165

LIST OF TABLES

Table 1.1: Sources of mean annual streamflow nutrient loads from Cayuga Inlet watershed compared to Cayuga Lake watershed using the GWLF model (Haith, 2009)...5	5
Table 1.2: Contributions of nutrients and sediment to Cayuga Lake from Cayuga Inlet...6	6
Table 4.1. Deployment periods for data acquisition...29	29
Table 4.2. Mean and median ADCP beam velocities before and after filtering over Deployment 1...32	32
Table 4.3. Mean and median HR Profiler beam velocities before and after filtering over Deployment 1...42	42
Table 4.4: Effect of <i>correlation</i> filter threshold on accuracy of ADCP data...55	55
Table 4.5.1: Comparison of Cornell ADCP and IAWWTP ADP velocity data over Deployment 1...59	59
Table 4.5.2: Comparison of Cornell and IAWWTP ADP velocity data over Deployment 2...60	60
Table 4.6: Adjustable parameters in U_{model} for each deployment...62	62
Table 5.1.1: Mean, median, standard deviation and maximum for raw turbidity over Deployment 2...80	80
Table 5.1.2: Mean, median, standard deviation and maximum for turbidity filtered by 2-hour periods over Deployment 2...82	82
Table 5.1.3: Mean, median, standard deviation and maximum for turbidity data filtered by every 100 measurements over Deployment 2...83	83
Table 5.2.1: Percentage frequency of described flow conditions in the inlet over Deployment 1...88	88
Table 5.2.2: Percentage frequency of described flow conditions in the inlet over Deployment 2...88	88
Table 5.2.3: Percentage frequency of described flow conditions in the inlet over Deployment 3 (based on IAWWTP ADCP)...89	89
Table 5.3. Mean, median, and standard deviation of layer 2 heights (height above bed at which direction of flow switches during an exchange flow), H_2 ...104	104
Table 5.4: Slopes and R^2 values for streamwise layer velocities compared to u_*^{water} predicted from wind stress...145	145
Table 5.5: Slopes and R^2 values for streamwise layer velocities compared to predicted streamwise layer velocities based on wind stress...147	147
Table A.1: Worst case 95% uncertainty intervals for field experimental measurements...169	169

Chapter 1 Motivation

1.1 Cayuga Lake Assessment

Characteristics of Cayuga Lake as listed by Schweitzer (2010):

Length: 61.4 km (38.2 miles)

Average width: 2.8 km (1.75 miles)

Maximum width: 5.6 km (3.5 miles)

Mean depth: 54.5 m (179 feet)

Maximum depth: 132.6 m (435 feet)

Watershed: 2033 km² (502365.2 acres)

Perennial Tributary Inflows: 140

Cayuga Lake is a main drinking water source as well as a popular recreation lake. Bolton Point Municipal Water System draws water from the lake for drinking water servicing approximately 30,000 people (NYSDEC, 2015). The southern end of Cayuga Lake, which Cayuga Inlet flows into, was listed as impaired in 1998, cited for “nutrient (phosphorus) and silt/sediment loads from various sources throughout the watershed result in the algal/plant growth” (NYSDEC, 2015). The New York State Department of Environmental Conservation lists the water supply on the southern end of Cayuga Lake as threatened and both public bathing and recreation as impaired due to “periodic algal blooms and aquatic plant growth along the shore”. The presence of light and nutrients, along with the temperature of water, impacts the growth rate, abundance, and species composition of phytoplankton. Diatoms, green algae, blue-green algae, and cryptophytes are the main phytoplankton species reported in Cayuga Lake (Callinan, 2001). The abundance of each species varies annually and these phytoplankton are the base of the food web. In terms of macrophytes, these species typically live in littoral zones, such as the southern shelf of the lake, and changes in the total biomass and species composition have been observed over time (Genesee/Finger Lakes Regional Planning Council, 2000).

Macrophytes can stabilize sediments with root structures and dissipate wave energy with stems and leaves, however if species become highly abundant this can interfere with water uses and certain nuisance species are a concern (Genesee/Finger Lakes Regional Planning Council, 2000).

Phosphorus has been identified as the limiting nutrient for algal growth in the lake (NYSDEC, 2007). The southern end of Cayuga Lake has been placed on the EPA 303d list of impaired waters, therefore it is required that a total maximum daily load (TMDL) be established for phosphorus (SPDES Permit NY0244741, 2013). To develop an appropriate standard, it is critical to determine the transport and fate of phosphorus entering this end of the lake. After a water quality study completed by Callinan (2001) the NYSDEC recommended continued efforts to control nutrient and sediment loads, specifically to the southern lake; studying hydrodynamics influencing of water quality of the southern lake; and assessing impairment sources and potential issues.

It is important to note the natural system on the southern end of the lake was a wetland until developed primarily for recreational use (Merrick, 2014). Thus, we should expect higher turbidity values and more plant growth in the southern end of the lake. Phosphorus sources are due to natural processes as well as human activities. The inlet transitioned from more industrial uses in the early 1900s to recreational as the city of Ithaca was further developed. The inlet was also dredged and shaped to be used as a flood control channel (Merrick, 2014). In the town of Ithaca, areas such as Stewart park, Treman Marine park, and the Ithaca High School used to be marsh lands, however, they have been developed to support the community. Studies completed by Effler (2014) with the Upstate Freshwater Institute (UFI) looking at the water quality of the southern end of Cayuga Lake found a disconnect between the phosphorus loading and the perceived degraded water clarity on the shelf. This perceived lower water clarity has been more associated with increased tripton, which is inorganic particle matter suspended in the water column, rather than phytoplankton, with which the state has voiced concern.

1.2 Cayuga Inlet Assessment

Cayuga Inlet and Fall Creek flow into the southern end of the lake (Figure 1.1), where Cascadilla Creek and Sixmile Creek enter the Inlet upstream of entering the lake, and account for 40% of the total inflow to the lake (Schweitzer, 2010).

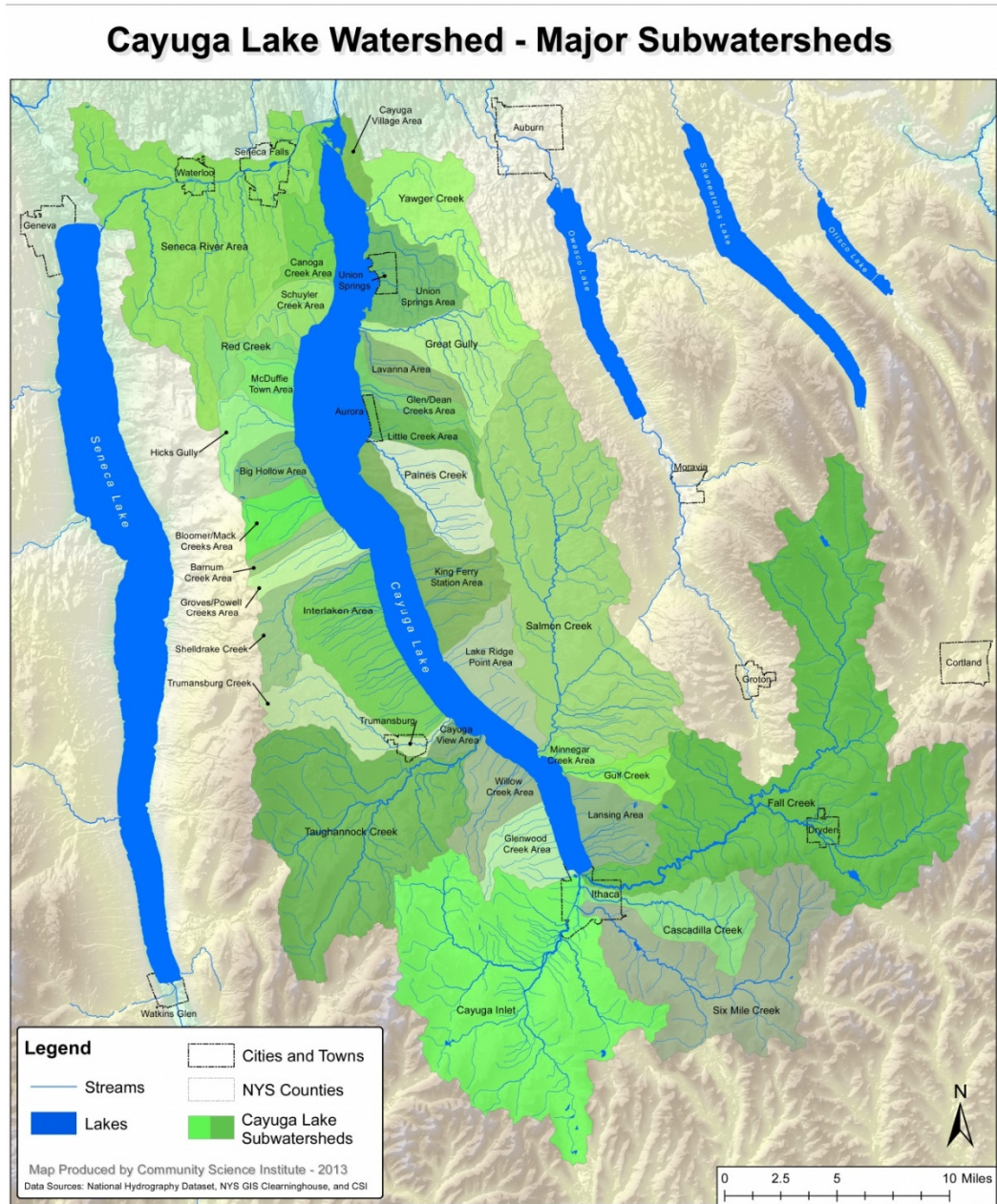


Figure 1.1: Subwatersheds of Cayuga Lake.

These inflows are known for carrying nonpoint source phosphorus and turbidity loadings. A lake monitoring and modeling study completed by UFI and Cornell University (2014) looking at the bioavailable phosphorus entering specifically the southern shelf of the lake found that 87% of this phosphorus entered from the tributaries while the two wastewater facilities only contributed 7% and the Lake Source Cooling facility contributed 6%. Figure 1.3 shows a visible suspended sediment plume entering the southern lake through the inlet in April, 2014.

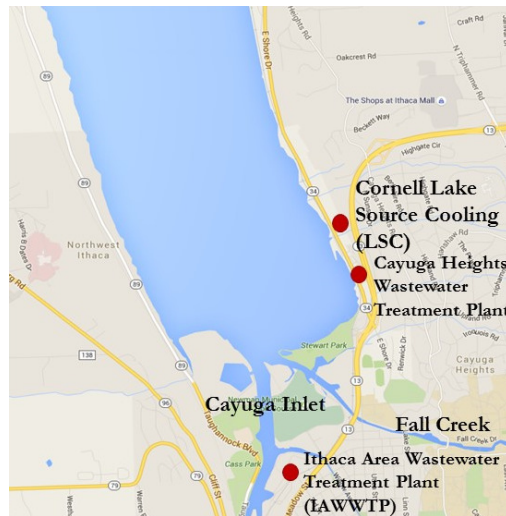


Figure 1.2: Map of the southern end of Cayuga Lake and Cayuga Inlet and Fall Creek inflows, as well as the three point sources which discharge into the southern end.



Figure 1.3: Visible suspended sediment load entering southern Cayuga Lake through Cayuga Inlet in April 2014.

The nutrient and sediment loads to Cayuga Lake were modeled in 2009 by Cornell's Department of Biological and Environmental Engineering and the Cayuga Lake Watershed Network. This study by Haith (2009) applied the GWLF model and revealed that phosphorus sources were primarily agricultural runoff (~50%) and groundwater (~23%). In the entire watershed farmland makes up approximately 52% of the land. In terms of per hectare sources of phosphorus, agricultural and urban lands contributed the same amount, ~0.5 kg/ha-yr. As mentioned the NYSDEC lists the southern end of the lake as impaired in part due to sediment loads, however using the GWLF model sediment loads overall were low, with about 0.08 Mg/ha per year for the whole watershed. The model does neglect sediment loads from roads and streambank erosion. The major source of sediment was identified as erosion from croplands and disturbed lands.

Table 1.1: Sources of mean annual streamflow nutrient loads from Cayuga Inlet watershed compared to Cayuga Lake watershed using the GWLF model (Haith, 2009).

	Cayuga Inlet Watershed (%)	Total Cayuga Lake Watershed (%)
<i>Areas</i>		
Agriculture	52	29
Forest and Brush	33	55
Other Rural	2	0
Urban	12	15
<i>Total Phosphorus</i>		
Runoff:		
Agriculture	47	27
Forest and Brush	3	4
Other Rural	6	11
Urban	12	15
Groundwater Discharge	23	9
Point Sources	7	29
Septic Systems	2	4

The evaluation of the Cayuga Lake Watershed found Cayuga Inlet watershed as the second largest sub-watershed at 24081 ha (Figure 1.1). The contributions of Cayuga Inlet watershed to the lake are shown in Table 1.2. The inlet watershed was the third largest source of total phosphorus

(12.9%) only behind Fall Creek (largest sub-watershed) and Salmon Creek (third largest sub-watershed) and the third largest source of sediment (9.7%) only behind Fall Creek watershed (15.4%) and Salmon Creek watershed (17.3%) (Haith, 2009). It is important to understand the processes controlling the transport of loadings from Cayuga Inlet. A better understanding of the physical transport processes in the inlet will enable a clearer evaluation of loading impacts and overall water quality.

Table 1.2: Contributions of nutrients and sediment to Cayuga Lake from Cayuga Inlet.

Dissolve Phosphorus (Mg/yr)	7.5
Total Phosphorus (Mg/yr)	12.6
Sediment (Mg/yr)	1477

A study completed by Prestigiacomio (2016) focused specifically on bioavailable phosphorus entering Cayuga Lake from four of the main tributaries; Salmon Creek, Fall Creek, Cayuga Inlet Creek, and Sixmile Creek (note Cayuga Inlet Creek and Sixmile Creek (along with Cascadilla Creek) enter Cayuga Inlet, that we are focused on for this study, before entering the lake). The study found nonpoint inputs were dominantly sourcing phosphorus to the lake. The highest mean bioavailable phosphorus was from the tributary with the highest agricultural land use (68%), Salmon Creek. Recall the agricultural land use for Cayuga Inlet is also significant, at 52%. Cayuga Inlet Creek and Sixmile Creek together introduced the largest load of particulate phosphorus, 24.9%, but the third largest load of bioavailable phosphorus, 9%, behind Fall Creek and Salmon Creek. It was also found in this study, agreeing with Effler (2014), that bioavailable phosphorus accounted for only a small percentage, 26%, of the total phosphorus. 70% of this bioavailable phosphorus entered the lake under high flow events.

Suspended sediment is listed as one of the impairment causes on the southern shelf of Cayuga Lake, along with nutrients. For this study, we focus on suspended sediment, which also affects the cycling of nutrients in a water body, such as phosphorus (Søndergaard, 2003). Suspended sediment can carry contaminants such as calcium carbonate, iron, sulfide, and nitrogen, all of which were found

in sediment cores studied by Ludlam (1964) in Cayuga Lake. Other sediment cores taken in 1994 and reported by the Genesee/Finger Lakes Regional Planning Council (2000) in nearshore regions of Cayuga Lake found cobalt, copper, lead, nickel, and zinc. Sediment samples taken in 1996 at depths of 1-3 meters found nearshore sediments in the southeastern lake contained cadmium, copper, mercury, and nickel in concentrations above regulation levels. Some of these samples also contained high levels of pesticides as well as polyaromatic hydrocarbons. For these reasons, and the claim by NYSDEC that high sediment loads are contributing to impairment of the southern end of the lake, the focus of this study is turbidity loads.

As Cayuga Inlet has been identified as a source of phosphorus and sediment loads to the lake (Haith, 2009; Prestigiacomo, 2016) and particularly significant to overall loadings entering the southern lake (UFI, 2014), it is important to understand the specific hydrodynamic processes which occur and influence ultimate transport of these loads. These processes are also important as residence time (period of water mass retention within defined boundaries), location along the water column, and distribution of sediment along with the lake chemistry impact the potential release of contaminants from the sediment into the water (Monsen, 2002).

Chapter 2 Characterization of Physical Mechanisms in Cayuga Lake and Inlet

2.1 Seasonal Stratification

An important characteristic of lakes, which influences the physical mixing processes, is the degree of stratification. For deeper lakes, the thin upper layer is most affected by solar radiation. It is this phenomenon that causes lakes to vary in terms of stratification over different periods throughout a year. The bottom layers of a lake will receive heat energy from the upper layers when the atmosphere is warmer (spring and summer) while when the atmosphere is cooler (fall and winter) the bottom

layers will release heat energy to the upper layers (Juday, 1940). The annual variations in stratification occurring in deep lakes is often characterized by four main phases related to each season. In the spring, the lake is typically well mixed vertically and circulation occurs across the entire water body. In the summer, with increased solar radiation, a stable stratification sets in, see Figure 2.1. Warmer water rises to the top, making up the epilimnion, while colder, heavier water falls to the bottom, making up the hypolimnion. A transition zone exists between these two layers of different densities due to the different temperatures, called the thermocline. During the summer, vertical circulation of the water body is vastly decreased. In the fall, the lake returns to full mixing and circulation. And lastly, in the winter, it is possible for the lake to have a thin layer of ice on the surface and warmer water just below (Juday, 1940).

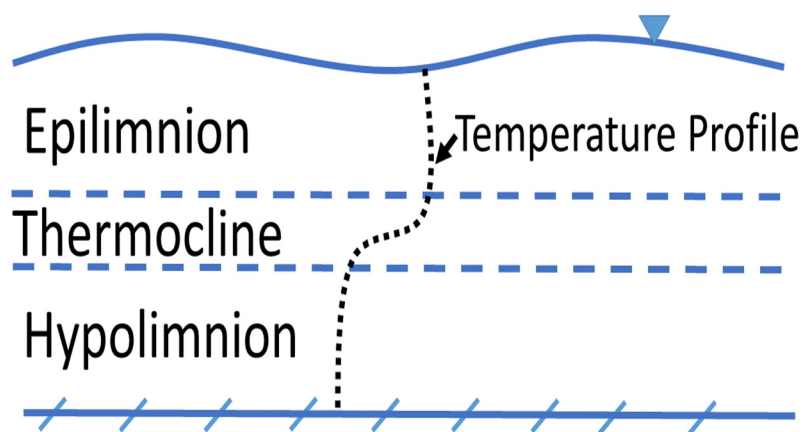
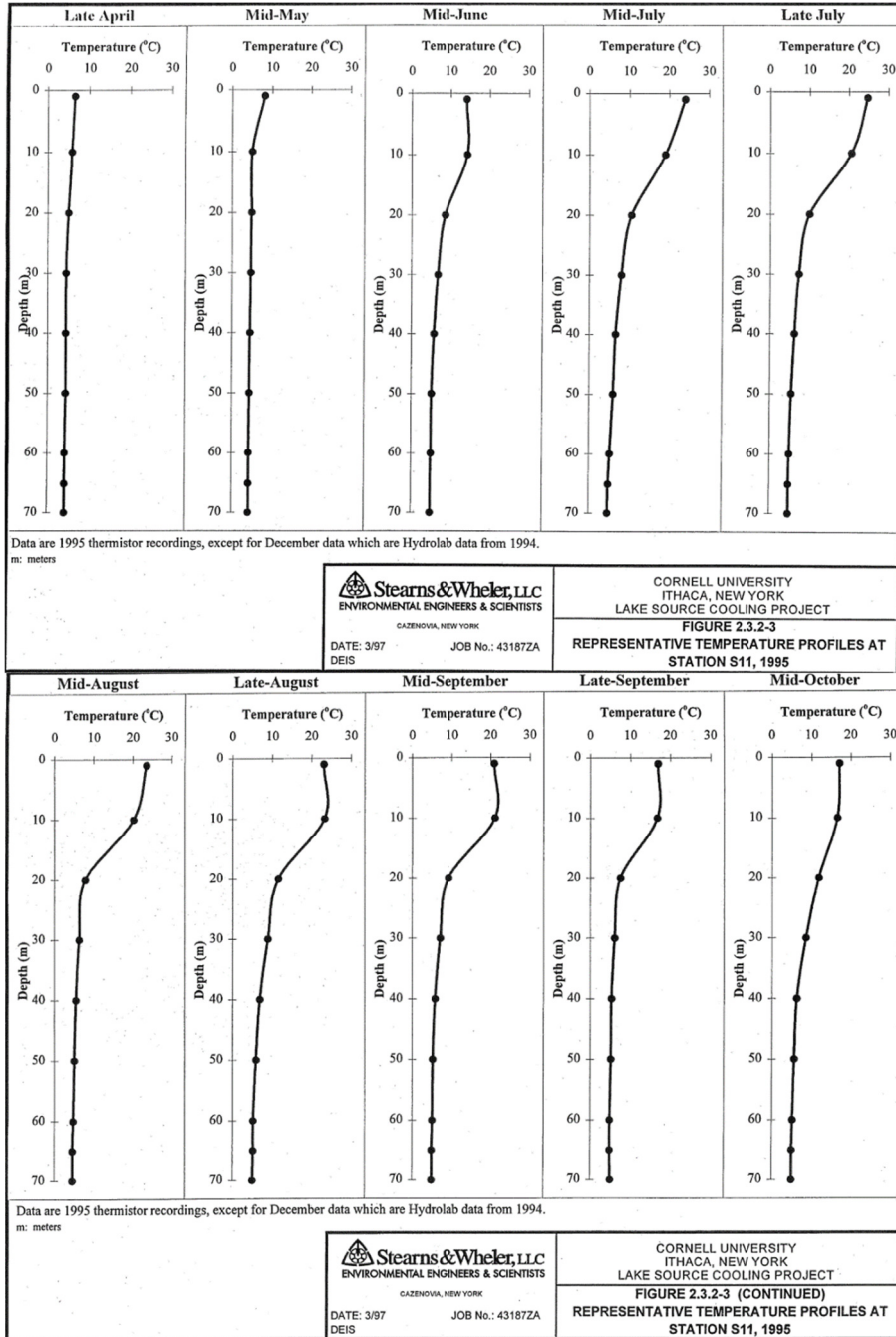


Figure 2.1: Expected temperature profile in Cayuga Lake in the summer.

Cayuga Lake follows the general stratification trends observed in deep lakes, as laid out by Juday, as shown by data from Stearns & Wheler (1997) in Figure 2.2. In the spring and the fall, the lake is typically well mixed while in the summer a stable stratification sets in. In the winter, the lake may have cooler water above warmer water, because 4°C is the densest temperature point for fresh water, thus water at a temperature between 0°C-4°C will float on 4°C water. Lambert & Sommer (2010) describe how the temperature structure in lakes and seasonal patterns influence where dissolved

oxygen is abundant and where other nutrients are abundant, which also has implications for the lake biology. Mixing across the thermocline during stable stratification can have significant impacts on the biology.



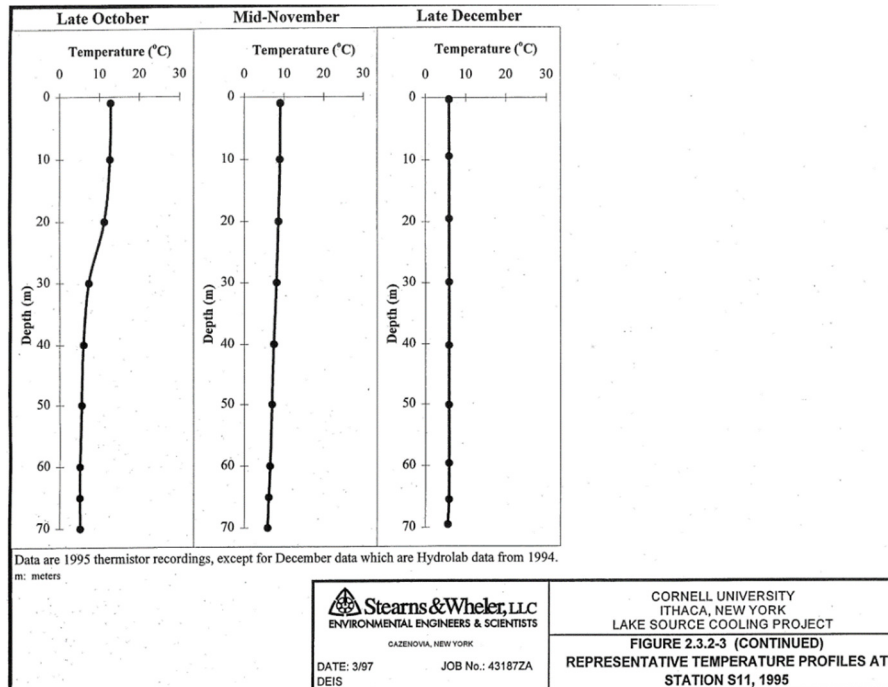


Figure 2.2: Vertical temperature profiles in Cayuga Lake from 1994 (Stearns & Wheler, 1997).

In Cayuga Lake, as in many lakes, a variety of complex physical processes occur such as internal waves, upwelling events, and gravity currents, all which are influenced by the degree of stratification in the lake as well as the temperature structures of the inflows. The vertical temperature, thus density, differences in water bodies are particularly important to the mixing. It should be noted that while temperature differences are the main cause of density differences in the water layers, the chemical composition also influences the density of these layers. Stratification and vertical fluxes in a water body are codependent. Primary production is influenced by the degree of stratification, which controls vertical fluxes, such as of nutrients, fundamental to primary production.

2.2 Lake Seiches and Upwelling Events

The main cause of water movement in lakes has been attributed to wind conditions, which influence circulation and mixing of the lake (Csanady, 1975). Seiches (oscillations in lake level) can be produced by surface-level changes caused by wind stresses. These surface waves are referred to as barotropic seiches. Various modes of basin-scale internal waves can be generated from the wind forces

over a lake. The energy in each mode is influenced by changes to the degree of stratification in the lake. In internal seiches, interface (thermocline) displacements are larger than surface displacements of typical seiches. These thermocline waves are referred to as baroclinic seiches (Csanady, 1975).

A two-layer exchange flow is proposed to exist in Cayuga Inlet. In this flow the inlet is stratified, primarily due to the temperature difference between the inflowing tributaries and southern lake which bound the inlet. Many different factors control the flow observed in the inlet, including the inflowing tributaries, lake seiches, and wind stresses over the water surfaces. A mechanism by which the exchange flow in the inlet can occur starts with a strong, sustained southerly wind stress, which is directed from the inlet out towards the lake, along its' long axis. When this wind is persistent and strong enough it will tilt the lake free water surface, causing an increased elevation downwind and a decreased elevation upwind. This results in a horizontal pressure difference, where the pressure is different at the same depth on the northern and southern ends of the lake. We represent this as the hydrostatic pressure difference, which is the difference in density between the air and water interface ($\Delta\rho$) times gravity (g) and the surface water displacement height (η_s).

$$\Delta P = \Delta\rho g \eta_s \quad (2.1)$$

When the lake is stratified, in an attempt to balance the hydrostatic pressure change, the thermocline will tilt in the opposite direction of the tilted surface. However, the displacement height at the interface is larger than that at the surface, because the density gradient across the air and epilimnetic water is orders of magnitude larger than the density gradient across the epilimnetic and hypolimnetic water, thus, the displacement at the thermocline is larger to account for this.

The bottom of the lake gently slopes up towards the south, reaching a depth of about 80m where the slope quickly increases up until the depth is about 15m. At this point, there is a gentle slope moving towards Cayuga Inlet and we refer to this area, which starts at approximately 15m deep, as the southern shelf of Cayuga Lake. When the displacement height of the thermocline is large enough the

lake's hypolimnetic water flows up onto the southern shelf. As this hypolimnetic water flows south up on the shelf, this displaces water sitting on the shelf and can force a layer of flow back into the inlet. The lake's physical characteristics are such that there is a strong potential for such events to occur. Cayuga Lake has a long main axis which is well aligned with prevailing southerly winds and the surrounding topography channels wind along the lakes axis, thus is an ideal location for the type of wind energy that sets up these events.

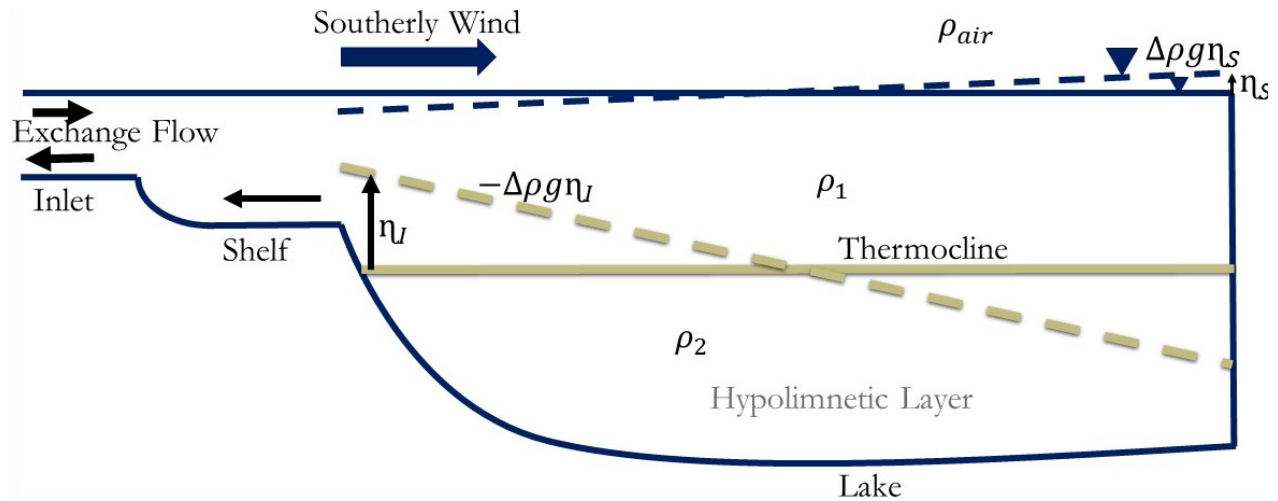


Figure 2.3: Processes causing exchange flow in Cayuga Inlet starting with a southerly wind.

This process is similar to tidal pumping effects on estuaries. With a dynamic thermocline forcing this system, the flow of hypolimnetic water to the southern shelf, which displaces previous water, acts as a source of energy to the flow conditions. Occasionally the displacement height of the thermocline can be large enough to cause an upwelling event, where hypolimnetic water reaches the surface at the southern end, filling the entire depth of the southern shelf. These upwelling events will also increase the horizontal temperature gradient which will contribute to water mass exchange between the inlet and the lake.

As the tilt at the thermocline is attempting to balance the hydrostatic pressure difference caused by a tilt in the water surface of the lake, it inevitable overshoots and oscillates. When the wind either decreases speed or changes direction, the tilt at the water surface will drop, so the tilt at the

thermocline will also drop, and again water will oscillate in the basin, attempting to restore equilibrium, but inevitably overshooting it, resulting in a rocking behavior. These seiches are expected to influence flow behavior in the inlet as well.

Wind stress is the initiating force of an upwelling event and of the seiching behavior in the lake, which are expected to influence flow conditions in the inlet. To parameterize the influence of the wind stress on the processes which occur in the lake the Wedderburn number is used (Schweitzer, 2010).

$$Wb = \frac{g'h_1^2}{u_*^2 L} \quad (2.2.1)$$

$$\text{where: } g' = \frac{\Delta\rho}{\rho_o} g \quad (2.2.2)$$

The Wedderburn number compares the balance of gravitational forces, which result in horizontal layers, and surface wind stresses, which can disrupt them. The gravitational forces are represented by g' the reduced gravity, which depends on the difference in density between the epilimnion and the hypolimnion, and the epilimnion depth, h_1 . The surface wind stresses are represented by the wind frictional velocity, u_* , and the length of the lake along the long axis at the thermocline depth, L (Fischer, 1979). For $|Wb| \gg 1$, gravitational forces are much greater than the surface wind stresses, thus, results in calm horizontal interface conditions. For $|Wb| \cong 1$, wind stresses are strong enough to cause a tilt of the water surface, which sets up the tilt of the thermocline discussed above, which leads to upwelling in the lake and potentially to an exchange flow in Cayuga Inlet. When $|Wb| = 0$, the lake is not significantly stratified. An experimental study completed by Monismith (1986) found the degree of upwelling in a reservoir is dependent on the degree of stratification.

A study on Cayuga Lake by Schweitzer (2010), calculated Wedderburn numbers for the lake for March through November using data from 1998-2009. Results showed that from March through May, as well as November, the lake was rarely stratified with Wedderburn numbers of essentially zero.

Strong stratification conditions were observed for June through October. There were multiple instances when the Wedderburn number was approximately one from June through November, which sets up the conditions for the described exchange flow in the inlet. However, much of this time the wind was not strong enough to significantly tilt the thermocline.

We are also interested in the influence of barotropic (bt) seiches, surface waves, and baroclinic (bc) seiches, thermocline waves, in Cayuga Lake on the flow behavior in Cayuga Inlet. The estimated period for the first mode of these seiches, T , depends on the length of the lake, L , and the wave speed, c . The wave speed of barotropic seiches depend on g and the depth of the lake, H , whereas the wave speed of baroclinic seiches depend on the reduced gravity, g' , and the thermocline depth, H_t .

$$T = \frac{2L}{c} \quad (2.3.1)$$

$$c_{bt} = \sqrt{gH} \quad (2.3.2)$$

$$c_{bc} = \sqrt{g'H_t} \quad (2.3.3)$$

Based on the lake average depth, the period of a 1st mode barotropic seiche is approximately 1 hour in Cayuga Lake. Based on the average thermocline depth, $\sim 20\text{m}$, and stratification (temperature difference between epilimnion and hypolimnion $\sim 15^\circ\text{C}$) the period of a 1st mode baroclinic seiche is on the order of 2.5 days in Cayuga Lake.

2.3 Two-Layer Exchange Flow

The described stratification in the inlet sets up two layers, which potential flow in different directions. Two-layer flows, such as occurring in Cayuga Inlet, can be characterized in a variety of ways, in terms of the driving forces and the interaction between the layers.

For this work, the flows observed in Cayuga Inlet were examined in terms of the internal hydraulic theory as laid out by Armi and Farmer (1986). Under this theory, three exchange flow regimes exist. The moderate flow regime represents exchange conditions, the strong flow regime

represents one layer dominating the flow, and the intermediate flow regime represents both layers present, but one is motionless. Armi and Farmer specifically looked at two-layer exchange processes through a contraction as well as over a sill. The possible solutions for a specific flow are parameterized by calculating the internal Froude number of each layer and plotting on the Froude number plane.

$$\text{Internal Froude number: } F_i = \frac{u_i}{\sqrt{g'h_i}} \quad (2.4.1)$$

i denotes the layer, where 1 represents the upper/surface layer and 2 represents the lower/bottom layer, u is the layer velocity, g' is the reduced gravity dependent on the density difference between the layers, and h is the layer height. These Froude numbers represent the balance between inertial and buoyancy forces. The composite Froude number, G , is determined by both internal Froude numbers.

$$G^2 = F_1^2 + F_2^2 \quad (2.4.2)$$

A high composite Froude number indicates inertial forces dominating, whereas a low composite Froude number indicates buoyancy forces dominating. The Froude number plane is a graph of the layer one Froude number vs the layer two Froude number.

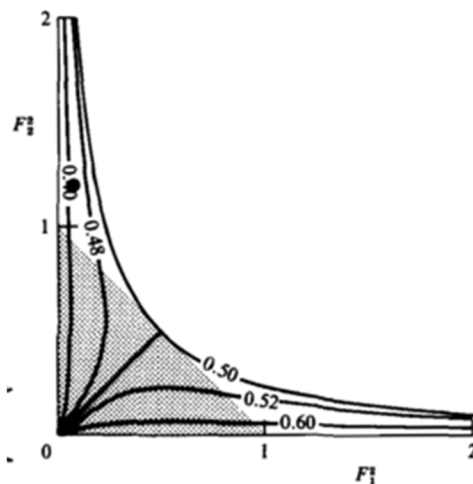


Figure 2.4: Froude number plane. The shaded region represents internally subcritical flow ($G < 1$) and the non-shaded region represents internally supercritical flow ($G > 1$) (Armi and Farmer, 1986).

When exchange flow conditions are internally subcritical ($G < 1$), buoyancy forces are dominating, thus either the flow velocities are very low or the water body is highly stratified.

The presence of net barotropic flows can cause many different types of flow in the area of interest. Past studies, by Rueda and Cowen (2005) on exchange between a freshwater embayment and a large lake, characterized the exchange process in terms of the mentioned flow regimes under internal hydraulic theory. In this study, it was found that the exchange process was determined by the difference in density of the two reservoirs and the amplitude of barotropic velocity oscillations in the channel. However, the maximal exchange condition in the embayment occurred when baroclinic forcing dominated, thus conditions of high stratification. A study of Little Sodus Bay revealed that certain winds over the Bay, when the water was stratified, caused upwelling of the lower hypolimnetic water. In the Bay, this caused an increased horizontal temperature gradient across the channel which can drive water mass exchange. In these conditions, baroclinic forcing was the main mechanism of circulation. The degree of stratification was also found to affect turbulence. Bottom friction can play a role in the exchange process, more so in shallow long straits than short deep straits. The internal dynamics of the embayment studied by Rueda and Cowen was shown to affect the exchange process depending on the degree of stratification and wind events. The internal mixing and exchange rate are related in a system. It was found that baroclinic processes in Little Sodus Bay were effective mechanisms for internal mixing. Density and wind driven processes were the main mechanisms of transport. An increase in transport was observed in the Bay under stronger and more frequent upwelling events. This transport was much higher than that observed under barotropic forcing. Transport was also increased in the surface layers under higher stratification. The study noted that the frequency and duration of upwelling events in the Bay also effects patterns of primary production, as hypolimnetic water entering the embayment could increase net phytoplankton production rates (Rueda and Cowen, 2005).

The upwelling that can occur at the southern shelf of Cayuga Lake and the general barotropic and baroclinic seiches within the lake can influence inlet flow behavior, impacting transport. Internal mixing in the inlet, particularly when the inlet is stratified to some degree, is also expected to be important to transport of suspended sediment.

2.4 Vertical Mixing

The greater the stratification in the inlet, the less vertical mixing is expected, as a strong vertical density gradient inhibits vertical transport of momentum and energy. However, an increase in horizontal mixing is expected as mechanical energy is restricted into horizontal planes. During exchange flows we expect greater stratification, which will reduce vertical mixing, but may also have increased shear, which increases turbulence and vertical mixing. To characterize the degree of stratification in a water body due to density differences, the Brunt-Vaisala frequency, N , is often used.

$$N^2 = -\frac{g}{\rho_0} \frac{d\bar{\rho}}{dz} \quad (2.5)$$

Sometimes referred to as the stability or buoyancy frequency, N , is related to the change in density over the depth in a water body. The change in density over the depth of fresh water bodies is often due to temperature differences, but high suspended sediment concentrations can also contribute. Mixing within a water body is also dependent on inflows and outflows, turbidity currents, wind, heat fluxes, and lake morphometry (Wüest, 1995).

The overall flow through the inlet and fate of turbidity loads is influenced by the amount of mixing between the exchange flow layers (Woods, 1970). For an exchange flow through a contraction, a study by Winters (2000) claimed that mixing at the controls was significant to the circulation and exchange between the connecting basins. It was also noted that two-layer exchange flows have an intermediate region between the two layers with low velocities. The intermediate region is expected to

account for a significant amount of horizontal transport during an exchange flow (Winters, 2000). As mixing between two separate layers and vertical entrainment increases, the intermediate region is expected to thicken as it gains fluid from each layer. If one of the layers is supercritical, it is expected to eventually lose half of its fluid to the interfacial layer.

A study completed by Hogg (2001), on mixing of exchange flows, found the amount of turbulent mixing significantly impacted the flux of volume and mass in exchange flows. The overall water dynamics were based on a balance between inertial forces, buoyancy forces, and turbulent forces. Wüest (1995) identified turbulence as a mechanism for vertical mixing in a stratified lake. When the vertical gradient of the horizontal velocity is relatively larger than N , turbulence can be generated which may increase mixing.

2.5 Bed Sediment Resuspension

The impact of bottom sediment resuspension in the inlet on overall turbidity loads and their fate is of interest. Increased suspended particles in the water column have been attributed to resuspension of bed particles in different studies. Studies have pointed to internal solitary waves causing bottom sediment resuspension, which increases turbidity loads in the lower layers of the water column (Bogucki, 1997). Wind waves, surface wind stresses, and inflows and outflows have been identified as the main mechanisms of sediment transport in lakes (Jin, 2004). Bottom shear stress, causing resuspension of bottom sediment, was associated with wind energy resulting in waves along with current velocities. Grant and Madsen (1986) discussed the continental-shelf bottom boundary layer and wave boundary layer where shear stress and total kinetic energy result from both waves and currents. Under conditions of similar bottom roughness and velocities, shear stresses resulting from waves will be higher than from currents. Surface waves influence the bed at water depths less than half their wavelength. Surface waves influence the growth of the surface mixed layer, as well as the

growth of the bottom boundary layer. In the presence of both waves and currents, waves are most significantly impacted by stratification. (Grant and Madsen, 1986).

A study completed by Jin (2004) found in Lake Okeechobee wave height, flow velocities, and bottom shear stress were all related to each other as well as the suspended sediment concentration in the lake. The current velocities were also found to be the main mechanism transporting the suspended sediment. A study completed by Lou (2000) found in Lake Michigan, high turbidity events could be attributed to wind waves passing, causing changes in turbulence and bottom shear stress. Other studies on the Great Lakes have shown that sediment resuspension contributes to suspended sediment concentrations in the water column more than external inputs (Eadie et al., 1984; Eadie & Robbins, 1987). However, these studies have noted sediment loads from tributaries are expected to be significant and should be considered. In Lou's study of Lake Michigan, waves and currents were found to be important in the development and transport of sediment plumes as well as the generated turbulence was found to influence bottom shear stress.

It is possible to predict bed stress using velocity profiles and applying the log law (von Karmen, 1931). As shown in Crimaldi (1998), very near the bed viscous forces dominate, however after a short distance turbulence dominates in what is referred to as the log layer/region where viscous stresses are negligible. The log law is described in Equation 2.6.1, where u is the horizontal velocity, u_* is the frictional velocity, K is the Von-Karmen constant which equals 0.41, z is the water depth, and z_o is the roughness height at the bed.

$$\frac{u}{u_*} = \frac{1}{K} \ln\left(\frac{z}{z_o}\right) \quad (2.6.1)$$

The frictional velocity is related to the energy lost into the bed or in other words the strength of the bed stress. We calculate bed shear stress by Equation 2.6.2, where ρ is the water density.

$$\tau_{bed} = \rho u_*^2 \quad (2.6.2)$$

A different method for calculating the bed shear stress involves obtaining the Reynolds stress, which can be captured through velocity measurements made by pulse-to-pulse coherent sonars (Lohrmann, 1990). The bed shear stress is then calculated by Equation 2.7, where $\overline{u'w'}$ is the Reynolds stress.

$$\tau_{bed} = -\rho \overline{u'w'} \quad (2.7)$$

In order to predict the movement of bottom sediment, the bed shear stress must be compared to a critical shear stress. When the calculated bed shear stress is greater than the critical shear stress for the bed, insipient motion of bed sediment will occur. Thus, with increased bed shear stress above a specific threshold we expect increased sediment resuspension. It should be noted that increased bed shear stress will also increase the forcing required for net transport to occur in an exchange flow (Winters, 2000). Various formulas have been used to calculate the critical shear stress of a bed and are mostly dependent on the type of sediment. The formulas presented below, from (Shields, 1936), show a critical shear stress dependent on the boundary Reynolds number, where ρ_s is the density of the sediment, ρ_f is the density of the fluid, D is the diameter of the sediment type, and ν is the kinematic viscosity of the fluid.

$$\tau_{critical} = \tau_{critical}^* (\rho_s - \rho_f) g D \quad (2.8.1)$$

$$\tau_{critical}^* = 0.22 Re_{p,ex}^{-0.6} + 0.06 (10^{-7.7 Re_{p,ex}^{-0.6}}) \quad (2.8.2)$$

$$Re_{p,ex} = \frac{\sqrt{\left(\frac{\rho_s}{\rho_f} - 1\right) g D D}}{\nu} \quad (2.8.3)$$

To determine the critical bed stress, we need an idea of the type of bed sediment. Several investigations of Cayuga Lake sediments have been completed (Ludlam, 1967; Nagle et. al., 2007). In

general, the lake sediments are made up of fluvial silts, sand, clay, gravel, shale fragments, and detrital organic matter. Closer to the tributaries the sediments are typically coarse, larger particles. Sediment cores from 1994 found coarse sediments trapped in the shallow shelf and inlets. Evaluation of sediment cores taken from the littoral zone of the lake in 1973 found sediments 10-20% clay, 45-80% silt, and as high as 80% sand (Genesee/Finger Lakes Regional Planning Council, 2000).

We expect an increase in bottom sediment resuspension to cause an increase in turbidity loads, as the resuspended bed sediment adds to the suspended sediment in the water column. Whether this added suspended sediment is significant may depend on characteristics of the suspension, sediment type, as well as prior existing sediment loads in the water.

Chapter 3 Methods

3.1 Field Instruments

Velocity, temperature, and turbidity measurements along with local meteorological information were the key data utilized in this investigation. The list of equipment used, what it measures, and how it generally works can be found below:

Teledyne RD Instruments 1200 kHz Workhorse Monitor Acoustic Doppler Current Profiler

(ADCP): The ADCP has four beams (two orthogonal beam pairs) which measure velocity profiles using the Doppler effect. The beam coordinates can be converted to xyz coordinates or earth coordinates, based on the trigonometry and assuming homogeneity at the same elevation. An error velocity is also measured which is the difference between the two independent estimates of vertical velocity from each orthogonal beam pair. This measurement is used to evaluate the data quality; if the error velocity is high this indicates unreliable data that likely should be filtered out. Pings of sound are transmitted out from the ADCP at a constant frequency. As these sound waves travel they will hit

suspended particles moving in the water and reflect to the instrument. If a particle is moving away from the ADCP, the returned sound wave will have a lower frequency whereas if a particle is moving towards the ADCP, the returned sound wave will have a higher frequency. The Doppler shift is the difference in the frequencies for the transmitted sound waves and the returned sound waves. Using this shift, the ADCP calculates how fast the particle is moving; the Doppler shift is linearly proportional to the particle velocity. The average speed of these small particles is the same average speed as the water carrying them, thus we have measured the water speed. Measuring the total time for a sound wave to be transmitted and returned, and assuming constant water density and a rigid reflecting surface, the ADCP determines the depth of the particle speed that is being measured. Therefore, the ADCP measures water velocities at various depths along the water column. The ADCP uses a monostatic system, meaning the same transducer pings and listens for acoustic returns. The water column is separated into 'cells'. For each of these cells a weighted average velocity is reported, where the edges of the cell contribute only to the leading and trailing edge of the transmit pulse and the velocity measurements at the center of the cell are more heavily weighted in the average. For precise velocity measurements, low boat traffic is beneficial and minimum heave, pitch, and roll of the instrument mounting. In this experiment, the ADCP was deployed in mode 12, a short lag mode. The short lag modes have greater profiling range and higher maximum measuring velocities, but the longer lag modes are known for more precise data. In mode 12, each ping has a sequence of sub-pings that are averaged to give the final measurement. This mode provides higher resolution data and a lower standard deviation in measurements than the other short lag mode 1. Another benefit of this mode is lower power consumption which is important in long deployments. A caution is any significant orientation changes while pinging can contaminate data (Gordon, 1996).

Nortek 2000 kHz High Resolution (HR) Profiler: The HR Profiler measures velocity profiles, using the same idea as the ADCP with the Doppler effect, by measuring phase shifts with acoustic

pulses sent out. The instrument used for this work had 3 beams, measuring in two components (vertical and one horizontal). The HR Profiler transmits a pair of acoustic pulses with a known lag time and computes the Doppler phase shift. The phase shift is computed using the covariance method, where the complex covariance of the two return signals is computed and the phase shift is the arctangent of the real and imaginary parts of the covariance function. The phase shift is used to calculate velocity of particles which scattered the pulses and obtain velocity profiles along each of the oriented beams. This type of mode is called pulse coherent. The advantages of using pulse coherent are that measurements will be more accurate with lower noise and smaller cell sizes can be obtained. However, it is possible for the two pulses to interfere with one another if the reflections are of equal intensity. This can create sections of bad data that must be filtered (Rusello, 2009).

Nortek Vector: The Vector measures water velocities at a specific depth, using the Doppler effect like the previous two instruments discussed and operates in a pulse coherent mode. The Vector has three receive transducers and one central transmit transducer, thus it is a bistatic sonar. The orientation of the receive beam paths, each slanted at 30° , is such that they intersect 0.157m from the transmit beam. Three beam velocities are obtained for the sample volume, defined by the intersection of cones originating from the transducers transmitting or receiving acoustic energy. The beam velocities can be converted to arbitrary components using the geometry and can be reported in beam, xyz , or earth coordinates (Nortek AS, 2005).

Yellow Spring Instrument (YSI) Water Quality Sonde 6600V2: The 6600V2 Sonde was used to take water quality measurements. Specifically, a turbidity sensor was placed on these sondes to measure suspended sediment. The turbidity sensor is an optical sensor that measures light scattered at 90 degrees from an incident light beam sent out. This measures the relative number of particles in the water which are causing cloudiness or haziness. Turbidity is measured in Nephelometric Turbidity

Units (NTU) and all the sensors were calibrated using standards which follow the Standard Methods for the Treatment of Water and Wastewater, Section 2130B (Eaton et. al., 1998).

Sea-Bird Electronics (SBE-39 and SBE-39plus) Thermistor: Thermistors were deployed to measure water temperatures at different locations and depths in the inlet.

Onset HOBO Data Logger (U22-001): Data loggers were used to record water temperatures of the major inflowing tributaries to the inlet and on the southern shelf of the lake.

3.2 Summer/Fall 2015 Field Deployment Setup

August 20th, 2015 through October 17th, 2015 instruments were deployed in Cayuga Inlet with the goal to investigate the flow structure and how suspended sediment and vertical mixing of sediment varied in the inlet. Specifically, we wanted to observe the influence of unidirectional flows versus exchange flows, water temperature structures, and bottom sediment resuspension on turbidity loads. The different deployment locations are displayed in Figure 3.1.

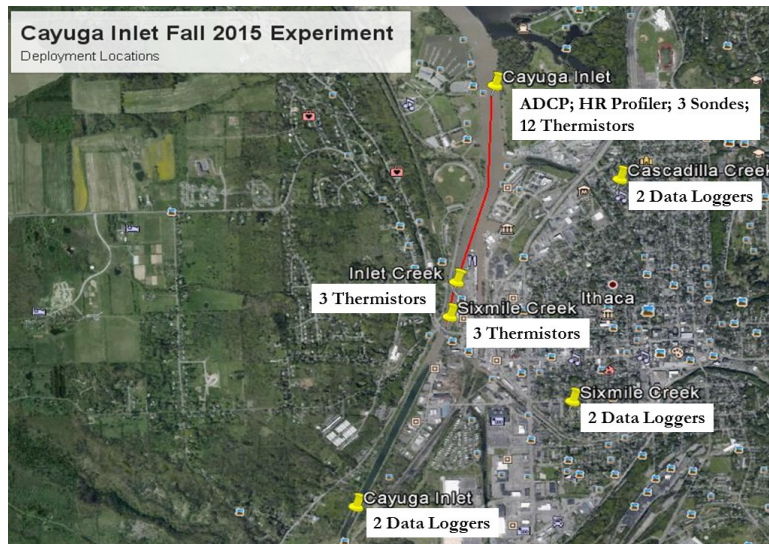


Figure 3.1: Deployment locations in Cayuga Inlet from Summer/Fall 2015 experiment and list of equipment at each location. Note Cayuga Inlet enters the lake at the top of this map.

The ADCP and HR Profiler were mounted on the base of the same frame (Figure 3.2) that rested on the bottom floor of the inlet at the top Cayuga Inlet location indicated in Figure 3.1, where

the inlet is approximately 2meters deep. The ADCP had screws holding it on the frame and the HR Profiler was strapped down to the PVC pipe. The ADCP measured 17 total cells along the water column, each 10cm tall, with the first cell approximately 0.9m above the bed. The location of the first depth cell is dependent on the blanking distance, which moves this first cell away from the transducer head, so transmit circuits can recover before the receive cycle begins. RDI suggests a minimum blanking distance of 44cm in mode 12. The requested profile from the ADCP extended from 1.19meters deep to above the water surface. Velocity measurements were recorded from August 27th, 2015 to October 5th, 2015 from the ADCP, which sent out pings every 2.5seconds for a 10minute burst, with internal averaging over every 3 pings, thus reported measurements are every 7.5seconds. The HR Profiler measured 53 total cells, each 20mm tall, with the first cell approximately 0.2m above the bed. The velocity profile from the HR Profiler extended from 1.79meters deep to 1meter deep. Velocity measurements were recorded from August 27th, 2015 to September 7th, 2015 from the HR Profiler, which sampled at 2Hz, and reported the average over every 1second, and 512 samples per burst. One sonde was mounted on the frame with the ADCP and HR Profiler, reading about 1.5meters deep, while another was mounted on the top buoy at the same location, reading about 0.5meters deep. The last sonde was just downstream of this location and approximately 0.5meters deep. All sondes were measuring the water turbidity every 2.73minutes, from August 20th, 2015 to September 29th, 2015. Two temperature measurements were taken with the HOBO data loggers at each of the inflowing tributaries indicated in Figure 3.1, Cayuga Inlet, Sixmile Creek, and Cascadilla Creek. Five HOBO data loggers were also attached to the piling cluster located on the southern shelf of Cayuga Lake (not shown in figure) at depths of 0.5meters, 1.0meters, 2.0meters, 2.5meters, and 3.0meters. All data loggers recorded water temperatures every 2minutes, for the entire deployment period. We also obtain air temperature and wind data, reported every 10minutes, from the meteorological station at this piling cluster. Thermistors were located at Sixmile Creek, Inlet Creek, and Cayuga Inlet as indicated in Figure

3.1. At Sixmile Creek three thermistors were deployed at depths of 0.2meters, 0.6meters, and 1.0meters. At Inlet Creek thermistors were deployed at depths of 0.5meters, 1.0meters, and 1.5meters. At the Cayuga Inlet location two temperature profiles were taken just downstream of this point, both with 5 temperature measurements at consistent intervals along total depths of 2.8meters and 2.4meters in the different locations. Two thermistors were also deployed at the same location as the frame with the ADCP, HR Profiler, and sondes, one 1.5meters deep and the other 0.5meters deep. All thermistors took temperature measurements every 30seconds for the entire deployment period.



Figure 3.2: Bottom frame setup deployed in the primary inlet location over Deployment 1. Holds the ADCP, ADCP battery case, HR Profiler, and 6600 Water Quality Sonde.

3.3 Summer 2016 Field Deployment Setup

June 22, 2016 through August 1, 2016 instruments were deployed in Cayuga Inlet with the goal to investigate the relation of flow conditions and temperature structures to sediment concentrations in the water column. One of the main focuses was to investigate under what flow conditions, in terms of exchange flows versus unidirectional flows and turbulence, sediment concentrations were highest in the inlet. The influence of the temperature structure in the inlet, along with the present flow conditions, on vertical mixing of sediment concentrations was also of interest. Lastly, a goal of these experiments was to reevaluate the significance of bottom sediment resuspension to turbidity loadings in the inlet, based on turbulence measurements. The different deployment locations can be seen in Figure 3.3.

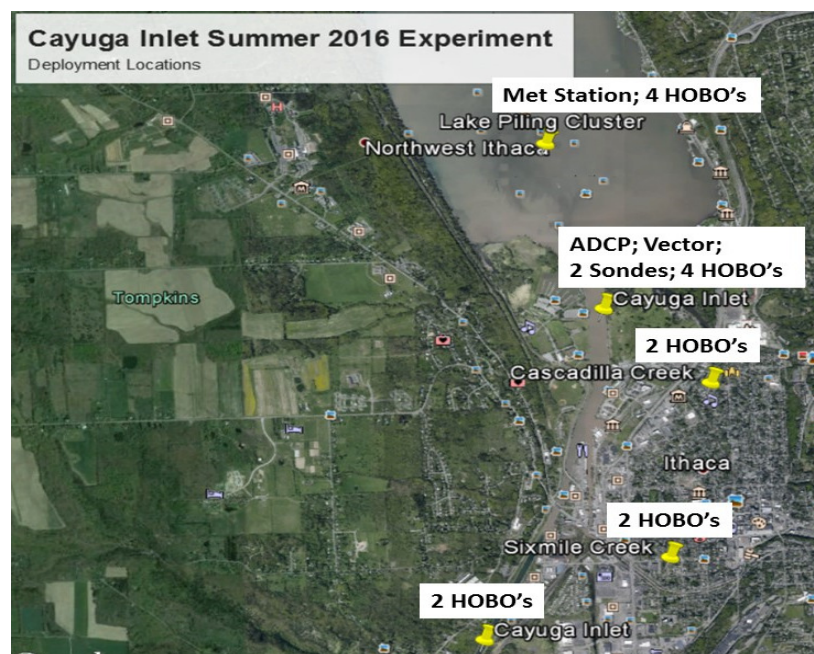


Figure 3.3: Deployment locations in Cayuga Inlet from Summer 2016 experiment and list of equipment at each location.

It should be noted that the location of the ADCP, Vector, and sondes was the same as used in the 2015 experiment and the temperature measurements for the three tributaries were also at the same locations used in the 2015 experiment. The ADCP, Vector and one sonde were mounted on the frame

resting on the bottom floor, where the inlet is approximately 2meters deep. The Vector and sonde were mounted on a vertical arm where the Vector transmitter was 69cm above the base of the frame and the sonde turbidity sensor was 54cm above the base of the frame, see Figure 3.4. The other sonde was mounted to the buoy, and the turbidity sensor was about 58cm below the surface of the water. The ADCP measured 36 total cells along the water column and above, each 10cm tall, with the first measurement approximately 0.8m above the bed. The ADCP was programmed to send out a ping per second recording 150 samples per burst within a 10-minute burst interval. The Vector measured velocity of the flow located 15cm from its transmitter, thus it was measuring approximately 0.84m above the bed. It was programmed at an 8Hz sampling rate with a burst interval of 1.5-hours, taking 1200 samples per burst. Both sondes measured turbidity and temperature in the water every 10minutes.

Temperature measurements were taken with HOBO data loggers at the piling cluster located on the southern shelf of Cayuga Lake, at the main Cayuga Inlet location where the main frame was deployed, and at Cayuga Inlet Creek, Sixmile Creek, and Cascadilla Creek tributaries. In the tributaries two data loggers were deployed, one near the deepest portion and another closer to the bank in shallower water. At the piling cluster 3 data loggers were deployed at depths of 0.5meters, 1.5meters, and 2.5meters. And at the main inlet site 4 data loggers were deployed at depths of 0.5meters, 1.0meters, 1.5meters, and 2.0meters. All data loggers recorded water temperatures every 2minutes.

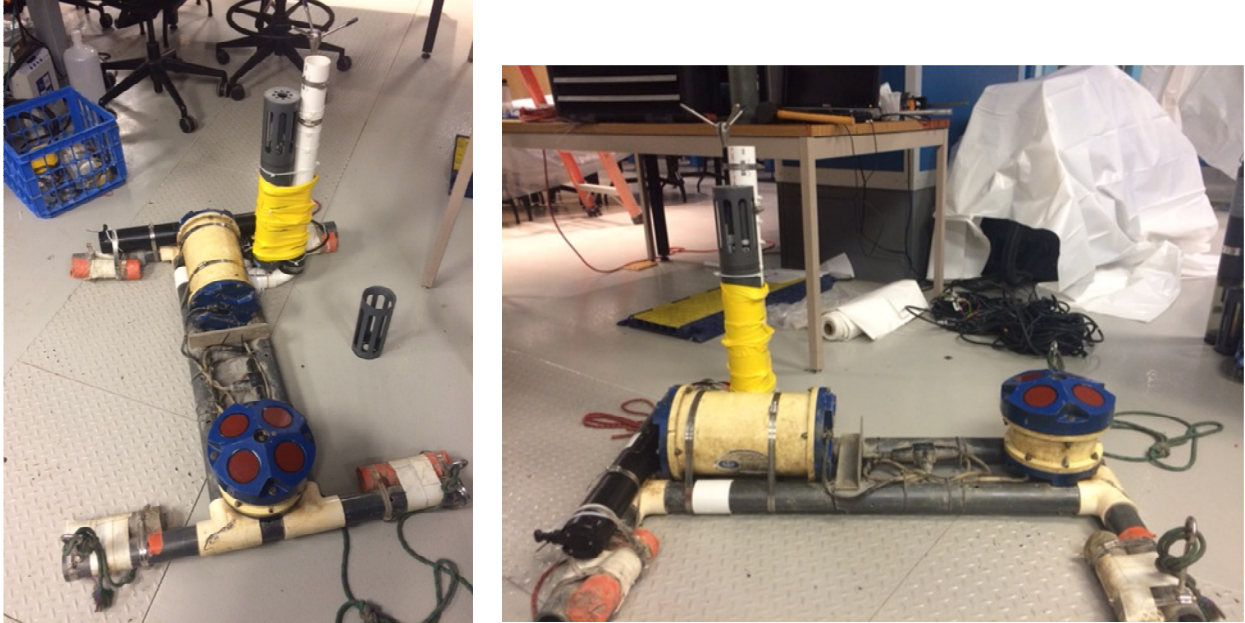


Figure 3.4: Bottom frame setup deployed in the primary inlet location. Holds the ADCP, ADCP battery case, Vector, Vector battery case, and 6600 Water Quality Sonde.

Another deployment was carried out from August 5, 2016 through September 20, 2016. However, during this deployment we encountered problems with the ADCP and were unable to obtain any data from this instrument. Also, the Vector internal program settings changed on August 22nd, 2016, which will be discussed in the results section, but this caused the Vector to use up battery life more quickly, thus the Vector lost power on August 31, 2016. All other instruments were functional and programmed and deployed with the same setup as described above.

Chapter 4 Data Validation Techniques

In the following analysis, data was gathered over 3 deployments, listed in Table 4.1.

Table 4.1. Deployment periods for data acquisition.

Deployment	Start Date	End Date
1	August 20 th , 2015	October 17 th , 2015
2	June 22 nd , 2016	August 1 st , 2016
3	August 5 th , 2016	September 20 th , 2016

4.1 Quality Control Analysis of Velocity Data

4.1.1 ADCP

The ADCP data was averaged externally, along with the internal averaging done for each set of sub-pings. Ensemble averaging was performed over set burst interval and useful to reduce random errors, potentially due to noise (i.e. thermal noise, electronic noise, etc.) in the instruments reported velocities. In Deployment 1 the instrument recorded in earth coordinates, using the heading, pitch, and roll data measurements were converted to beam coordinates. The heading, pitch, and roll measure the rotation and translation of the ADCP while deployed. In Deployment 2 the instrument recorded in beam coordinates. Recall no data from the ADCP was recovered for Deployment 3.

Correlation, reported by the ADCP, gives a measure of data quality. More precisely it measures the strength of the cross-correlation peak which determines the Doppler shift. For the ADCP maximum *correlation* is 128. This measure can indicate whether velocity measurements experienced degradation due to other particles entering along the transmit and return acoustic paths. *Echo amplitude*, reported by the ADCP, is a measure of the receivers' signal strength. The *echo amplitude* should indicate when the ADCP signal encounters the water surface as well as if big objects, such as fish or boats, pass by. Based on *echo amplitudes* recorded by all beams we determined the bin location of the water surface and all data at higher bins was discarded. In Figure 4.1, *echo amplitude* shows the water surface was detected by bin 13 for all deployments. Based on the bin length, blanking distance, height of the ADCP (defined as the base to the transducer head), and expected depth at the deployment site for Deployment 1 we expected the surface to show up near bin 13, however for Deployment 2 we expected the surface to show up near bin 14. However, overall flow conditions were very low over Deployment 2, with very little rainfall and drought conditions resulting in a shallower depth at our deployment site.

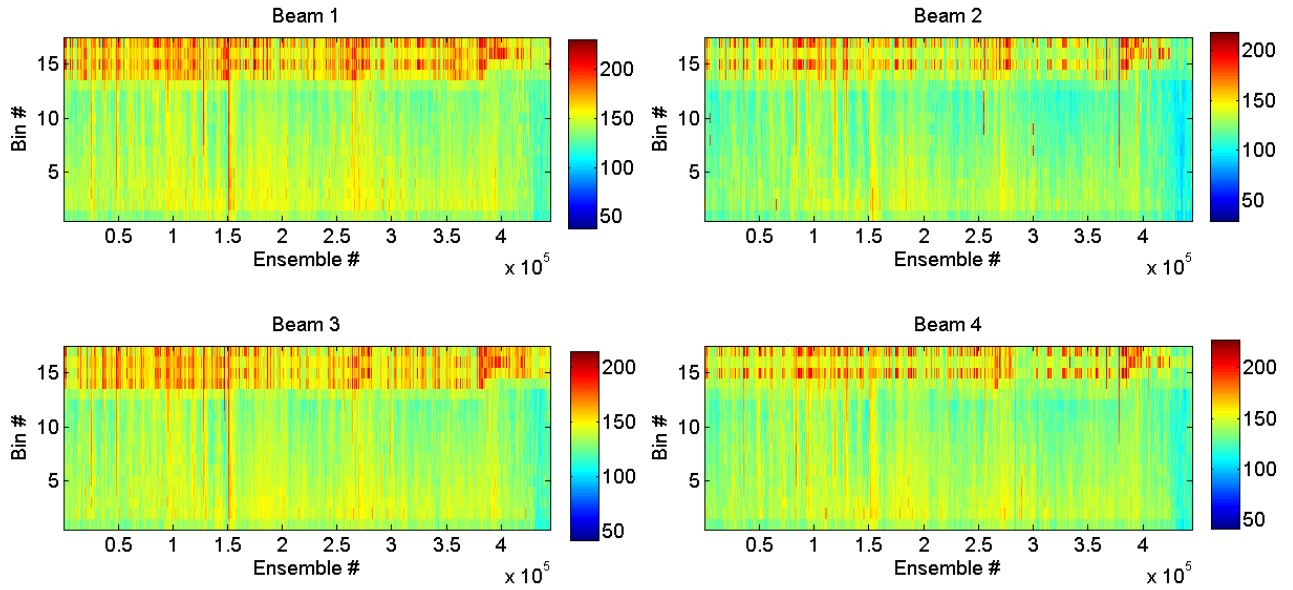


Figure 4.1: *Echo amplitudes* during Deployment 1 for each beam over all ensembles and bins.

There are no universally recommended values for *correlation* or *echo amplitude* filters and filters may vary for different data sets. For our purposes, we want coarse *correlation* and *echo amplitude* filters to remove the distinctly unreliable data. Based on histograms of *correlation* for the various deployments (Figure 4.2), a filter of *correlation* below 40 was selected. After applying this filter, 9.34% and 7.84% of data was removed from Deployment 1 and Deployment 2, respectively. For *echo amplitude*, we want to filter out abnormally high values indicating false solid targets, thus a filter of *echo amplitude* greater than 200 was selected. After applying this filter 1.21% and 4.26% of data was removed from Deployment 1 and Deployment 2, respectively. Much of the data removed under this filter occurred in isolated events, with a single peak in *echo amplitude* along the time series. For Deployment 1 and 2 there were 4 and 6 time segments, respectively, the *echo amplitude* was greater than 200 for an entire burst (2.5minutes), potentially due to significant suspended sediment loads we would not want to remove. However, turbidity measurements taken within the inlet remained below 25NTU corresponding to all these times, so we filter out these times as well.

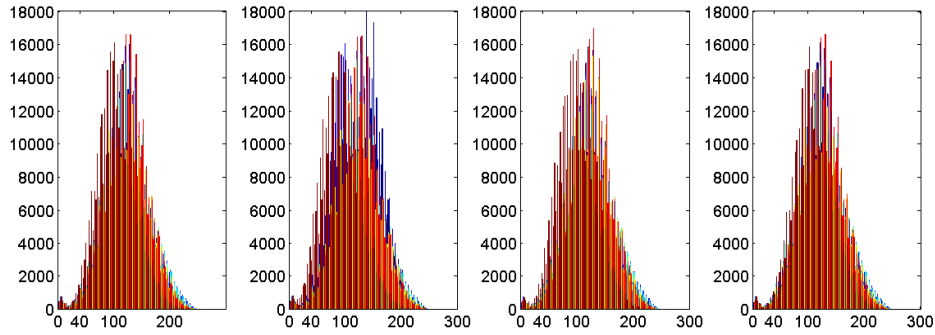


Figure 4.2: Histograms of ADCP *correlation* values for each beam.

An adaptive Gaussian window (AGW) filter, originally developed by Cowen and Monismith (1997), was used on the beam velocities, which helps remove noise within the data set. We assume the data are roughly Gaussian and noise is uniform, which was confirmed based on histograms of the raw data. Based on statistics of the data, outliers are iteratively removed. Minimum and maximum thresholds were set at extreme values ($>5000\text{mm/s}$). This filter was run for each beam velocity within each bin over each burst. If one beam velocity was removed by the filter, all corresponding beam velocities at the same timestamp in that bin were removed. Results of this filter are shown in Figure 4.3, as data that falls in the tails of a normal distribution plot was removed.

Table 4.2. Mean and median ADCP beam velocities before and after filtering over Deployment 1.

Beam	Mean Velocity before filters (m/s)	Median Velocity before filters (m/s)	Mean Velocity after filters (m/s)	Median Velocity after filters (m/s)
1	1.53	-0.0061	-0.0049	-0.0023
2	0.775	-0.0047	-0.00046	-0.00076
3	3.28	0.0043	-0.0014	-0.0011
4	6.06	0.00049	-0.0031	-0.0019

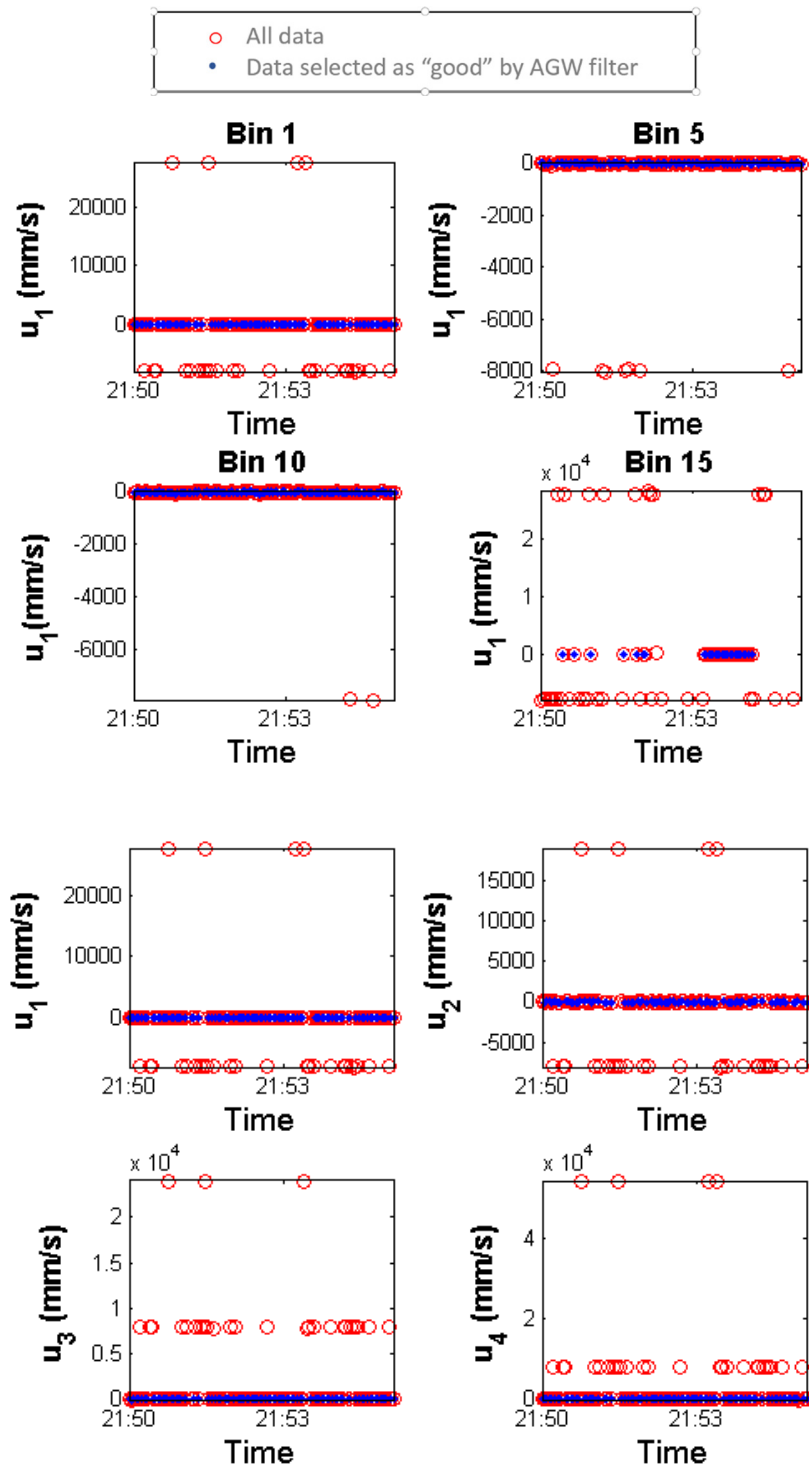


Figure 4.3.1: ADCP beam velocities for different bins at burst 1000 before and after the AGW filter applied to Deployment 1.

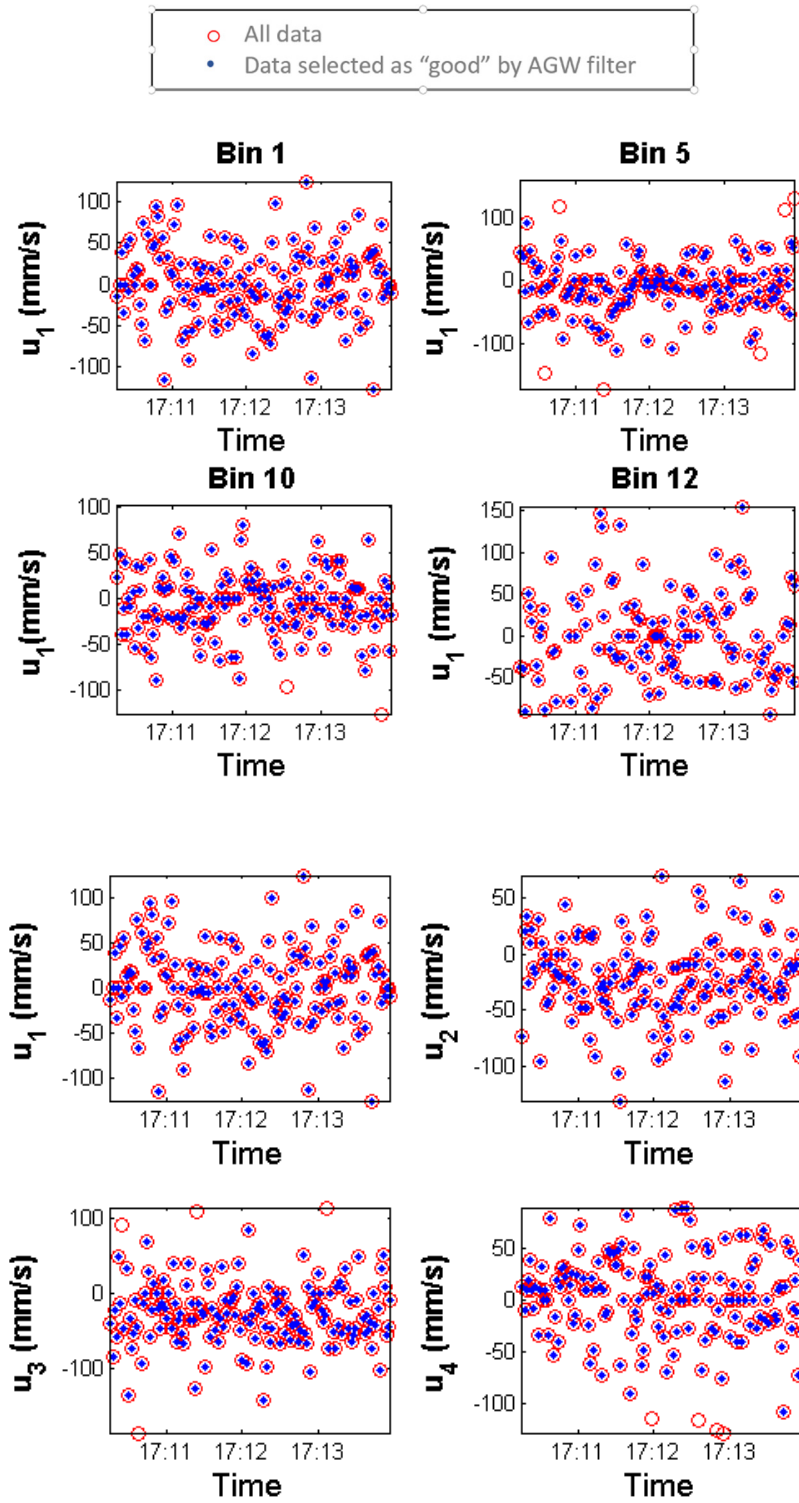


Figure 4.3.2: ADCP beam velocities at burst 50 and beam 1 velocities at different bins at burst 50 before and after the AGW filter applied to Deployment 2.

Once beam velocities were filtered, we converted to xyz coordinates. Equations (4.1.1)-(4.1.3) convert the reported beam velocities to xyz velocities. The ADCP beam angle is represented by θ , which is 20 degrees, and u_i represents the i beam velocity. The converted velocities u , v , and w are shown in Figure 4.4, where u and v are the horizontal velocities and w is the vertical velocity in the inlet.

$$u = \frac{u_3 - u_4}{2 \sin \theta} \quad (4.1.1)$$

$$v = \frac{u_1 - u_2}{2 \sin \theta} \quad (4.1.2)$$

$$w = \frac{u_1 + u_2 + u_3 + u_4}{4 \cos \theta} \quad (4.1.3)$$

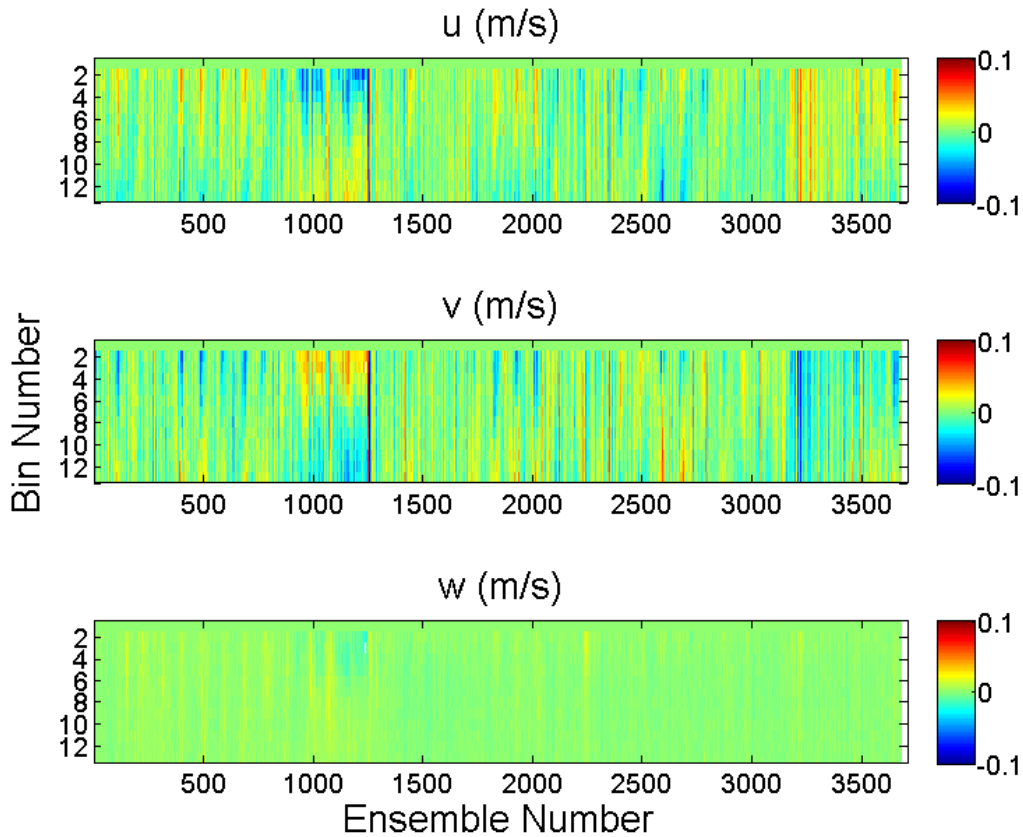


Figure 4.4.1: Velocities in xyz coordinates from the ADCP for Deployment 1, over the ensemble number (time) and bin number (depth), where the lower bin numbers are at greater depths and highest bin number near water surface (scale set to $\pm 0.1 \text{ m/s}$, with few larger velocities: $-0.14 \text{ m/s} < u < 0.15 \text{ m/s}$; $-0.19 \text{ m/s} < v < 0.15 \text{ m/s}$; $-0.04 \text{ m/s} < w < 0.03 \text{ m/s}$).

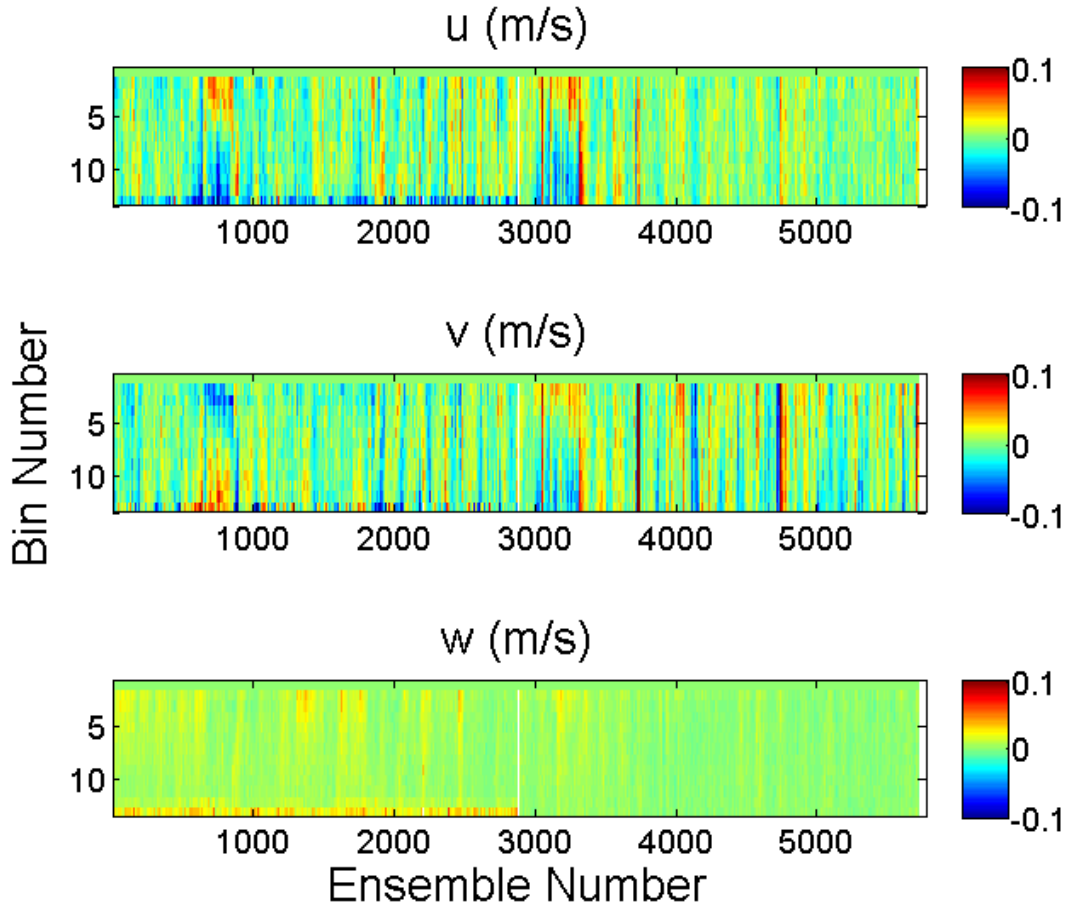


Figure 4.4.2: Velocities in xyz coordinates from the ADCP for Deployment 2, over the ensemble number (time) and bin number (depth), where the lower bin numbers are at greater depths and highest bin number near water surface (scale set to $\pm 0.1\text{m/s}$, with few larger velocities: $-0.33\text{m/s} < u < 0.14\text{m/s}$; $-0.23\text{m/s} < v < 0.30\text{m/s}$; $-0.03\text{m/s} < w < 0.12\text{m/s}$).

Each time the frame holding the ADCP was redeployed its' orientation changed. The streamwise velocity, u_{sw} , is calculated from Equation 4.2:

$$u_{sw} = u\cos(\theta) + v\sin(\theta) \quad (4.2)$$

Where θ is dependent on the orientation of our horizontal velocity components relative to the streamwise direction (dominant flow direction through the inlet), determined by $\tan^{-1}(v/u)$, where we find the most frequent angle over each redeployment. Over Deployment 1 the most frequent θ was 128 degrees. Over Deployment 2, the ADCP frame was redeployed three times. The most frequent

θ for each were 97.4, 100, and 92.8 degrees. The mean and median streamwise velocities over each burst were calculated. In the following analysis, a positive streamwise velocity indicates flow directed out towards the lake while a negative streamwise velocity indicates flow from the lake into the inlet.

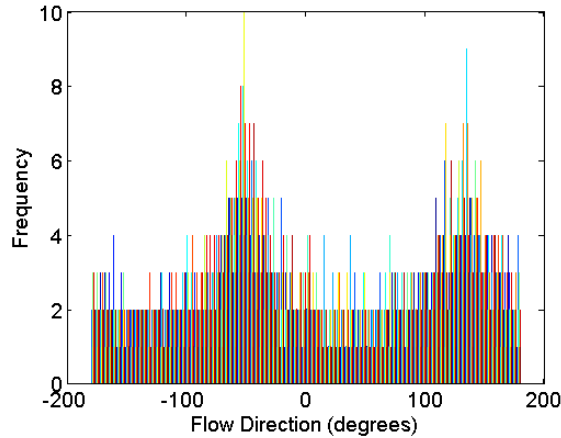


Figure 4.5.1: Histogram of θ , angle between ADCP recorded u and dominant flow direction through the inlet for Deployment 1.

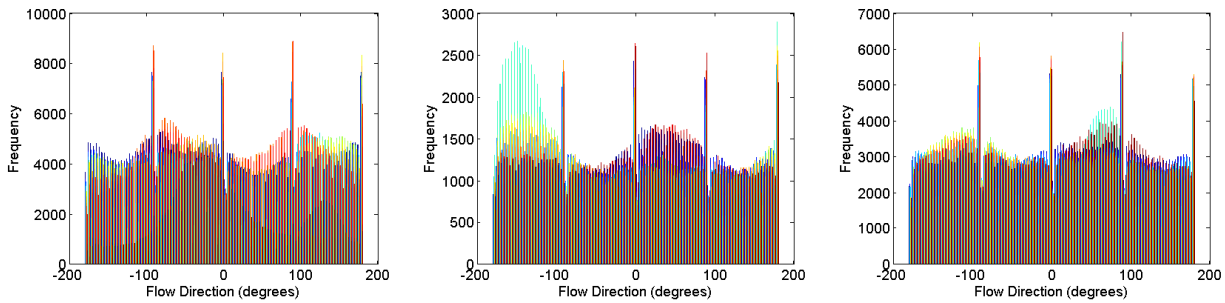


Figure 4.5.2: Histogram of θ , angle between ADCP recorded u and dominant flow direction through the inlet over Deployment 2.

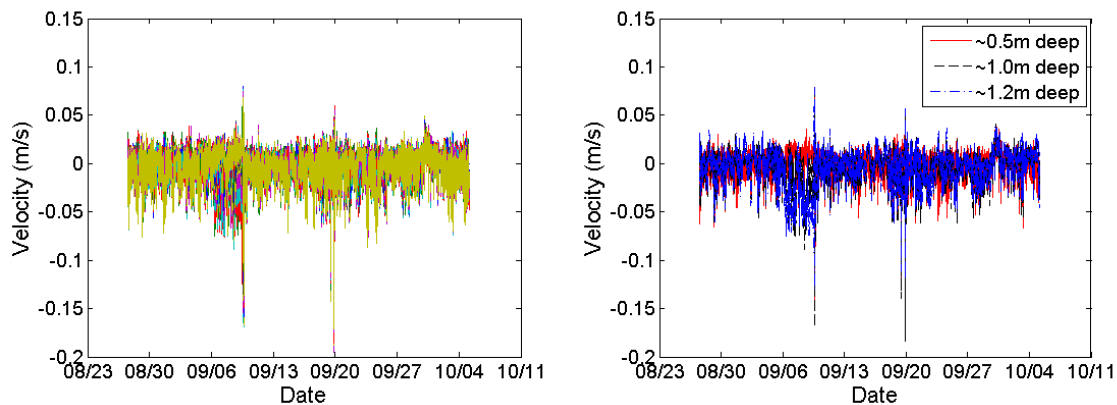


Figure 4.6.1: Individual ADCP streamwise bin velocities, u_{SW} , over time over Deployment 1 (all bins: left; bins at approximately 0.5m, 1m, and 1.5m deep: right).

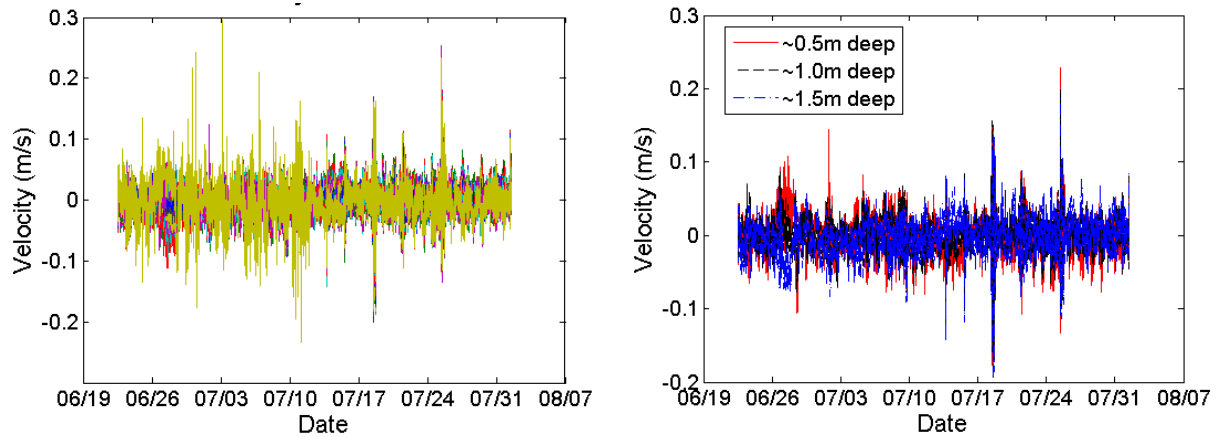


Figure 4.6.2: Individual ADCP streamwise bin velocities, u_{sw} , over time over Deployment 2 (all bins: left; bins at approximately 0.5m, 1m, and 1.5m deep: right).

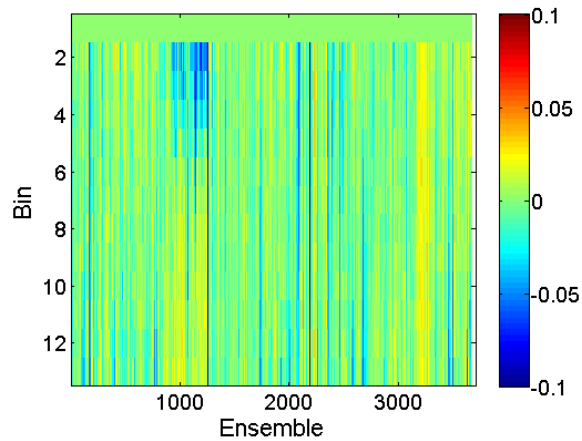


Figure 4.7.1: ADCP streamwise velocities, u_{sw} , (m/s) over the ensemble number (time) and bin number (depth) over Deployment 1.

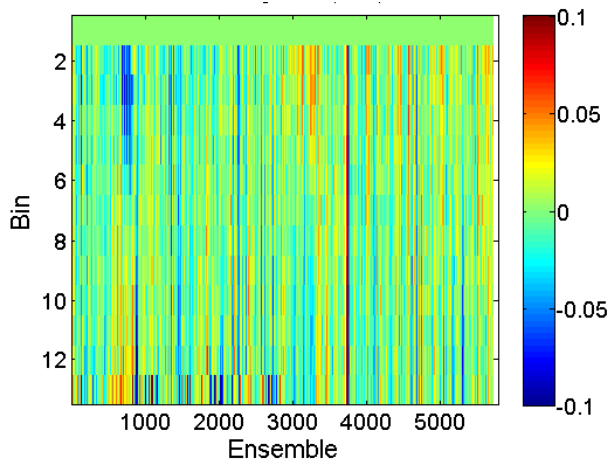


Figure 4.7.2: ADCP streamwise velocities, u_{sw} , (m/s) over the ensemble number (time) and depth, over Deployment 2.

The xyz coordinate velocities from the ADCP revealed, as expected, the streamwise velocities were much higher than the vertical velocities or the cross-channel velocities (horizontally orthogonal to streamwise). Still streamwise velocities through the inlet remained low, almost always below 0.1 m/s, with only a few exceptions, reaching as high as 0.3 m/s.

To obtain depth average streamwise velocity, U , ADCP velocity profiles were extrapolated to the bed and interpolated over the water column (to find velocities between our reported measurements) using the Piecewise Cubic Hermite Interpolating Polynomial, PCHIP, function in MATLAB. Velocity at the bed was forced to zero. Select examples of extrapolated/interpolated velocity profiles are shown in Figure 4.8. Using these profiles, we obtain U from Equation (4.3.1), where H is total depth over the water column, u_i is streamwise velocity and z_i is the depth (for each layer along the water column, i).

$$U = \frac{\sum u_i z_i}{H} \quad (4.3.1)$$

Upon inspection of the extrapolated velocity profiles, at times a surface acceleration is observed. While this is possible due to wind stresses, it is also potentially an unrealistic characteristic from the extrapolation using the piecewise cubic hermite interpolating polynomial. In this case, we are extrapolating over a depth of 0.39m, from the surface to our shallowest ADCP measurement. The velocities obtained from this extrapolation contribute to 18.7% of the calculated U .

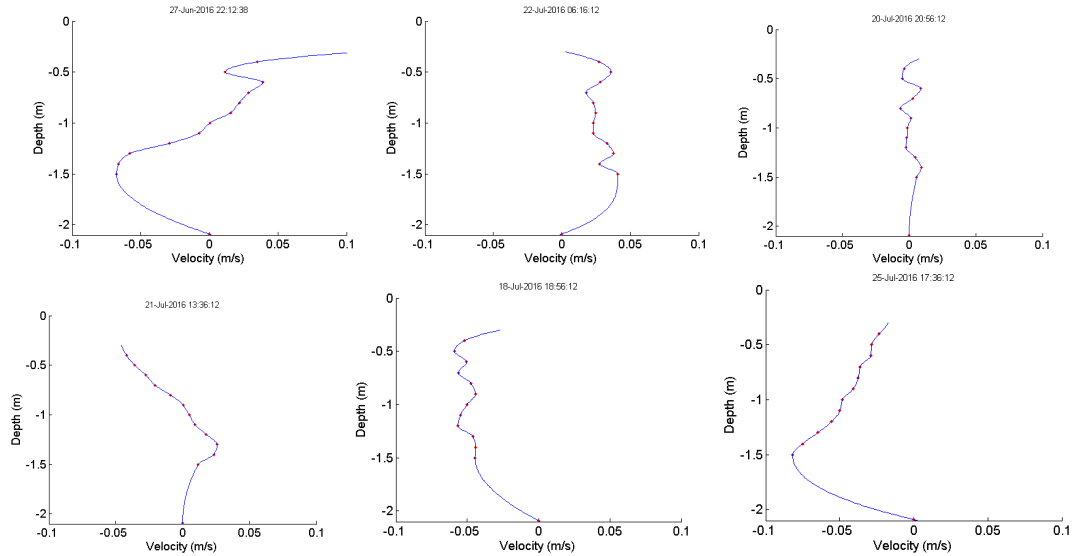


Figure 4.8: Various velocity profiles measured by ADCP interpolated and extrapolated using PCHIP. Measured data in red dots and interpolated and extrapolated data in blue lines.

Depth averaged streamwise velocity reveals an oscillating behavior over time in terms of the bulk flow direction through the inlet. At times inlet water is dominantly sourced from the tributaries and other times from the southern lake. On average, velocities were faster from the tributaries and flowing out towards the lake. The magnitude of U in the inlet remained below 0.05 m/s, with a few exceptions reaching as high as 0.175 m/s.

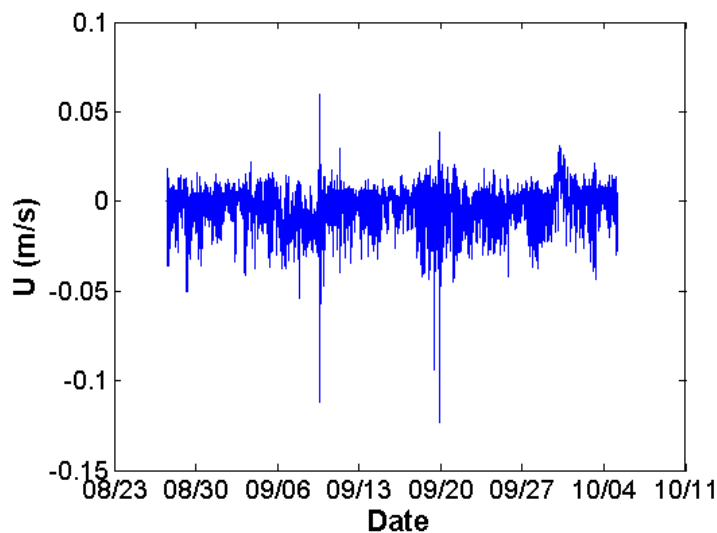


Figure 4.9.1: Depth average streamwise velocity (U) over Deployment 1, using extrapolated/interpolated ADCP velocity profiles.

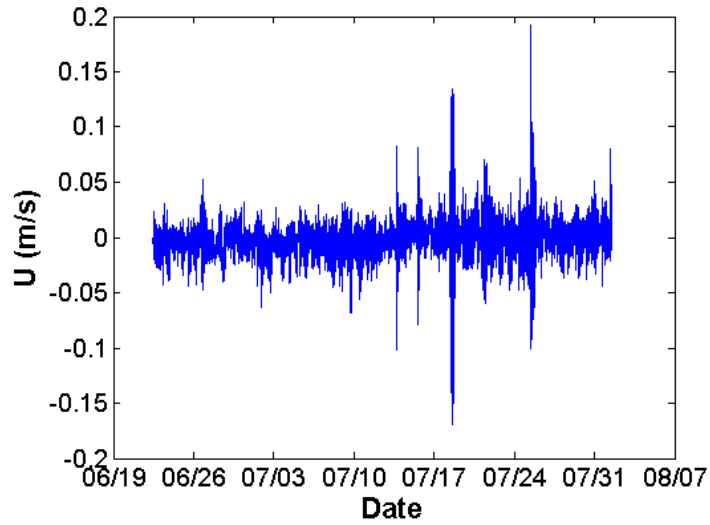


Figure 4.9.2: Depth average streamwise velocity (U) over Deployment 2, using extrapolated/interpolated ADCP velocity profiles.

The depth average absolute velocity, U_{abs} , (Figure 4.10) was calculated using the same method as the depth averaged streamwise velocity, but taking the absolute value of all layer velocities.

$$U_{abs} = \frac{\sum |u_i| z_i}{H} \quad (4.3.2)$$

With U_{abs} , we may gain a better understanding of the total velocity magnitude in the inlet, where layers flowing in opposite directions no longer counteract one another in the calculation.

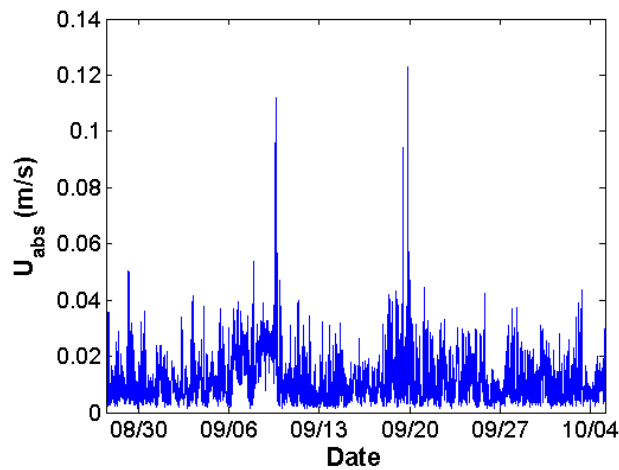


Figure 4.10.1: Depth average absolute velocity over Deployment 1, using extrapolated/interpolated ADCP velocity profiles.

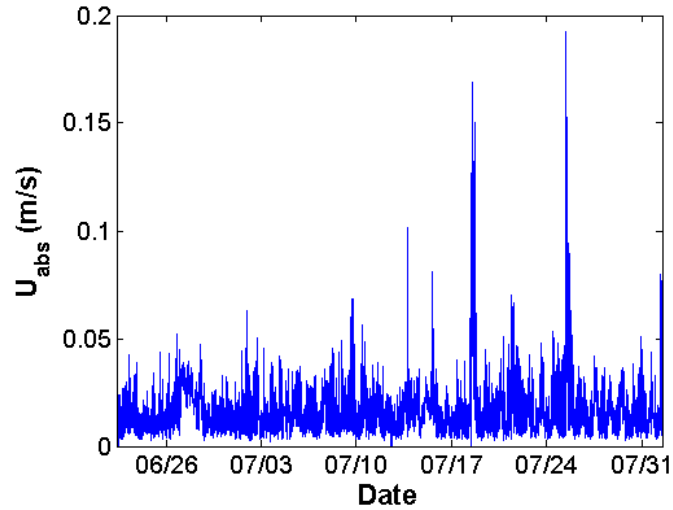


Figure 4.10.2: Depth average absolute velocity over Deployment 2, using extrapolated/interpolated ADCP velocity profiles.

4.1.2 HR Profiler

Correlation from the HR Profiler was on average much higher than that from the ADCP. Based on histograms of the *correlation*, a filter of *correlation* below 60 was selected, which was more than three standard deviations below the mean across all beams. After applying this filter 12.29% of the data was removed. We again use a filter of *echo amplitude* greater than 200. After applying this filter no data was removed. We used an AGW filter on the beam velocities in each bin over each burst to remove most noise. After applying this filter 3.24% of the data was removed. Results of the filter are shown in Figure 4.11.

Table 4.3. Mean and median HR Profiler beam velocities before and after filtering over Deployment 1.

Beam	Mean Velocity before filters (m/s)	Median Velocity before filters (m/s)	Mean Velocity after filters (m/s)	Median Velocity after filters (m/s)
1	-0.0015	-0.0030	-0.0015	-0.0024
2	0.00024	0.00030	0.00023	0.00024
3	0.0019	0.0029	0.0019	0.0023

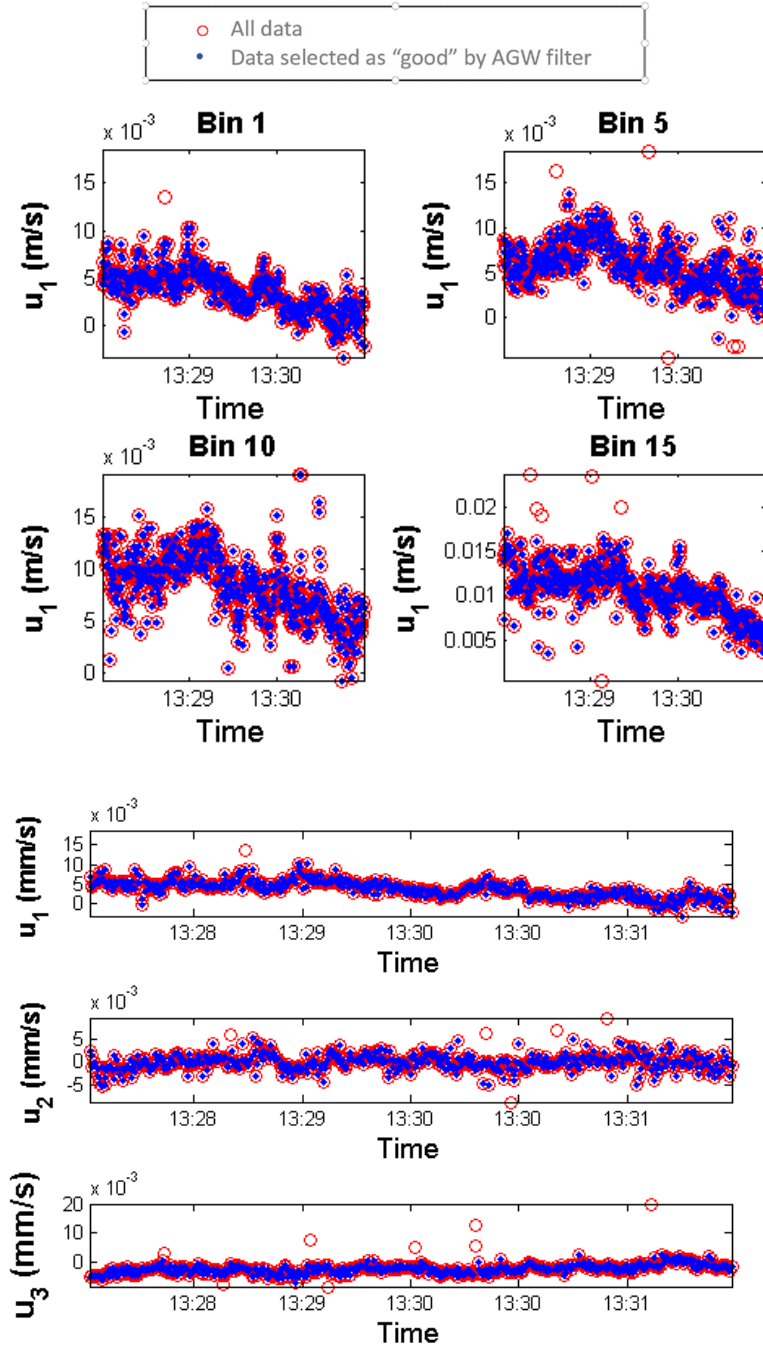


Figure 4.11: HR Profiler beam velocities for bins at burst 100 before and after applying AGW filter. Beams of the HR Profiler were oriented directly upstream and downstream and one vertical. Thus, the vertical beam was used for the vertical velocity, w , and the beams oriented downstream and upstream were used to find u , the streamwise velocity. Equations (4.4.1)-(4.4.3) convert from beam coordinates to u and w velocities, where θ was set at 30 degrees.

$$beam\ 1 = u\sin(\theta) + w\cos(\theta) \quad (4.4.1)$$

$$beam\ 2 = w \quad (4.4.2)$$

$$beam\ 3 = -u\sin(\theta) + w\sin(\theta) \quad (4.4.3)$$

Lastly, mean and median streamwise velocities over each burst were calculated.

Streamwise velocities captured by the HR Profiler, measuring over the bottom 1 meter of the water column, in general were slow and occasionally reached up to 0.1 m/s. Earlier in this short deployment streamwise velocities in the bottom layer of the inlet were more frequently directed from the lake into the inlet and towards the end streamwise velocities in the bottom layer of the inlet were more frequently directed from the inlet out towards the lake.

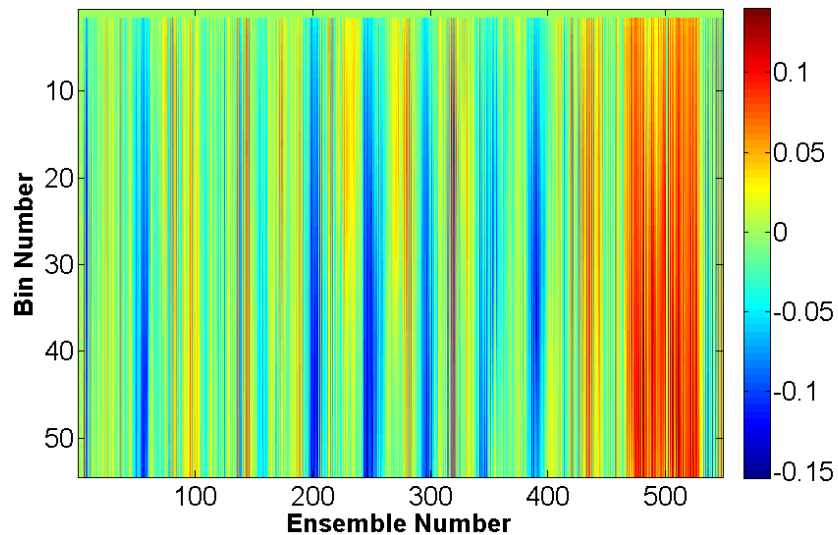


Figure 4.12: Streamwise velocity along the inlet from the HR Profiler, over the ensemble number (time: August 27th, 2015 to September 7th, 2015) and bin number (depth), where lower bin numbers are at greater depths and highest bin number is at approximately 1m deep.

4.1.3 Vector

Vector velocity data were run through filters based on reported *correlation* and *echo amplitude*. *Correlation* was reported as a normalized *correlation* coefficient in percentage. Based on the histograms of *correlation* values (Figure 4.13), a filter of *correlation* below 90% was selected, where both the mean and median of *correlation* values for each beam were above 98%. *Correlation*

for the Vector was on average much better than for the ADCP, which is expected to have more noise. This *correlation* filter removed 0.88% and 0.98% of the data for Deployment 2 and 3, respectively. The *echo amplitude* filter was selected the same as previously used at 200, although no data was removed. An acceleration filter was used in which any measurement resulting in an acceleration greater than the maximum velocity observed in beam coordinates (8 cm/s for Deployment 2 and 9.5 cm/s for Deployment 3) multiplied by the sampling rate, 8Hz, was removed. The acceleration was determined by consecutive velocity measurements in the same burst with the given sampling rate. This filter removed 0.02% and 0.01% of the data from Deployment 2 and 3, respectively. After applying each of these filters the mean and median for each beam velocity were not significantly changed, given the low percent of data removed.

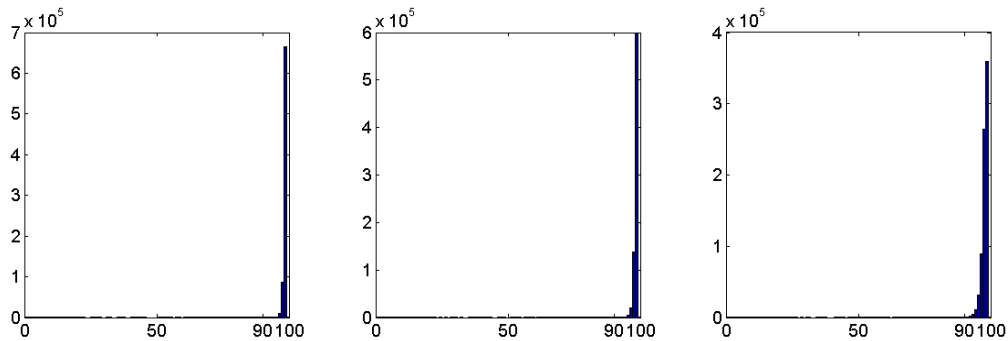


Figure 4.13: Histograms of Vector *correlation* for each beam.

The same AGW filter discussed was applied to the Vector beam velocities over each burst. Results of this filter are shown in Figure 4.14.

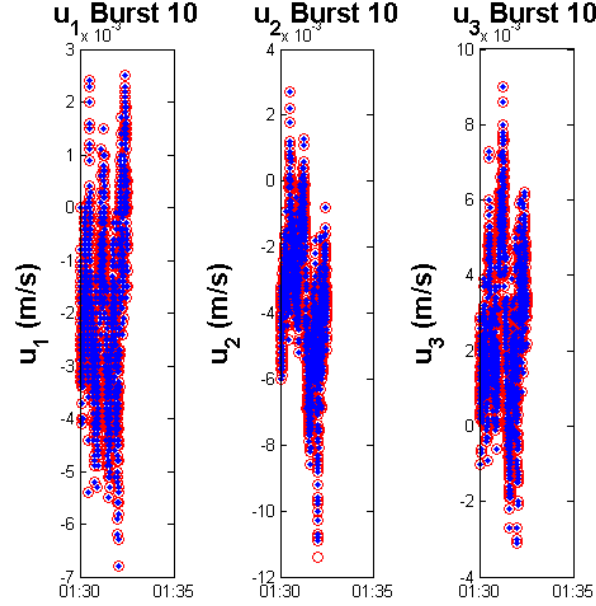


Figure 4.14: Vector beam velocities at burst 10 before and after applying the AGW filter.

Beam velocities were converted to the x,y,z coordinate system using the transformation matrix below and Equations (4.5.1)-(4.5.3):

$$T = \begin{bmatrix} 2.6812 & -1.3613 & -1.3267 \\ -0.0215 & 2.2754 & -2.2581 \\ 0.3530 & 0.3445 & 0.3357 \end{bmatrix}$$

$$u = T_{1,1}u_1 + T_{1,2}u_2 + T_{1,3}u_3 \quad (4.5.1)$$

$$v = T_{2,1}u_1 + T_{2,2}u_2 + T_{2,3}u_3 \quad (4.5.2)$$

$$w = T_{3,1}u_1 + T_{3,2}u_2 + T_{3,3}u_3 \quad (4.5.3)$$

u and v are the horizontal velocities, from which we can calculate the streamwise velocity based on the orientation of the Vector when deployed using the same method as described with the ADCP. w is the vertical velocity in the inlet. Over Deployment 3, on August 21st, 2016 around 21:00, internal programmed settings changed in the Vector. The number of samples per burst as well as the burst interval changed to inconsistent values. We are unsure what caused this, but a low battery voltage may have contributed. This change in settings caused the battery to die more quickly than expected, with shorter burst intervals set. However, power spectra of velocities (which are discussed below) and

pressure data following this change resemble prior measurements, therefore we present data collected through August 31st, 2016.

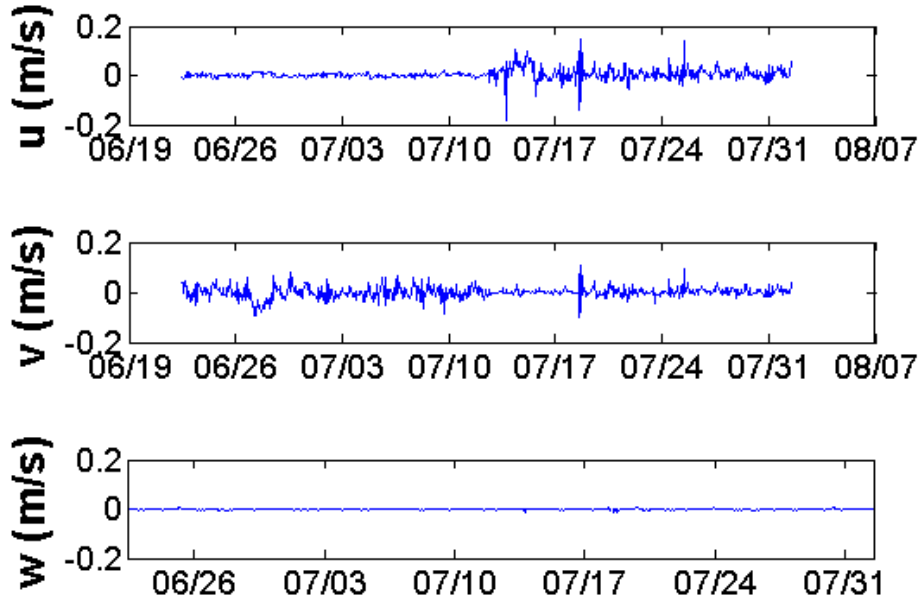


Figure 4.15.1: Vector velocities in xyz coordinates over Deployment 2.

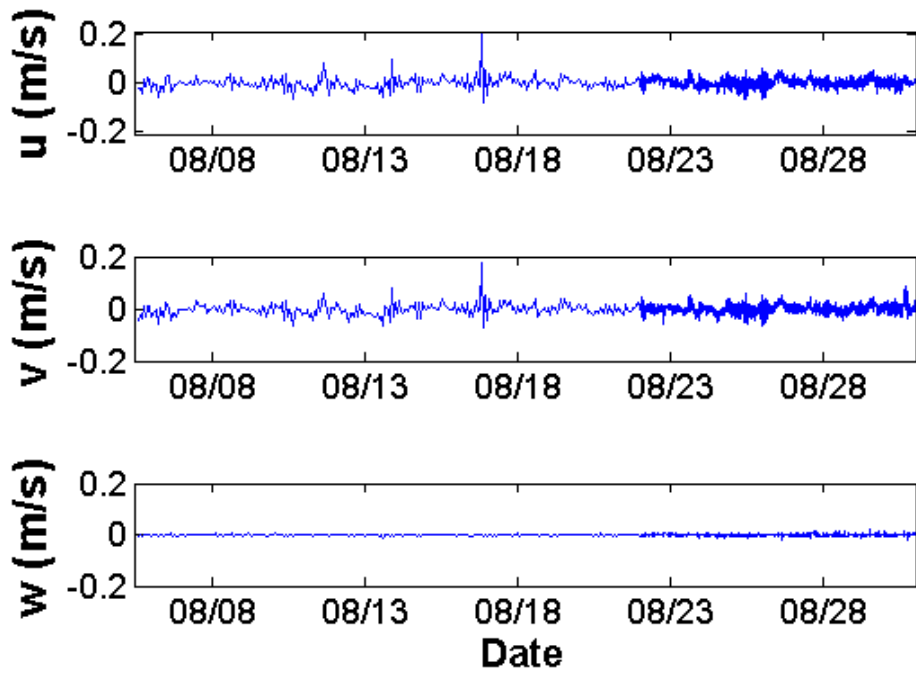


Figure 4.15.2: Vector Velocities in xyz coordinates over Deployment 3.

The same method described with the ADCP data to find streamwise velocities, based on the predominate flow directions through the inlet, was applied to the Vector data.

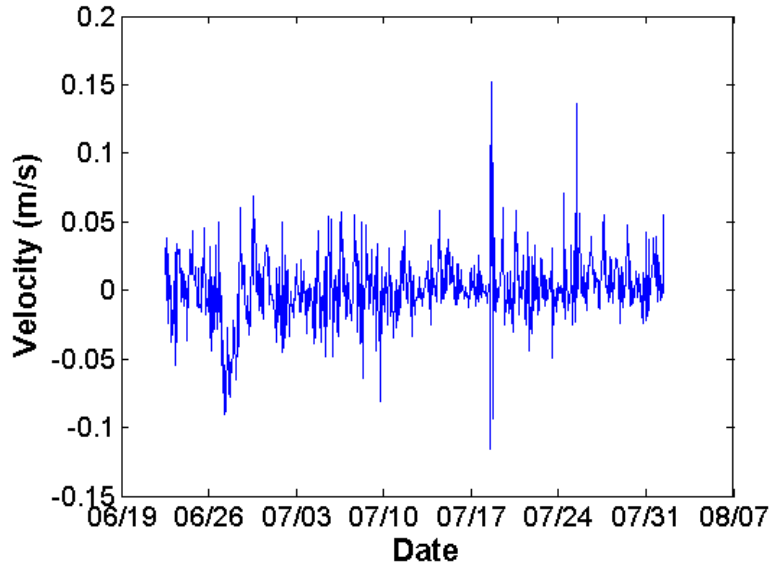


Figure 4.16.1: Streamwise velocity based on Vector data over Deployment 2, for flow out of the inlet towards the lake (+) and in to the inlet from the lake (-).

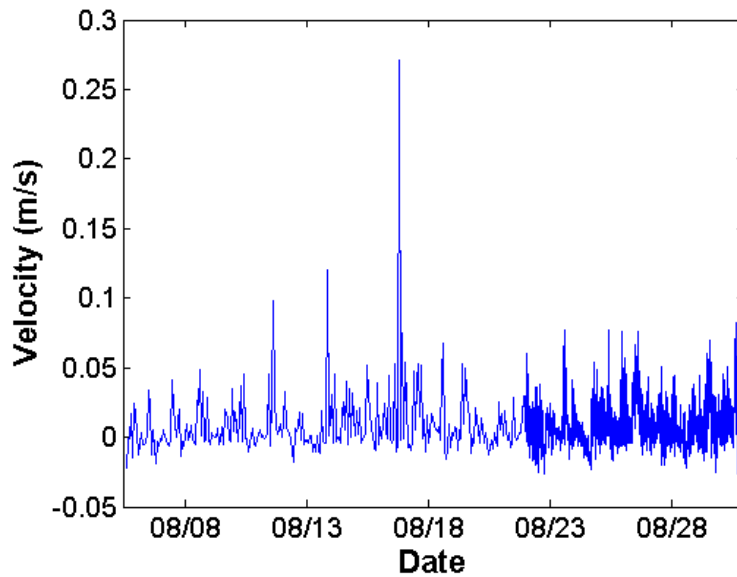
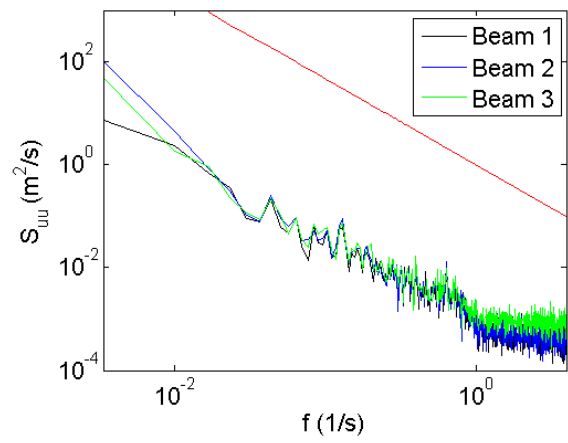
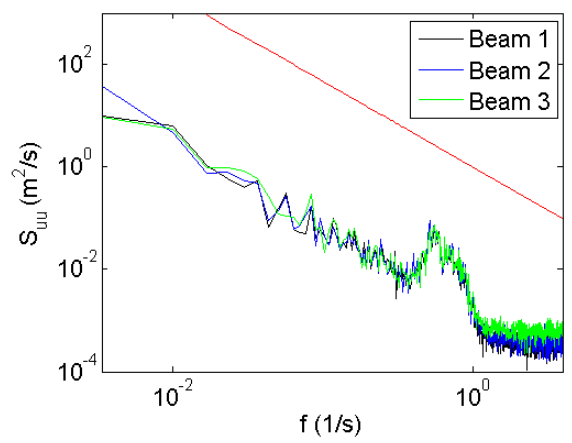
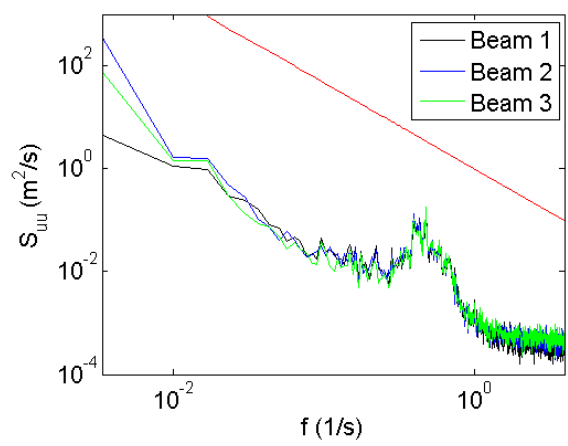
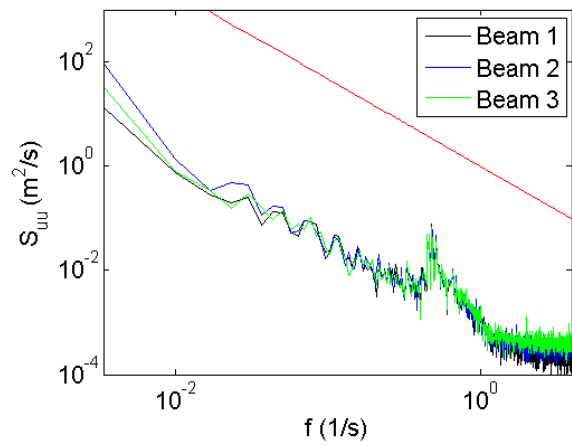


Figure 4.16.2: Streamwise velocity based on Vector data over Deployment 3, for flow out of the inlet towards the lake (+) and in to the inlet from the lake (-).

The power spectral density function indicates the portion of the total signal variance accounted for at specific frequency bands. Spectra for velocity data from the Vector were calculated for each

ensemble, over the 2.5minute burst interval, and then as a 1 day average, which included 16 ensembles. We average spectra to smooth noise towards a flat line, allowing us to more clearly distinguish the signal of interest. Figure 4.17, displays the calculated spectra for the beam velocities, spaced at approximately 5 day intervals. We do not capture the barotropic scale processes, with a period of 1 hour, in the inlet with these measurements. Noise clearly interferes around 1.2 Hz. Many of the spectra exhibit a peak on the time scale of approximately 2 seconds, which we expect is related to surface gravity waves. In these cases, we sometimes observed harmonics with smaller spikes following. Prior to these spectral peaks, the slope of the spectra was $\approx -5/3$. This is expected, as the $-5/3$ slope characterizes the internal subrange of turbulence. After the spectral peak around 2 seconds, the slope of the spectra appears to be steeper than $-5/3$.



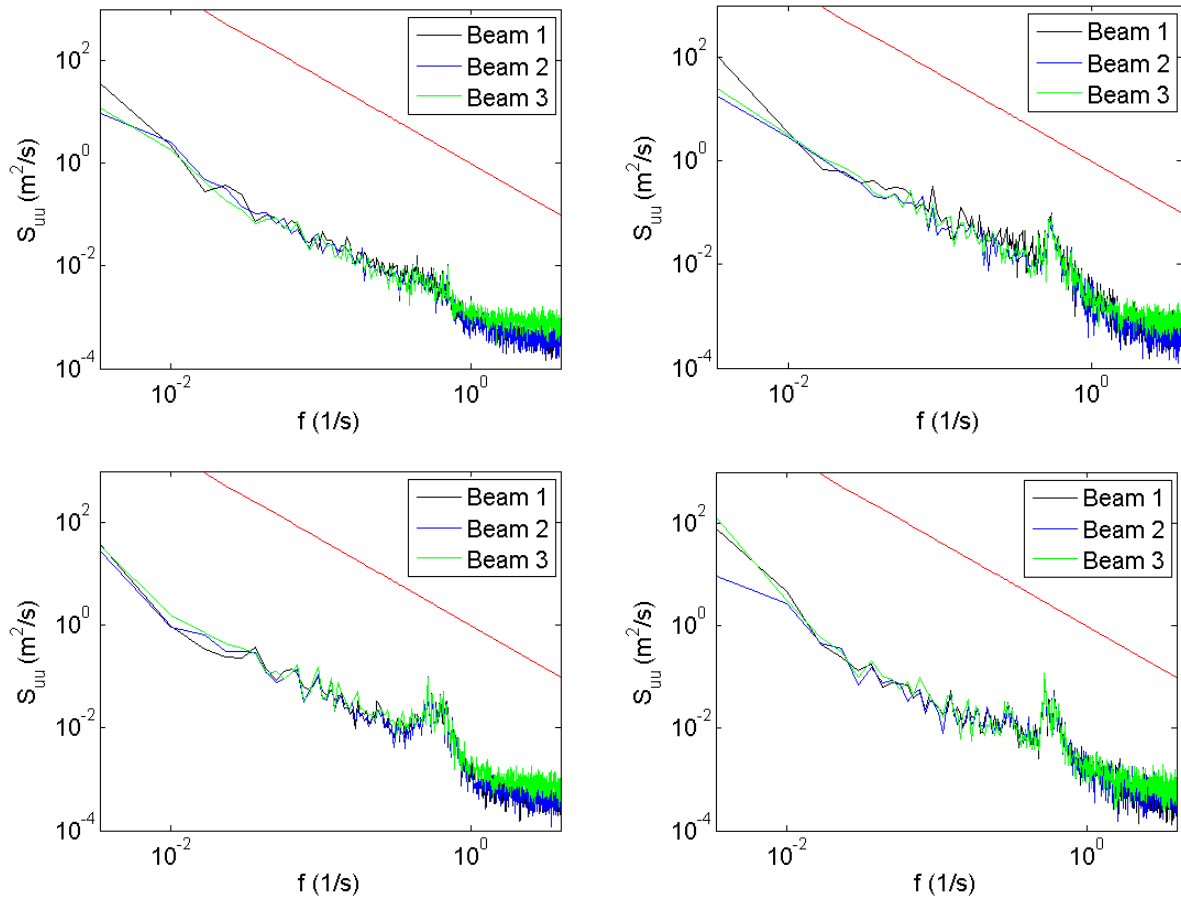


Figure 4.17: Power spectra of Vector beam velocities. Spectra were calculated for each ensemble, which was over the 2.5minute burst interval the instrument was recording. The above plots are averages of those spectra over 1day. Red line indicates the $-5/3$ slope that characterizes turbulence to compare to power spectra slope. (analyzed averaged spectra at 5 day intervals over deployment, beginning \rightarrow end: left, top \rightarrow right, bottom)

Surface waves appear to add energy and interfere with turbulence measures. A study by Grant (1986) found the presence of surface waves can distort the inertial range of the spectrum. Significant wind speeds along the axis of the inlet occurred over time intervals the spectra showed evidence of waves. Figure 4.18, shows a few of these wind records with the corresponding spectra. The greater spectral peaks appeared to correspond to greater wind magnitudes along the axis of the inlet.

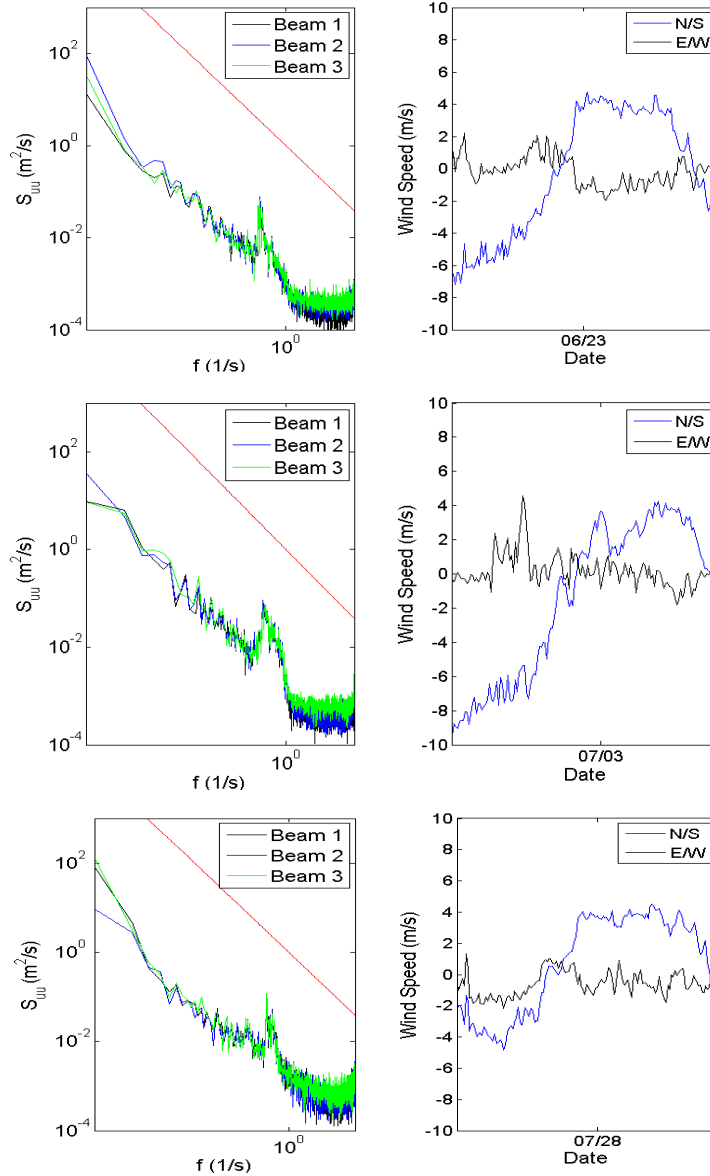


Figure 4.18: Wind records (right) corresponding to select velocity spectra (left) from previous Figure. N/S indicates magnitude of wind along North/South axis, where North is positive and E/W indicates magnitude of wind along East/West axis, where East is positive.

Pressure perturbations were a good indication for the presence of surface waves. We will discuss filtering techniques to remove the effects of surface waves and isolate turbulence measurements in a later section on bed stress.

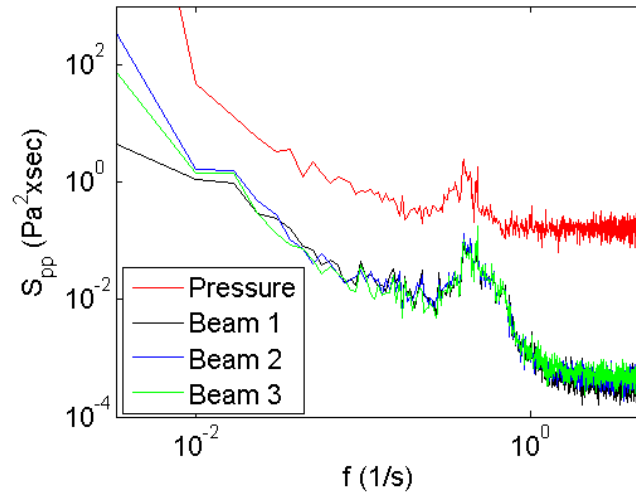


Figure 4.19: Power spectra for pressure corresponding to selected power spectra for beam velocities.

4.2 Comparison of Velocity Data from Different Instruments

For Deployment 1 streamwise velocities, measured at approximately the same depth over the same time from the ADCP and HR Profiler were compared. As the HR Profiler had a greater resolution, we averaged the streamwise velocities from the HR Profiler bins over the ADCP bin depths where the two overlapped, which ranged from 1.0 meters to 1.2 meters deep. A perfect agreement between the ADCP and HR Profiler would be a 1 to 1 relationship in Figure 4.20, thus the slope of the best fit line should be 1. However slopes were 0.33, 0.30, and 0.22 with R-squared values of 0.85, 0.81, and 0.73 at 1.2 meters, 1.1 meters, and 1.0 meters deep, respectively. On average, velocities measured by the HR Profiler were more than three times that measured by the ADCP at approximately the same time and depth.

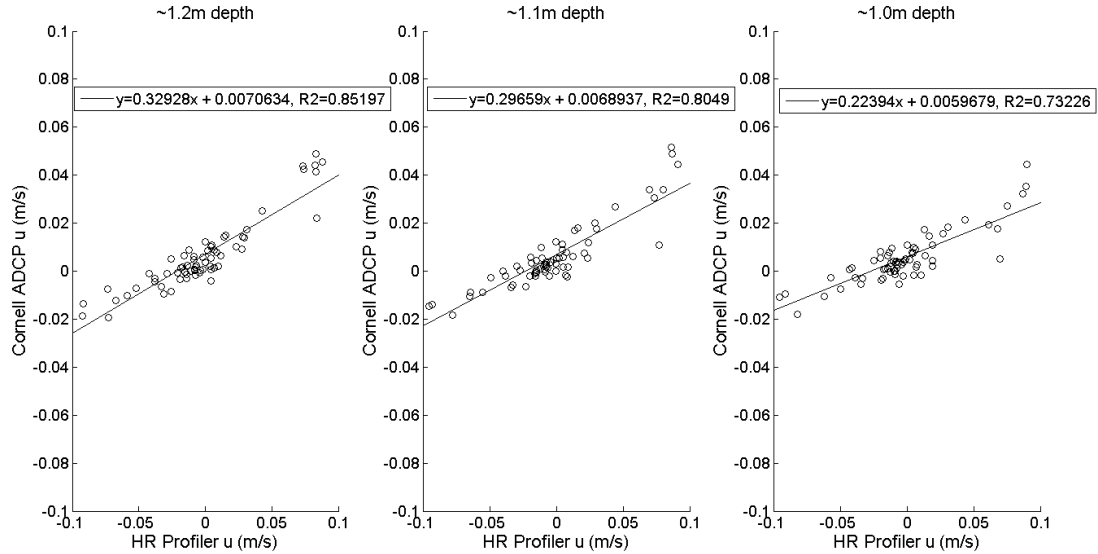


Figure 4.20: Comparison of streamwise velocities measured by the ADCP versus the HR Profiler at depths of approximately 1.2 meters (left), 1.1 meters (middle), and 1.0 meters (right).

For Deployment 2 velocities from the ADCP and the Vector were compared over the same period and approximate depth. Based on the field set up, Vector velocities were recorded at a depth closest to velocities recorded in the 3rd bin for the ADCP. Averages of the 2.5 minute bursts recorded by each instrument for overlapping times were used for comparison. For the Vector and ADCP, where a 1:1 relationship would be perfect agreement, we found a 0.78:1 relationship with an R-squared value of 0.721. Comparing the magnitude of the horizontal velocity components, which removes any rotational errors, improves this relationship between instruments to 0.82:1, with an R-squared value of 0.727.

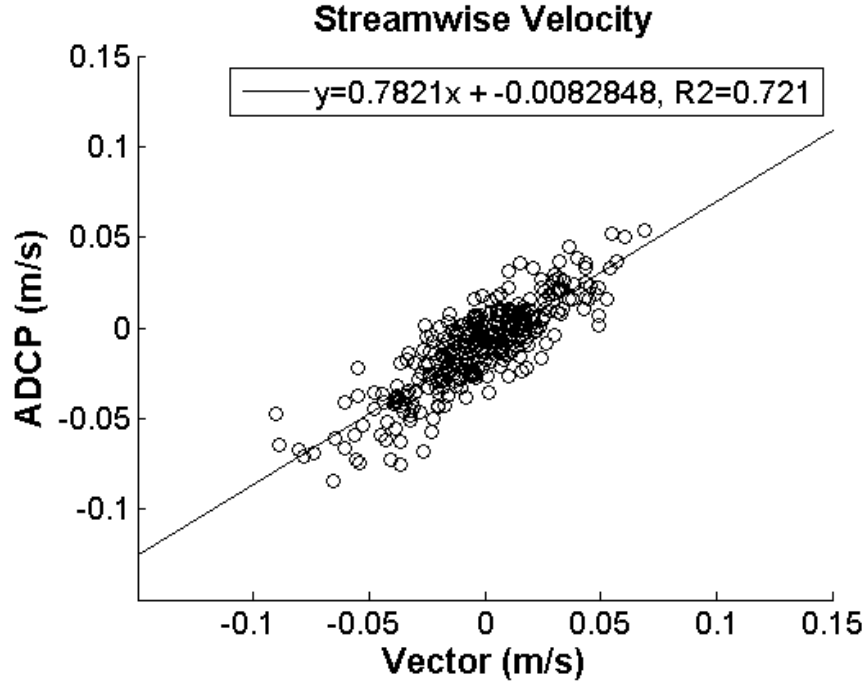


Figure 4.21: Comparison of Vector and ADCP streamwise velocities at approximately the same depth and time.

The selected *correlation* filter threshold of 40 on ADCP data was confirmed by observing effects of different *correlation* thresholds on the comparison of Vector and ADCP data. Table 4.4, shows using thresholds above 40 decreased the R-squared value for the relationship between the two instruments. This suggests more restrictive filters may be removing good data. Lower threshold values resulted in higher R-squared values, however the relationship between ADCP and Vector data is slightly closer to a 1:1 relationship using a threshold of 40. Therefore, we conclude a *correlation* filter threshold of 40 is the best option for our ADCP data.

Table 4.4: Effect of *correlation* filter threshold on accuracy of ADCP data.

<i>Correlation</i> Filter Threshold	ADCP:Vector relationship (1:1 match perfectly)	R² value
30	0.78077:1	0.72664
40	0.78210:1	0.72100
50	0.78213:1	0.72094
60	0.77818:1	0.71891
70	0.76640:1	0.70663

The Ithaca Area Wastewater Treatment Plant (IAWWTP) deployed a SonTek Argonaut XR ADP over similar periods and located on the bottom of the inlet approximately 10m downstream from our ADCP. The IAWWTP ADP was deployed on a biweekly schedule and here we analyze data starting August 7th, 2015 to October 3rd, 2015 (referred to as Deployment 1') and data starting June 21st, 2016 to October 4th, 2016 (referred to as Deployment 2'). The IAWWTP ADP was deployed in a pulse incoherent mode and reported velocities as a weighted average within 5 bins along the water column, starting 20cm above the bed, with bin sizes of 40cm each. The ADP recorded a single measurement every 15minutes based on internal averaging of measurements taken every 2.5minutes, sampling at 0.4Hz. Velocities were measured in earth coordinates, where North refers to magnetic north. The magnetic declination of Cayuga Lake is 11.98°W. To convert from magnetic to true north:

$$\text{True } N \text{ Velocity} = \cos(11.98) (\text{Magnetic } N \text{ Velocity}) - \sin(11.98)(\text{Magnetic } E \text{ Velocity}) \quad (4.7)$$

Filters were selected based on signal-to-noise ratio (SNR) and location of the first and last cell to which the ADP was measuring. We removed data where SNR was less than 40 and/or cell end, the vertical distance above the bed to which the ADP measured to the water surface, was less than 1.4m. After filtering by SNR 1.20% and 16.03% of the data was removed and 0.02% and 0% of the data was removed by the minimum cell end filter over Deployment 1' and Deployment 2', respectively. Over Deployment 2' one of the biweekly deployments, in the middle of July, reported very poor data quality, thus most of this data was removed.

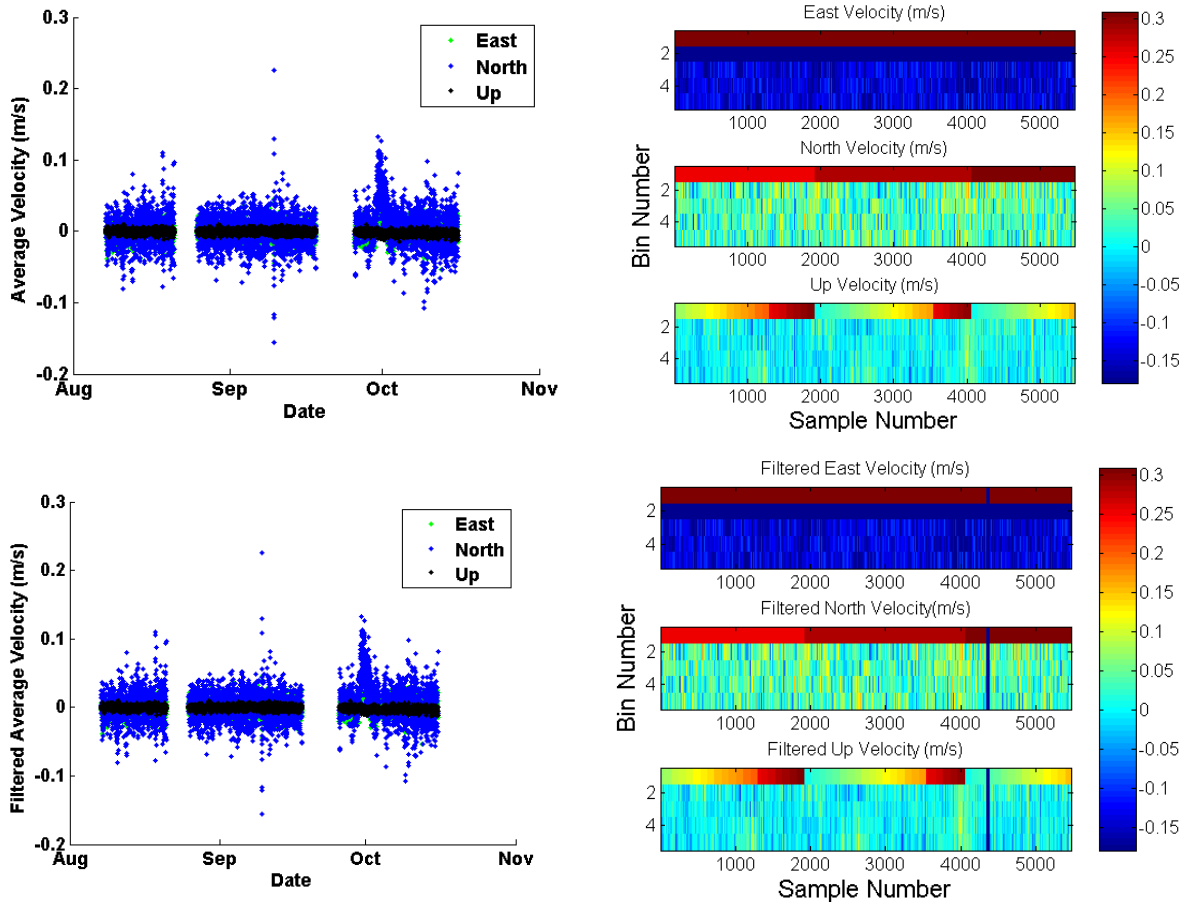
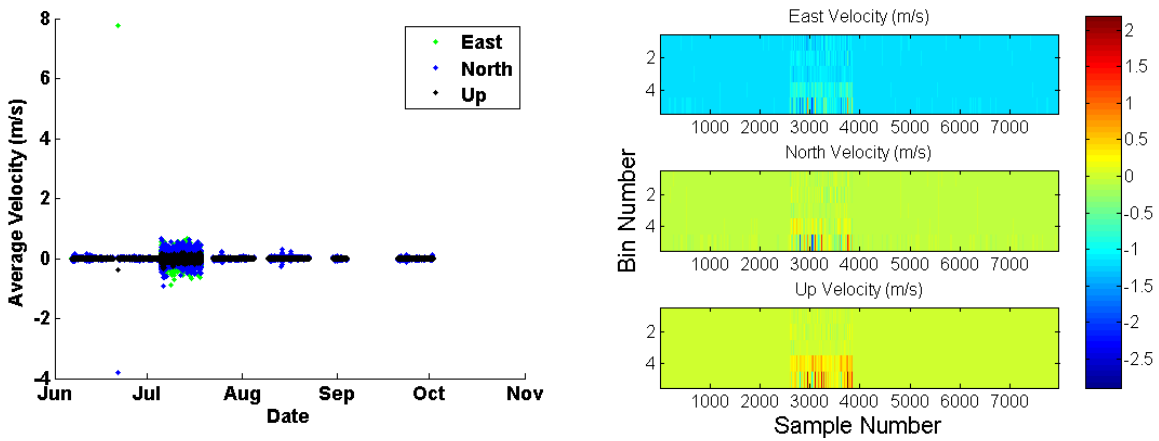


Figure 4.22.1: Depth average velocities from the IAWWTP ADP (left) and velocity profiles recorded from the IAWWTP ADP (right) over Deployment 1' before and after filtering (top and bottom, respectively). Note dark blue values on bottom right plot are removed data and North refers to magnetic north.



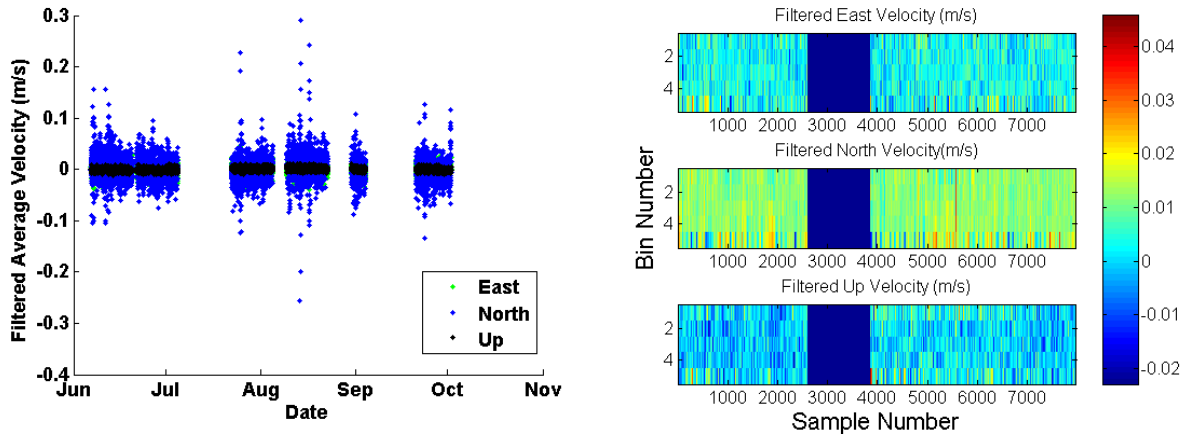


Figure 4.22.2: Depth average velocities from the IAWWTP ADP (left) and velocity profiles recorded from the IAWWTP ADP (right) over Deployment 2' before and after filtering (top and bottom, respectively). Note dark blue values on bottom right plot are removed data and North refers to magnetic north.

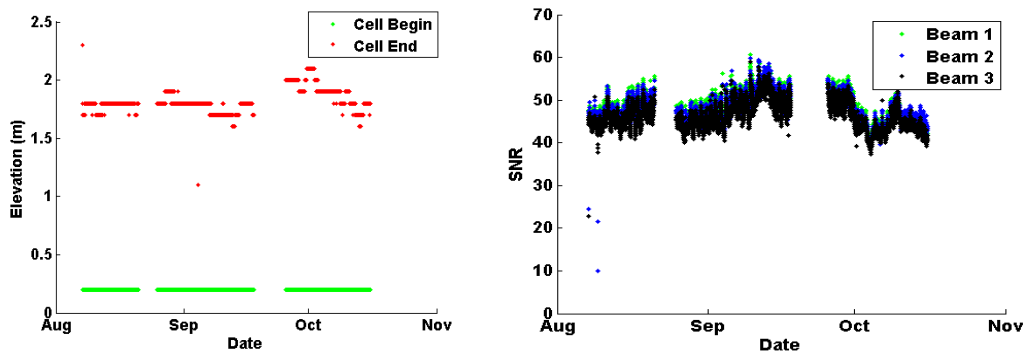


Figure 4.23.1: IAWWTP ADP cell end (left) and SNR (right) over Deployment 1', parameters used to set filters as described above.

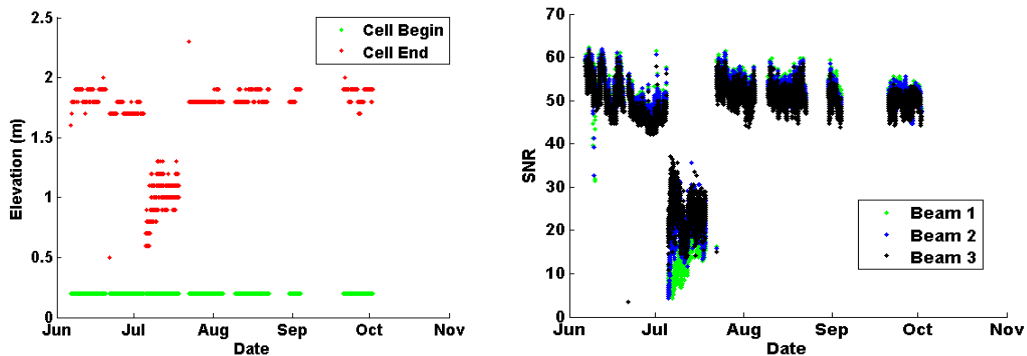


Figure 4.23.2: IAWWTP ADP cell end (left) and SNR (right) over Deployment 2', parameters used to set filters as described above.

A histogram of the dominant flow direction of IAWWTP ADP velocities confirmed this was along the recorded north/south axis. Therefore, we assume the reported magnetic north velocity recorded by the ADP was the streamwise velocity. We compared the depth average streamwise velocity determined by the IAWWTP ADP and Cornell ADCP, shown in Figure 4.24. We also compared bin streamwise velocities recorded by both at similar depths within the inlet (see Table 4.5). However, the comparison here is shockingly poor, particularly over the first deployment. In Deployment 1 the instruments measured the same sign of the velocity, thus the same direction of flow either towards the lake (+) or coming from the lake (-), only 56.1% of the time.

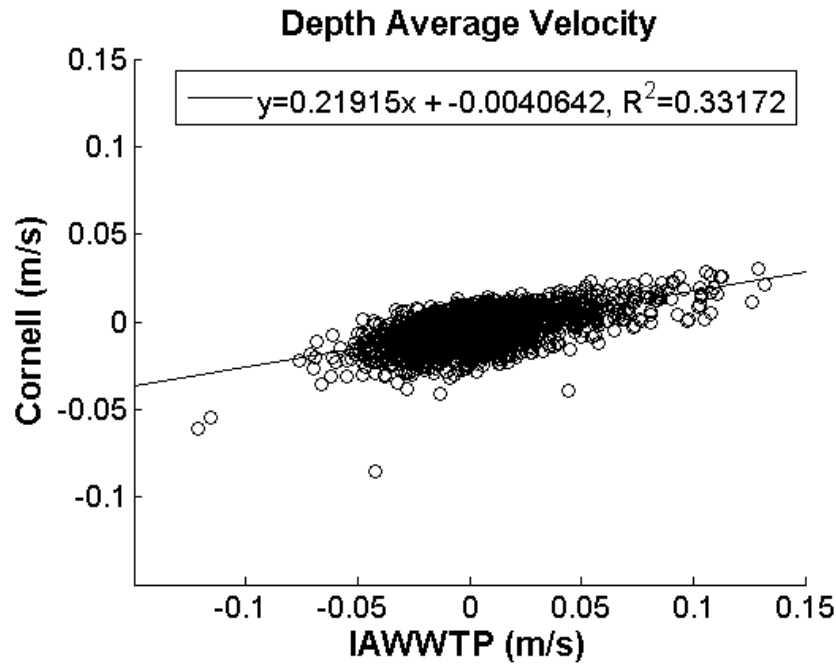


Figure 4.24.1: Comparison of depth average streamwise velocity determined by the Cornell ADCP versus the IAWWTP ADP over Deployment 1.

Table 4.5.1: Comparison of Cornell ADCP and IAWWTP ADP velocity data over Deployment 1.

Velocity Data	Cornell:IAWWTP relationship (1:1 match perfectly)	R ² value
Depth-Average	0.22:1	0.33
~0.5 m deep	0.21:1	0.073
~0.9 m deep	0.13:1	0.037
~1.3 m deep	0.17:1	0.038

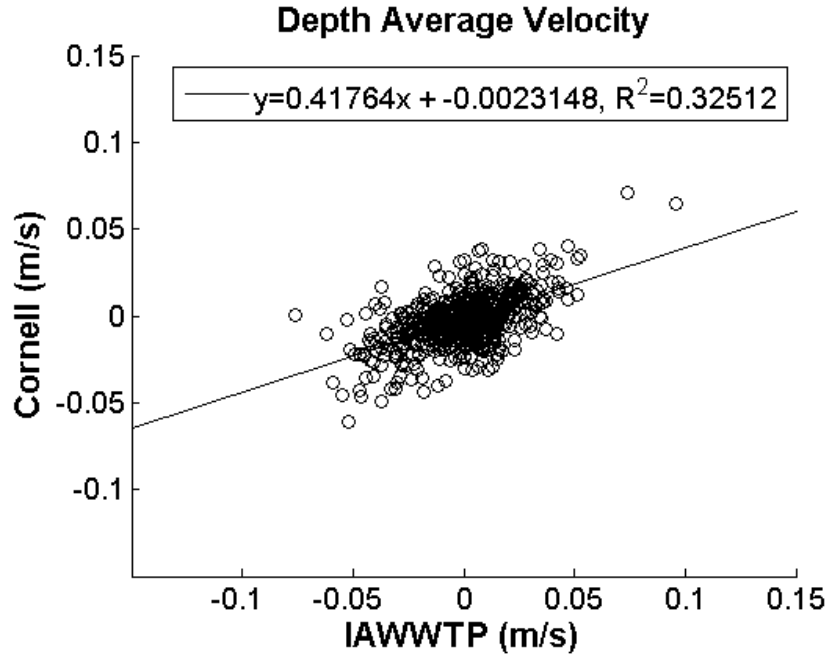


Figure 4.24.2: Comparison of depth average streamwise velocity determined by the Cornell ADCP versus the IAWWTP ADP over Deployment 2.

Table 4.5.2: Comparison of Cornell and IAWWTP ADP velocity data over Deployment 2.

Velocity Data	Cornell:IAWWTP relationship (1:1 match perfectly)	R ² value
Depth-Average	0.42:1	0.33
~0.5 m deep	0.48:1	0.46
~0.9 m deep	0.39:1	0.25
~1.3 m deep	0.45:1	0.32

For Deployment 3 we use IAWWTP ADP data to determine the flow type present in the inlet. For Deployment 2 our comparison of Cornell’s ADCP data and IAWWTP ADP data resulted in low R-squared values (ranged from 0.25 to 0.46) and slopes slightly less than 0.5 (indicating IAWWTP ADP velocities were on average greater than double what the Cornell ADCP recorded). Our ADCP velocity magnitudes were on average consistently lower than that recorded by all other instruments (HR Profiler, Vector, and IAWWTP ADP). While this is a poor agreement, it improves if we exclusively look at faster velocities. When we remove the streamwise velocities less than 2 cm/s recorded by IAWWTP, the R² values range from 0.61 to 0.67 for the different bins and all slopes are greater than 0.6. If we do this for the depth average streamwise velocity the relationship now has a

slope of 0.8 and R^2 of 0.91, with the instruments always agreeing on direction of bulk flow through the inlet. In terms of comparing velocities at the relative bins, on average 66% of the time both instruments measured the same flow direction through the inlet, with discrepancies occurring at near zero velocities. After removing streamwise velocities less than 2 cm/s recorded by IAWWTP, on average 93% of the time both instruments measured the same flow direction. Even just removing velocities less than 1 cm/s improved to 83% of the time that the instruments agreed on flow direction. If we remove velocities less than 3 cm/s, slopes when comparing relative bins are now above 0.8 and R^2 ranges from 0.82 to 0.87, with agreement in flow direction on average 98% of the time.

Figure 4.25, shows IAWWTP ADP streamwise velocities at bin 2 over Deployment 3, which was approximately at the same depth the Vector was recording (~1.26m deep). In general, both instruments agreed on the overall patterns in the streamwise velocity at this depth and the occurrence of larger events.

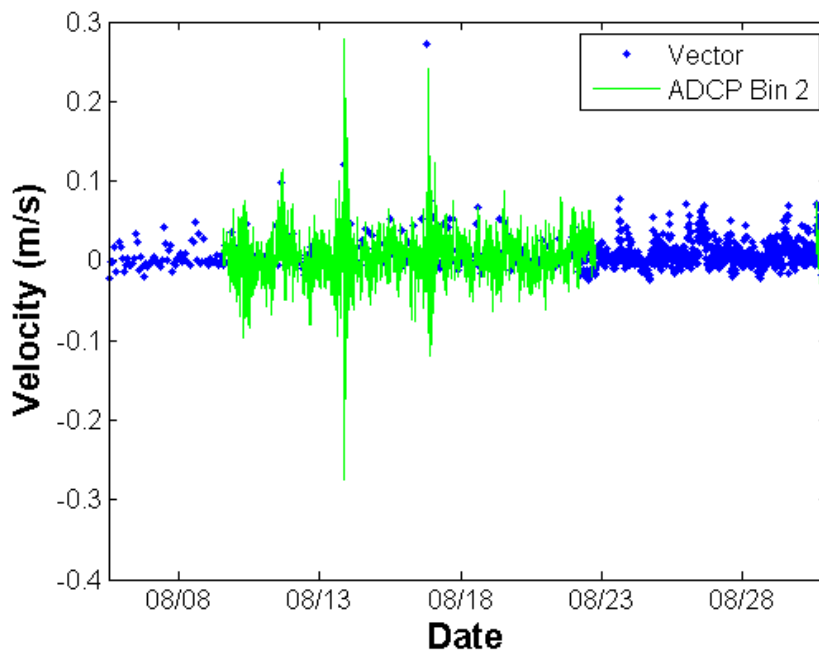


Figure 4.25: Streamwise velocity through the inlet recorded by the Vector compared to that recorded by bin 2 of IAWWTP ADP over Deployment 3.

4.3 Model of Inlet Depth Average Flow

We used a mass balance approach, outlined by King, 2014, to calculate the depth averaged velocity through Cayuga Inlet based on the flowrate of the three main tributaries entering the inlet and gage height within the inlet. Data for Cayuga Inlet Creek, Sixmile Creek, and Cascadilla Creek was obtained from the USGS. We assume a horizontal surface in the inlet for this method, thus the depth averaged velocity is estimated using Equation (4.7).

$$U_{model} = \frac{Q}{A_c} - \frac{A_s}{A_c} \frac{dh}{dt} + U_o \quad (4.7)$$

U_{model} is the depth average velocity in the inlet, Q is the total flowrate from the three tributaries, A_c is the cross-sectional area of the channel (219 m², reported by King in 2013 and measured in google earth pro), h is the water surface elevation in the inlet and A_s and U_o are two parameters of the model. A_s represents the surface area of the water volume upstream of the inlet that is influenced by the lake and U_o represents the background mean velocity. These parameters were adjusted to minimize the sum of residual error between the depth average streamwise velocity measured by the ADCP and that of the model. The best fit of modeled to measured depth average velocities are shown in Figure 4.26. The selected adjustable parameters are shown in Table 4.6.

Table 4.6: Adjustable parameters in U_{model} for each deployment.

Deployment	A_s (km ²)	U_o (cm/s)
1	0.31	-0.742
2	0.31	-0.384
3	0.31	-0.0694

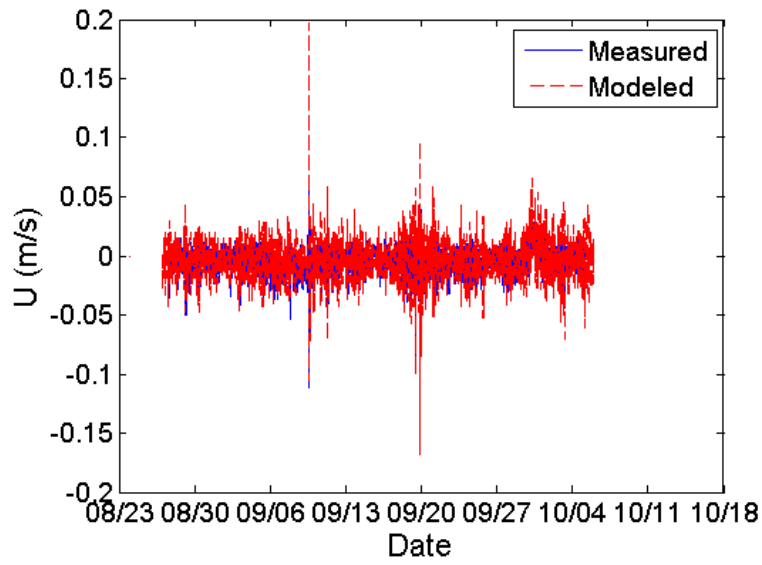
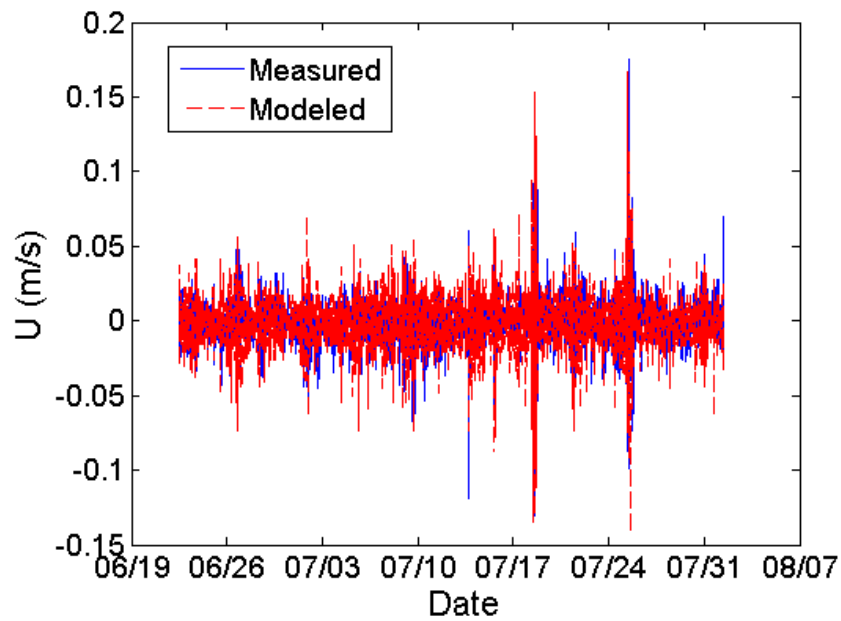


Figure 4.26.1: Measured and modeled depth average velocity in Cayuga Inlet using ADCP data and above mentioned model with best fit parameters over Deployment 1.



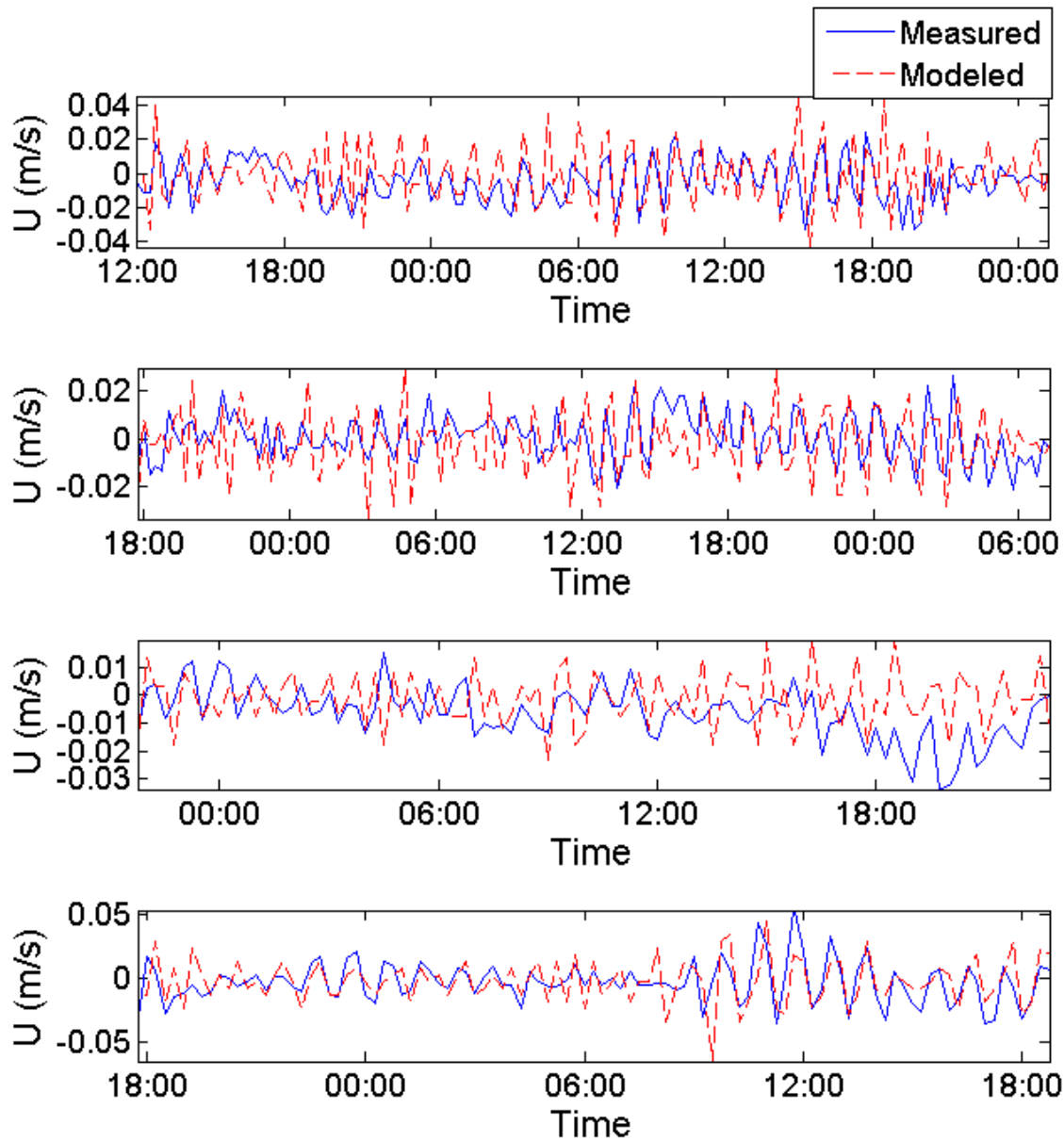


Figure 4.26.2: Measured and modeled depth average velocity in Cayuga Inlet using ADCP data and above mentioned model with best fit parameters over Deployment 2. Top shows the entire time series while the rest are zoomed in on a few selected dates.

U_{model} does a good job predicting larger flow events captured by ADCP data and the general pattern in the inlet. There are discrepancies in measured and modeled data over time, possibly due to the influence of stronger inlet-lake interactions or errors in the measurements. Over Deployment 3, the background velocity for the best fit model was much smaller. This period contained the most

significant increase in the water surface elevation, but this can be primarily attributed to higher tributary flows due to increased frequency of precipitation. Also, the overall average $U_{measured}$ was 0.28 cm/s, whereas for Deployment 1 and 2 it was -0.35 cm/s and -0.18 cm/s, respectively. Recall a positive velocity indicates flow directed from the tributaries into the inlet and a negative velocity indicates flow directed from the lake into the inlet.

For Deployment 3 the measured depth average velocity was from IAWWTP ADCP data. We first looked at the same best fit parameters used in Deployment 2 for the model. While larger events appear to correspond between the two, the sum of residual error was high at 5.39 (Figure 4.26.3). However, if we change our adjustable parameters to the values in Table 4.6 for Deployment 3, we minimize our residual error down to 0.0000585 (Figure 4.26.4).

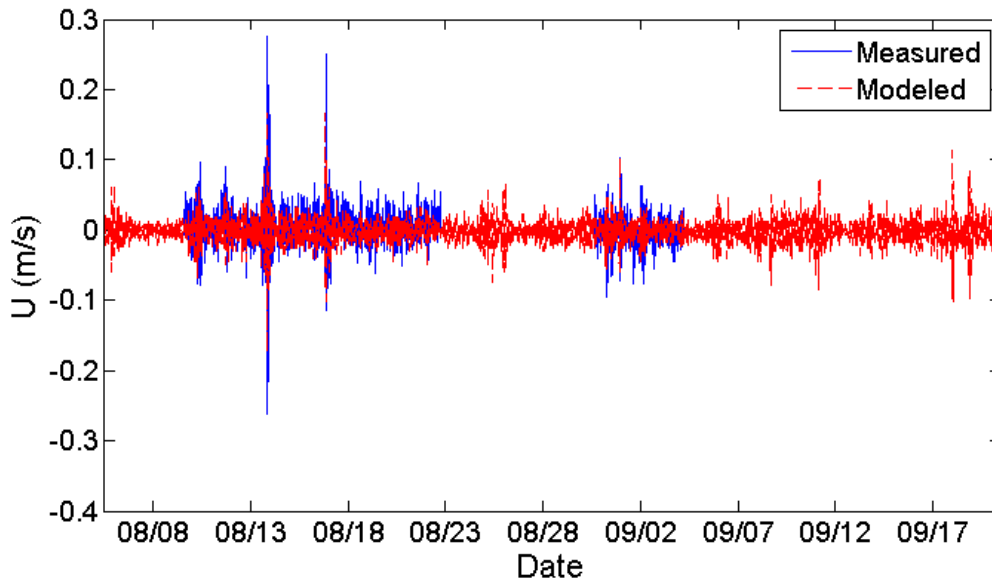


Figure 4.26.3: Measured and modeled depth average velocity in Cayuga Inlet using IAWWTP ADCP data and previously described model with USGS gage data over Deployment 3 with best fit parameters of Deployment 2.

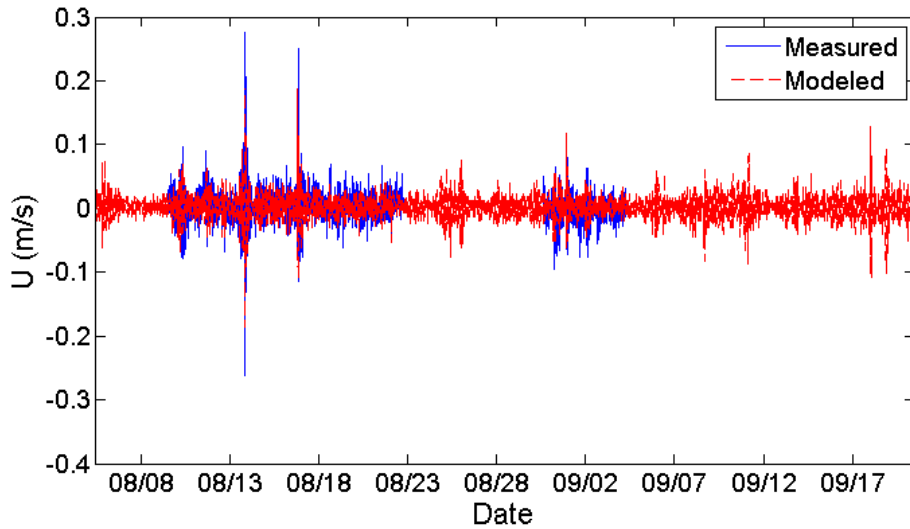


Figure 4.26.4: Measured and modeled depth average velocity in Cayuga Inlet using IAWWTP ADCP data and previously described model with USGS gage data over Deployment 3 with new best fit parameters.

Chapter 5 Results and Discussion

5.1 General Conditions in Cayuga Inlet

5.1.1 Temperature

To compare temperature measurements at different locations around and in the inlet, all temperature data was averaged on to the same 15-minute time scale. The stream temperature, for tributary flows into the inlet, was calculated by averaging temperatures in the three tributaries weighted based on their flowrates from the USGS gage stations. Cascadilla Creek does not have a gage station; however, it is reasonable to obtain the creeks flowrate based on the Sixmile Creek flowrate and the relative areas:

$$Q_{Cascadilla} = \frac{A_{Sixmile}}{A_{Cascadilla}} Q_{Sixmile} \quad (5.1)$$

Lake temperature on the southern shelf was obtained by averaging temperature measurements at different depths located at the piling cluster.

The average water temperature at the southern shelf of the lake was warmer than the average water temperature of the three tributaries flowing into the inlet for Deployment 1, except for a short stretch from September 6th through September 10th, 2015. Over Deployment 2 the inlet was always warmer than the southern lake, both of which, on average, were cooler than the three tributaries. Over Deployment 3 the inlet was warmer than the southern lake, except at the beginning of September 2016, when air temperatures dropped, and after mid-August 2016, the inlet and southern lake were more consistently warmer than the three inflowing tributaries.

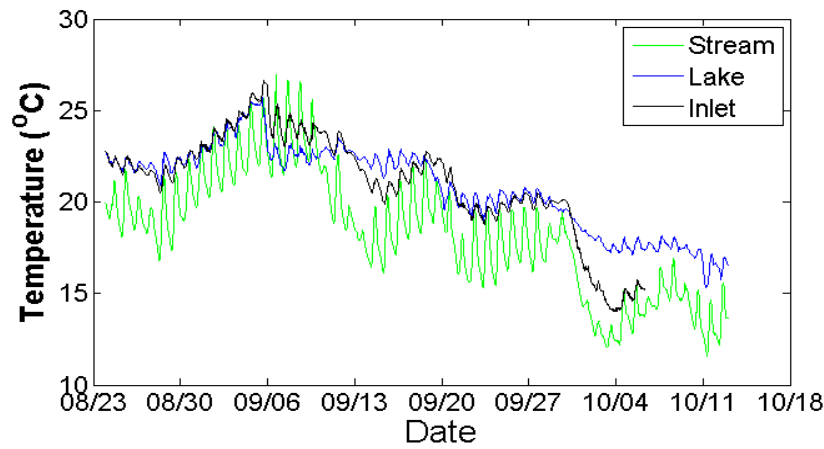


Figure 5.1.1: Average temperatures of tributaries (Inlet Creek, Sixmile Creek, and Cascadilla Creek), southern Cayuga Lake, and Inlet over Deployment 1, based on 15-minute average.

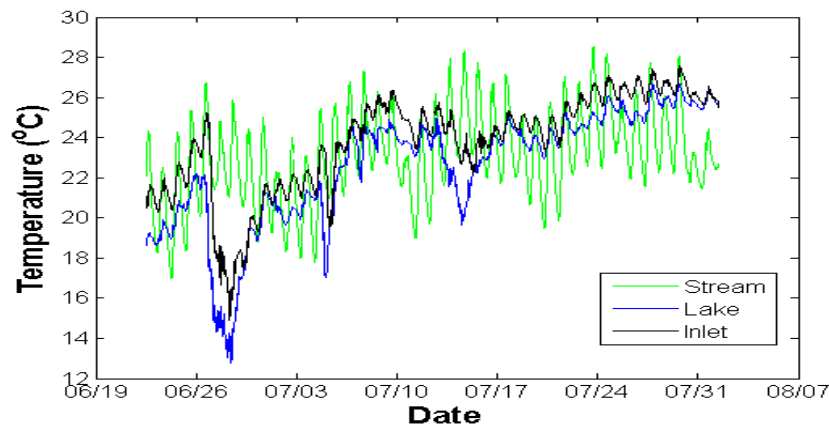


Figure 5.1.2: Average temperatures of tributaries (Inlet Creek, Sixmile Creek, and Cascadilla Creek), southern Cayuga Lake, and inlet over Deployment 2, based on 15-minute average.

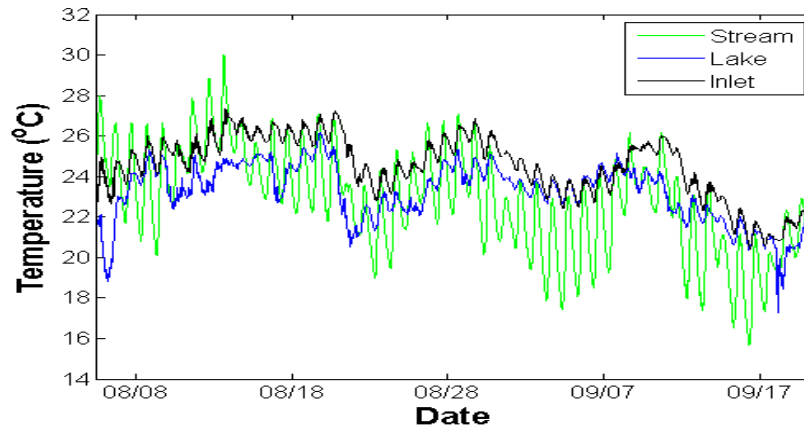


Figure 5.1.3: Average temperatures of tributaries (Inlet Creek, Sixmile Creek, and Cascadilla Creek), southern Cayuga Lake, and Inlet channel over Deployment 3, based on 15-minute average.

The tributary temperatures experienced greater fluctuations over time and, as we would expect, these shallow streams closely follow the air temperature. The tributaries display a warming period during the day and a cooling period at night. We applied a method for predicting the tributary temperatures based on the air temperature. This method considers that at the water surface, air influences the water temperature by conduction and air temperature and water temperature both respond to changes in solar heating. Two averaging time-intervals were utilized. The first was a backwards average, at each time step averaging prior air temperature data, to account for changes in the water temperature by conduction at the surface. The second was a centered average, at each time step averaging the air temperature before and after that time, to account for the idea that the air and water temperatures are responding to the same changes in solar heating, although at different rates. The tributary temperatures were then predicted based on the moving average, adding the backwards and centered time intervals, of the measured air temperature. We found the best fit moving averaging interval based on minimizing the mean square error between the predicted and measured tributary temperatures. Figure 5.2, shows how the best fit moving averaging interval was selected. Figure 5.3, compares the predicted tributary temperatures based on the above method to the measured tributary temperatures and air temperature for the beginning of Deployment 1.

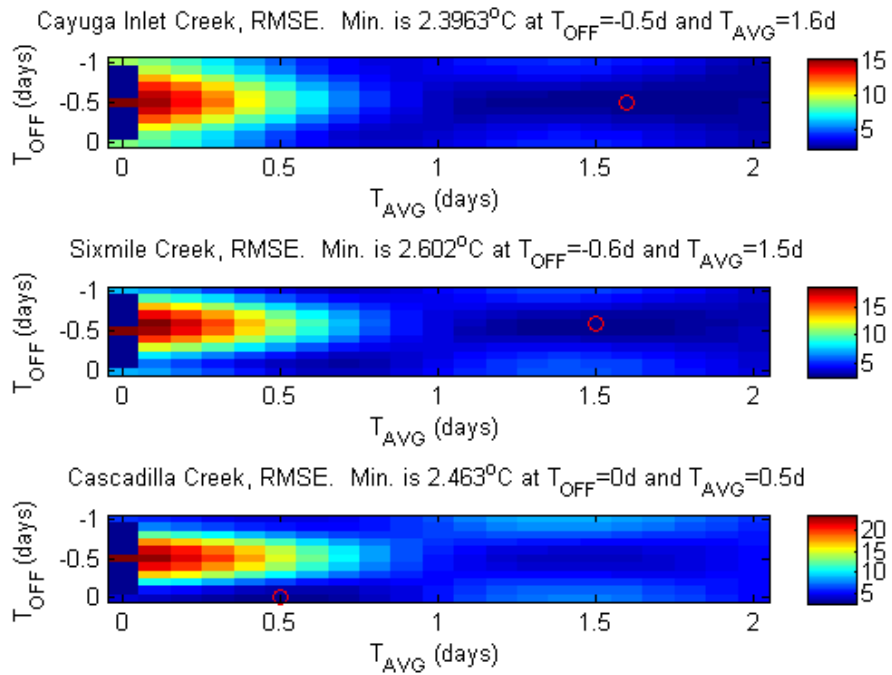
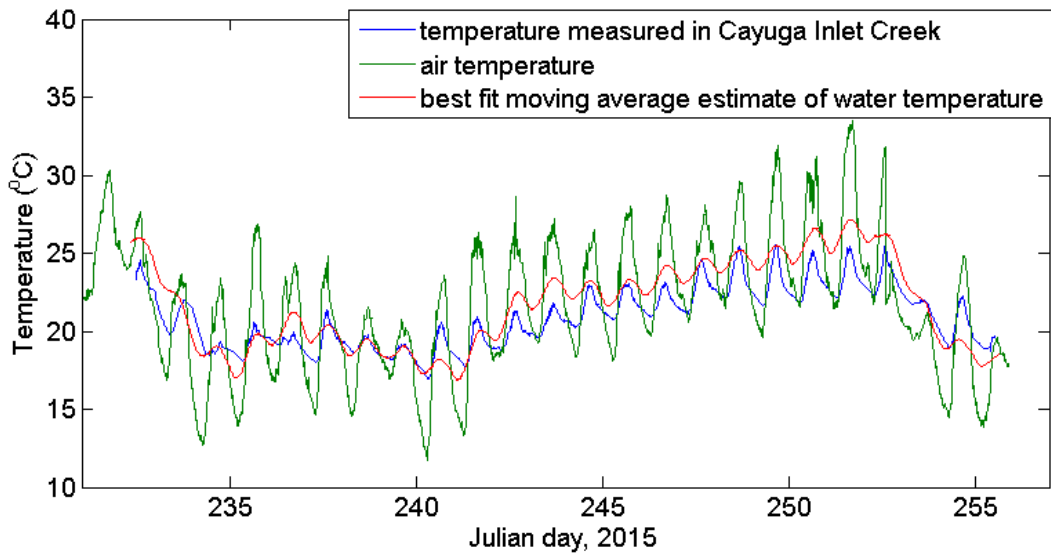


Figure 5.2: Root mean square error (RMSE) between measured and predicted tributary temperatures from range of combinations with backward (T_{OFF}) and center (T_{AVG}) averaging intervals. Location of lowest RMSE indicated by red circle.



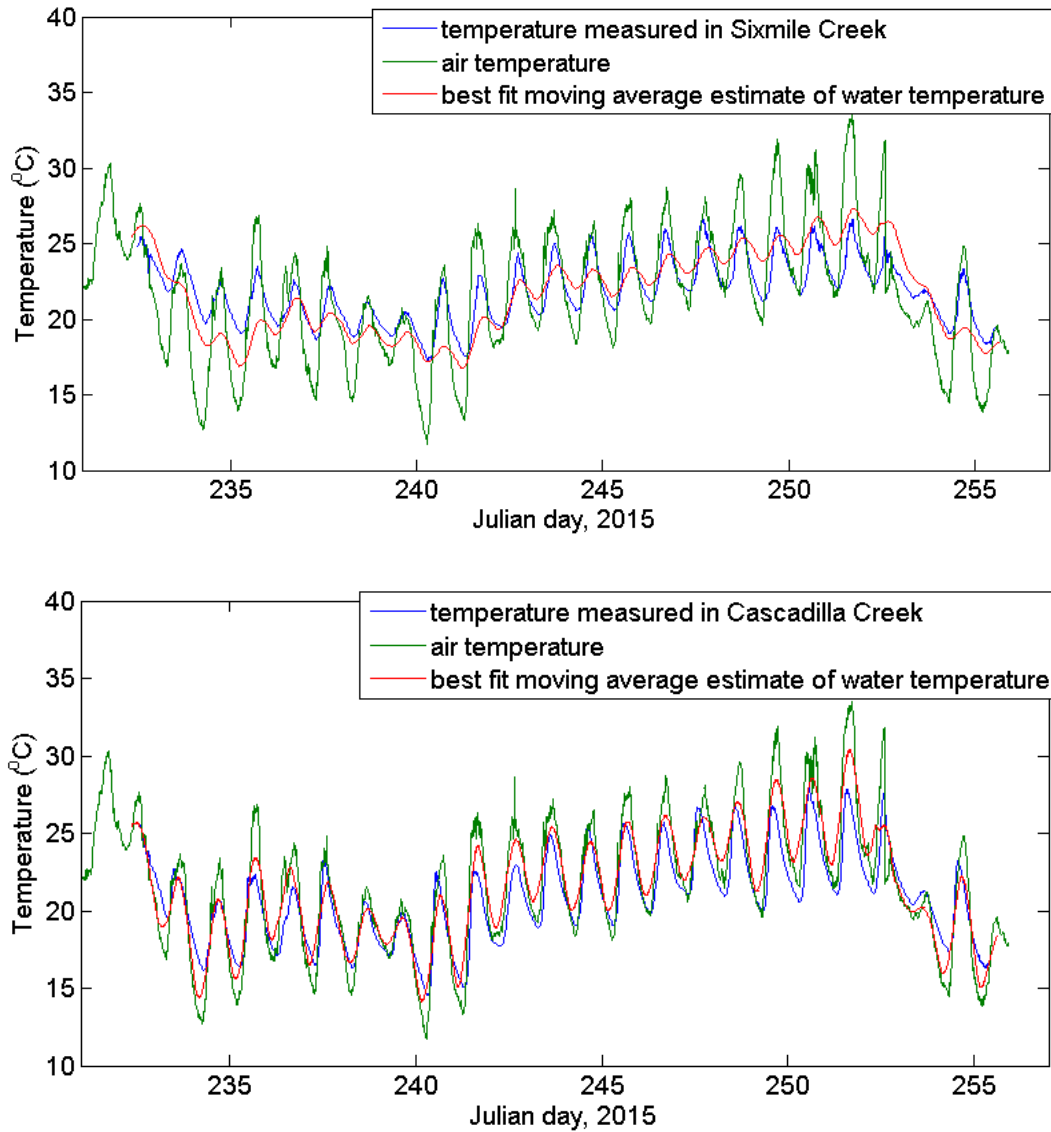


Figure 5.3: Predicted tributary temperatures based on air temperature and best fit moving average.

Recall, we are particularly interested in upwelling or near upwelling events, which can be indicated by a rapid drop in the water temperature on the southern shelf of the lake. In Deployment 1 and Deployment 3, which were in late summer and into fall, we cannot clearly identify any such events based on temperature. Over Deployment 1 the most significant decrease to the southern lake temperature occurred on 9/5/2015. Over Deployment 3 the most significant decrease to the southern lake temperature occurred on 8/21/2016 and the stream temperature decreased at that time as well.

However, over Deployment 2 the southern lake temperature rapidly drops over 3 different periods, shown more closely in Figure 5.4, and such events will be thoroughly discussed in future sections.

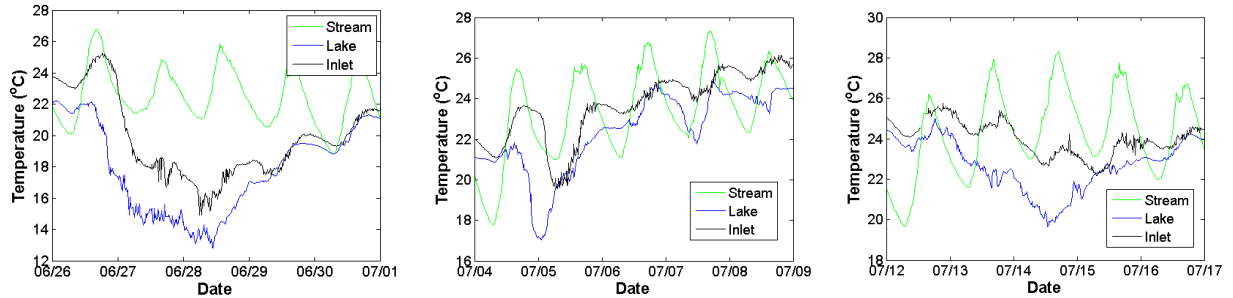


Figure 5.4: Average temperatures of inflowing tributaries (Inlet Creek, Sixmile Creek, and Cascadilla Creek), southern Cayuga Lake, and Inlet over periods of interest during Deployment 2.

Temperature structures starting at the main tributary outlets, going through the inlet, and moving into the southern shelf of the lake over Deployment 1 are plotted in Figure 5.5. Some profiles have greater resolution, as more thermistors were deployed in these locations. Blank spaces occur where no data was available. Surface water temperatures were greater than water temperatures closer to the bed, as we expect. Temperature in all locations starts out around 20°C to 22°C, then experiences a warming period at the beginning of September, increasing up to 26°C, and then for the rest of the deployment begin to cool, dropping to around 14°C into October.

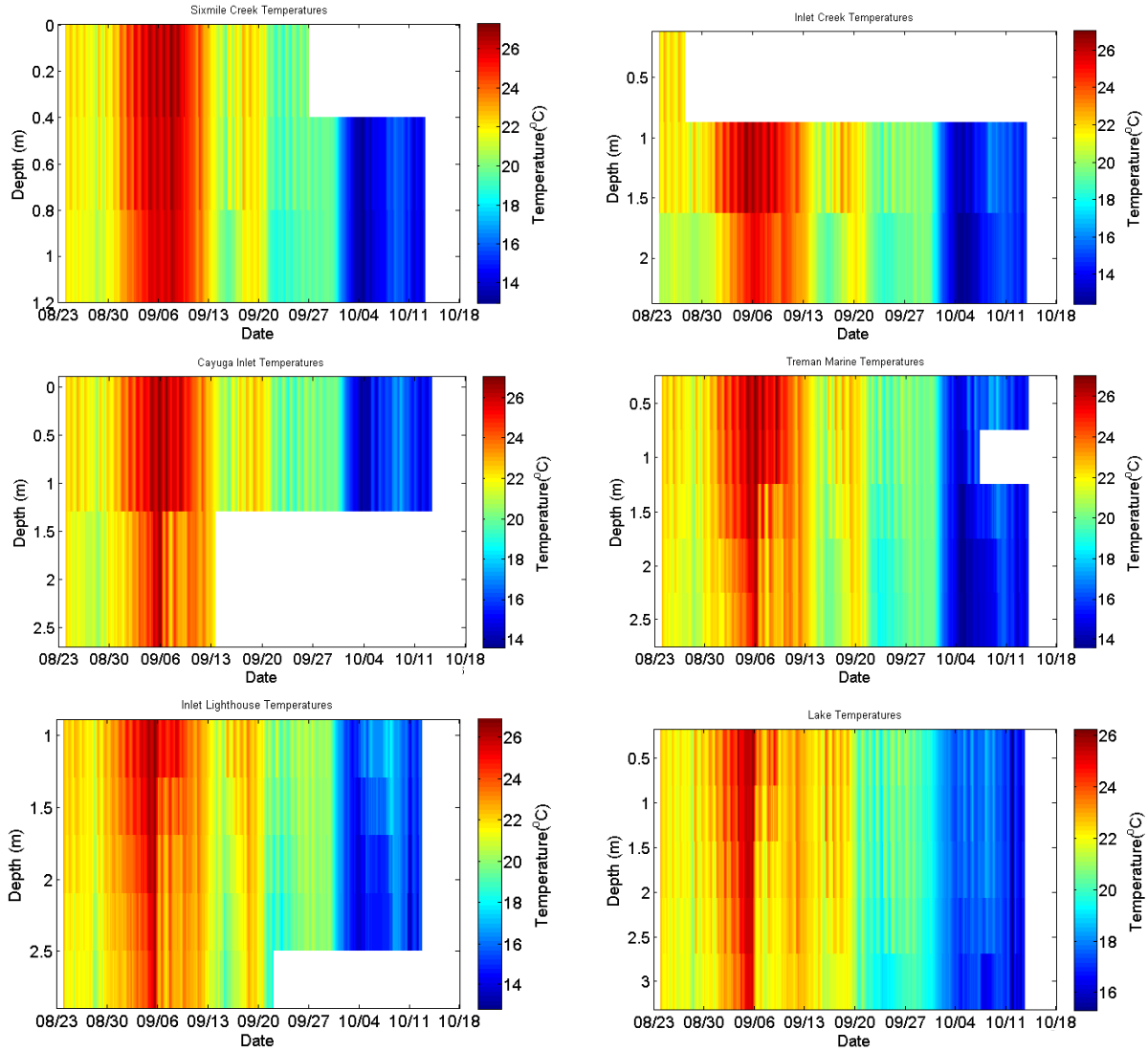


Figure 5.5: From left to right and top to bottom, water temperature profiles over Deployment 1 moving downstream through Cayuga Inlet, into the southern lake (see Figure 5.6 for exact locations). Approximate depths of thermistors is the center of each bin plotted. White spaces indicate missing data.

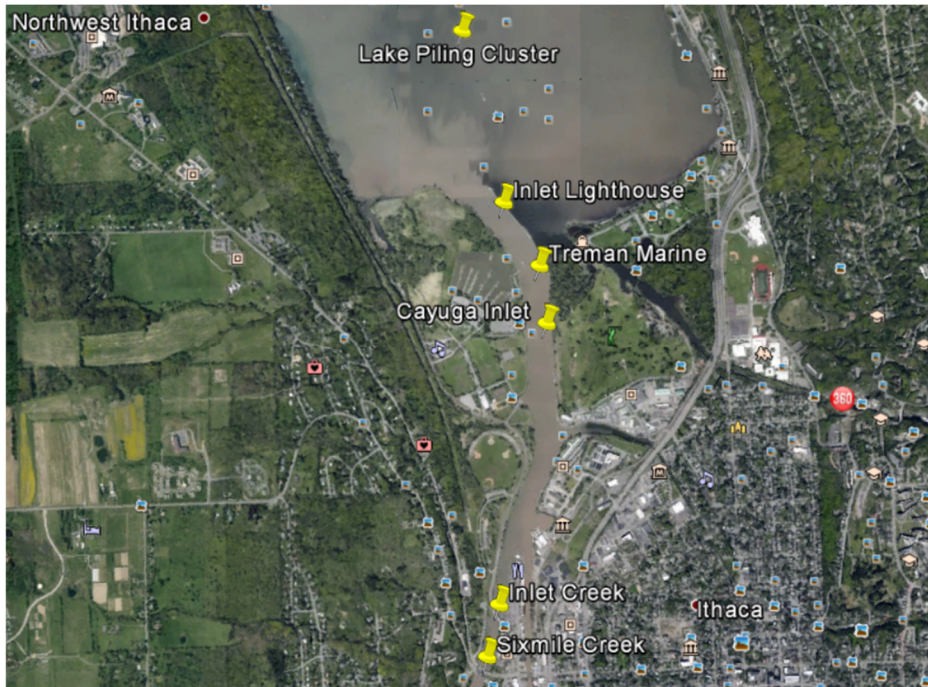


Figure 5.6: Locations of thermistor chains deployed in Cayuga Inlet for temperature profiles.

A horizontal temperature profile from the main tributary outlets, moving through the inlet, and into the southern shelf of the lake over Deployment 1 (Figure 5.7) demonstrates the same trends over time mentioned above. At times water is warmer towards the tributary end of the inlet (more common at the beginning of Deployment 1) as well as times water is warmer towards the lake end of the inlet (more common towards the end of Deployment 1). The temperature differences within and bounding the inlet are expected to influence the observed flow behavior.

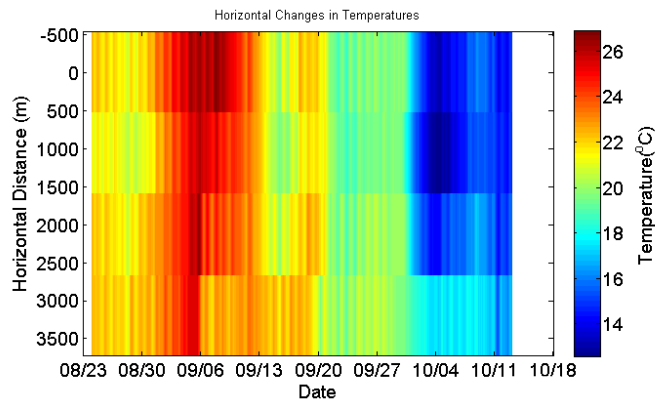


Figure 5.7: Average horizontal temperature profile over Deployment 1, where horizontal distance of 0 indicates the main inlet location and positive values indicate moving out towards the lake.

5.1.2 Vertical Mixing

Vertical mixing in the inlet is expected to be influenced by the degree of stratification. To characterize the degree of stratification we use the Brunt-Vaisala frequency, N (Equation (2.5)). We calculate the change in density between vertical layers of the inlet based on temperature measurements at given depths. For Deployment 1, N in the inlet was calculated based on temperature measurements taken at the Treman Marine site along the water column, closest to our turbidity and velocity measurements in the inlet. For Deployment 2 and 3, N in the inlet was calculated based on temperature measurements taken at the inlet site at the same location as our turbidity and velocity measurements along the water column. Overall N remained very low in the inlet, as temperature differences over the water column were typically within 1°C .

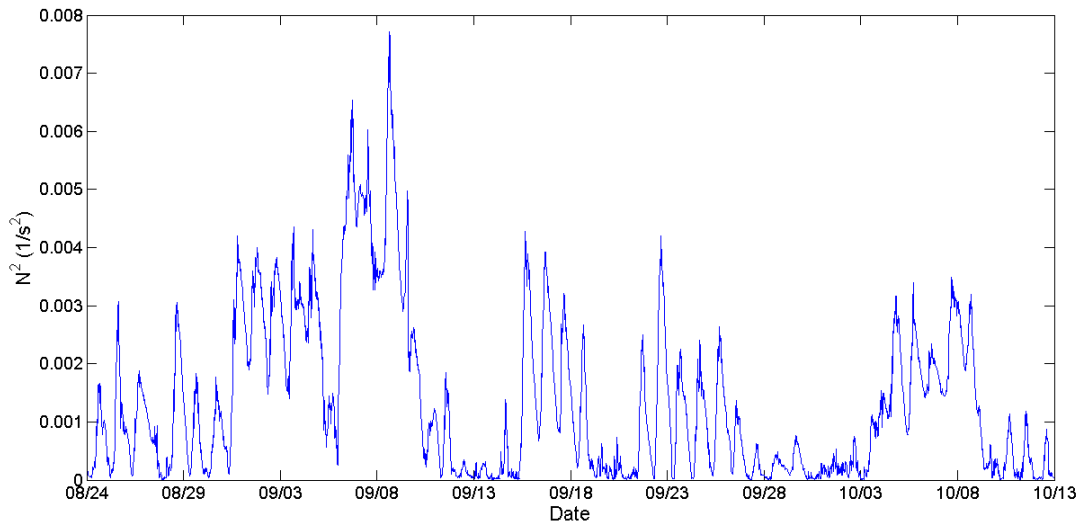


Figure 5.8.1: N^2 in the inlet over Deployment 1 at Treman Marine site.

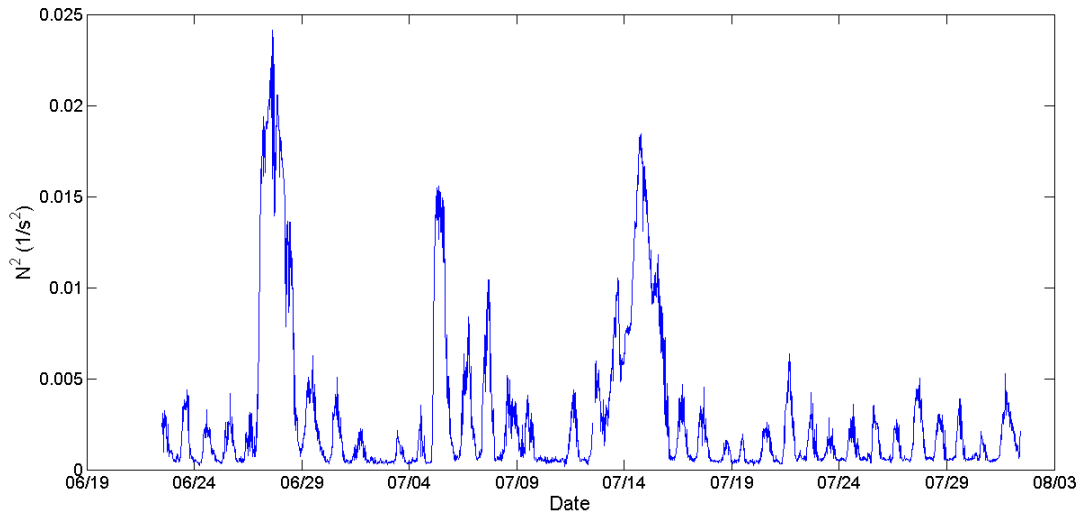


Figure 5.8.2: N^2 in the inlet over Deployment 2.

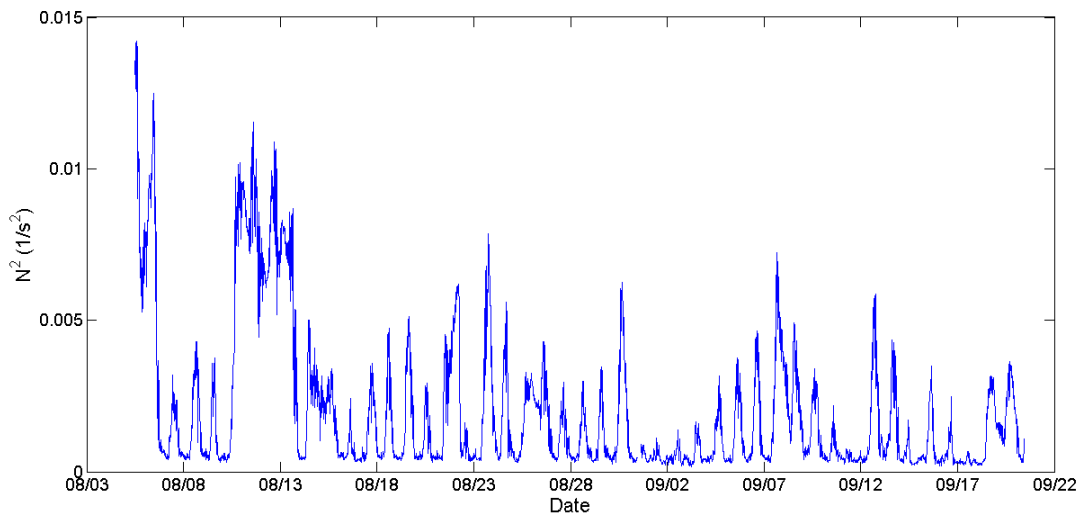


Figure 5.8.3: N^2 in the inlet over Deployment 3.

Another way to look at the vertical mixing in the inlet is through a timescale analysis. If the timescale of vertical mixing due to turbulence (τ_z) is much smaller than the advective timescale (τ_A), in other words vertical mixing occurs faster than water is flowing through the inlet, we expect the inlet to be well-mixed. We will distinguish the advective timescale as much larger than the vertical mixing timescale when it is greater by an order of magnitude (i.e. $\tau_A > 10\tau_z$). We calculate the advective timescale as follows:

$$\tau_A = \frac{L}{U} \quad (5.2)$$

L is the length of the inlet, for which we use 3000m, the approximate distance from the upstream Inlet Creek marker (by the USGS gage station) to the location of the ADCP in the inlet and U is the depth average streamwise velocity calculated from the ADCP data. We calculate the vertical mixing timescale as follows:

$$\tau_z = \frac{H^2}{D_z} \quad (5.3.1)$$

$$D_z = l_m^2 \left| \frac{\partial u}{\partial z} \right| \quad (5.3.2)$$

$$l_m = l_{m,0} f(Ri) \quad (5.3.3)$$

$$l_{m,0} = kz \sqrt{1 - \frac{z}{H}} \quad (5.3.4)$$

$$f(Ri) = \begin{cases} (1 + 40Ri)^{-1/2} & \text{if } Ri > 0 \\ (1 - 14Ri)^{1/4} & \text{if } Ri < 0 \end{cases} \quad (5.3.5)$$

$$Ri = \frac{N^2}{\left(\frac{\partial u}{\partial z}\right)^2} \quad (5.3.6)$$

H is the total depth of the inlet, D_z is the vertical eddy diffusivity, l_m is the mixing length, k is the von-Karman constant (0.41), u is the streamwise velocity, z is the depth, and Ri is the Richardson number (King, 2013).

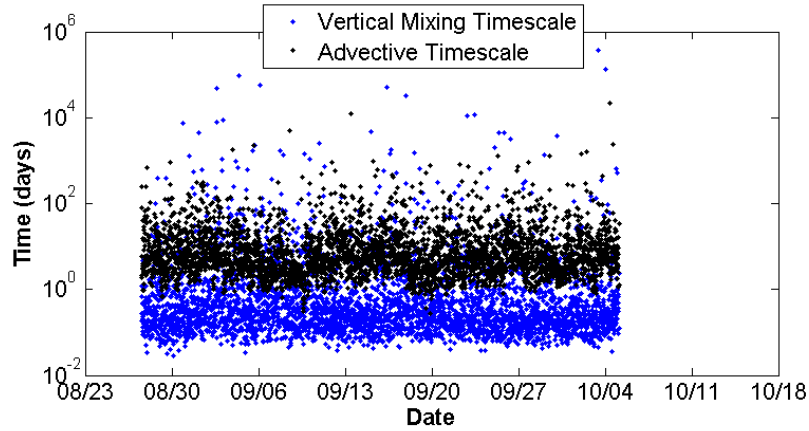


Figure 5.9.1: Comparison of vertical mixing and advective timescales in inlet over Deployment 1.

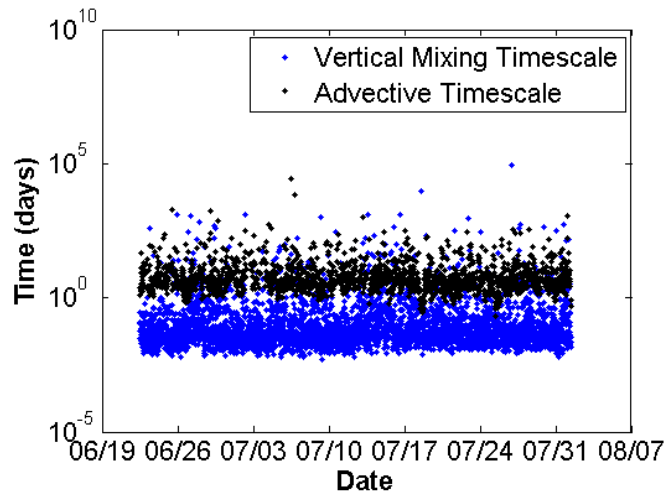


Figure 5.9.2: Comparison of vertical mixing and advective timescales in inlet over Deployment 2.

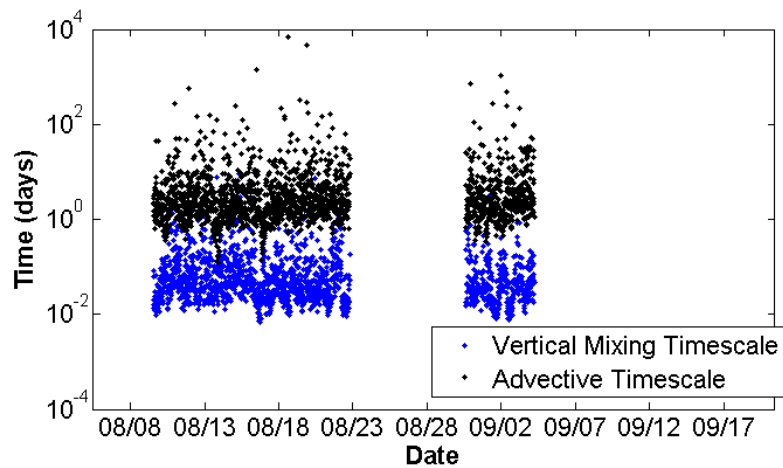


Figure 5.9.3: Comparison of vertical mixing and advective timescales calculated using IAWWTP ADCP data, for velocity profile and depth average velocity, over Deployment 3.

The majority of time the inlet was well mixed, with τ_z on the order of hours and τ_A on the order of days. For Deployment 1, 89.9% of the time $\tau_A > \tau_z$ and 63.9% of the time $\tau_A > 10\tau_z$. For Deployment 2, 95.2% of the time $\tau_A > \tau_z$ and 83.3% of the time $\tau_A > 10\tau_z$. For Deployment 3, 93.3% of the time $\tau_A > \tau_z$ and 81.5% of the time $\tau_A > 10\tau_z$. The percentage of time $\tau_A > 10\tau_z$ indicates how often we expect the inlet was well-mixed. With τ_z on the order of hours, changes in the inlets velocity gradient due to the barotropic seiche, which has an approximate period of 1 hour, does not have time to significantly contribute to the turbulent mixing. Specifically, any influence of the barotropic seiche on inlet velocities happens faster than vertical mixing is occurring.

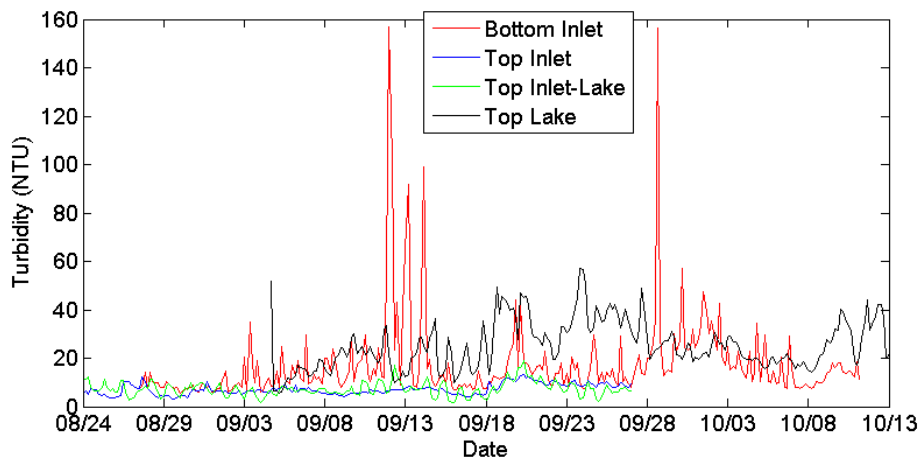
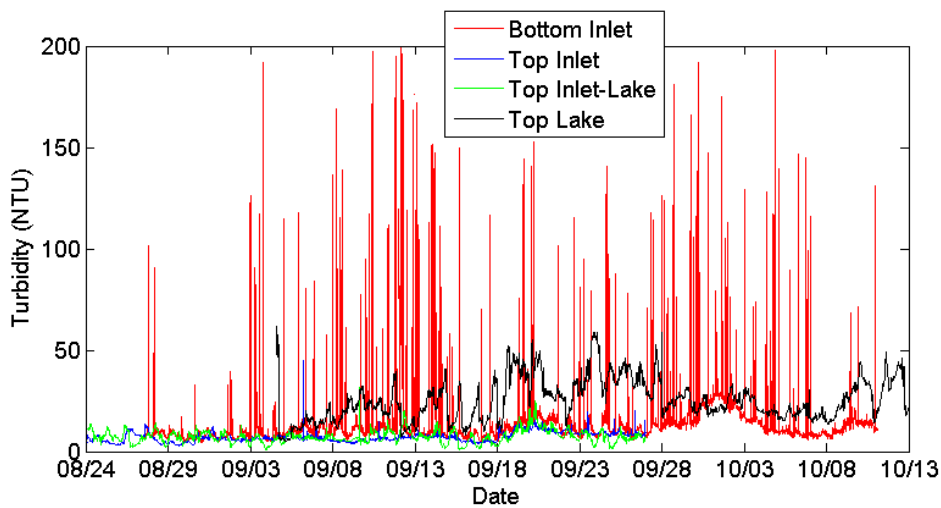
5.1.3 Turbidity

In this study turbidity measurements were used to assess the water quality and the influence of various physical mechanisms on the fate of sediment traveling through the inlet.

A month into Deployment 1, turbidity measurements in the top layer of the water column at the Cayuga Inlet location experienced an uncharacteristic increase. YSI claims for unattended sampling the water quality sonde can take effective field measurements from 30 up to 150 days, depending on the sensors used and fouling conditions of the site. The water quality sonde taking the turbidity measurements was deployed facing up and directly attached to a buoy. The turbidity sensor has a wiper which periodically cleans the optical surface. In the summer a month-long period in this system where the sonde was deployed such that the wiper likely had a difficult time keeping the sensor clean we suspect biofouling on the sensor occurred, which would explain the uncharacteristic increase in turbidity. Therefore, all turbidity data from this sonde deployed in the top layer, a month after the start of Deployment 1 was removed from analysis.

In Deployment 1 we were interested in observing the turbidity data over different averaging periods to observe any general trends (Figure 5.10). Over the shorter averaging period, 15 minutes,

there were many short spikes in turbidity in the bottom layer of the inlet, reaching up to 200 NTU. At the longer averaging period, 1 day, there were a few sustained increases in the bottom layer turbidity, reaching up to 43 NTU. The largest increase in turbidity on the southern end of the lake occurred shortly after the greatest increase in the bottom layer inlet turbidity. Turbidity in the top layer of the water column remained low throughout Deployment 1; less than 15 NTU for the 4-hour and 1-day averaging periods and only one short spike up to 43 NTU for the 15-minute averaging period, aside from which it remained below 20 NTU. Much of the following analysis focuses on turbidity in the bottom layer of the inlet, which experienced the greatest fluctuations and more significant turbidity loads in general, and the potential phenomena influencing changes in these measurements.



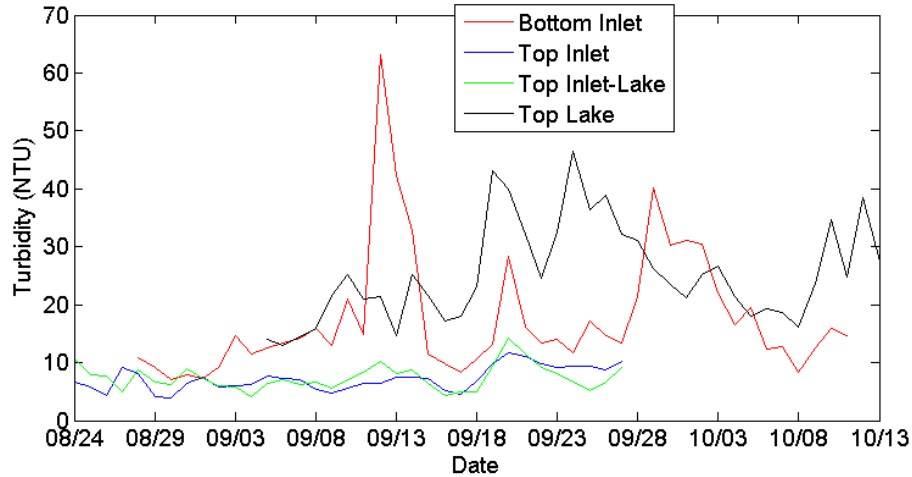


Figure 5.10: Turbidity averaged over 15 minutes (top), 4 hours (middle), and 1 day (bottom). Bottom Inlet: turbidity ~1.5m deep at Cayuga Inlet location; Top Inlet: turbidity ~0.5m deep at Cayuga Inlet location; Top Inlet-Lake; turbidity ~0.5m deep downstream towards lake of Cayuga Inlet location; Top Lake: turbidity ~0.5m deep at piling cluster on southern shelf of lake.

With turbidity data over Deployment 2, we considered various filters to remove random spikes, which are potentially due to a large particle passing over the sensor at the time of a reading and not representative of the local turbidity. However, we want to avoid removing any real event based increases in turbidity. Raw turbidity data and select statistics, before any filtering, are shown in Table 5.1.1 and Figure 5.11. The mean and median of the turbidities were relatively close (within 1.9 NTU and 0.4 NTU for readings taken in the bottom and top layer of the water column, respectively). We therefore expect most high turbidity readings were due to real events rather than spikes, that would have skewed the mean further from the median.

Table 5.1.1: Mean, median, standard deviation and maximum for raw turbidity over Deployment 2.

Location	Mean T_N (NTU)	Median T_N (NTU)	Standard Deviation (NTU)	Maximum (NTU)
Inlet Bottom	19.3880	17.5000	16.6275	764.100
Inlet Top	7.9735	7.6000	2.5473	36.3000

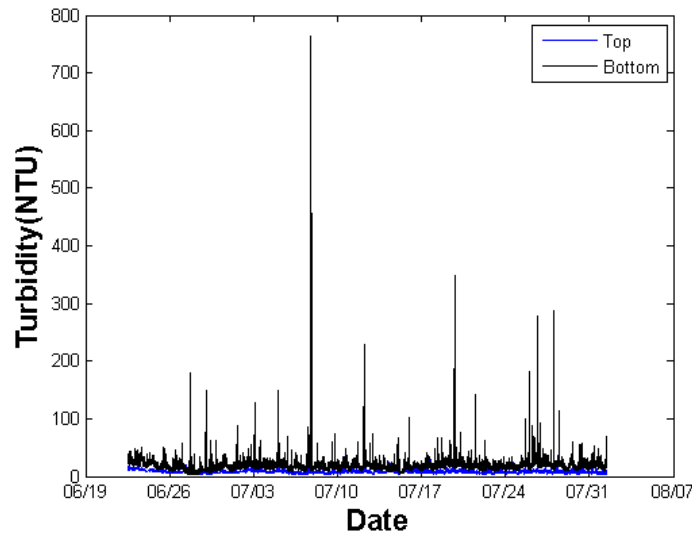


Figure 5.11: Raw inlet turbidity over Deployment 2.

To distinguish between event versus spike increases in turbidities we look at data over shorter periods. We expect turbidity readings taken at adjacent sampling times for an event based increase to exhibit elevated turbidity as well whereas spikes are one extreme measurement and we do not see elevated turbidity in adjacent times. An example of this distinction is shown in Figure 5.12.

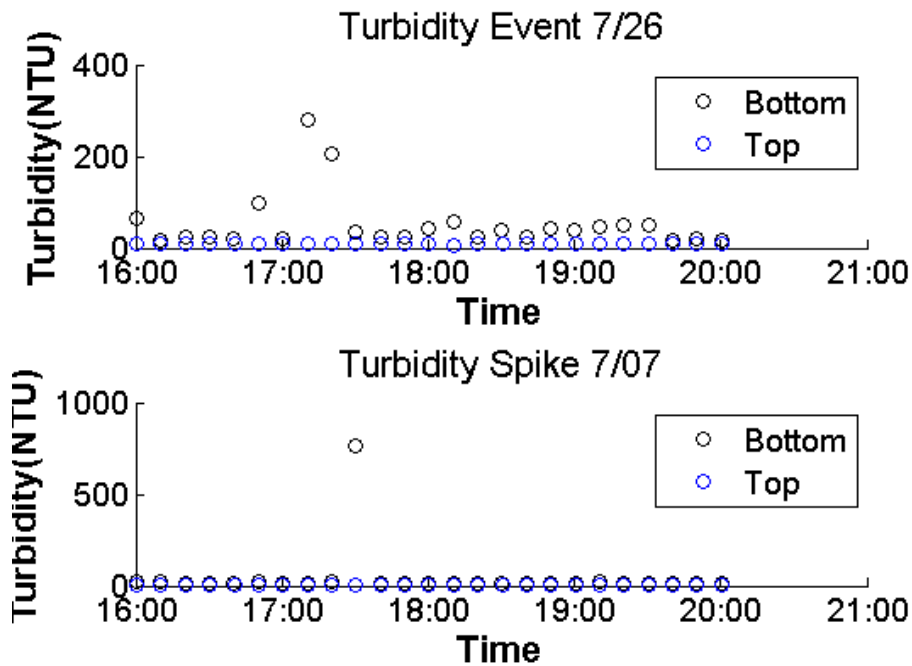


Figure 5.12: Distinguishing between real event based increases in turbidity (top) and spikes (bottom).

We filtered the turbidity data by removing measurements more than three standard deviations from the mean, over different periods. First, we filtered using one hour and two hour periods. In the case of one hour, no data were removed. In the case of two hours, 0.8% of the bottom layer turbidity data were removed and 0.16% of the top layer turbidity data were removed. The remaining data and select statistics are shown in Table 5.1.2 and Figure 5.13.1. Most measurements in the bottom layer turbidity above 100 NTU were removed, however the event shown in Figure 5.12 in late July is still present whereas the spike from early July was removed. We also filtered the data using a specific number of consecutive measurements. Looking at every 100 measurements any data more than 3 standard deviations away from the mean were removed. With this filter, 2.17% of the bottom layer turbidity data was removed and 1.37% of the top layer turbidity data was removed. The remaining data and select statistics are shown in Table 5.1.3 and Figure 5.13.2. Most measurements above 100 NTU were removed in this case. However, we may be losing data from real events, as for example data for the event observed in Figure 5.12 in late July were removed. For these reasons, filtering by 2-hour periods was selected. Applying the selected filter to data from Deployment 3, 1.42% of the bottom layer turbidity data and 0.33% of the top layer turbidity data was removed.

Table 5.1.2: Mean, median, standard deviation and maximum for turbidity filtered by 2-hour periods over Deployment 2.

Location	Mean T_N (NTU)	Median T_N (NTU)	Standard Deviation (NTU)	Maximum (NTU)
Inlet Bottom	18.6480	17.5000	8.5662	278.5000
Inlet Top	7.9442	7.6000	2.4213	24.9000

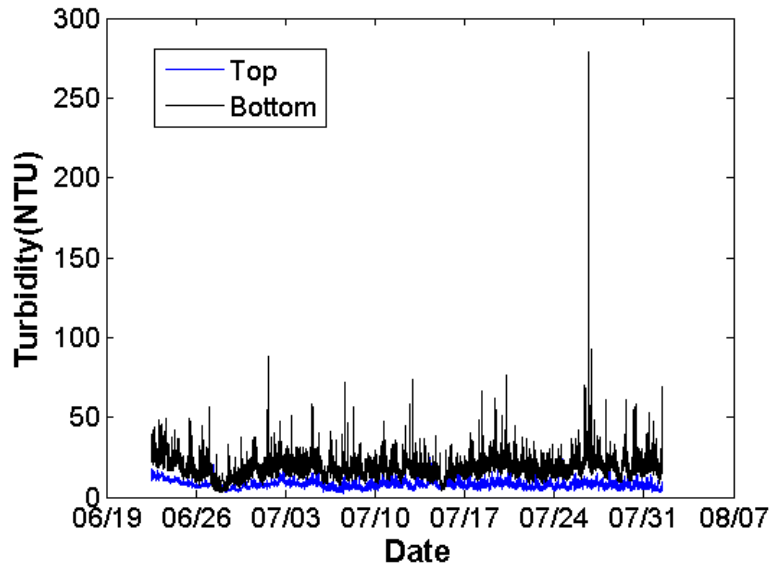


Figure 5.13.1: Inlet turbidity filtered by 2-hour periods over Deployment 2.

Table 5.1.3: Mean, median, standard deviation and maximum for turbidity data filtered by every 100 measurements over Deployment 2.

Location	Mean T_N (NTU)	Median T_N (NTU)	Standard Deviation (NTU)	Maximum (NTU)
Inlet Bottom	18.2402	17.3000	6.8149	129.3000
Inlet Top	7.8528	7.6000	2.2557	21.6000

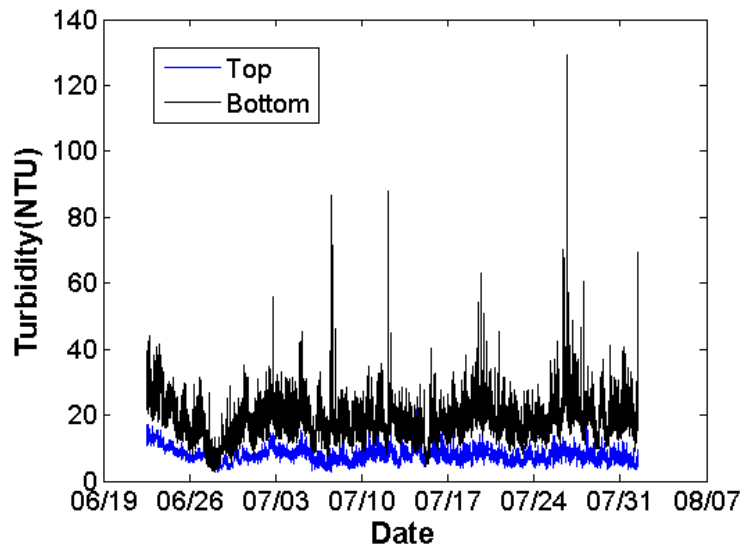


Figure 5.13.2: Inlet turbidity filtered by every 100 measurements over Deployment 2.

In the interest of observing changes in turbidity relative to changes in flow conditions on the barotropic timescale we averaged turbidity data onto the same 15-minute time axis. We set limits for low ($5 < \text{NTU} < 25$), medium ($25 < \text{NTU} < 50$), high ($50 < \text{NTU} < 100$), and extreme ($\text{NTU} > 100$) turbidity. These values were selected based on typically water quality standards concerning turbidity in surface waters and the general trend of turbidity collected over multiple deployments. Over Deployment 2, generally water with low turbidity traveled through the inlet, though medium events passed through the bottom layer. There were only a few high events and one extreme event specifically in the bottom layer. Neither the top layer of the inlet nor the southern lake had any high nor extreme turbidity events captured. While the southern lake captured a few medium events, the top layer of the inlet only experienced low turbidity, with a maximum turbidity of 23.9 NTU. For Deployment 3 at the beginning of August 2016, the southern lake had medium to high turbidity whereas the top layer inlet turbidity was low and the bottom layer inlet turbidity was low to medium. In mid-August, the bottom layer inlet turbidity spiked a few times to extreme values. However, late on August 21st, 2016 the bottom layer inlet turbidity began to quickly increase and eventually reached above 600 NTU. After this date, the bottom layer inlet turbidity repeatedly spiked to such levels while the top layer inlet and southern lake turbidities remained in the low to medium range.

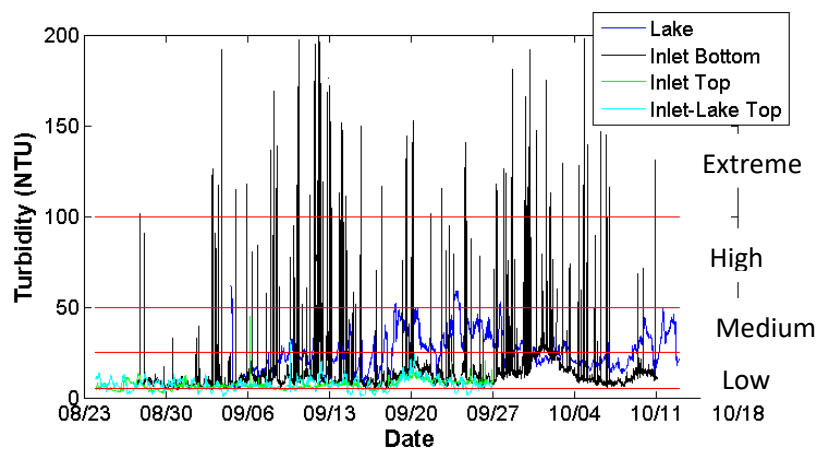


Figure 5.14.1: Turbidity in southern lake and inlet averaged onto 15-minute time axis over Deployment 1.

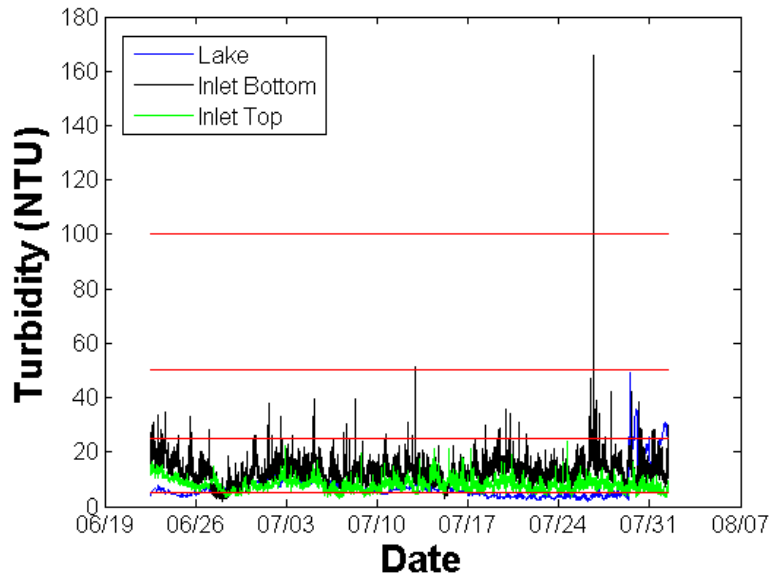


Figure 5.14.2: Turbidity in southern lake and inlet averaged onto 15-minute time axis over Deployment 2. Range of low, medium, high, and extreme turbidity indicated.

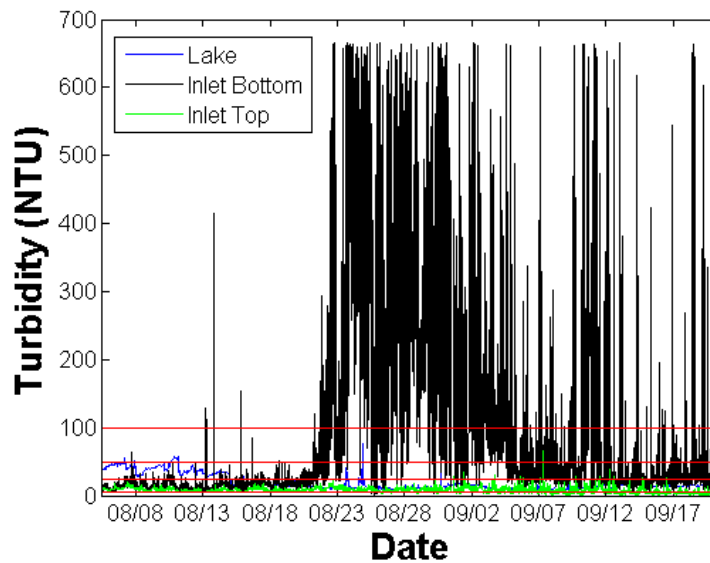


Figure 5.14.3: Turbidity in southern lake and inlet averaged onto 15-minute time axis over Deployment 3.

We are also interested in the percent difference in turbidities between the top and bottom layers of the inlet, as another way to evaluate the vertical mixing in the inlet:

$$\% \text{ Difference } T_N = \frac{T_{N_{bottom}} - T_{N_{top}}}{T_{N_{bottom}}} \times 100 \quad (5.4)$$

5.1.4 Flow Conditions

The direction of U in the inlet oscillates with approximately a 1 hour period, which is the period we expect of barotropic seiches in Cayuga Lake.

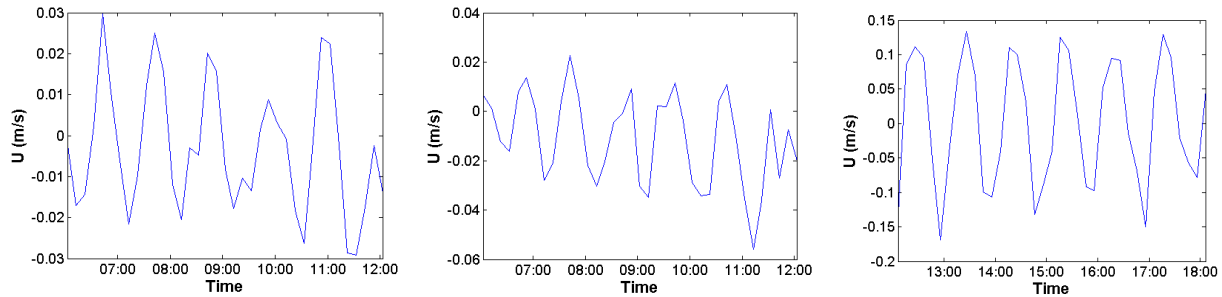


Figure 5.15.1: U over short time intervals to observe period of oscillations (left→right: 6/28/16, 7/10/16, 7/18/16).

This pattern persisted even when tributary flowrates increased, such as on 7/25/2016.

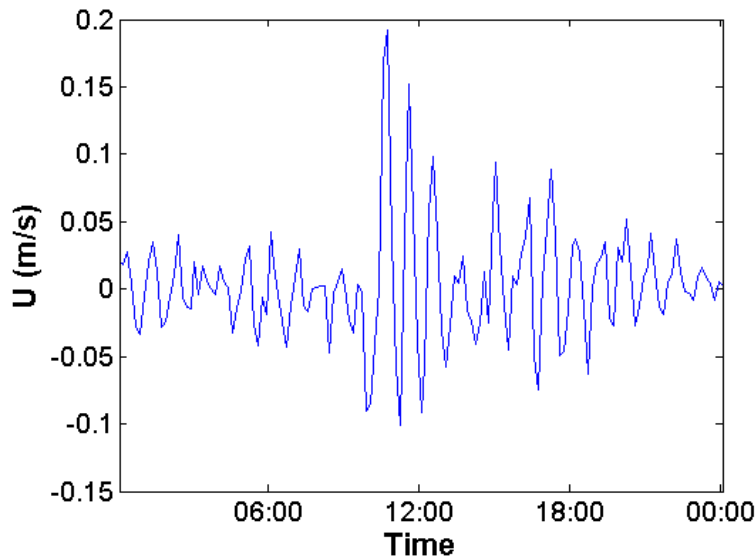


Figure 5.15.2: U on 7/25/16, when tributary flowrates reached maximum for Deployment 2.

Flow conditions the inlet were investigated based on vertical streamwise velocity profiles from an ADCP. Plotting the streamwise velocity over the water column revealed unidirectional flows from the inlet into the lake as well as from the lake into the inlet and exchange flows all occurred. Figure 5.16.1 shows examples of the raw velocity profiles for such flows.

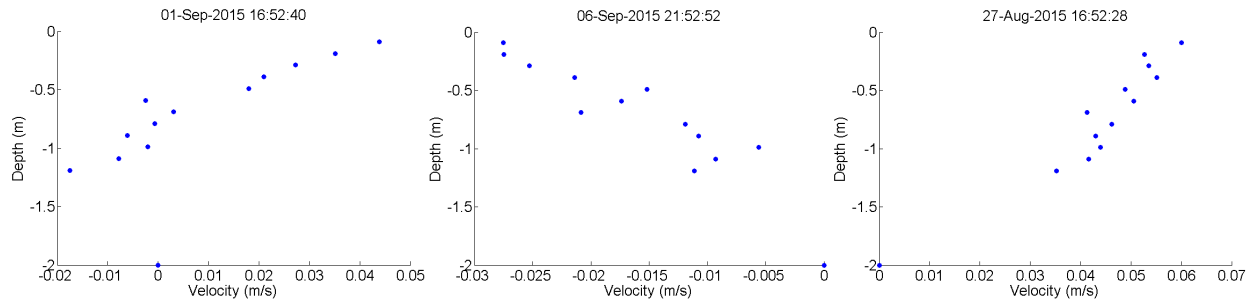


Figure 5.16.1: Vertical streamwise velocity profiles from ADCP at various times during Deployment 1, demonstrating an exchange flow (left) and unidirectional flows (middle and right).

Vertical streamwise velocity profiles from the HR Profiler were constrained to the bottom 1m of the inlet and had a higher resolution over the water column. We still captured unidirectional flows in both directions and exchange flows within this bottom 1m.

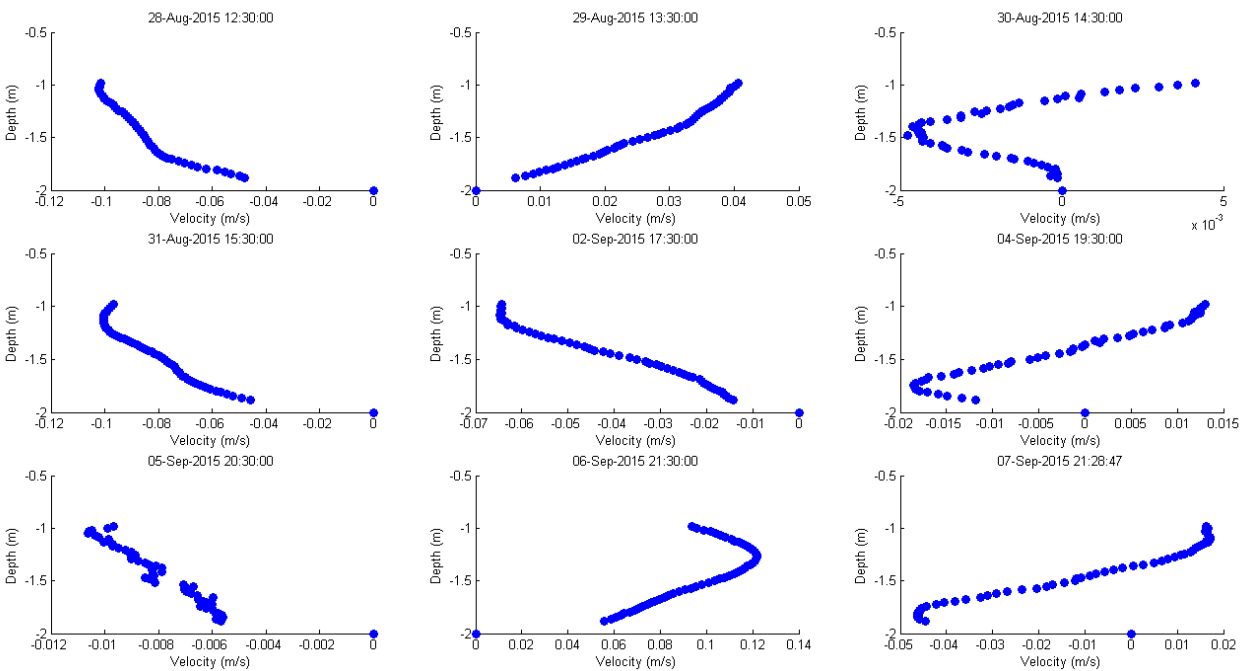


Figure 5.16.2: Vertical streamwise velocity profiles from HR Profiler at various times during Deployment 1, demonstrating exchange flows and unidirectional flows in bottom meter of inlet.

Flow conditions in the inlet were categorized into four groups. The four distinguished groups and frequency of occurrence (as a percent) of each for the three deployments are described in Table 5.2. Flow conditions were based on the vertical streamwise velocity profiles from an ADCP. Flow directed from the lake into the inlet has been denoted as a negative velocity while flow directed from

the inlet out to the lake has been denoted as a positive velocity. In some cases, velocity profiles captured more than one change in flow direction over the water column. Our analysis is restricted to a maximum of two layer flows; thus, in cases with more than two layers we selected the greatest change in velocity from one direction to another between adjacent measurements in the velocity profile as the location separating the two layers.

Table 5.2.1: Percentage frequency of described flow conditions in the inlet over Deployment 1.

Flow Conditions	Percentage Frequency (%)	Average Velocity (m/s)
Exchange flow with bottom layer flowing from lake to inlet and top layer flowing from inlet to lake (1)	32.8	Bottom: -0.0106 Top: 0.0026
Exchange flow with bottom layer flowing from inlet to lake and top layer flowing from lake to inlet (2)	37.6	Bottom: 0.0049 Top: -0.0040
Unidirectional flow from inlet to lake (3)	11.6	0.0135
Unidirectional flow from lake to inlet (4)	18.0	-0.0246

Table 5.2.2: Percentage frequency of described flow conditions in the inlet over Deployment 2.

Flow Conditions	Percentage Frequency (%)	Average Velocity (m/s)
Exchange flow with bottom layer flowing from lake to inlet and top layer flowing from inlet to lake (1)	37.5	Bottom: -0.0105 Top: 0.0042
Exchange flow with bottom layer flowing from inlet to lake and top layer flowing from lake to inlet (2)	35.4	Bottom: 0.0096 Top: -0.0079
Unidirectional flow from inlet to lake (3)	11.3	0.0269
Unidirectional flow from lake to inlet (4)	15.8	-0.0260

Table 5.2.3: Percentage frequency of described flow conditions in the inlet over Deployment 3 (based on IAWWTP ADCP).

Flow Conditions	Percentage Frequency (%)	Average Velocity (m/s)
Exchange flow with bottom layer flowing from lake to inlet and top layer flowing from inlet to lake (1)	34.7	Bottom: -0.0123 Top: 0.0172
Exchange flow with bottom layer flowing from inlet to lake and top layer flowing from lake to inlet (2)	36.8	Bottom: 0.0034 Top: -0.0041
Unidirectional flow from inlet to lake (3)	19.0	0.0384
Unidirectional flow from lake to inlet (4)	9.5	-0.0422

An exchange flow occurred more frequently in the inlet than a unidirectional flow. The average velocity magnitudes for the unidirectional flows were greater than for the exchange flows, which have competing velocities. Over Deployment 3 a unidirectional flow from the inlet to the lake was more frequent than from the lake to the inlet however, over Deployment 1 and 2 the opposite was true. Low flowrates in the tributaries due to the unusually dry weather over Deployment 2 likely played a role. Over each deployment period the water surface elevation in the inlet on average increased. As previously mentioned, the water surface elevation increased the most over the third Deployment, under the greatest tributary flowrates, the first Deployment had the second greatest increase in the water surface elevation, under the second greatest tributary flowrates, and the second Deployment had the smallest increase in the water surface elevation, under the lowest tributary flowrates, but an average increase did occur. Over Deployment 3 average velocities for all flow conditions, except condition 2, increased from Deployment 2. However, recall when comparing IAWWTP ADP and Cornell ADCP data over the same period, the IAWWTP ADP recorded on average double the velocities recorded by the Cornell ADCP.

We are interested in the distribution of various conditions in the inlet under the different flow types described above. The highest observed $|U|$ was always during a unidirectional flow (as expected since exchange flows have layers counteracting one another in this calculation). However, for all flow types, $|U|$ was predominantly less than 0.025m/s. $|U|$ was rarely above 0.1m/s and this only occurred during unidirectional flows. Similar observations were true for U_{abs} over Deployment 1 and 2, where higher U_{abs} occurred during unidirectional flows. Over Deployment 3, using the IAWWTP ADP, U_{abs} was most frequently between 0.1m/s and 0.2m/s for all flow types, but the highest observed U_{abs} was still during a unidirectional flow. There were more instances of $N > 0.1$ during exchange flows, while N was typically very low during unidirectional flows. However, N was dominantly low across all flow types. While most of the time the inlet was well-mixed, indicated by $\frac{10\tau_z}{\tau_A} < 1$, under all flow types there were times the timescale analysis indicated the inlet was not well-mixed, though infrequent. All flow types exhibited similar distributions of τ_z , typically on the order of hours. τ_A was more frequently higher during exchange flows, thus bulk water was moving slower through the inlet, which again reflects the counteracting layers.

The component of the wind speed along the East-West axis was predominately below 1m/s. For Deployment 1, under the second type of exchange flow southerly and northerly winds appear to be equally prevalent, while southerly winds were slightly more prevalent during both unidirectional flows and more so during the first type of exchange flow. For Deployment 2, the first flow type most frequently corresponded to southerly winds. It is this southerly wind, if sustained, which sets up the seiching behavior in the lake to cause an upwelling on the southern shelf, that pushes cooler water from the lake into the bottom layer of the inlet, causing such an exchange flow. The second type of exchange flow corresponded most frequently to moderate southerly and northerly winds. Both unidirectional flows most frequently corresponded to a southerly wind. However, the unidirectional

flow from the lake into the inlet occurred during strong northerly winds but not strong southerly winds. Over Deployment 3, southerly winds were dominant and particularly so during the first type of exchange flow. Again, this is what we expect, with a strong, sustained southerly wind setting up conditions for an approaching upwelling event on the southern shelf. Southerly winds were also particularly dominant during flow type 3, which is the unidirectional flow out of the inlet into the lake (same direction as a southerly wind). The only flow type a southerly wind was not significantly dominant was flow type 4, which is flowing directly opposite such a wind. For both exchange flows, strong sustained winds along the axis of the lake set up the seiche behavior in the lake and have the potential to dampen if counteractive to existing seiches. The lake seiches can cause a layer of water to flow back into the inlet and another layer can flow out to the lake when tributary flows are significant. Density differences between the tributaries and the southern lake, due to differences in temperature, but more importantly suspended sediment concentrations, could influence in which layer we see which flow direction, with denser water flowing into the bottom layer of the inlet. While wind stresses may influence the direction of a surface layer in the inlet, this did not appear to be the case with our recorded velocities, as we will discuss more in depth in a later section focused on wind. We also checked if identifying the colder source (tributaries or southern lake) accurately predicted which layer was flowing which direction (with the colder source flowing into the bottom layer), but this was not always the case either, which is why we suspect concentrations of suspended sediment from each source are important to this regard. It was likely, given the vertical mixing timescale was on the order of hours and the advective timescale was on the order of days, water sourced to the inlet from the tributaries or the southern lake mixed over the water column faster than it reached our inlet location. This may explain why we do not always see the colder source flowing in to the bottom layer. We were potentially measuring in a “zone of quiet” and the observed flow behavior here was due to the tributary flows and the history of the barotropic seiche.

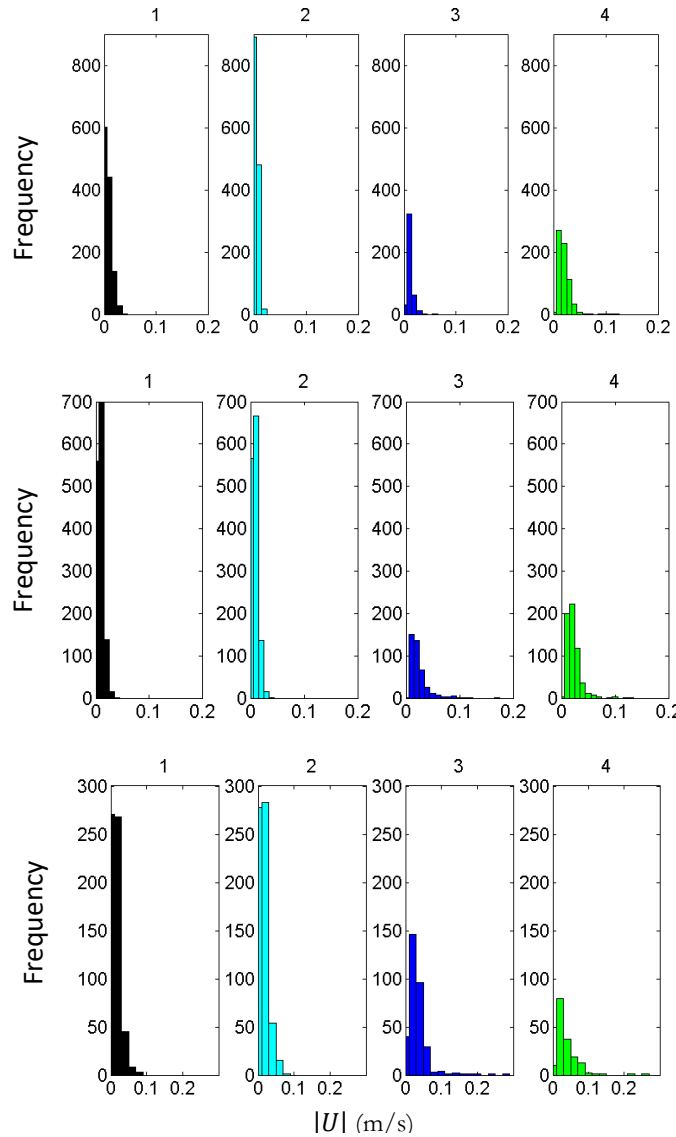
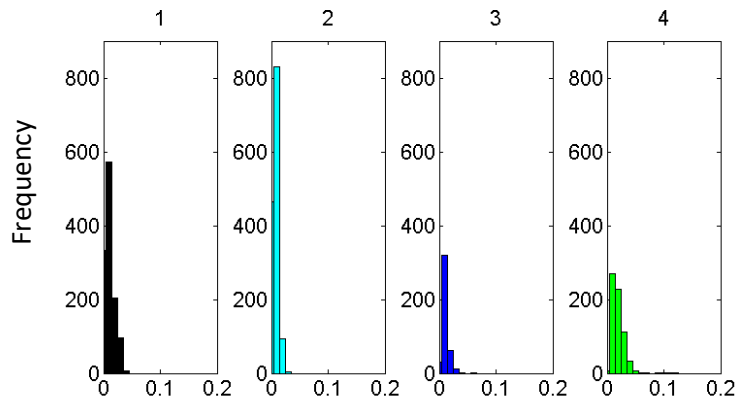


Figure 5.17: Distribution of $|U|$ (m/s) through inlet under different flow conditions. Top: Deployment 1; Middle: Deployment 2; Bottom: Deployment 3.



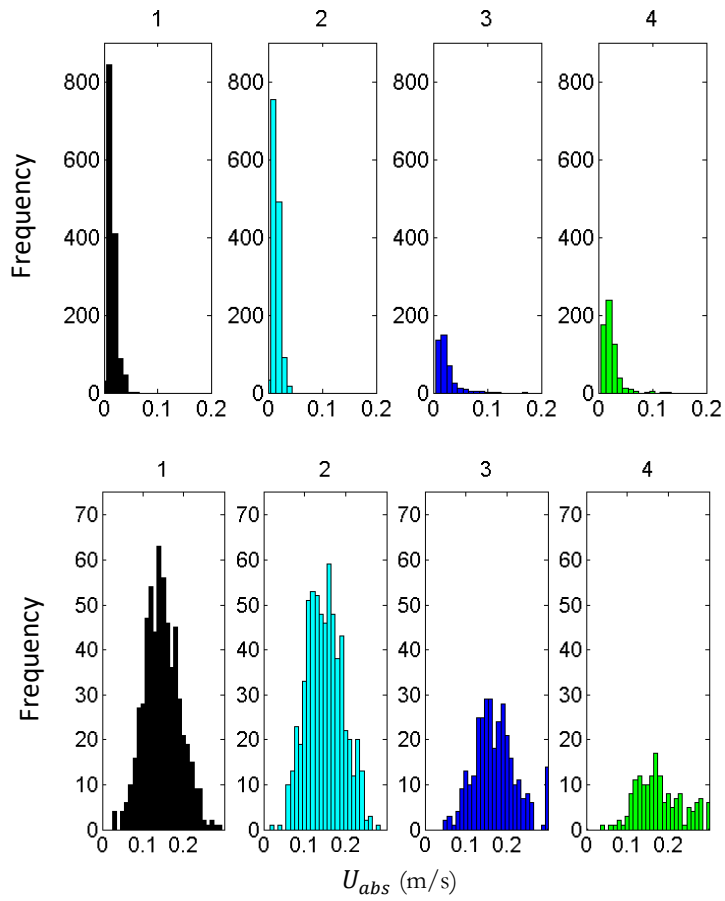
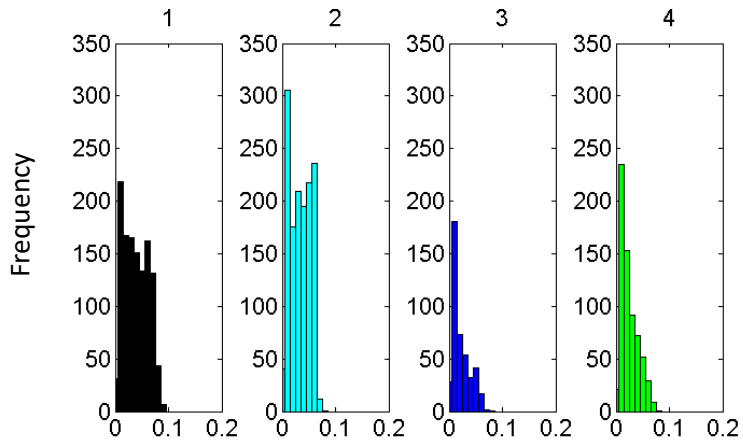


Figure 5.18: Distribution of U_{abs} (m/s) through inlet under different flow conditions. Top: Deployment 1; Middle: Deployment 2; Bottom: Deployment 3.



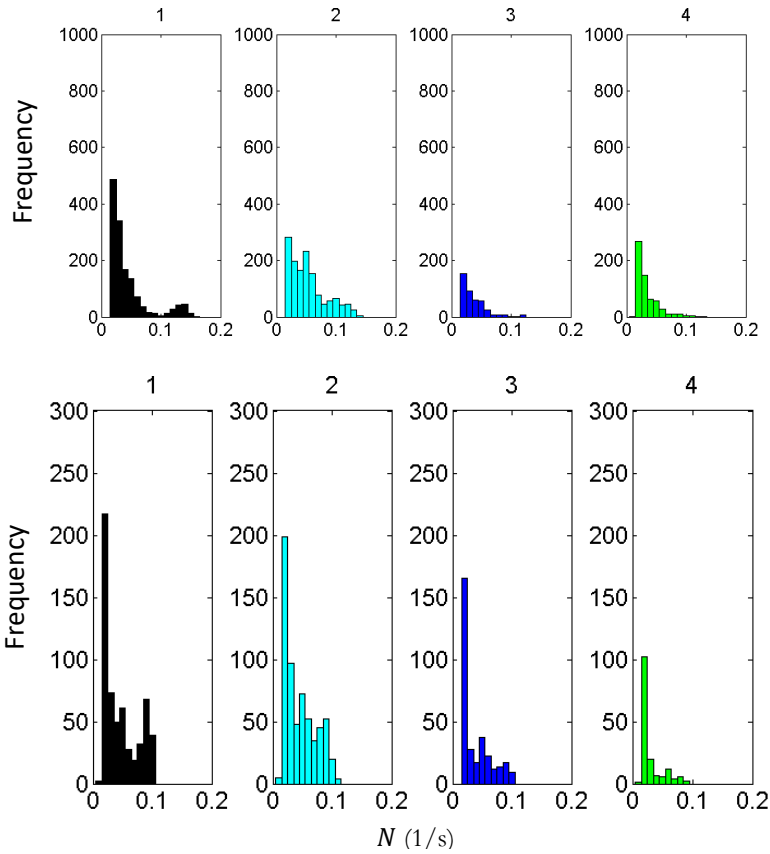
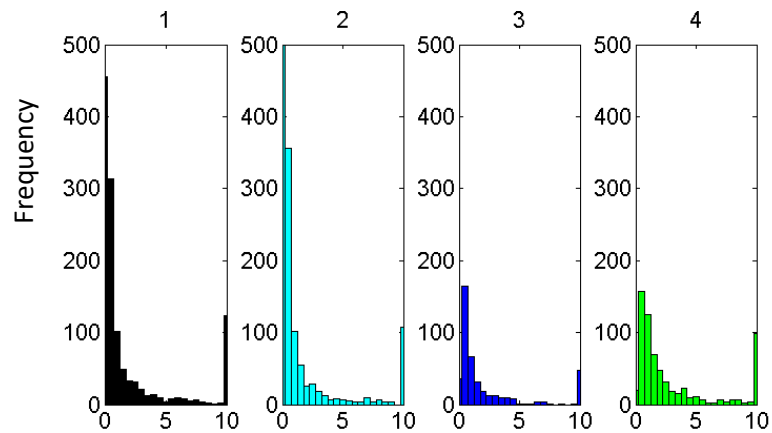


Figure 5.19: Distribution of $N (1/s)$ in inlet under different flow conditions. Top: Deployment 1; Middle: Deployment 2; Bottom: Deployment 3.



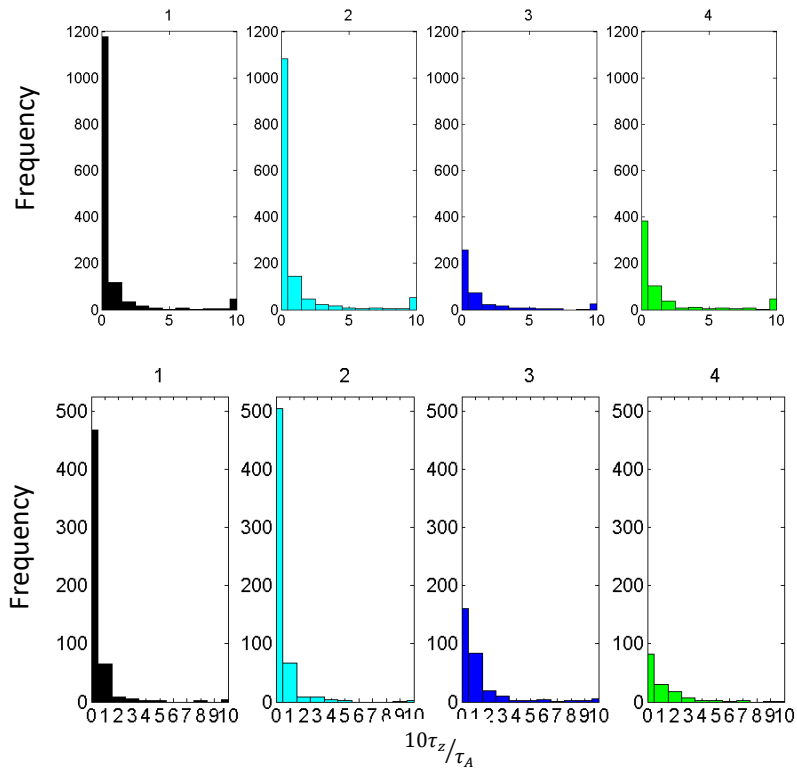
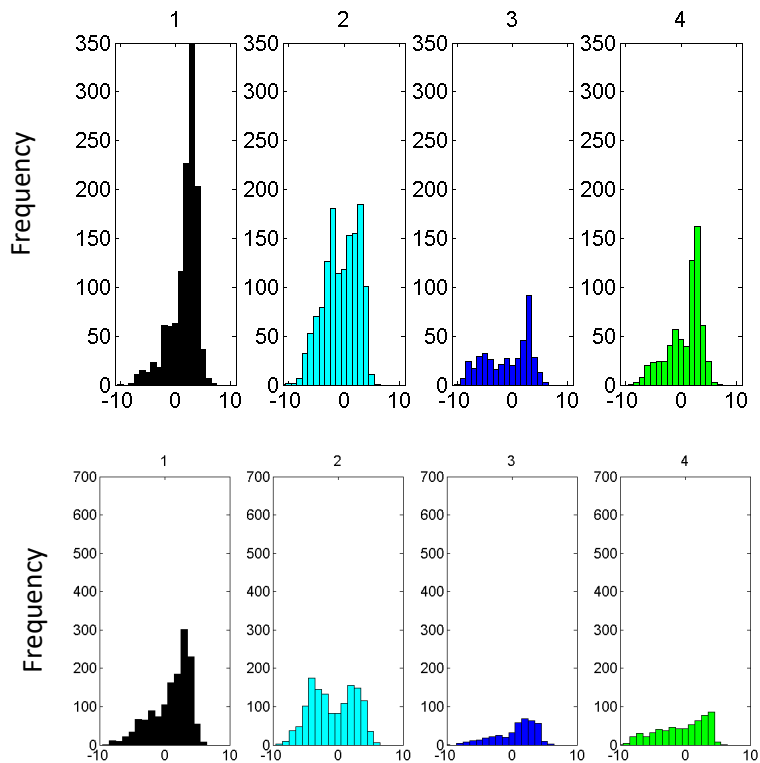


Figure 5.20: Distribution of $\frac{10\tau_z}{\tau_A}$ in the inlet under different flow conditions. When $\frac{10\tau_z}{\tau_A} < 1$, expect the inlet to be well-mixed. (Note: all timescale comparisons greater than 10, when advective timescale faster than vertical mixing timescale, placed into the 10 bin) Top: Deployment 1; Middle: Deployment 2; Bottom: Deployment 3.



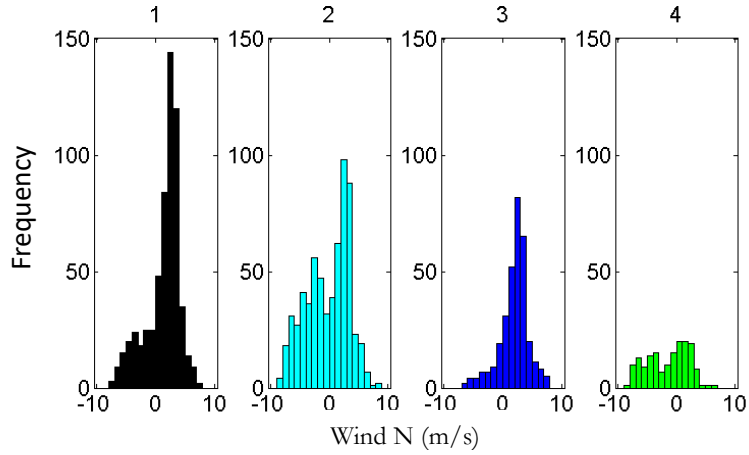


Figure 5.21: Distribution of southerly wind speed (m/s) over Cayuga Lake under different inlet flow conditions. Top: Deployment 1; Middle: Deployment 2; Bottom: Deployment 3.

We evaluated different “energies” under the different flow types described. The kinetic energy of the tributary inflow was based on the velocity through the inlet due to the tributary flowrates, where Q is the sum of the three tributary flowrates and A_c is the cross-sectional area of the inlet. The kinetic energy of wind was based on the wind stress, where C_{10} is the drag coefficient (1.5×10^{-3}) and U_{10} is the wind velocity along the lake/inlet axis measured approximately 10 meters above the water surface. The raw wind velocity data from the piling cluster was measured approximately 3m above the water surface, U_3 , thus we used the power law, assuming neutral stability conditions, to calculate the wind speed at the 10m height. Lastly, the potential energy in the inlet was based on the change in the water surface elevation, measured at the Cayuga Inlet USGS gage station, ΔH .

$$KE_{trib} = \rho u_Q^2; \quad u_Q = \frac{Q}{A_c} \quad (5.5)$$

$$KE_{wind} = \tau_{wind} = \rho_{air} C_{10} U_{10}^2; \quad U_{10} = U_3 \left(\frac{10}{3}\right)^{1/7} \quad (5.6)$$

$$PE = \rho g \Delta H \quad (5.7)$$

The distribution of the kinetic energy of tributary inflow was on average slightly higher during flow types 2 and 3, thus the unidirectional flow sourced from the tributaries and the exchange flow where

the bottom layer was sourced from the tributaries. Overall, the kinetic energy of wind was higher than that of tributary inflows, however had very similar distributions across all flow types. The distribution of the potential energy was wider for unidirectional flows, thus, more significant changes in the surface water elevation occurred under unidirectional flows than exchange flows. Over Deployment 2, which had the lowest tributary flowrates, the distribution of the potential energy under flow type 3 (unidirectional flow sourced from the tributaries) was skewed towards the negative side, thus the surface water elevation was typically decreasing over these times and under flow type 4 (unidirectional flow sourced from lake) was skewed towards the positive side, thus the surface water elevation was typically increasing over these times.

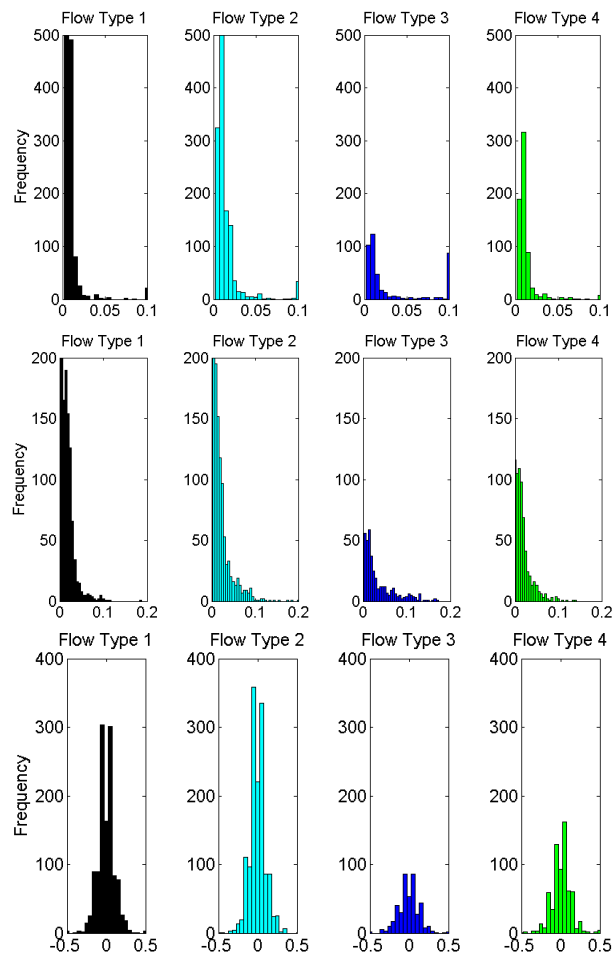


Figure 5.22.1: Distribution of KE_{trib} (top), KE_{wind} (middle), and PE (bottom) under different inlet flow conditions over Deployment 1.

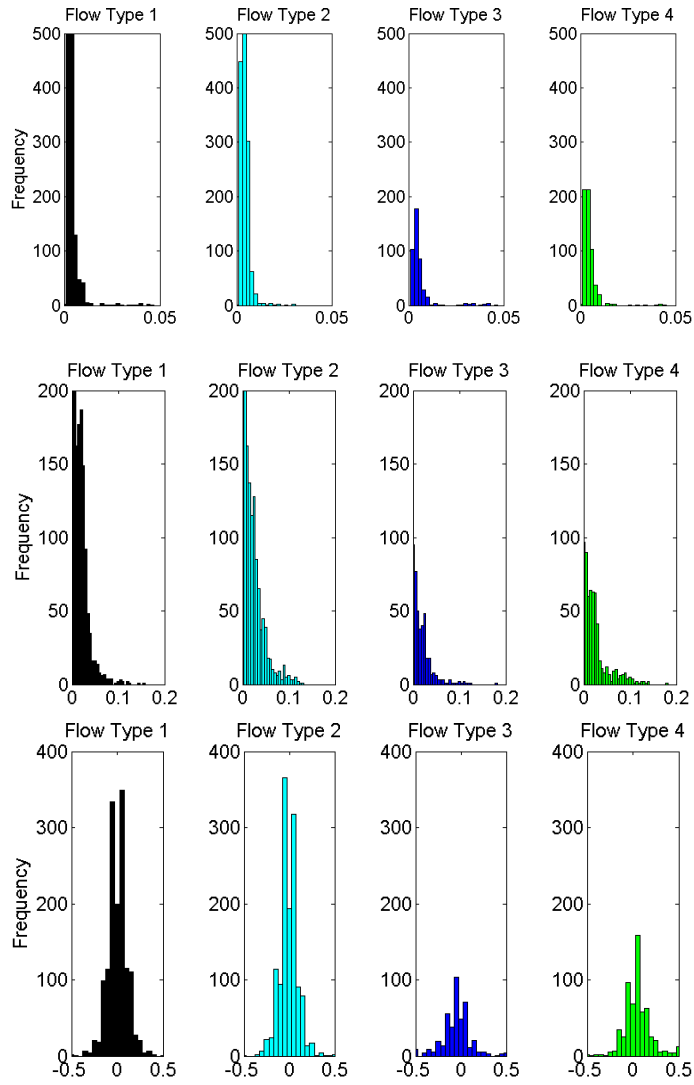
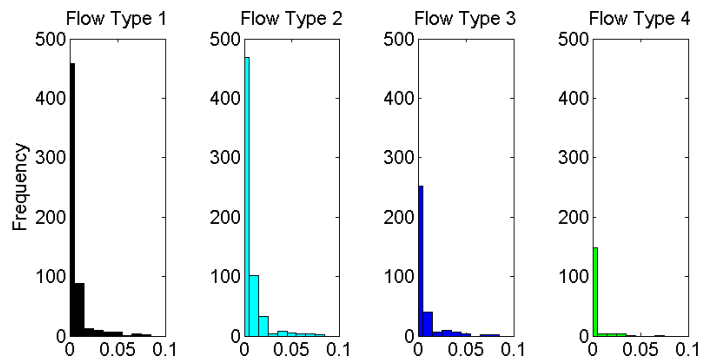


Figure 5.22.2: Distribution of KE_{trib} (top), KE_{wind} (middle), and PE (bottom) under different inlet flow conditions over Deployment 2.



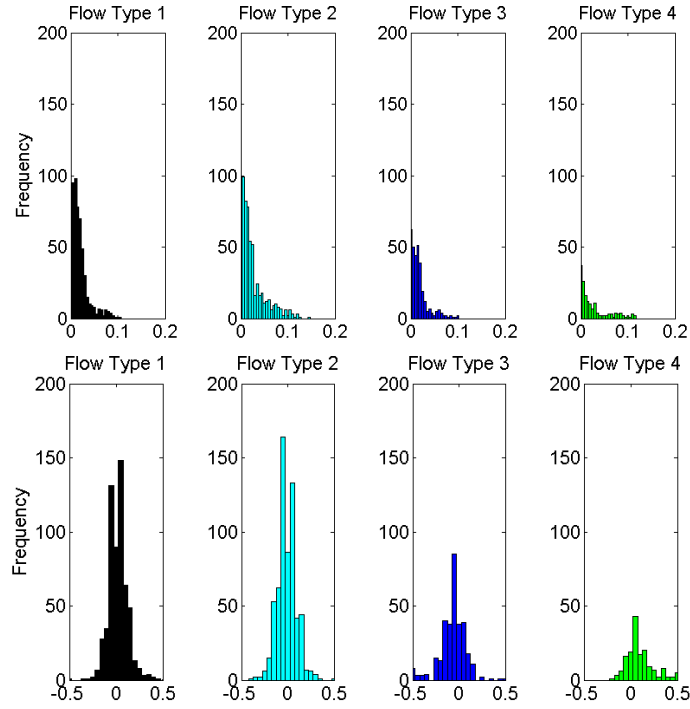


Figure 5.22.3: Distribution of KE_{trib} (top), KE_{wind} (middle), and PE (bottom) under different inlet flow conditions over Deployment 3.

5.2 Froude Number Analysis

From the temperature and velocity data, we computed bulk and internal Froude numbers in the inlet. Both internal Froude numbers (Equation 2.4.1) are relevant when an exchange flow is present. The layer heights, H_1 and H_2 , during an exchange flow were determined based on the streamwise velocity profiles and identifying the bin depth at which the streamwise velocity changed signs and thus direction through the inlet. Recall these Froude numbers indicate the ratio of the inertial to buoyancy forces. Figure 5.23 breaks down each component of the bulk Froude number calculation. Figure 5.24 breaks down each component of the internal Froude numbers.

$$\text{Bulk Froude number: } Fr_{bulk} = \frac{U}{\sqrt{g'H}} \quad (5.8)$$

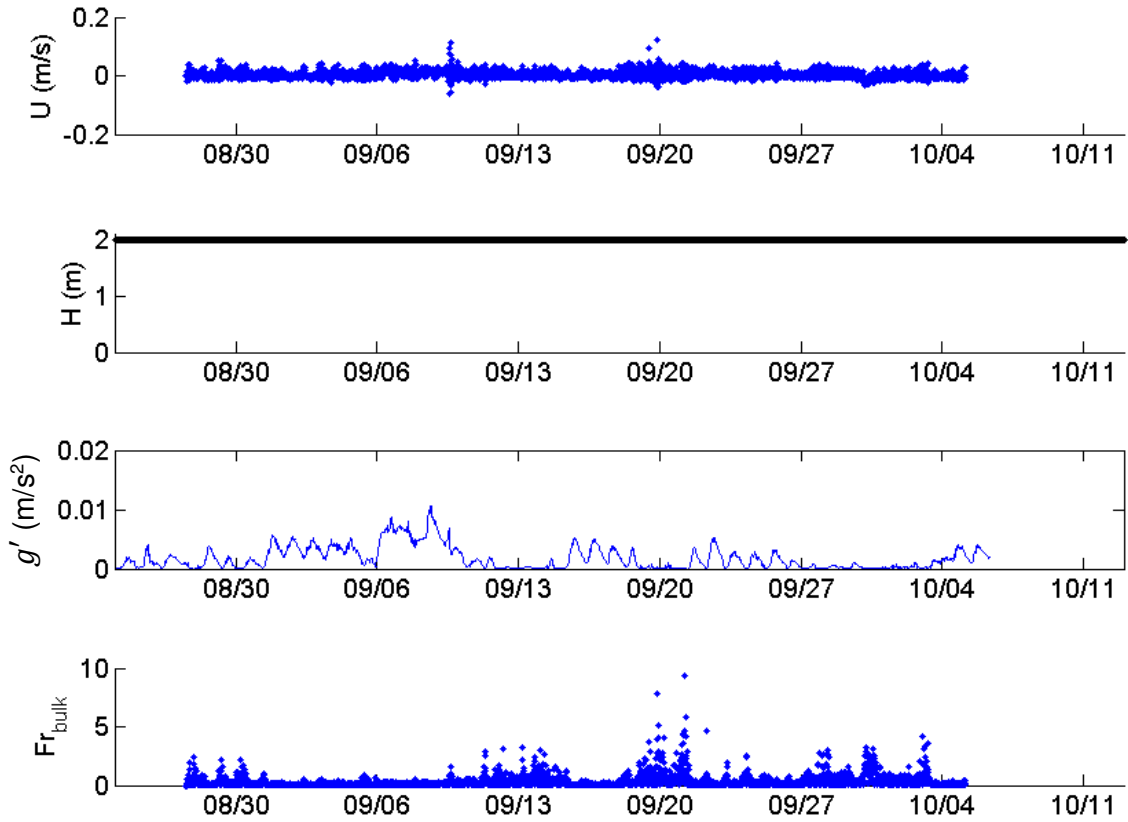


Figure 5.23.1: Depth average velocity, total depth and reduced gravity in inlet to calculate the bulk Froude number over Deployment 1.

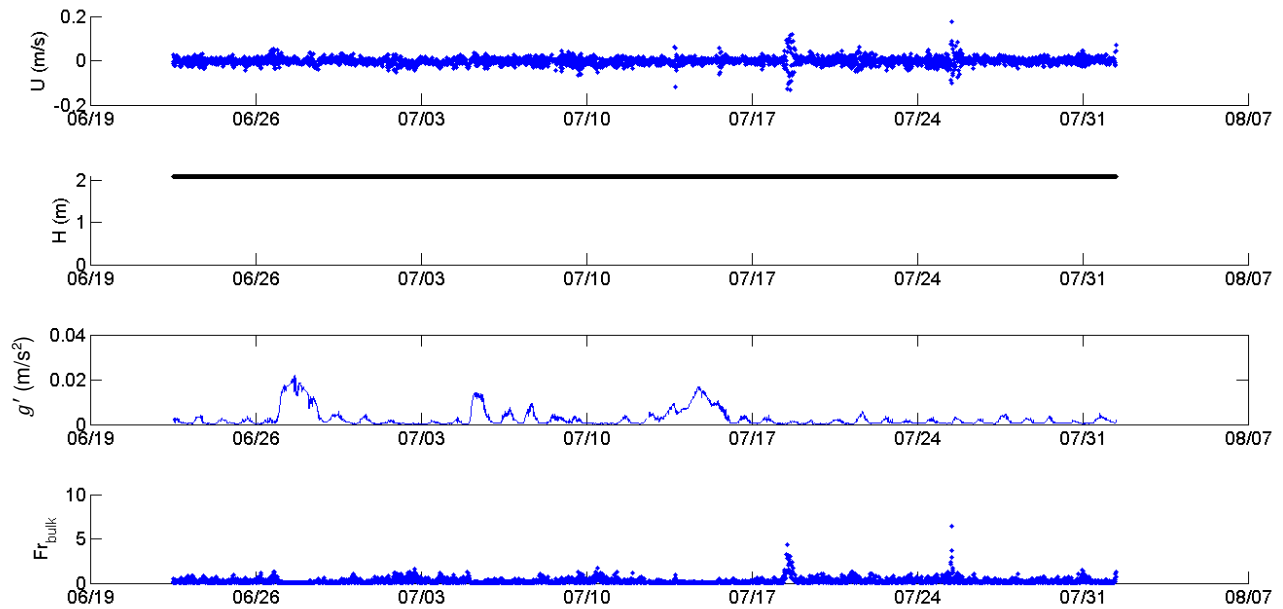


Figure 5.23.2: Depth average velocity, total depth and reduced gravity in inlet to calculate the bulk Froude number over Deployment 2.

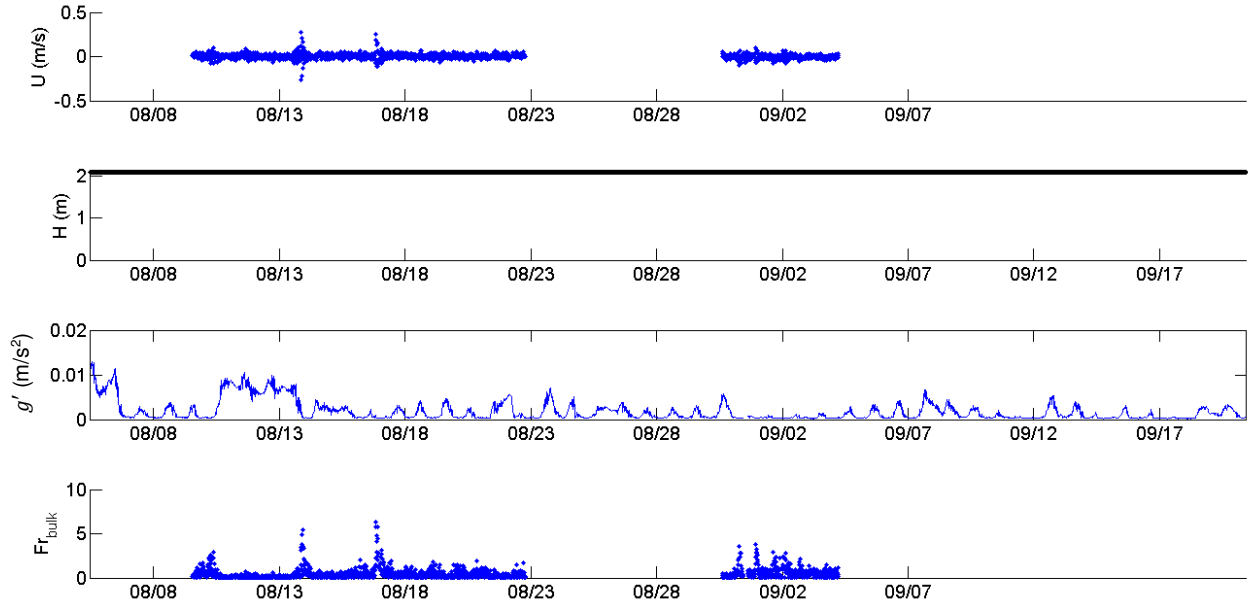


Figure 5.23.3: Depth average velocity, total depth and reduced gravity in inlet to calculate the bulk Froude number over Deployment 3.

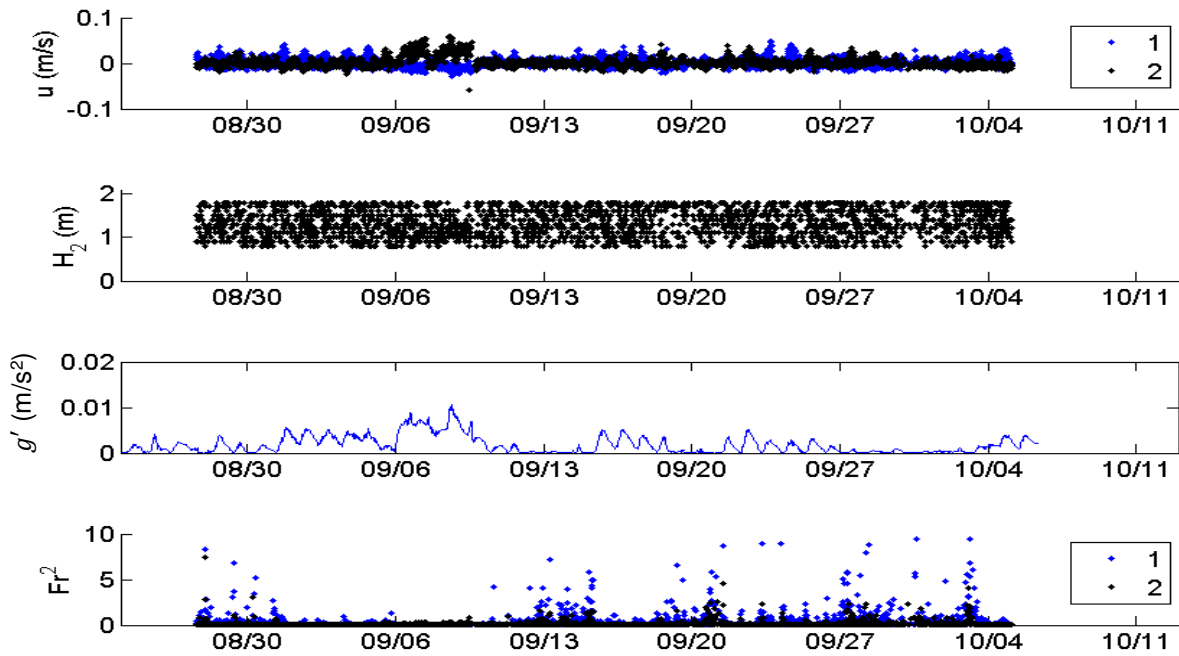


Figure 5.24.1: Layer velocities, heights and reduced gravity during exchange flows in inlet to calculate internal Froude numbers over Deployment 1 (1 represents the top layer and 2 represents the bottom layer in inlet).

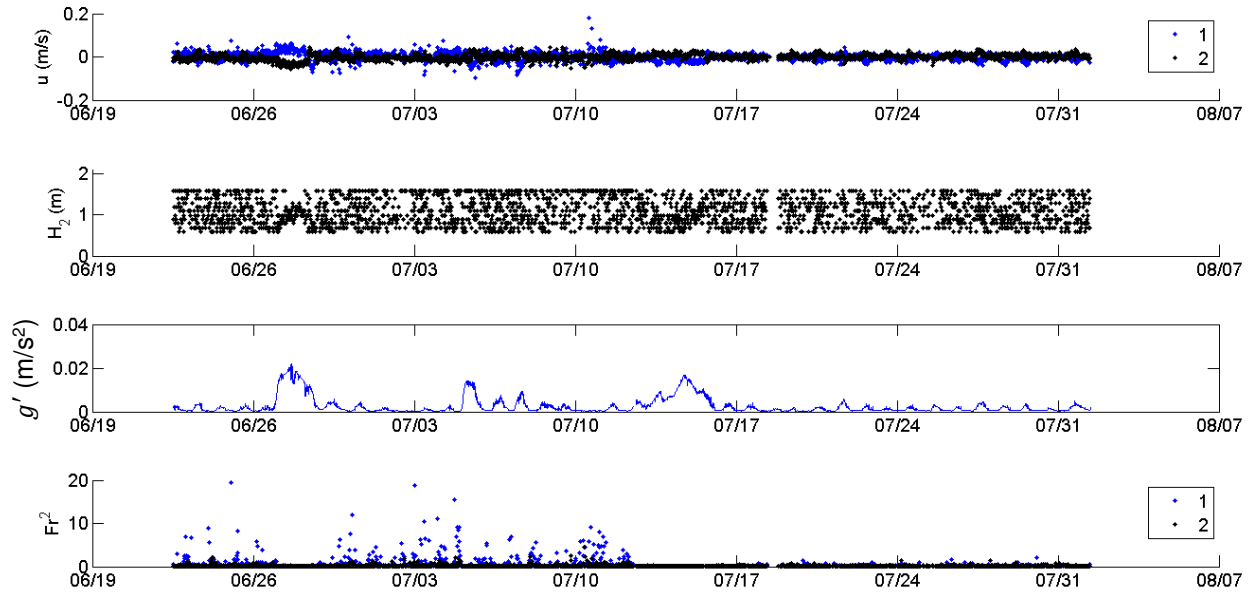


Figure 5.24.2: Layer velocities, heights and reduced gravity during exchange flows in inlet to calculate internal Froude numbers over Deployment 2 (1 represents the top layer and 2 represents the bottom layer in inlet).

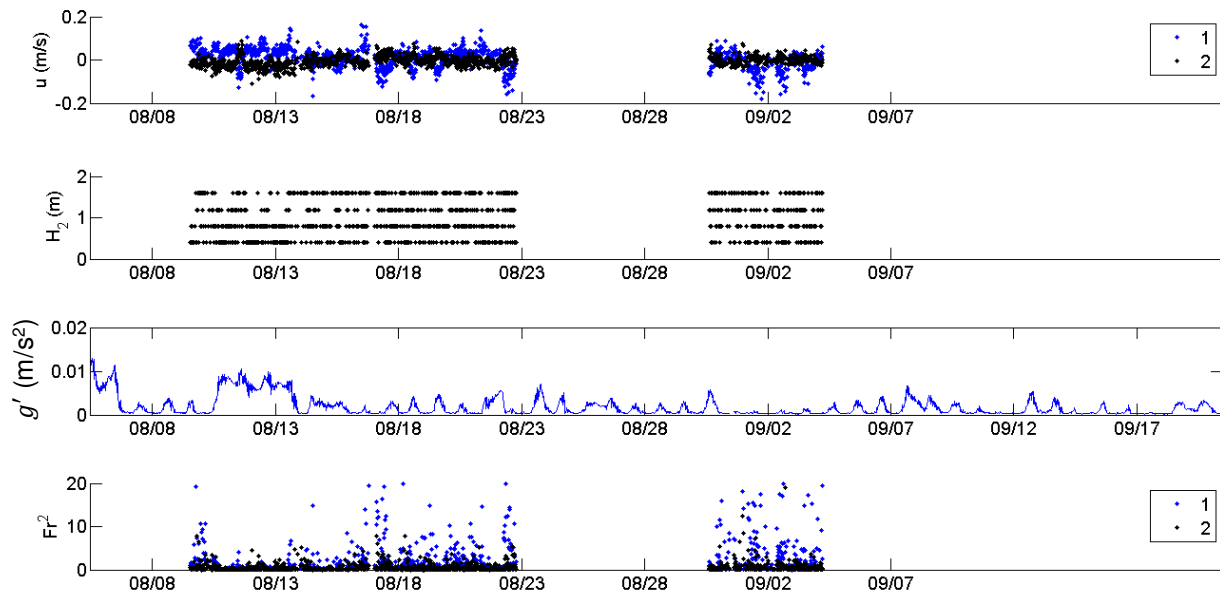


Figure 5.24.3: Layer velocities, heights and reduced gravity during exchange flows in inlet to calculate internal Froude numbers over Deployment 3 (1 represents the top layer and 2 represents the bottom layer in inlet).

Fr_{bulk} was greatest when U was high and the stratification in the inlet was very low, therefore inertial forces dominating buoyancy forces. Over Deployment 1 this clearly occurred around 9/20/2015. The other significant increase in U earlier in the deployment corresponded to a period of

relatively high stratification in the inlet, thus we do not observe as high an increase in Fr_{bulk} , though it still exceeded 1 at the time of highest U . Higher bulk Froude numbers were mostly due to higher velocities, but sometimes due to extremely low reduced gravity (low stratification) in the inlet. This was particularly the case over Deployment 3, near the beginning of September when reduced gravity was notably lower than throughout August. We saw similar patterns with the layer Froude numbers, with larger values over periods of g' very near zero, even though a two-layer flow was detected by the velocity profiles. In general, $F_1 > F_2$ because on average the magnitude of velocities in the top layer was greater than that of the lower layer. Layer velocities were based on the mean velocity of measurements within that layer. During Deployment 1, in early September the bottom layer velocity significantly increased, but during the same period g' increased most significantly as well.

As shown in Figure 5.24, by the range in heights of layer 2 (bottom layer, thus height above the bed), H_2 , the location within the water column of the separation between the two layers in an exchange flow continually changed throughout the deployments. The mean, median, and standard deviation of H_2 over each deployment are shown in Table 5.3. Recall our turbidity measurements in the top and bottom layer were approximately 0.5m and 1.5m deep, respectively. Over Deployment 1, 2, and 3 we find 72.4%, 85.9%, and 75.9% of the time, respectively, the top layer turbidity measurement was in the top layer of the exchange flow and 100%, 94.2%, and 76.2% of the time, respectively, the bottom layer turbidity measurement was in the bottom layer of the exchange flow. We note this is dependent on the resolution of the velocity profile from the ADCP/ADP. Recall, for the 3rd Deployment, the IAWWTP ADP provides a much lower resolution velocity profile (only 5 bins over the water column) by which we determined the layer heights during an exchange flow. Also, over the first deployment the deepest velocity measurement was ~ 1.2 m deep, due to the blanking distance set. Therefore the 100% of time for the bottom layer turbidity measuring in the bottom layer

of the exchange flow is because our deepest measurement for the velocity profile determining the exchange flow was shallower than the location of the bottom layer turbidity measurement. This is also likely why the mean and median H_2 were greater over Deployment 1.

Table 5.3. Mean, median, and standard deviation of layer 2 heights (height above bed at which direction of flow switches during an exchange flow), H_2 .

Deployment	Mean (m)	Median (m)	Standard Deviation (m)
1	1.22	1.21	0.31
2	1.09	1.09	0.32
3	0.97	0.80	0.44

Over Deployment 2, during the three mentioned periods of greater stratification in the inlet, the buoyancy forces clearly dominated, with low internal Froude numbers. There were two extreme layer one Froude numbers around 7/10/2016 that corresponded to the greatest mean layer velocity as well as very low reduced gravity. After 7/12/2016 there were markedly less frequent high Froude numbers for the remaining time of Deployment 2. Layer velocities in general were slightly less for this later period, but also there were less frequent extremely low values of reduced gravity. Even though the temperature differences in the two layers were not extremely different for this period, temperatures later in the summer were higher and at higher water temperatures the same temperature difference is a greater density difference. While the reduced gravity did not significantly increase, there was less frequency of extremely low reduced gravity, which would result in high Froude numbers.

We are also interested in the shear Froude number (Equation 5.9). This calculation specifically looks at the difference in velocities between two layers of an exchange flow. When the shear Froude number is greater than 1, which we consistently saw for our data in Figure 5.25, we expect increased vertical mixing between the layers of an exchange flow. Over Deployment 1, at the beginning of September we had the strongest stratification in the inlet and during this time was the longest period the shear Froude number remained below 1, so we expect very little mixing between the layers. Over

Deployment 2, the shear Froude number spiked more frequently over the first half of the deployment. While a greater difference between layer velocities often contributed to these spikes, it appears more heavily influenced by extremely low stratification in the inlet, and thus extremely low reduced gravity. The greatest difference between layer velocities occurred on 7/10/2016 and was significantly higher than all other times, resulting in one of the highest shear Froude numbers. The next two greatest differences between layer velocities did not result in as high a shear Froude number, as both were during one of the three notable peaks in the reduced gravity. The last and most sustained of these peaks, starting around 7/12/2016, resulted in consistently lower layer Froude numbers and shear Froude numbers for the rest of Deployment 2. Over Deployment 3, the greatest difference in layer velocities occurred when the reduced gravity was also relatively high, however the shear Froude number still jumped above 1 for that time.

$$\text{Shear Froude number: } F_{\Delta}^2 = \frac{\Delta u^2}{g'H} \quad (5.9)$$

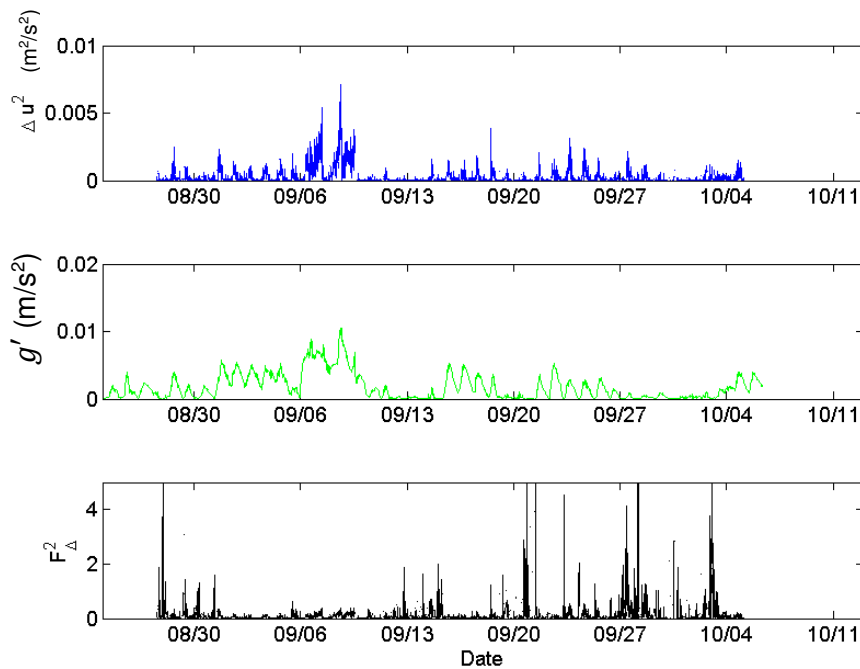


Figure 5.25.1: Difference in layer velocities and reduced gravity during exchange flows in the inlet to calculate the shear Froude number over Deployment 1.

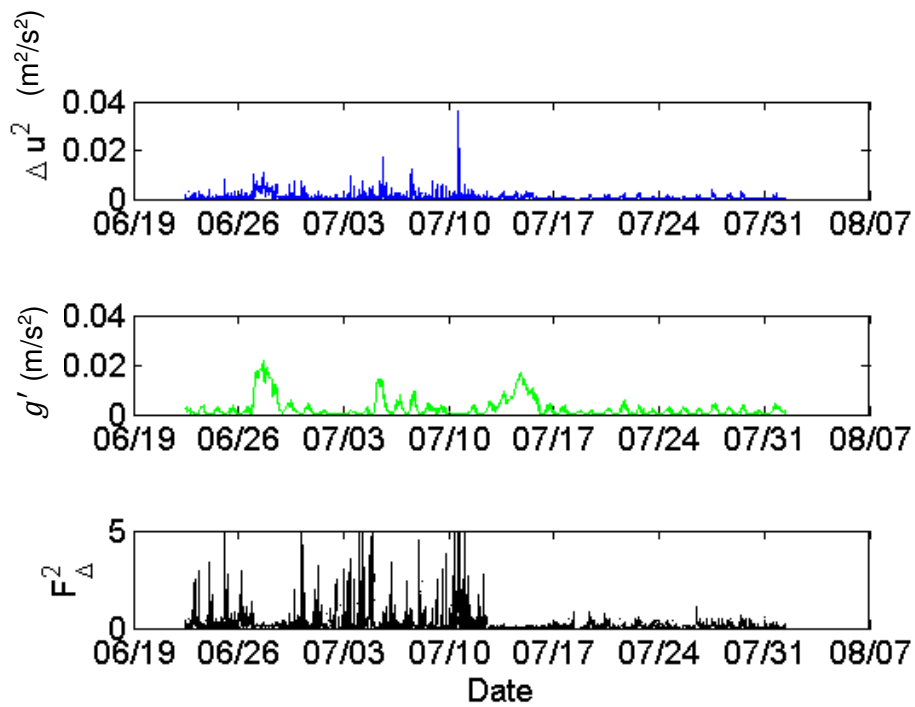


Figure 5.25.2: Difference in layer velocities and reduced gravity during exchange flows in the inlet to calculate the shear Froude number over Deployment 2.

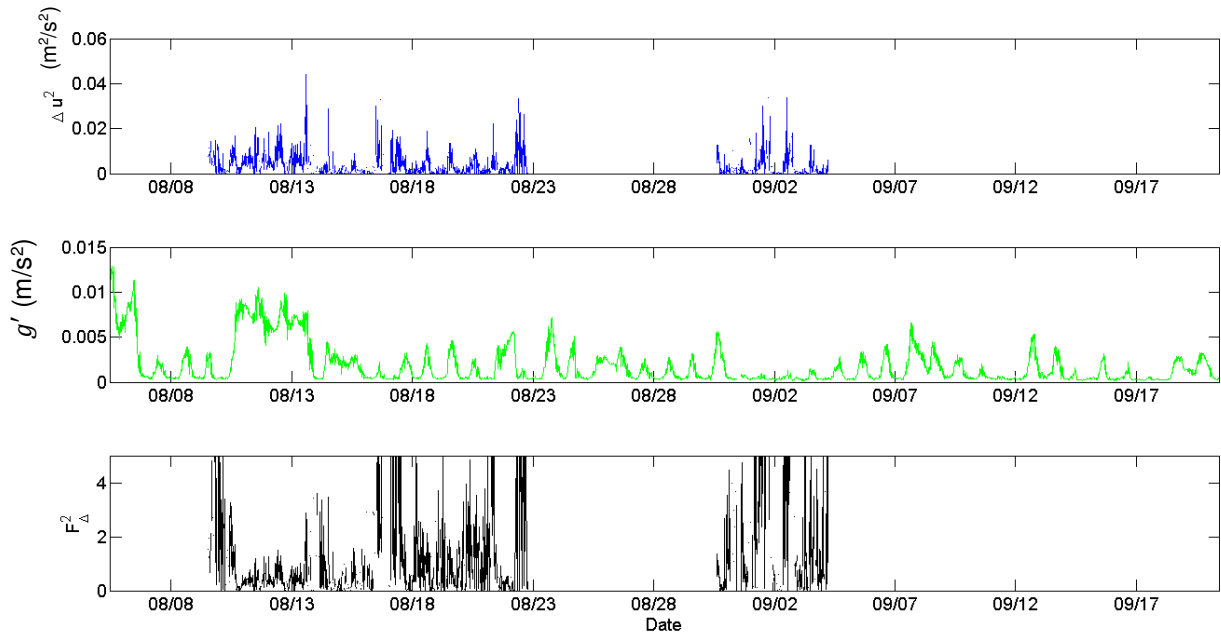
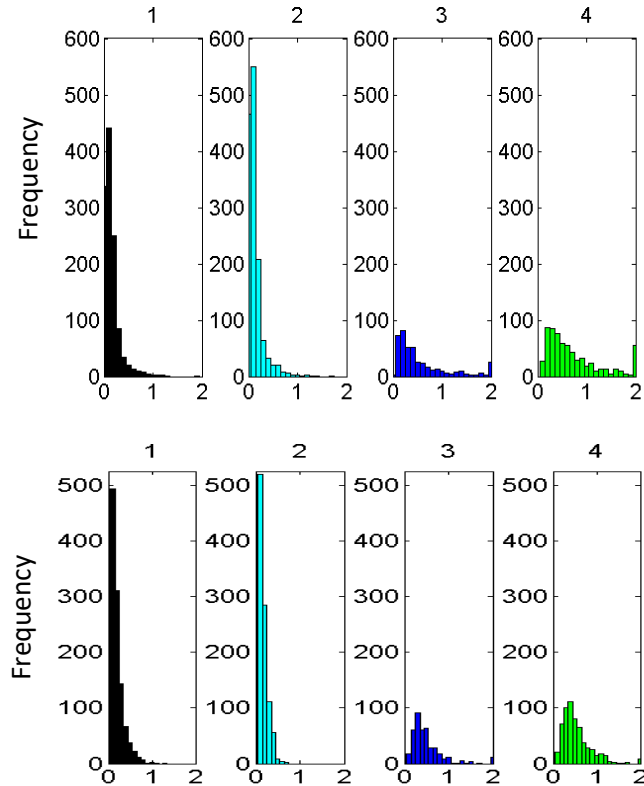


Figure 5.25.3: Difference in layer velocities and reduced gravity during exchange flows in the inlet to calculate the shear Froude number over Deployment 3.

Distributions of the Froude numbers under the different flow conditions in the inlet are shown in Figures 5.26-5.28. Under exchange flows, the bulk Froude number was almost always less than one, thus buoyancy forces dominated, while under unidirectional flows at times inertial forces were dominant. Over Deployment 3, particularly the unidirectional flow into the inlet from the lake was close to evenly distributed between Fr_{bulk} less than 1 and greater than 1. Distributions of the shear Froude numbers and composite Froude numbers under the different types of exchange flows did not show any significant difference. Mostly $F_{\Delta} < 1$, thus we expect low mixing due to shear forces during exchange flows.



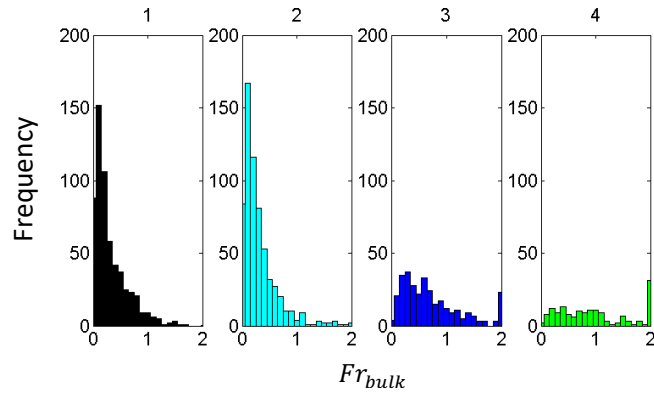


Figure 5.26: Distribution of Fr_{bulk} in inlet under different flow conditions. Top: Deployment 1; Middle: Deployment 2; Bottom: Deployment 3.

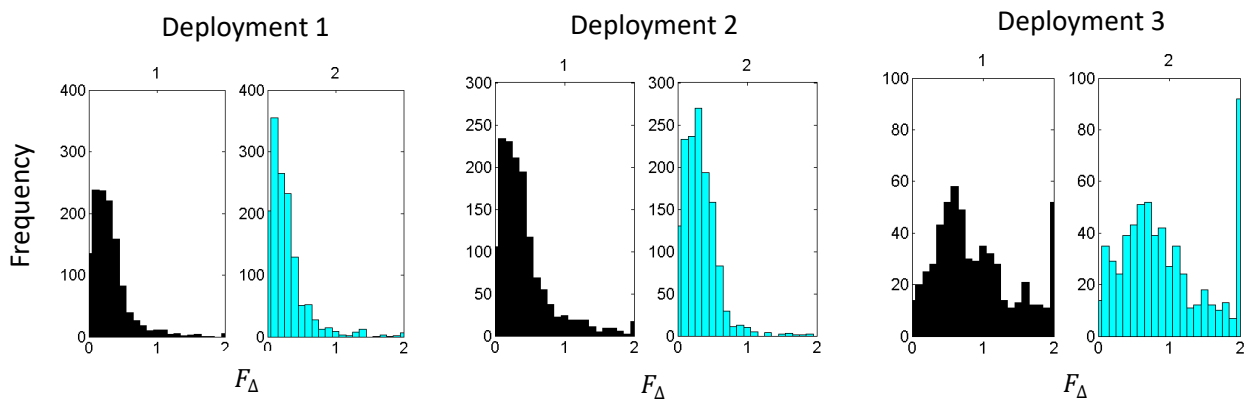


Figure 5.27: Distribution of F_{Δ} under different exchange flows in the inlet.

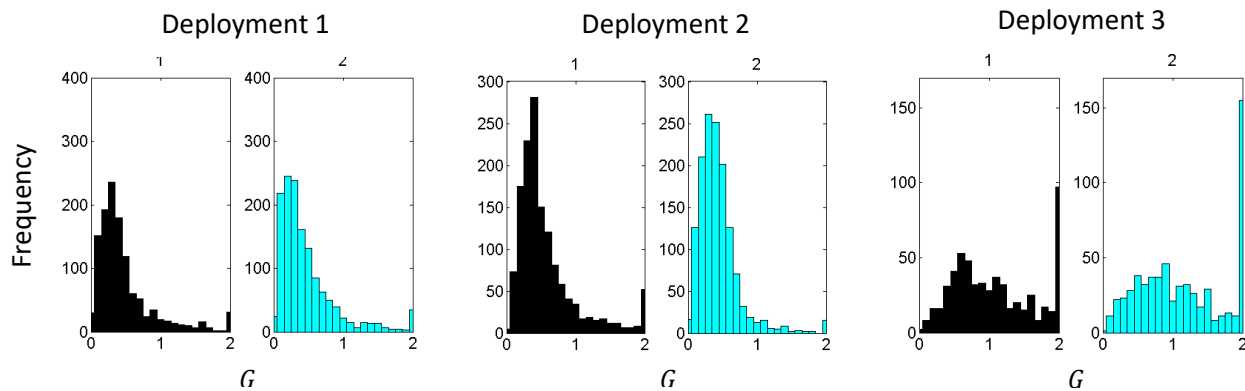
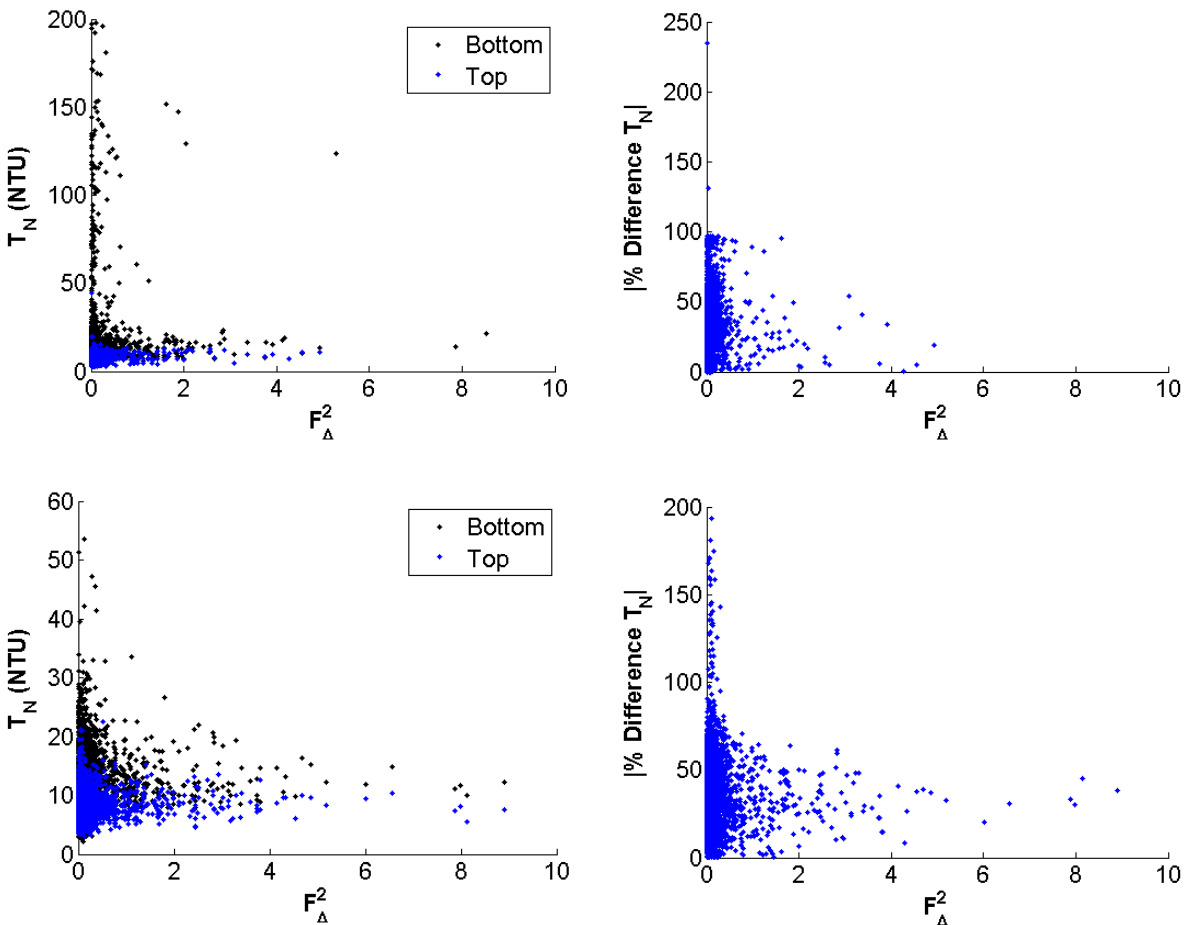


Figure 5.28: Distribution of G under different exchange flows in the inlet.

Over Deployments 1 and 2, when $F_{\Delta}^2 > 1$ turbidities were below 20 NTU, with some exceptions in the bottom layer of the inlet, and the percent difference in turbidity was most frequently below 50%, as we expect more mixing between the layers at higher F_{Δ}^2 . For $1 < F_{\Delta}^2 < 2$, there were some exceptions when the percent difference in turbidity was still near 100% during Deployment 1. The highest turbidities in both layers occurred during $F_{\Delta}^2 < 1$. Over Deployment 2, the maximum

observed bottom layer turbidity exponentially decreased as F_{Δ}^2 increased above 1, leveling off around 10 NTU, which the bottom layer turbidity rarely dropped below. Deployment 3 experienced much higher bottom layer turbidities and while at maximum F_{Δ}^2 turbidities were near their minimum, high bottom layer turbidities frequently occurred during $F_{\Delta}^2 > 1$. There were also high percent differences in turbidity at the higher F_{Δ}^2 for Deployment 3. This suggests during exchange flows turbidities will be highest when little mixing occurs between the layers, thus concentrated to a smaller layer. While we expect a lower percent difference in turbidity under greater shear Froude numbers, this was not always true over Deployment 3. This suggests when turbidity loads are significantly high, as they were at times over Deployment 3, they can remain concentrated in the bottom layer of the inlet and any mixing across the layers due to shear is relatively insignificant.



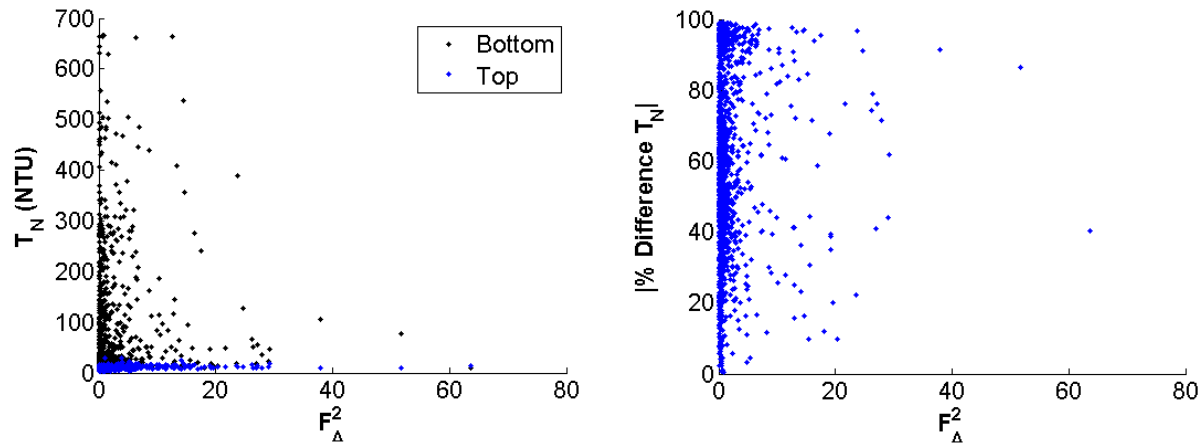
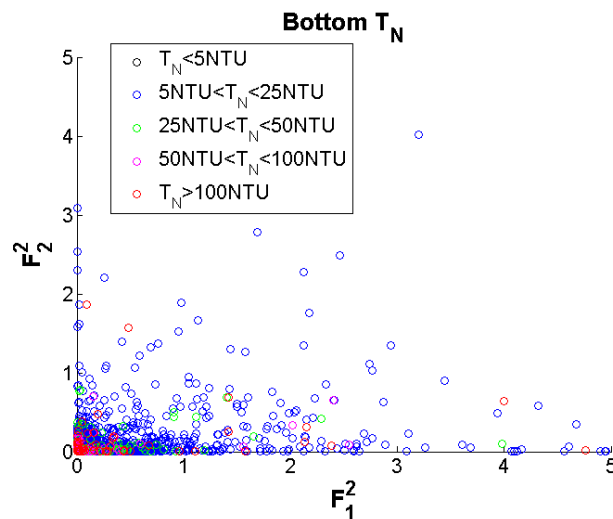


Figure 5.29: F_{Δ}^2 compared to inlet turbidities (left) and percent difference in turbidities in the inlet (right). Top: Deployment 1; Middle: Deployment 2; Bottom: Deployment 3.

Based on the Froude number plane using F_1 and F_2 , shown in Figure 5.30, the majority of time the inlet flow was internally subcritical. For Deployments 1 and 2 when the bottom layer turbidity was above 150 NTU, the flow had very low F_1 and F_2 , thus highly subcritical. In general, turbidity in the bottom layer was highest when buoyancy forces were dominant, thus at higher stratification and low flow through the inlet. When bottom layer turbidities were classified as extreme, above 100 NTU, the majority of time flow in the inlet was internally subcritical, however there were a few instances which fell in the internally supercritical zone. This was the case for any bottom layer turbidity above the low range; the majority of cases fell within the internally subcritical zone with a few exceptions. Figure 5.31, reiterates these findings. As Froude numbers increased, the maximum observed turbidity decreased. The highest turbidities in the top and bottom layer of the inlet occurred during very low Froude numbers. For the highest Fr_{bulk} , F_1 , F_2 , and G during Deployments 1 and 2 turbidities in both layers were below 20 NTU. Therefore, when inertial forces dominate, we expect low turbidity loads traveling through the inlet. When flow was internally supercritical, turbidities in the inlet were typically low. Over Deployments 1 and 2, the top layer turbidity in the inlet was always below 15 NTU when the top layer was supercritical. The bottom layer turbidity in the inlet was below 20 NTU when

the bottom layer was supercritical, except for three outliers during Deployment 1 that occurred at $F_2^2 \approx 2$.

Over Deployment 3, at higher F_1 and F_2 turbidities in the inlet were low. This agrees with the previous deployments, that the highest turbidities in the inlet occurred when buoyancy forces dominated inertial forces. Also, when inertial forces were dominant we expect relatively low turbidity loads traveling through the inlet. Unlike Deployments 1 and 2, however, on the Froude number plane while the highest turbidities were more concentrated within the internally subcritical zone, turbidities from all ranges, even the extreme range, fell in the internally supercritical zone. The highest bottom layer turbidities were associated with $F_1 < 1$ and $F_2 < 1$, but also some bottom layer turbidities above 400 NTU were associated with $F_1 > 1$ and $F_2 > 1$.



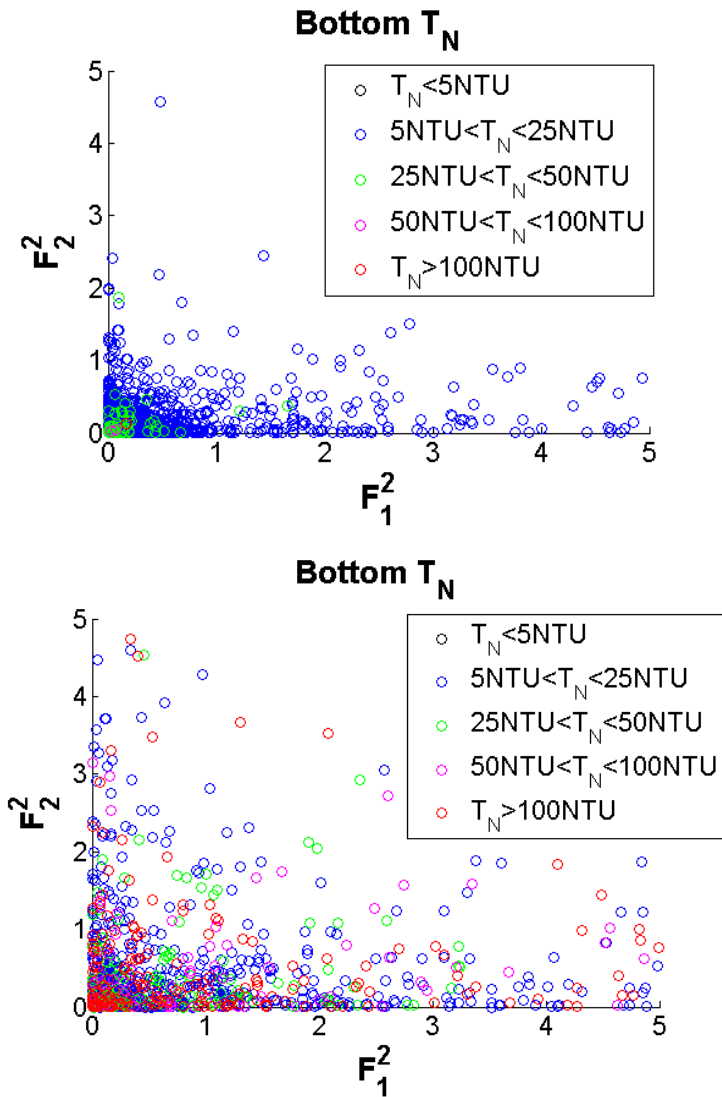


Figure 5.30: Ranges of bottom layer turbidities in the Froude Number plane. Top: Deployment 1; Middle: Deployment 2; Bottom: Deployment 3.

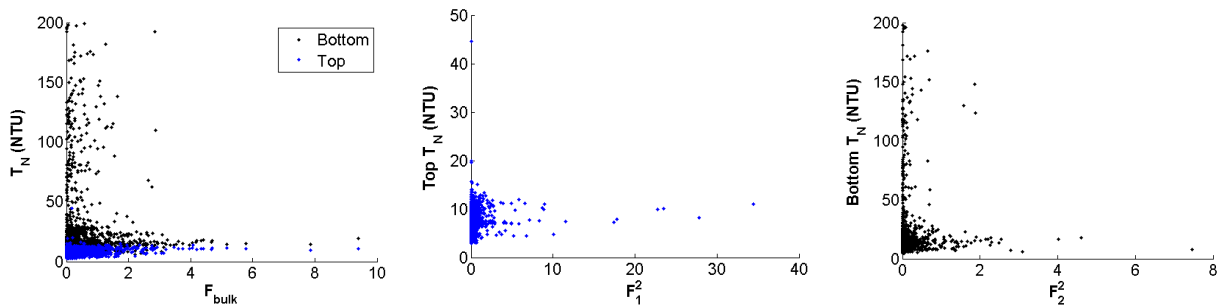


Figure 5.31.1: Fr_{bulk} (left), F_1 (center), F_2 (right) compared to inlet turbidities over Deployment 1.

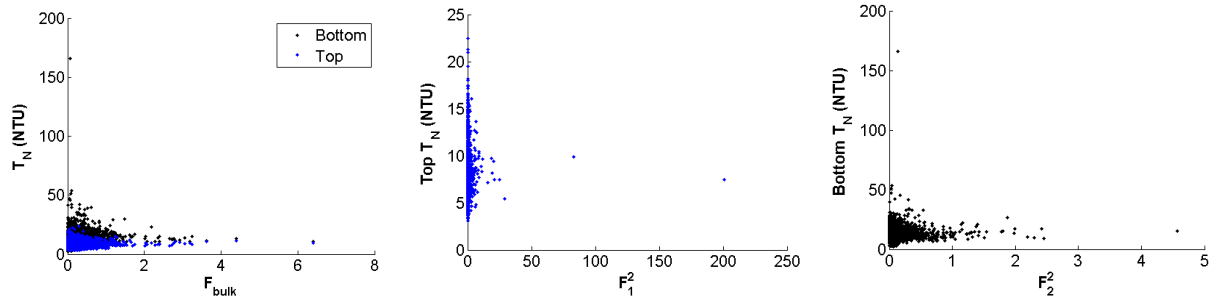


Figure 5.31.2: Fr_{bulk} (left), F_1 (center), F_2 (right) compared to inlet turbidities over Deployment 2.

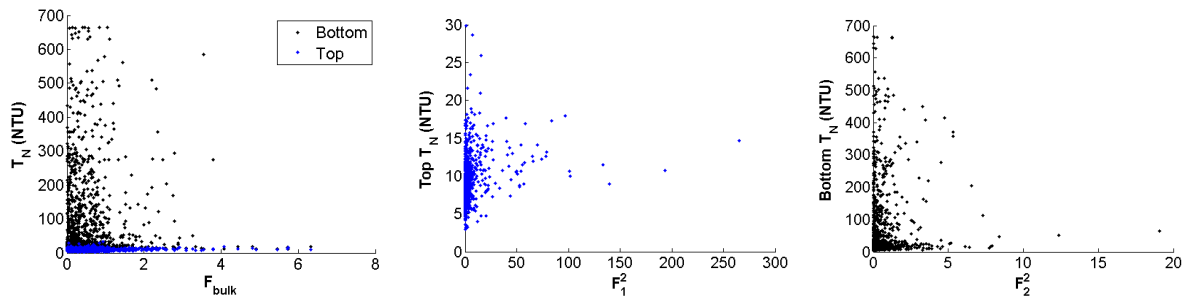


Figure 5.31.3: Fr_{bulk} (left), F_1 (center), F_2 (right) compared to inlet turbidities over Deployment 3.

A negative percent difference in turbidity indicates the top layer turbidity was higher than the bottom layer and a positive indicates the opposite. In general, greater percent differences in turbidity were observed at lower Froude numbers. The greater the percent difference, the less mixing of sediment between the layers, and the lower the Froude number, the greater the stratification relative to the velocities, thus less vertical mixing is expected. Over Deployment 1 at higher Froude numbers, the percent difference in turbidity tended closer to zero, indicating the inlet was well mixed between layers. At $G > 2$, turbidity in the bottom layer was almost always greater than the top layer of the inlet.

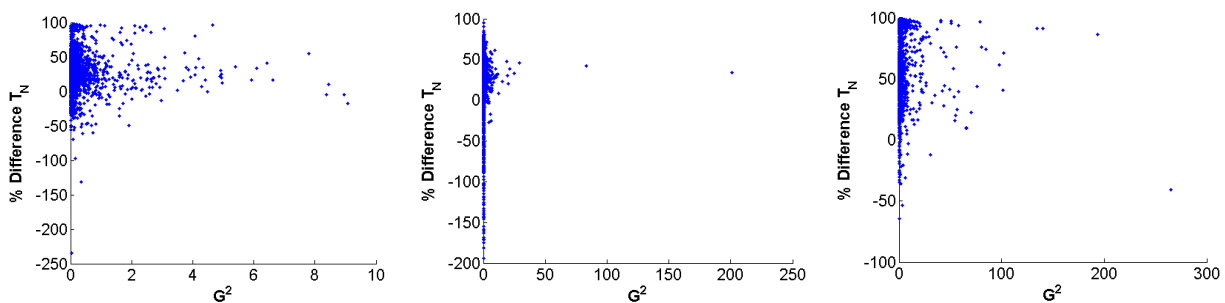


Figure 5.32: G^2 compared to percent difference in layer turbidities within the inlet. Left: Deployment 1; Center: Deployment 2; Right: Deployment 3.

5.3 Influence of Physical Mechanisms on Turbidity Loads

5.3.1 Bed Sediment Resuspension

The incipient motion of bottom sediment can be predicted based on shear stress and critical shear stress at the bed. In Section 2.5 we discussed when the bed stress is greater than the critical bed stress, movement of bottom sediment, or bed load transport, is expected. From the HR profiler velocity profiles, recording over Deployment 1, we utilize the log law from Equation (2.6.1), forcing velocity to zero at the bed, to obtain the bed stress at our inlet location. Velocity profiles reaching 0.2m above the bed were fit to the log law to obtain the frictional velocity, u_* . It was for this height above the bed, with the closest measurements within 0.12m, the data best fit the log law, see an example of this fit shown in Figure 5.33.

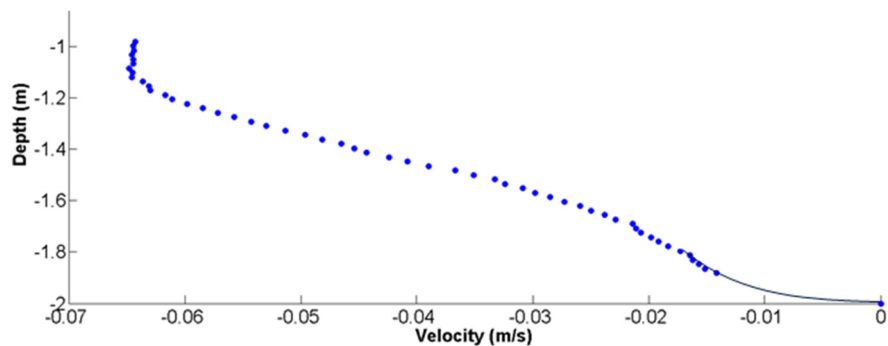


Figure 5.33: Dotted blue line shows a velocity profile from HR Profiler and the solid line shows the log law fit to the profile 0.2m above the bed.

The bed stress was calculated based on Equation (2.6.2). The critical bed stress was calculated based on Equation (2.8), where bed sediment was assumed as a silty clay. This assumption was based on results from various sediment studies in Cayuga Lake and Inlet (Ludlam, 1967; Genesee/Finger Lakes Regional Planning Council, 2000; UFI, 2014). From the United States Department of Agriculture (USDA) Soil Classification System (USDA, 1987) for a silty clay we select $\rho_s=1260 \text{ kg/m}^3$ and $D=0.0024 \text{ mm}$, thus when calculated $\tau_{critical} = 0.0273 \text{ Pa}$. There were many times throughout the shorter deployment of the HR Profiler (12 days) the bed stress was higher than the critical bed stress, thus we expect bottom sediment was mobile.

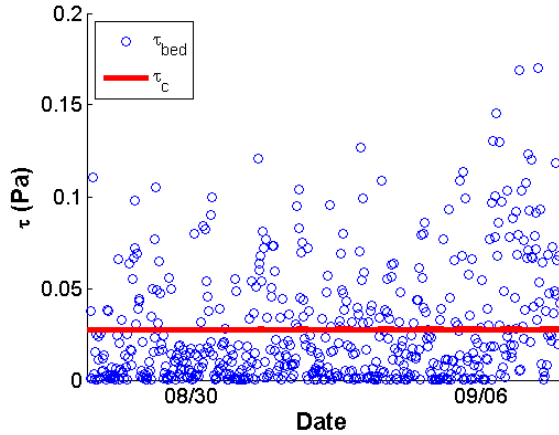


Figure 5.34: Compare bed stress (blue dots) to critical bed stress (red line) at the inlet bed.

The impact of bottom sediment resuspension to turbidity loads in the inlet is of interest. Higher u_* , increases bed stress, and when the bed stress is greater than the critical bed stress this causes motion of bed sediment. An even greater bed stress is required for sediment resuspension to be possible, which would be expected to increase turbidities, particularly in the bottom layer, closest to the bed. However, increases in u_* did not always coincide with increases in the bottom layer turbidity. In fact, from this data there was no indication increased frictional velocity, and thus bed stress, had a significant effect on turbidities in the bottom layer of the inlet. Therefore, no significant bed sediment resuspension was observed.

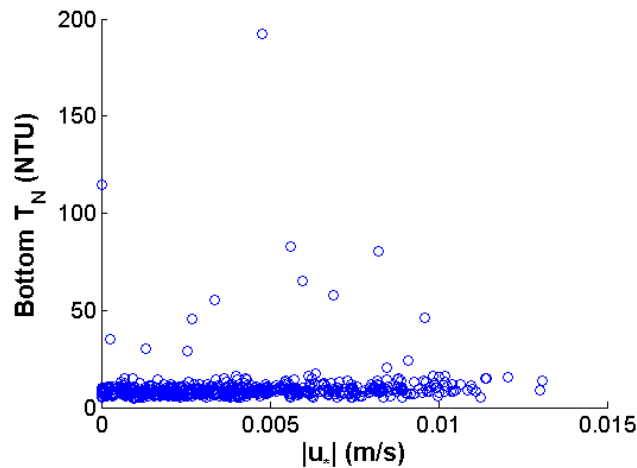


Figure 5.35: Effect of $|u_*|$, based on HR Profiler, on bottom layer turbidity in the inlet.

The assumption of silty clay bed sediment in the inlet is very broad. Based on shields curve (Figure 5.36) the critical bed stress we calculate, assuming a silty clay sediment, is near the lower limit of this threshold, by which we predict insipient motion of bed sediment. Therefore, any changes to this threshold, by which we predict insipient motion of bed sediment. Therefore, any changes to the assumption of the bed sediment type will likely decrease even further the motion of bed sediment under shear stresses, thus there is even less of a possibility resuspension of bed sediment is significantly occurring. Also, in this analysis, bed sediment is assumed to be uniform, when it is likely more of a mixture, which would impact the critical bed stress as well.

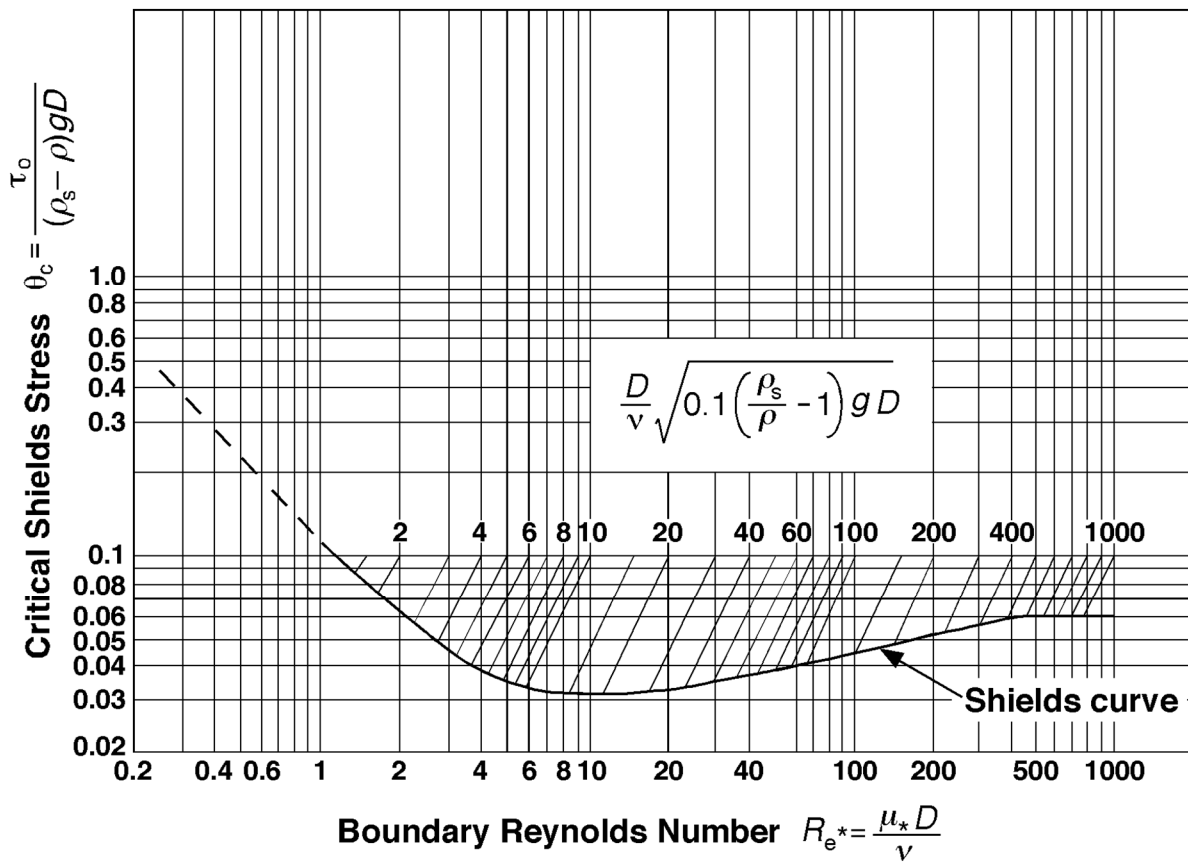


Figure 5.36. Shields curve for critical bed stress.

We apply the same log law to the ADCP data from Deployment 1, fitting to the bottom 3 bins which reach approximately 1 meter above the bed. We recognize this generally extends beyond the log layer in to the outer layer, thus the log law is less valid, but can still provide an estimate of the

frictional velocity. Recall the HR Profiler recorded velocities on average triple that recorded by the ADCP. The HR Profiler in general calculated higher bed stresses than the ADCP, and thus predicted more instances of motion of bed sediment. The instruments in general agreed on the timing of greater bed stresses. We expect more accurate predictions of the bed stress from the HR Profiler with more measurements closer to the bed and better fits to the log law.

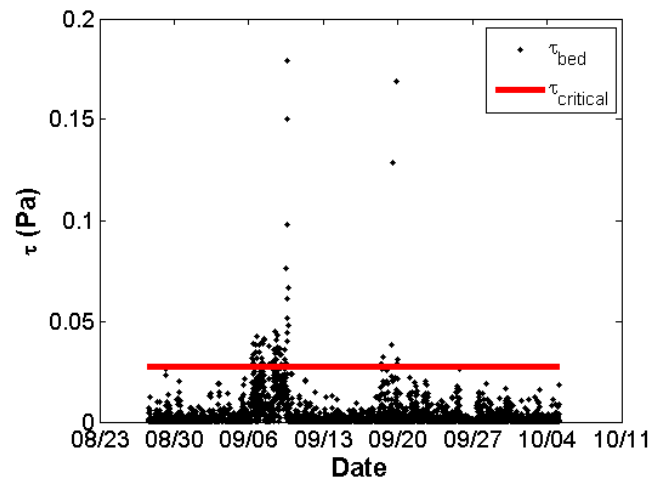


Figure 5. 37: Bed stress predicted by applying log law to ADCP data over Deployment 1.

At greater bed stresses, as predicted by the ADCP data over Deployment 1, turbidity in the inlet and the southern lake were very low. For bed stress above our critical bed stress, aside from one outlier, turbidity in the bottom layer of the inlet remained below 30 NTU. The highest bottom layer turbidities occurred when the bed stress was extremely low. As we will show in Section 5.4.3, focused on precipitation events, the highest bottom layer turbidities appear in response to precipitation events, without any apparent contribution from internal loading from bed sediment resuspension due to increased bed stress. However, for bed stress greater than 0.04 Pa, the bottom layer turbidity was always greater than top layer turbidity in the inlet.

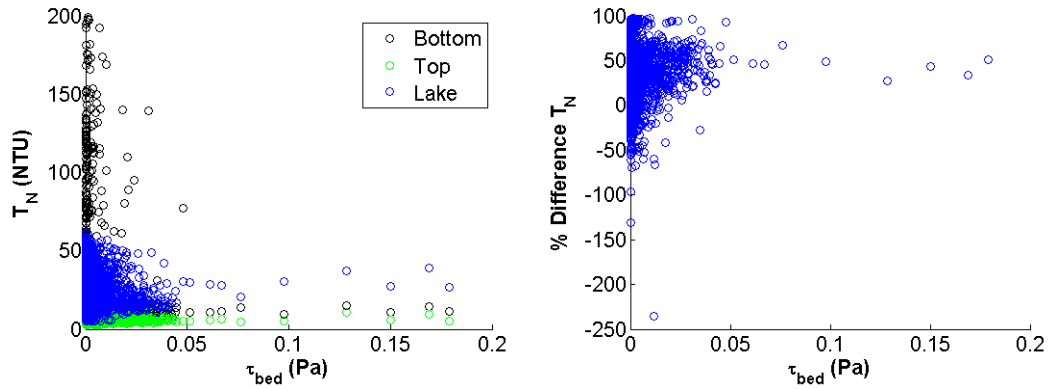


Figure 5.38: Bed stress predicted by applying log law to ADCP data compared to turbidities (left) and percent difference in turbidity (right) along inlet water column over Deployment 1.

For the 2nd Deployment we fit the log law to the bottom 3 bins of the ADCP data, which reach approximately 0.8m above the bed. We tried fitting the log law to the bottom 5 bins, which reach approximately 1.0m above the bed, as well as the entire profile. However, fits were much closer using only the first 3 bins. Log law fits to the ADCP data over Deployment 2 are shown in Figure 5.39. There were discrepancies in these fits, as we were extended beyond the log layer, but this still provides an estimate of the frictional velocity.

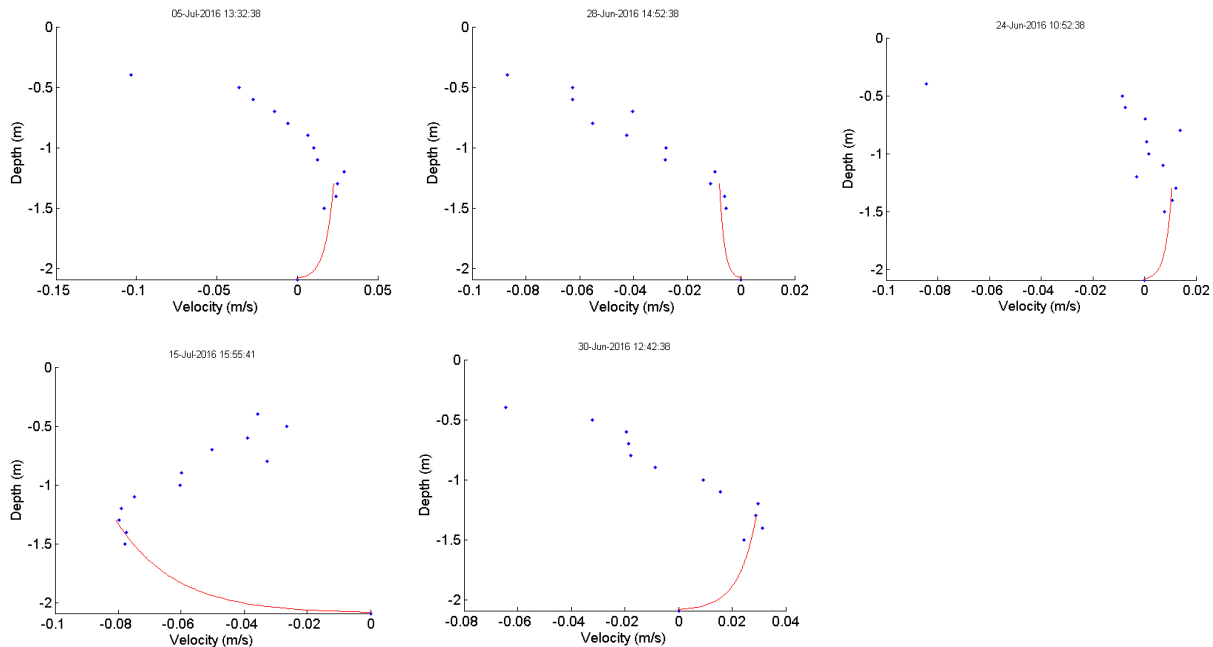


Figure 5.39: Streamwise velocity profiles from ADCP over Deployment 2 in blue dots and log law fits to 0.8m above the bed in red lines.

Over Deployments 2 and 3 we utilize the Vector data to calculate the Reynolds stress following methods from Lohrmann (1990), then calculate the bed stress by Equation (2.7). Recall the Vector sampling volume was approximately 0.84m above the bed. Figure 5.40, shows u' and w' , based on local means, over Deployment 2. The maximum average u over all the bursts was 14.87 cm/s and the maximum average w over all the bursts was 0.96 cm/s.

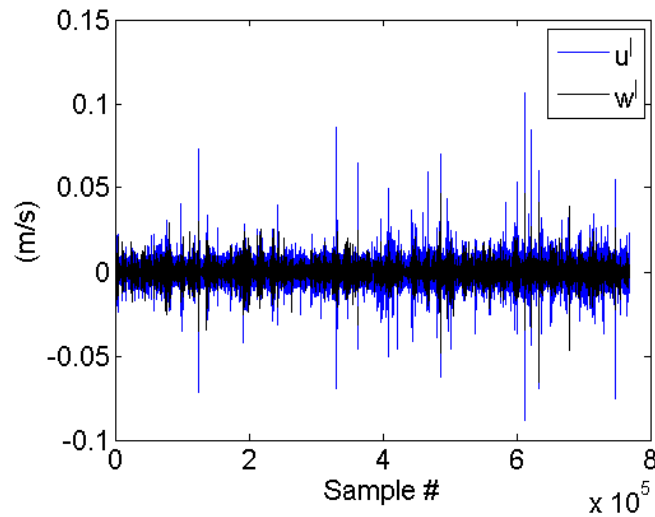


Figure 5.40: Instantaneous u' and w' from Vector data over Deployment 2.

We observed data over Deployment 2 for multiple bursts with high average velocities and high fluctuating velocities (Figure 5.41). Over the burst intervals containing the maximum average velocities, velocity fluctuations in the streamwise and vertical directions were overall smaller than that over the burst intervals containing the maximum instantaneous velocities. Peaks in fluctuating velocities were not associated with any significant changes in SNR or *Correlation*. The mean SNR and *Correlation* for such bursts were also not significantly different from their means over the entire deployment. Most peaks in the fluctuating velocities occurred at the beginning or end of a burst. Following the peak, an oscillatory behavior was observed around the mean velocity for that burst, which dampened over a few seconds. Recall the Vector sampled at 8 Hz, thus there was 0.125 seconds between each sample.

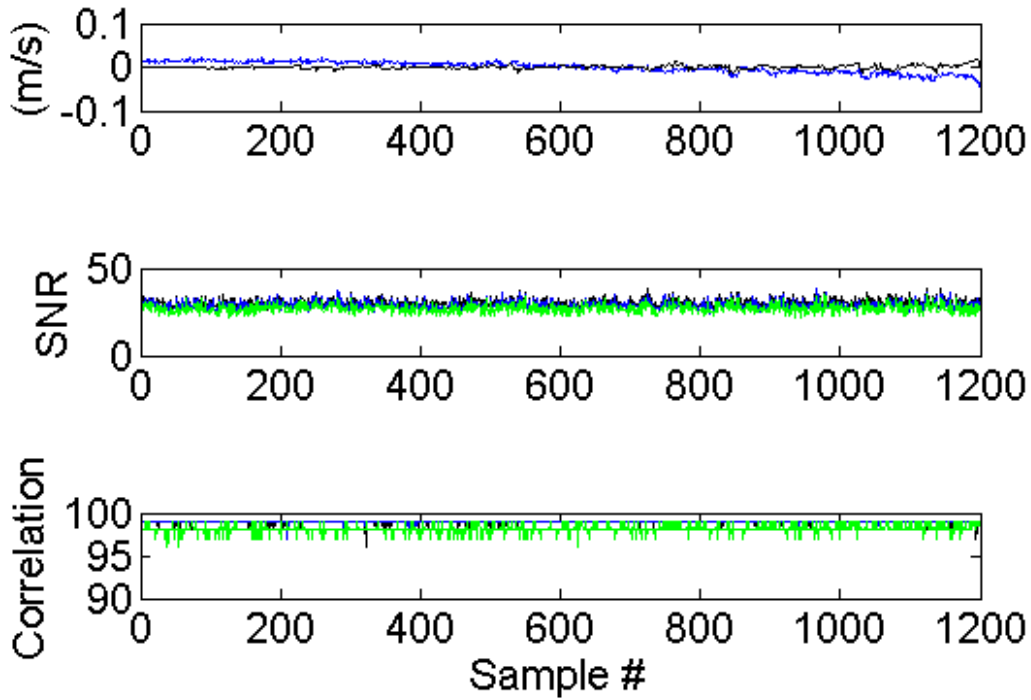


Figure 5.41.1: u' (blue) and w' (black) for burst with maximum average u (top) and corresponding SNR (middle) and *Correlation* (bottom) for beam 1 (black), 2 (blue), and 3 (green).

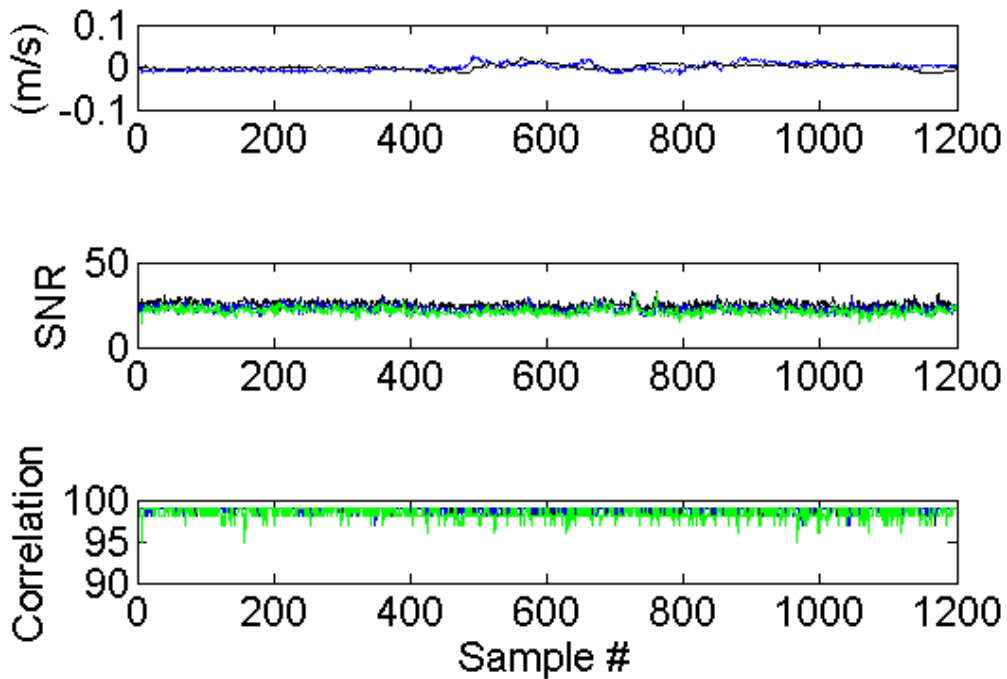


Figure 5.41.2: u' (blue) and w' (black) for burst with maximum average w (top) and corresponding SNR (middle) and *Correlation* (bottom) for beam 1 (black), 2 (blue), and 3 (green).

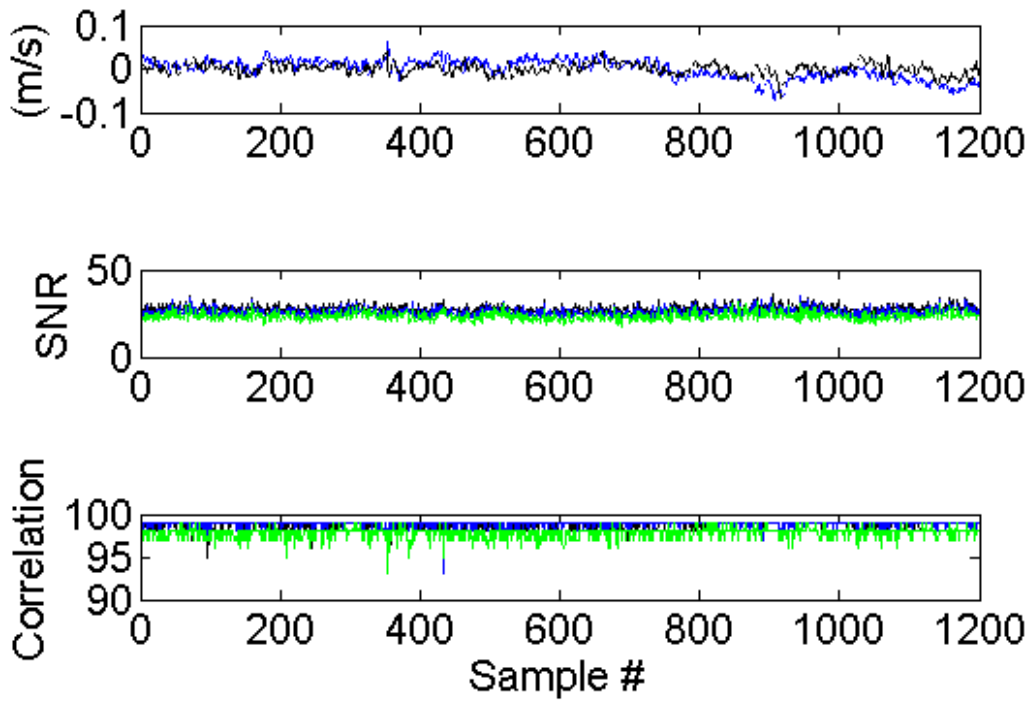


Figure 5.41.3: u' (blue) and w' (black) for burst with maximum single u (top) and corresponding SNR (middle) and *Correlation* (bottom) for beam 1 (black), 2 (blue), and 3 (green).

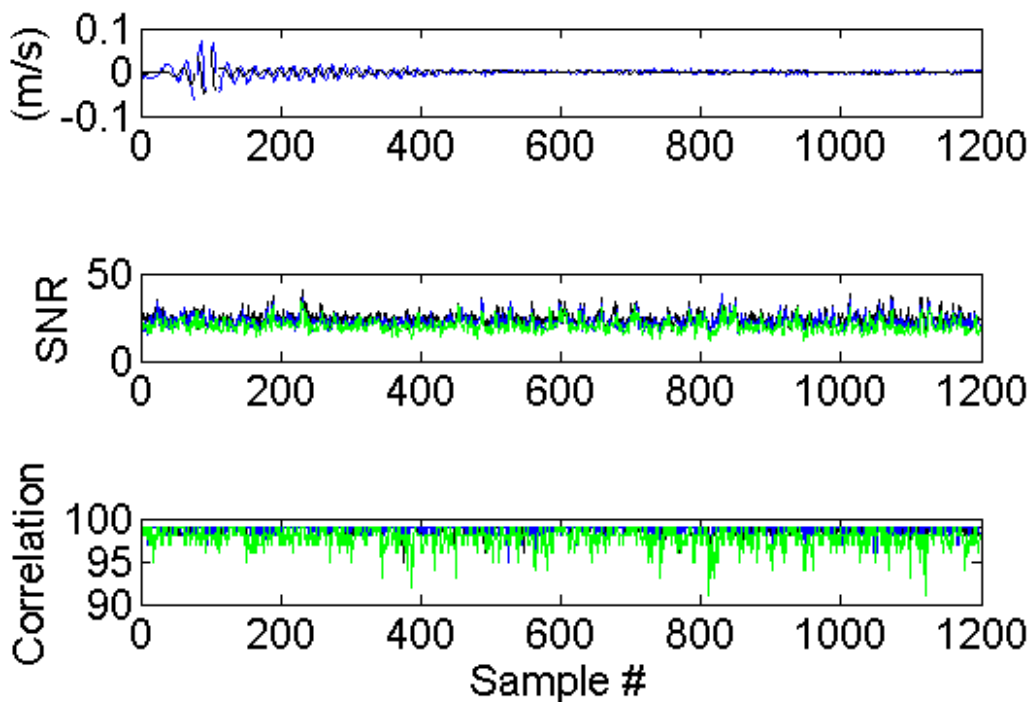


Figure 5.41.4: u' (blue) and w' (black) for burst with maximum single w (top) and corresponding SNR (middle) and *Correlation* (bottom) for beam 1 (black), 2 (blue), and 3 (green).

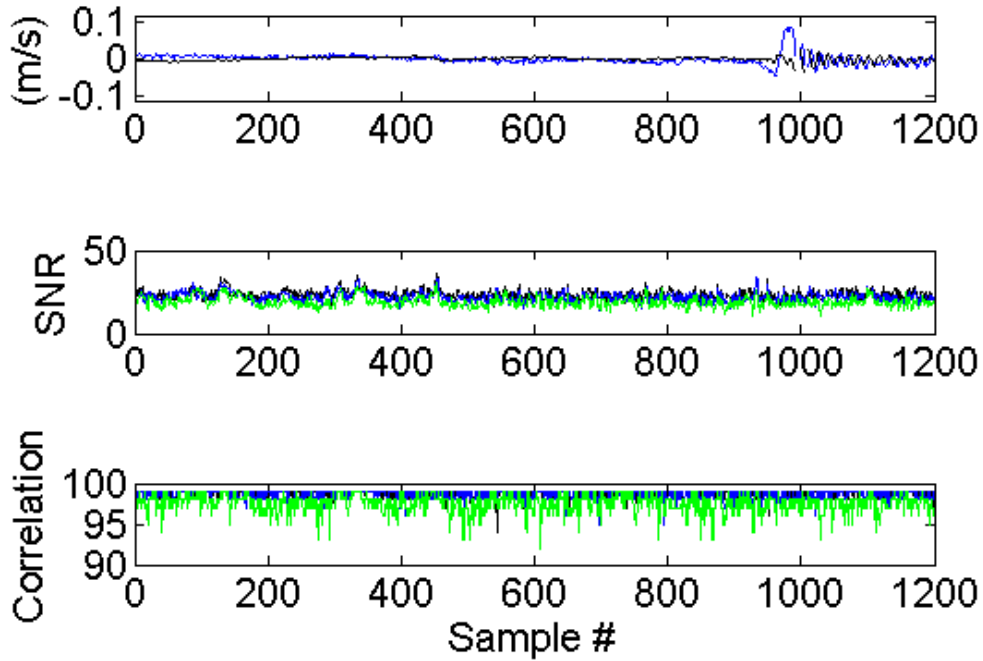


Figure 5.41.5: u' (blue) and w' (black) for burst with peak u' (top) and corresponding SNR (middle) and *Correlation* (bottom) for beam 1 (black), 2 (blue), and 3 (green).

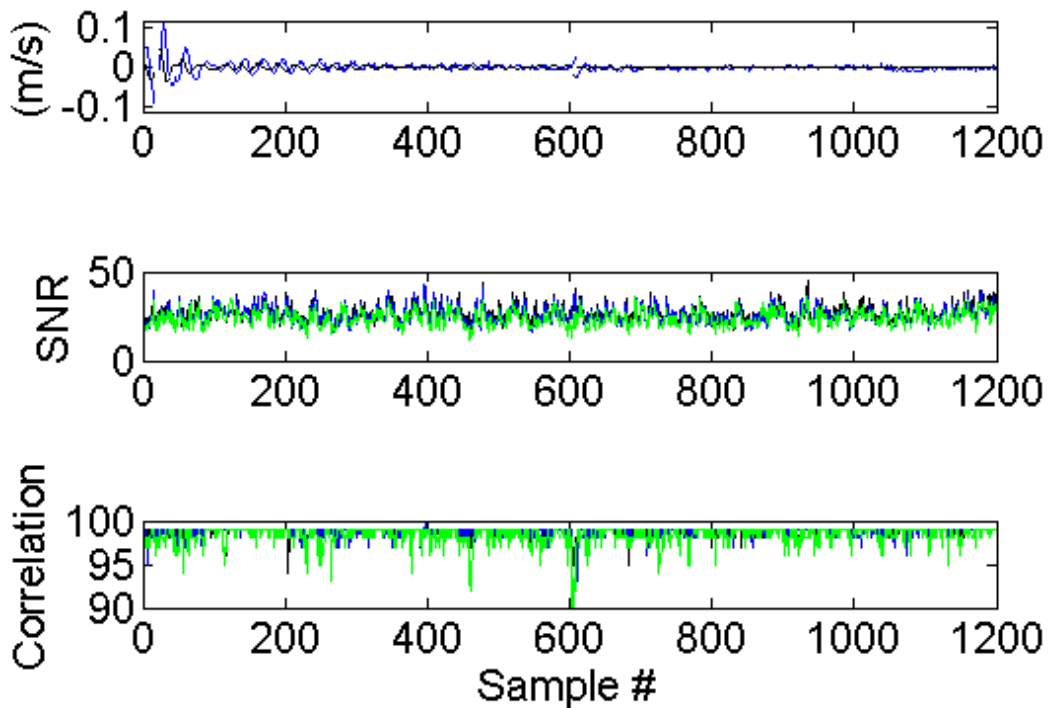


Figure 5.41.6: u' (blue) and w' (black) for burst with peak w' (top) and corresponding SNR (middle) and *Correlation* (bottom) for beam 1 (black), 2 (blue), and 3 (green).

The bed stresses calculated based on both methods (log law fits and Reynolds stress) over Deployment 2 are shown in Figure 5.42.

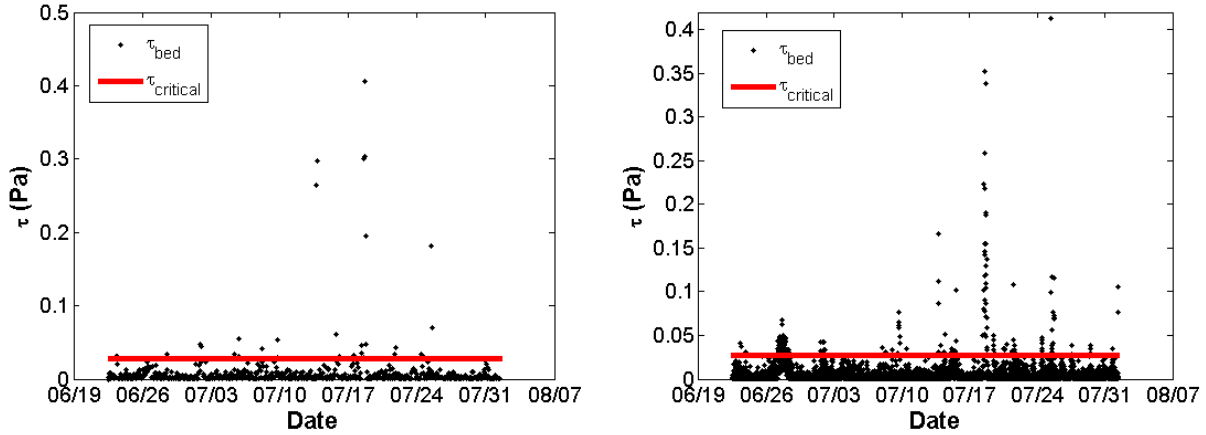


Figure 5.42: Bed stress based on Reynolds stress, from Vector measurements, (left) and log law, from ADCP measurements (right) over Deployment 2.

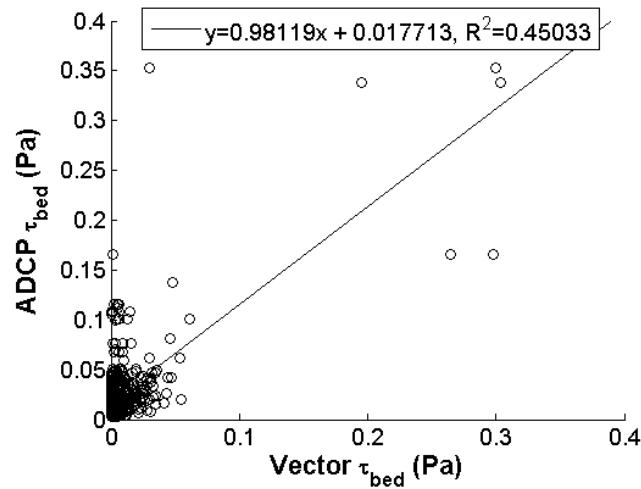


Figure 5.43: Bed stress based on log law (ADCP) vs Reynolds stress (Vector) over Deployment 2.

However, as discovered based on the power spectra, surface waves interfered with the turbulence measures from the Vector. Using methods described in Kitaigorodskii (1983) we separated the wave and turbulent components in the velocity fluctuations and filtered out the added energy from waves to obtain the Reynolds stress. Based on measured pressure perturbations we calculated the wave height using the hydrostatic approximation. The average surface wave height throughout Deployment

2 was 13.7 cm. We applied the Boussinesq approximation during exchange flows in the inlet, which is justified given $g' \ll g$. The velocities calculated based on the pressure perturbations, attributed to the surface waves, were an order of magnitude smaller than the observed velocities. Subtracting the velocity fluctuations attributed to the surface waves from our original calculation of Reynolds stress we observed a decrease in most. However, the maximum bed stress over Deployment 2, on 7/18/2016, was not affected by this filter. Surface waves on average contributed to 9.91% of the velocity fluctuations. After applying this filter there were fewer times the bed stress was expected to exceed the critical bed stress.

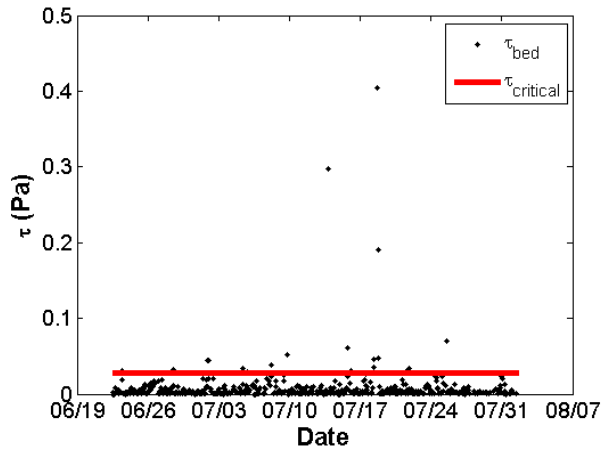


Figure 5.44.1: Bed stress based on Reynolds stress, from Vector measurements, after filtering out wave component over Deployment 2.

We applied the same method, however evaluating the velocity fluctuations due to the surface waves based on a moving average of 15 seconds, instead of the entire burst interval. We observed a greater decrease in the Reynolds stress. Surface waves on average contributed to 29.6% of the velocity fluctuations. Comparing to the previously calculated bed stress based on the log law resulted in a best fit linear regression represented by $\tau_{bed}^{ADCP} = 1.0197\tau_{bed}^{Vector} + 0.018122$ and $R^2 = 0.428$. It is this filtering method, with a moving average of 15 seconds, we used in future analysis involving the bed stress.

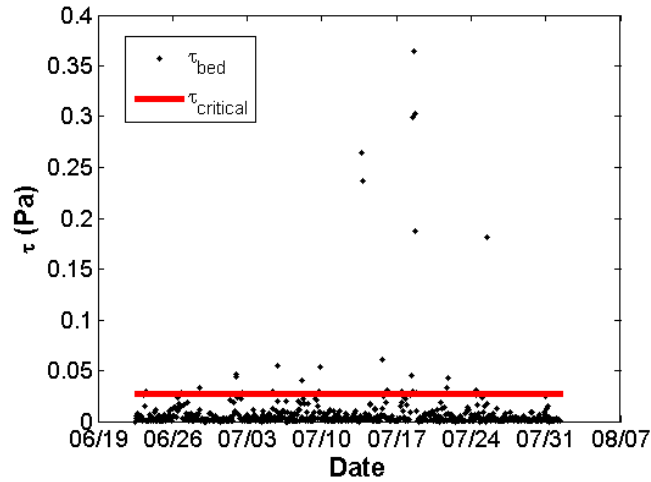


Figure 5.44.2: Bed stress based on Reynolds stress after filtering out wave component, using a 15 second average, over Deployment 2.

Another filtering method called the phase method, proposed by Bricker (2007), was applied to our data set from Deployment 2. This method does not require independent measures of the surface waves, however uses characteristics of the velocity power spectra to pull out the wave component from the Reynolds stress calculation. This wave component is defined in Equations (5.10.1) and (5.10.2).

$$\overline{\tilde{u}\tilde{w}} = \sum_{j=\text{wave peak}} |\tilde{U}_j| |\tilde{W}_j| \cos(\angle W_j - \angle U_j) \quad (5.10.1)$$

$$\angle U_j = \arctan \left[\frac{\text{Im}(U_j)}{\text{Re}(U_j)} \right] \quad (5.10.2)$$

$|\tilde{U}_j|$ and $|\tilde{W}_j|$ were calculated based on the difference between the raw power spectra data and a linear least squares regression fit to the spectrum at frequencies outside the wave peak. Frequencies ranging from 0.2 Hz to 1.0 Hz have been defined as the range of surface wave peaks. Figure 5.45, displays how $|\tilde{U}_j|$ and $|\tilde{W}_j|$ were found.

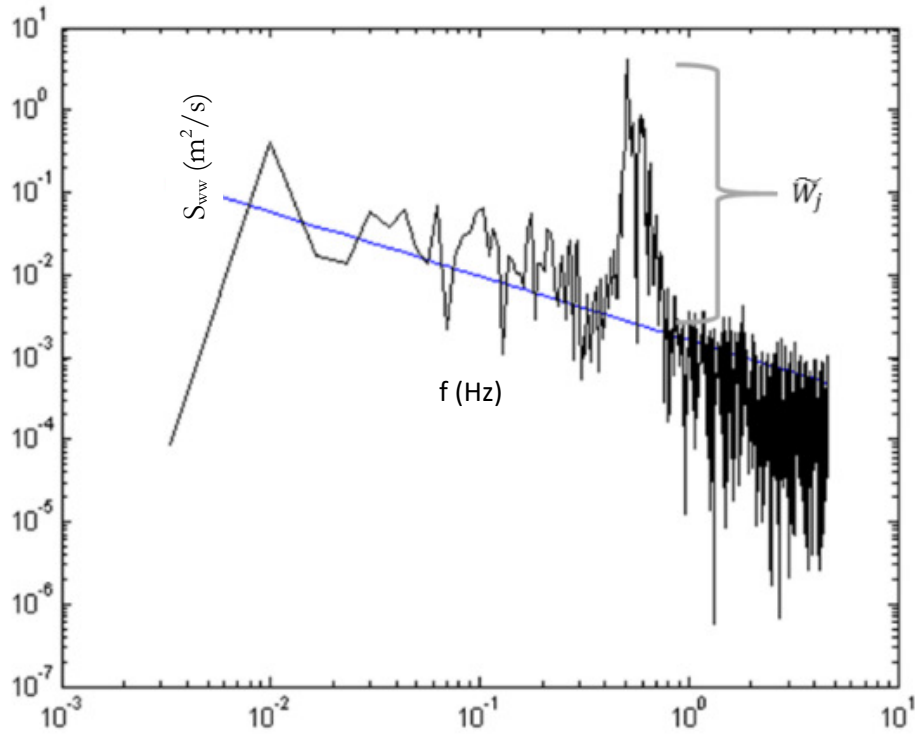


Figure 5.45: Method for finding $|\widetilde{W}_j|$ based on power spectra, S_{wv} (m^2/s). Blue line represents the least squares regression for spectra outside wave peak frequencies.

By this method, there were again fewer times bed stress was expected to exceed the critical bed stress.

This filter produced very similar results to our filter based on the pressure measurements when averaging by each burst, which was 2.5 minutes.

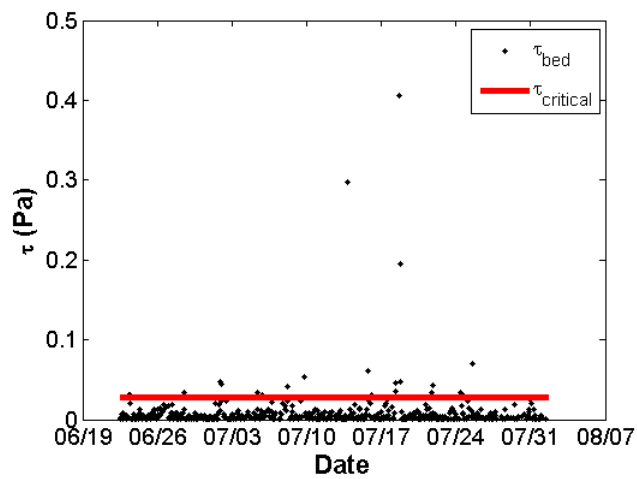


Figure 5.46: Bed stress based on Reynolds stress after filtering by phase method to remove wave component over Deployment 2.

Based on the bed stress over Deployment 2, calculated by the two described methods (using the selected filtering method on the Reynolds stress), the turbidities in all locations were highest at low bed stress and were always low during higher bed stresses. This indicates resuspension of bed sediment had little contribution to turbidity loads traveling through the inlet. There may be a small influence on the bottom layer turbidity from resuspended sediment, as a high bed stress (>0.08 Pa) always corresponded to the bottom layer turbidities greater than top layer turbidities.

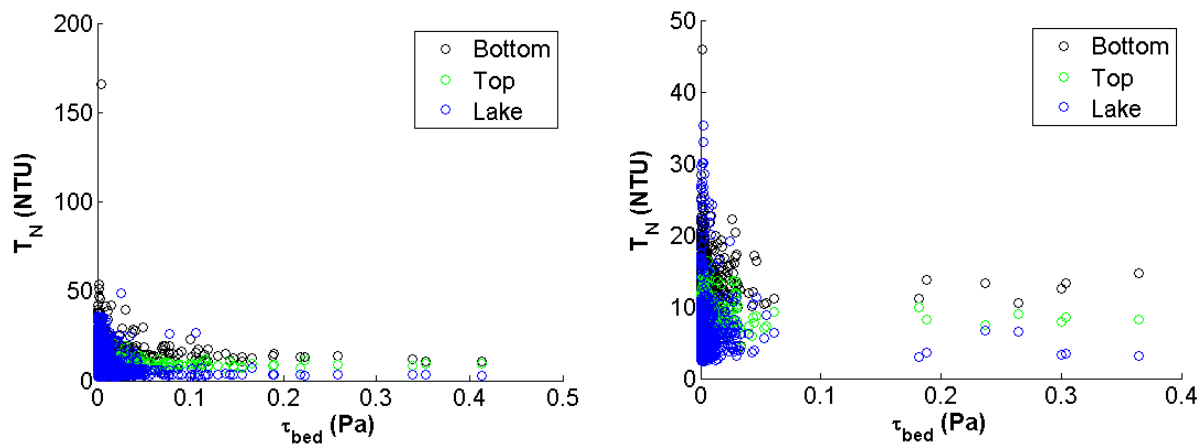


Figure 5.47.1: Bed stress compared to inlet and southern lake turbidity over Deployment 2. (Left: bed stress based on log law and ADCP measurements; Right: bed stress based on Reynolds stress and Vector measurements—different averaging times due to frequency of measurements)

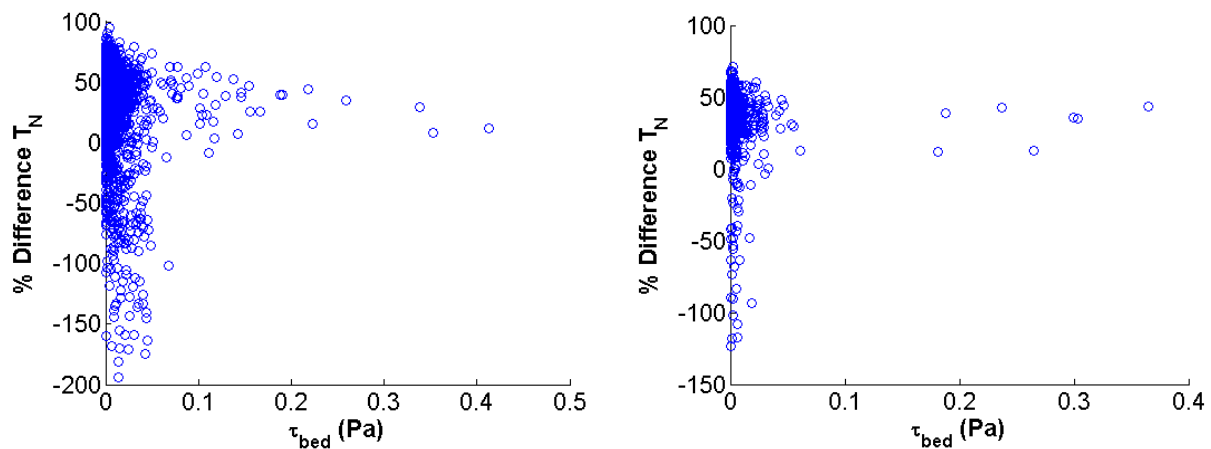


Figure 5.47.2: Bed stress compared to percent difference in turbidity in the top versus bottom layer of the inlet over Deployment 2. (Left: bed stress based on log law and ADCP measurements; Right: bed stress based on Reynolds stress and Vector measurements—different averaging times due to frequency of measurements)

For Deployment 3, we only have the Vector data to calculate the bed stress based on the Reynolds stress. Due to the change in settings in the Vector midway through the deployment, we calculated the bed stress using this method up until 8/22/2016. The velocity fluctuations are shown in Figure 5.48 and the bed stress, based on applying the selected filter on surface waves described for Deployment 2, are shown in Figure 5.49. As expected velocity fluctuations in the horizontal were greater than in the vertical. There were only a few instances the bed stress was greater than the critical bed stress, predicting insipient motion of bed sediment.

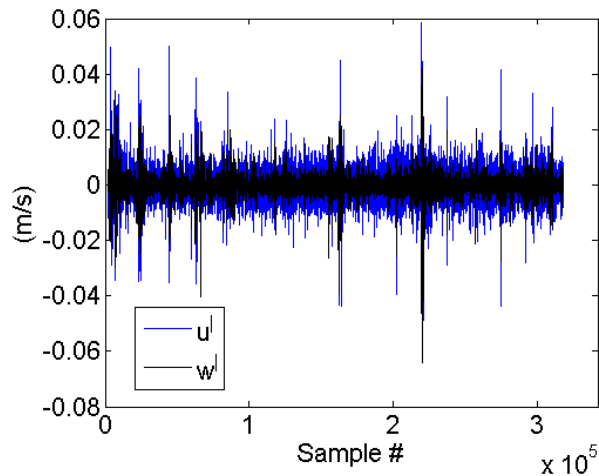


Figure 5.48: Instantaneous u' and w' from Vector data over Deployment 3.

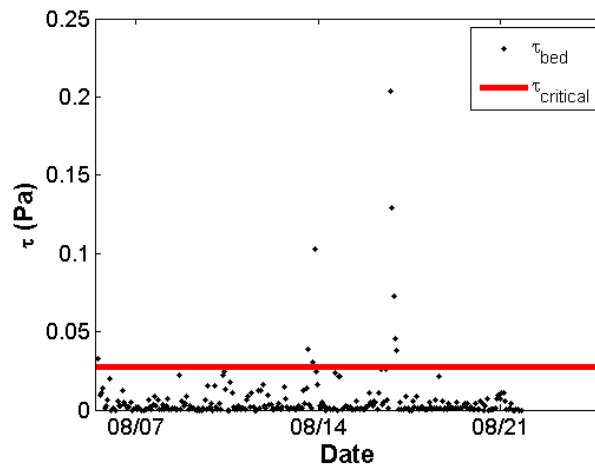


Figure 5.49: Bed stress based on Reynolds stress after filtering out wave component, using a 15 second average, over Deployment 3.

While in general a higher bed stress was associated with relatively low inlet turbidities, over Deployment 3 the greatest bottom layer turbidity occurred at a bed stress of 0.0302 Pa, which is greater than our critical bed stress. However, all other turbidities above 40 NTU, in the inlet or southern lake, occurred during bed stresses less than our critical bed stress. Over Deployment 3 any time the bed stress was above our critical bed stress, the bottom layer turbidity was greater than top layer turbidity.

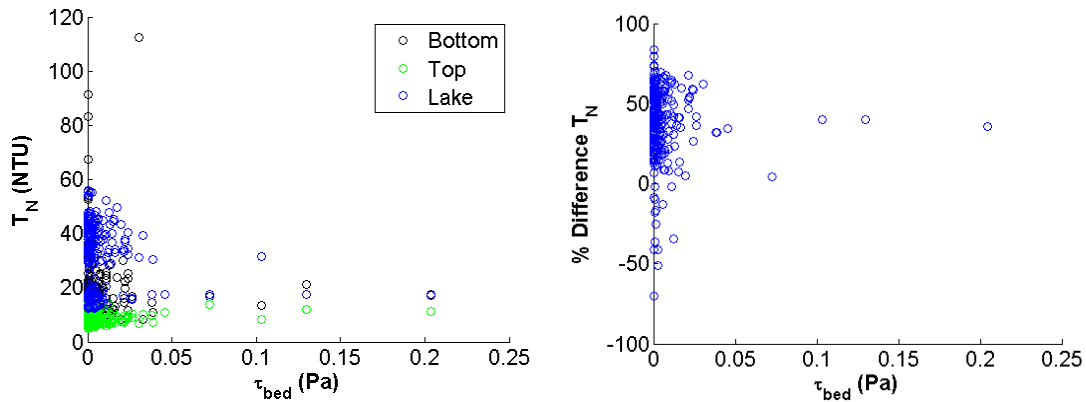


Figure 5.50: Bed stress compared to inlet and southern lake turbidity (left) and percent difference in turbidity in the top versus bottom layer of the inlet (right) over Deployment 3.

Over all deployments and using multiple measuring techniques, we found minimal contribution of bed sediment resuspension to turbidities in the inlet and out to the southern lake. However, there is likely a small contribution as higher bed stresses were always associated with the bottom layer turbidities greater than the top layer turbidities in the inlet. We suspect turbidity loads are more dependent on conditions of inflowing tributaries as well as the southern lake to the inlet and bed sediment resuspension does not play a significant role. It is also possible brief increases in the bottom layer turbidity are due to random events, such as a large stick or fish activity along the bottom causing bed sediment resuspension not captured in our analysis.

5.3.2 Flow Conditions and Vertical Mixing

When turbidities in the inlet and the southern end of the lake were at their highest values, $|U|$ was low. For $|U| > 0.06 \text{ m/s}$ turbidity in the bottom layer of the inlet was greater than in the top

layer, except for two outliers over Deployment 3. Whereas during low $|U|$ there were a significant number of times the top layer turbidity was higher than the bottom layer turbidity in the inlet. Similar patterns were true for U_{abs} compared to the turbidities. We observed very similar patterns between the inlet velocities and turbidities as described above using different averaging periods, ranging from our original 15 minutes up to 24 hours. We also attempted different lag times on the turbidity data, ranging from 2 hours to 96 hours, as time series did show delayed responses of increased turbidities following increased velocities through the inlet. However, no consistent lag time could be identified. We also looked at the difference in layer velocities and turbidities, but no clear pattern was observed.

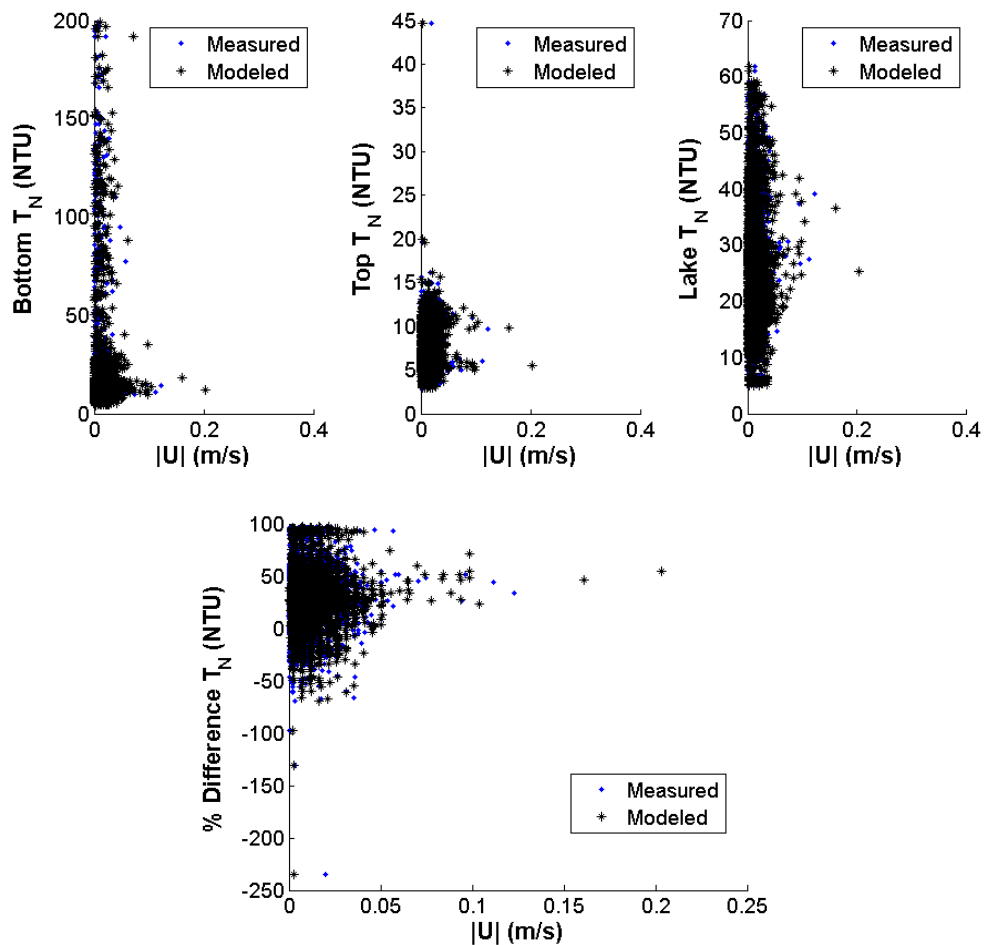


Figure 5.51.1: Turbidities versus $|U|$ as measured by the ADCP and as determined by the model using USGS flowrates in the tributaries over Deployment 1.

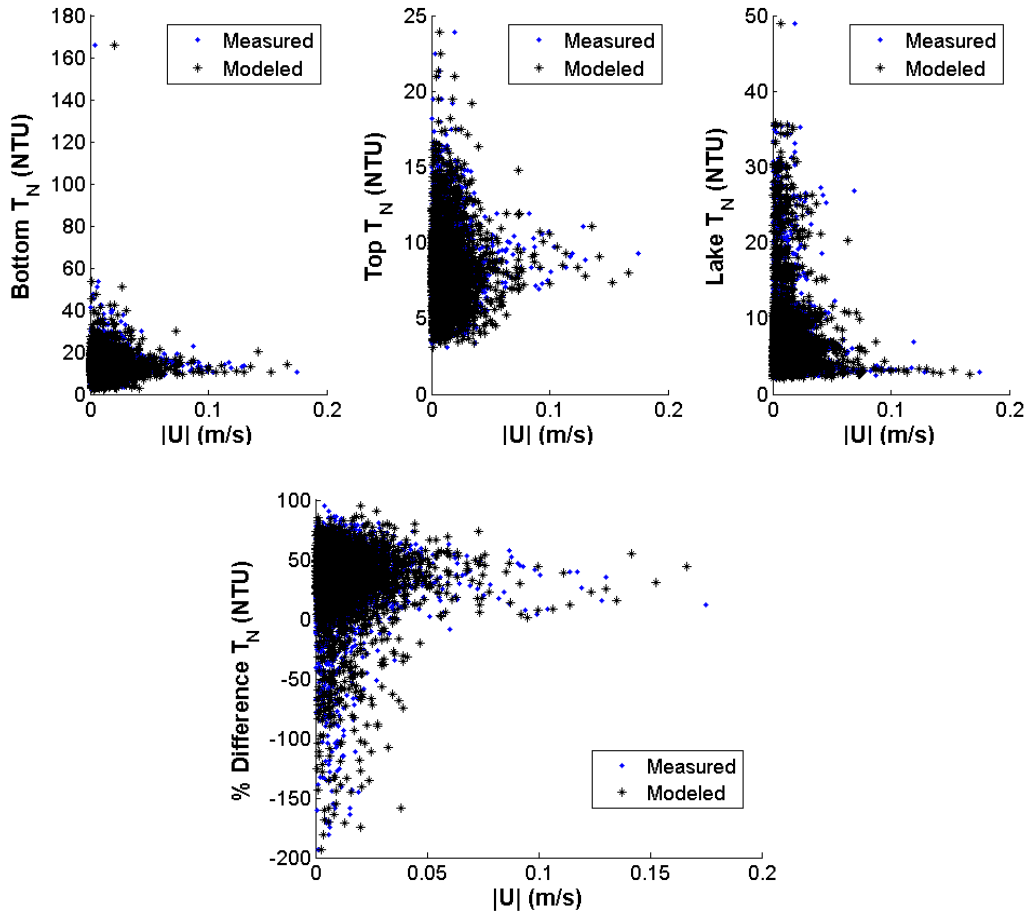
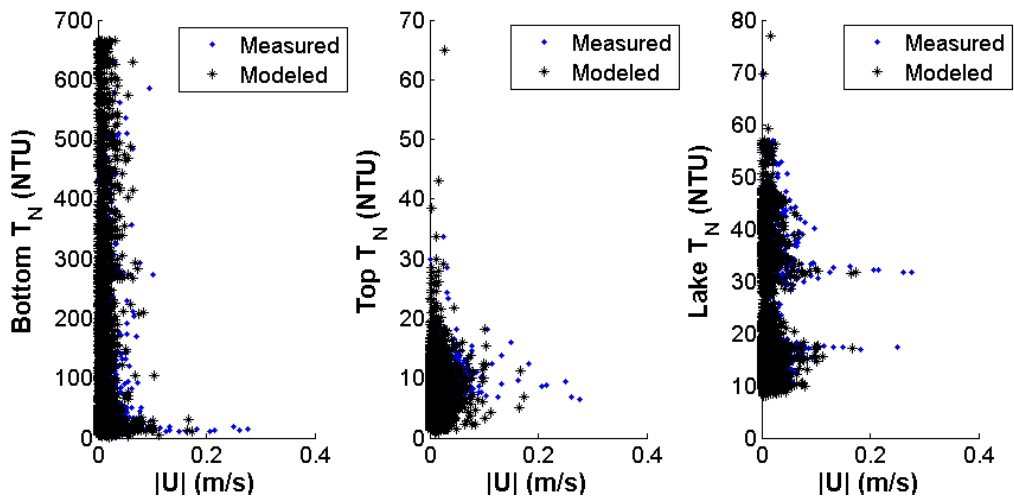


Figure 5.51.2: Turbidities versus $|U|$ as measured by the ADCP and as determined by the model using USGS flowrates in the tributaries over Deployment 2.



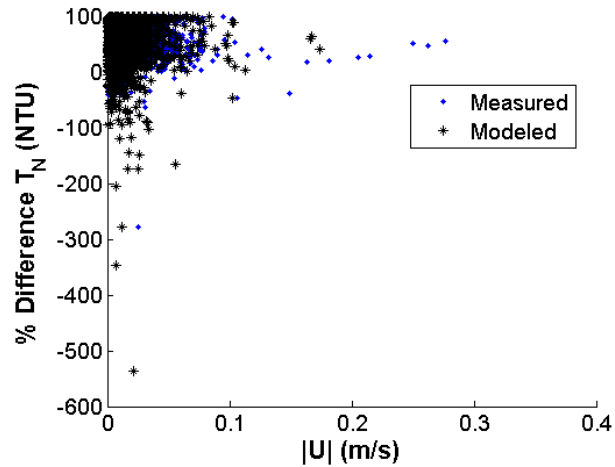
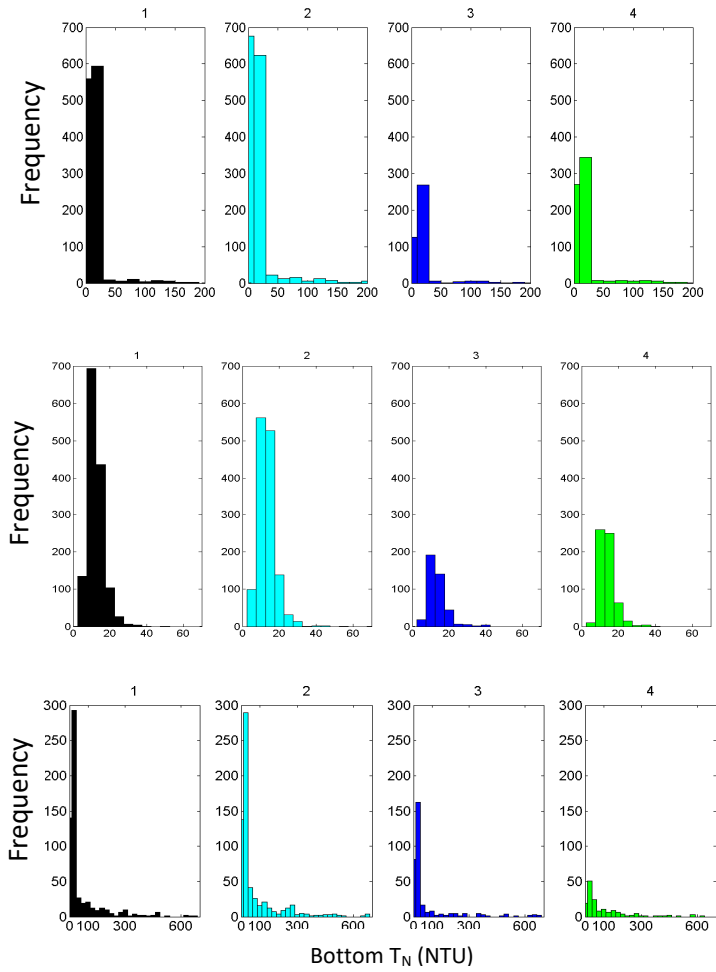


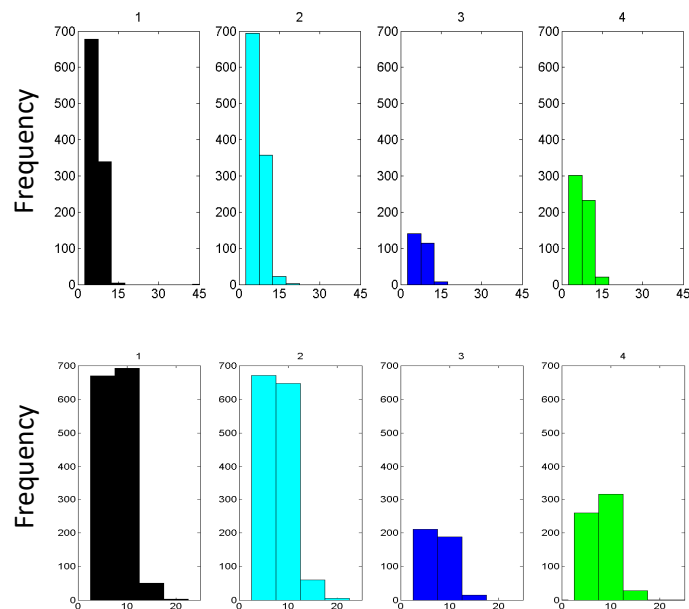
Figure 5.51.3: Turbidities versus $|U|$ as measured by the ADCP and as determined by the model using USGS flowrates in the tributaries over Deployment 3.

No significant differences were found in the distribution of the turbidities under the different flow types in the inlet. All turbidities most frequently remained below 30 NTU, where turbidity in the bottom layer of the inlet experienced the most events above this value. The southern lake also experienced a significant number of events above this value. The highest top layer turbidities were during exchange flows. Turbidity in the top layer was double that of the turbidity in the bottom layer only during exchange flows, though only in a few instances. Over Deployment 3 the bottom layer turbidity was dominantly below 100 NTU for all flow conditions, but turbidities above 600 NTU occurred within all flow conditions. The southern lake turbidity was predominately below 20 NTU for all flow conditions, but turbidities above 70 NTU occurred within all flow conditions. The lack of any significant difference in turbidity loads from the two sources to the inlet, the tributaries and the southern lake, suggest suspended sediment may be acting more as a tracer. While the tributaries or southern lake may initially have higher turbidity, due to the typical exchange flow and the consistently oscillating flow direction in the inlet, sediment can be transported through the inlet from source A towards source B and then be transported right back into the inlet from source B.



Bottom T_N (NTU)

Figure 5.52: Distribution of bottom layer turbidity (NTU) in the inlet under different flow types. Top: Deployment 1; Middle: Deployment 2; Bottom: Deployment 3. (Note over Deployment 2, flow condition 2 missing outlier ~ 165.7 NTU)



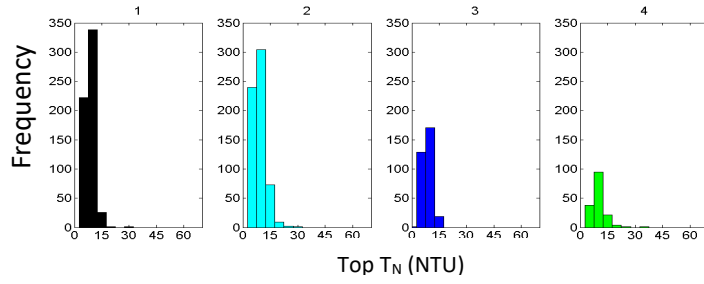


Figure 5.53: Distribution of top layer turbidity (NTU) in the inlet under different flow types. Top: Deployment 1; Middle: Deployment 2; Bottom: Deployment 3.

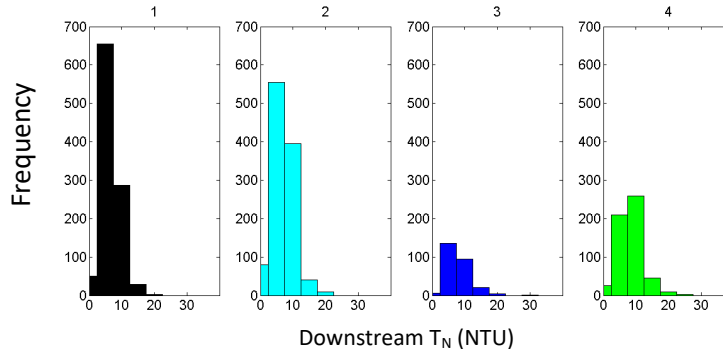
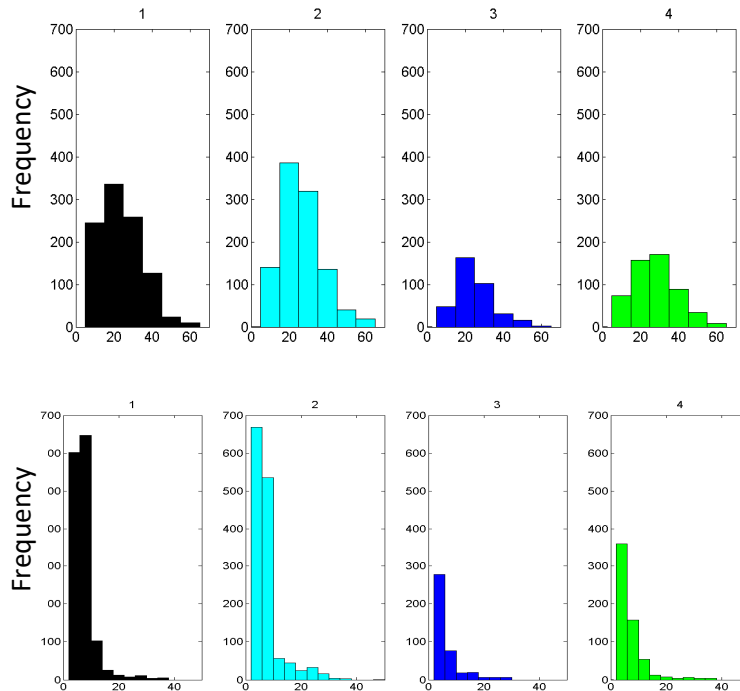


Figure 5.54: Distribution of top layer turbidity (NTU) in the inlet downstream from primary inlet location (where ADCP located) under different flow types over Deployment 1.



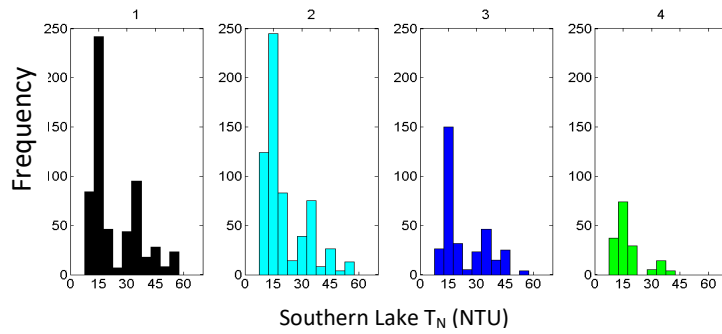


Figure 5.55: Distribution of southern lake turbidity (NTU) under different inlet flow types. Top: Deployment 1; Middle: Deployment 2; Bottom: Deployment 3.

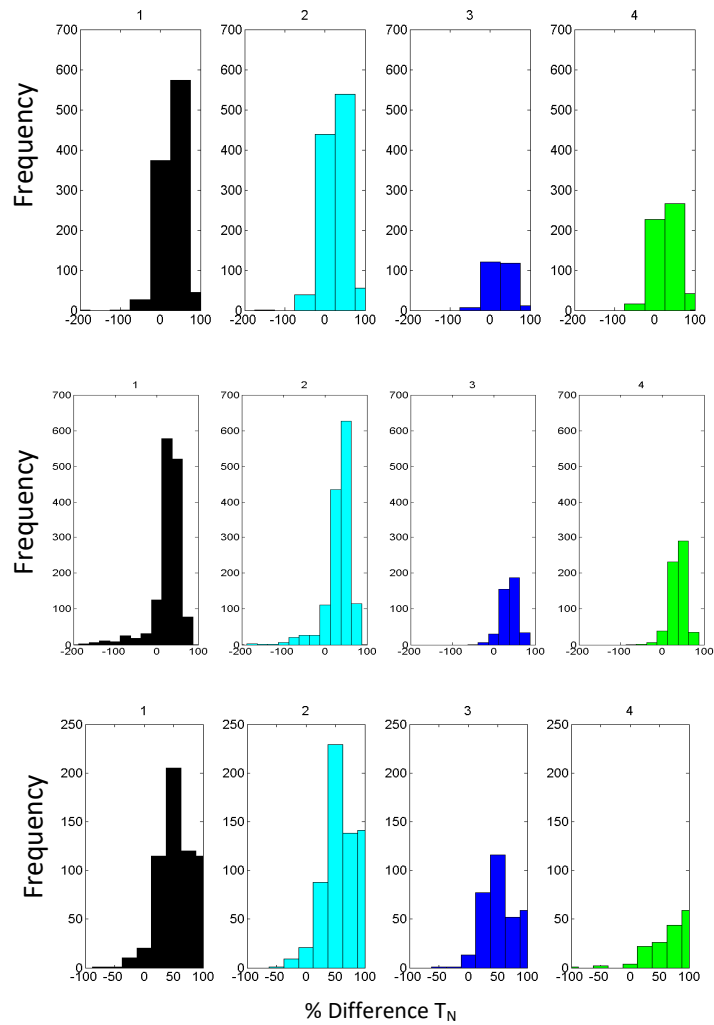


Figure 5.56: Distribution of percent difference in layer turbidities in inlet under different flow types. Top: Deployment 1; Middle: Deployment 2; Bottom: Deployment 3.

Over Deployment 1 N in the inlet did not appear to have any influence on the turbidities in any location or even the distribution of turbidity within the water column as we may have expected.

However, recall the location of the temperature measurements determining N in the inlet were downstream of the top and bottom layer turbidity measurements in the inlet. Over Deployments 2 and 3, when N was determined by temperature measurements in the same location as the top and bottom layer turbidity measurements, at higher N there was an increase in the number of times the top layer turbidity was greater than the bottom layer turbidity in the inlet.

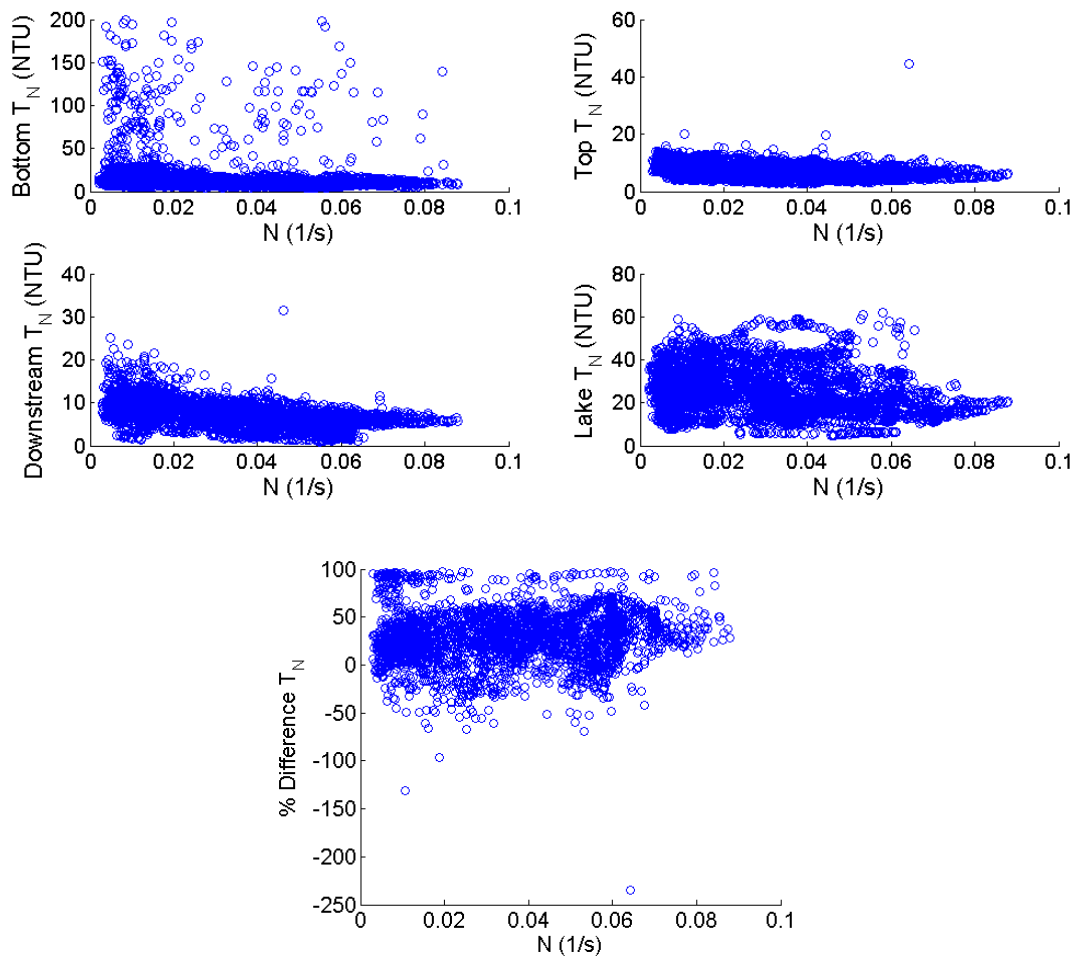


Figure 5.57.1: Turbidities versus N over Deployment 1.

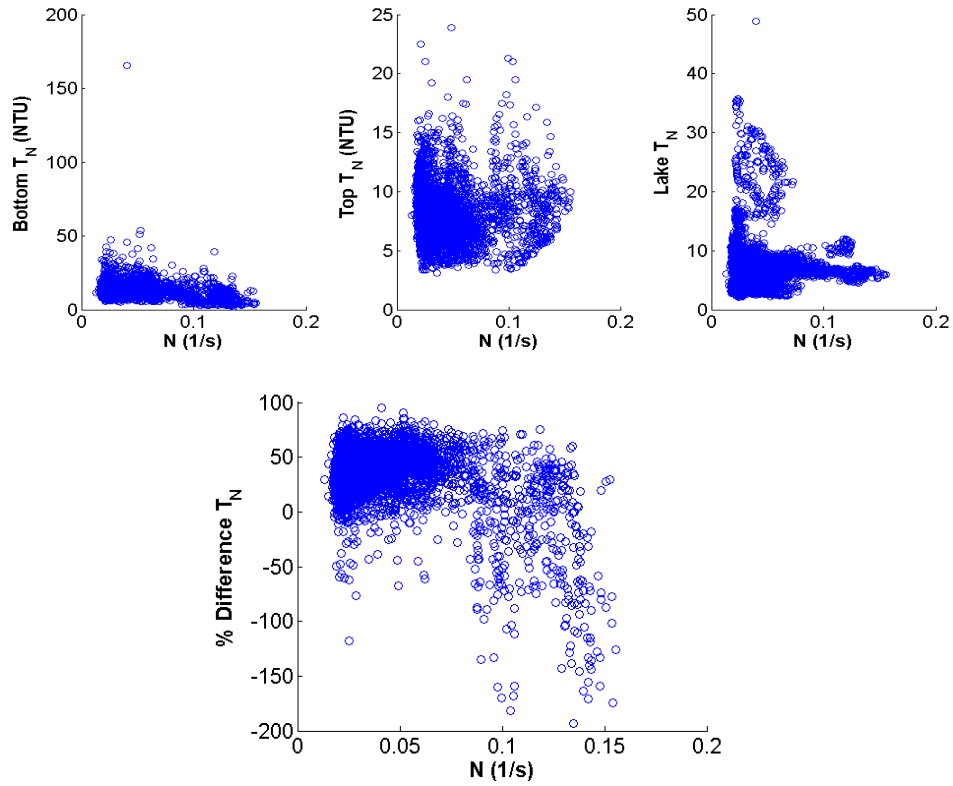


Figure 5.57.2: Turbidities versus N over Deployment 2.

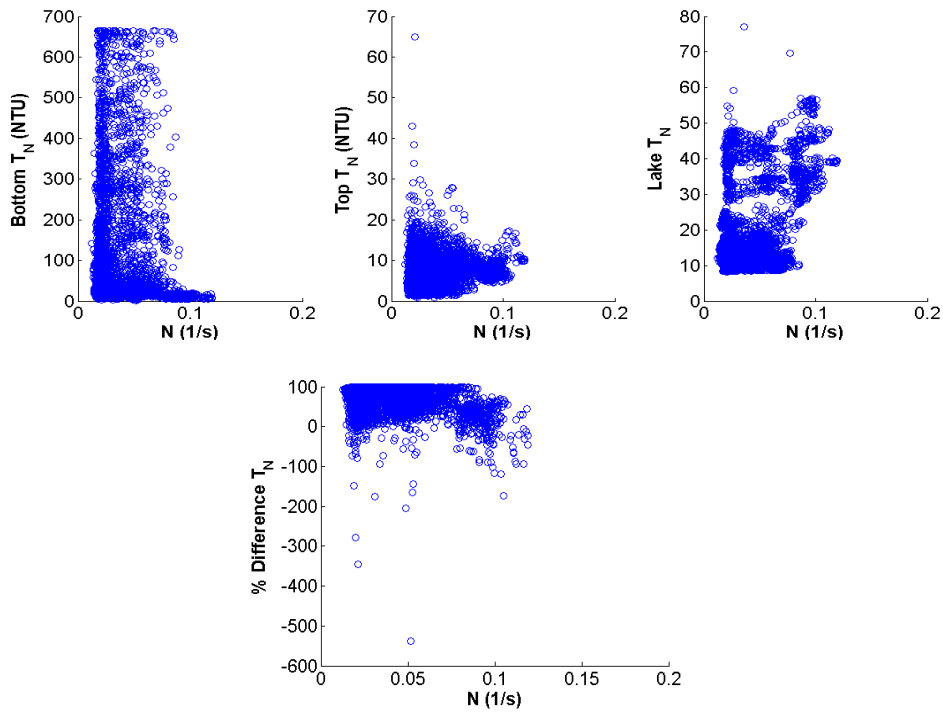


Figure 5.57.3: Turbidities versus N over Deployment 3.

Distributions of the turbidities when the inlet was well mixed, based on the timescale analysis previously described, versus all other times were not significantly different (Figure 5.58).

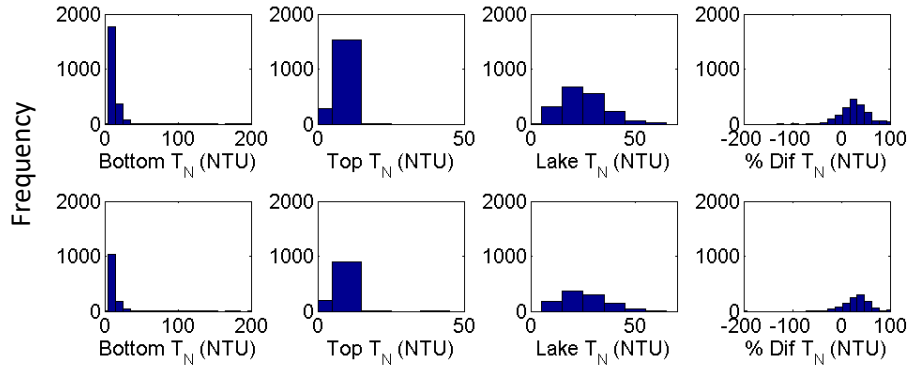


Figure 5.58.1: Distribution of turbidities when assume inlet is well mixed (i.e. $\tau_A > 10\tau_z$) (top) and all other times (bottom) over Deployment 1.

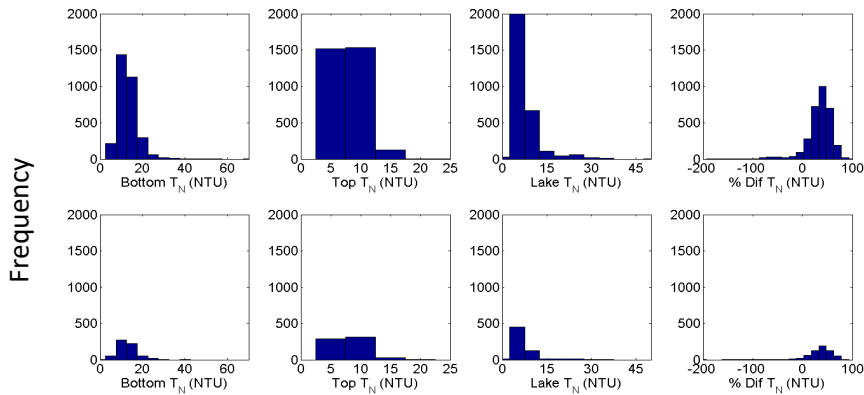


Figure 5.58.2: Distribution of turbidities when assume inlet is well mixed (i.e. $\tau_A > 10\tau_z$) (top) and all other times (bottom) over Deployment 2.

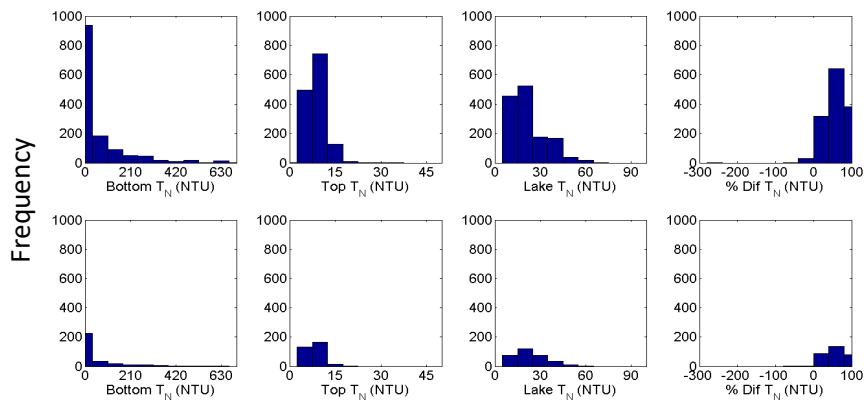
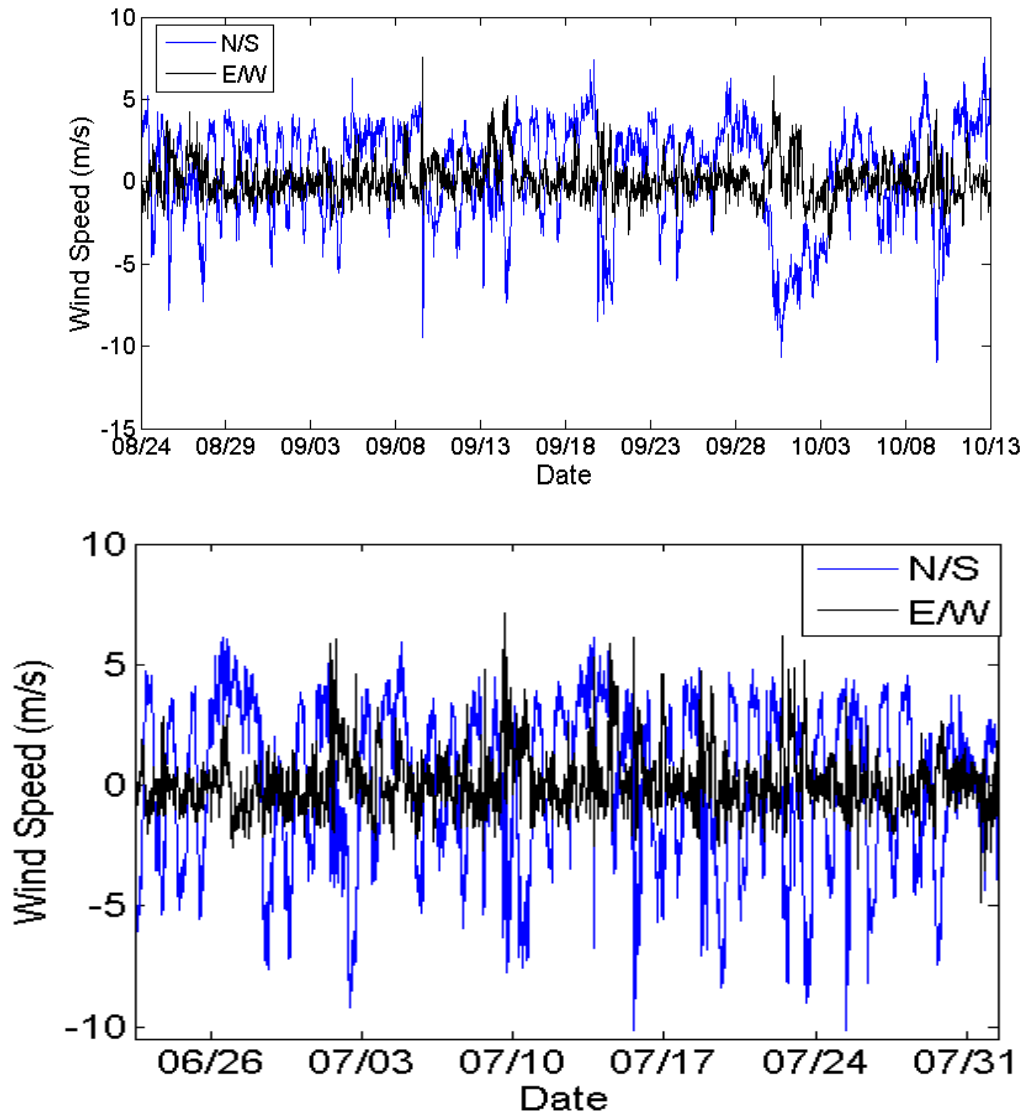


Figure 5.58.3: Distribution of turbidities when assume inlet is well mixed (i.e. $\tau_A > 10\tau_z$) (top) and all other times (bottom) over Deployment 3.

5.3.3 Wind Stress

Wind over Cayuga Lake is expected to play an important role in the inlet flow conditions. Figure 5.59, displays the predominate wind along the lake and inlet axis, consistently switching directions from true North to South and back, typically on a daily period. As we have discussed, this predominant wind influences lakes seiches (which impact flow conditions in the inlet).



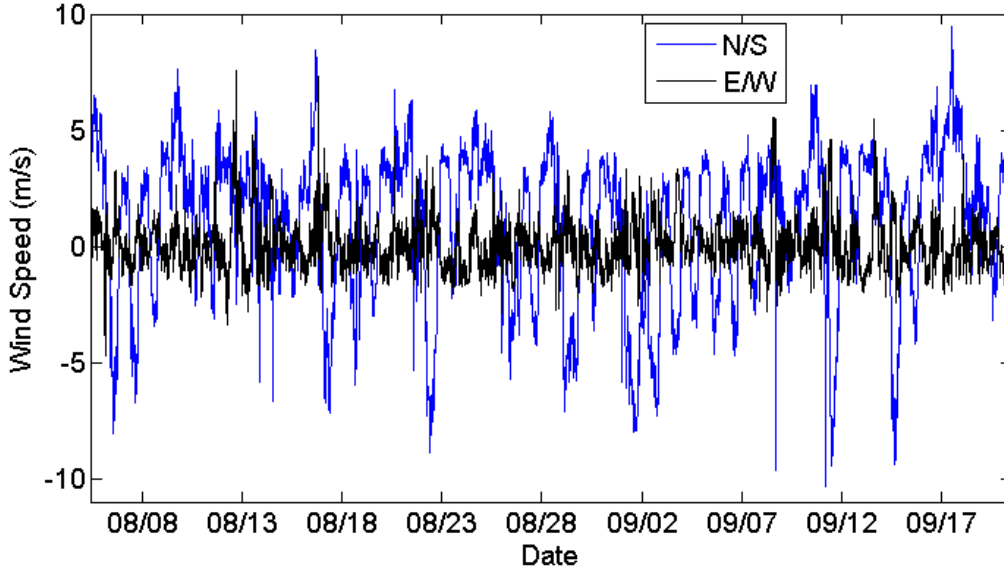


Figure 5.59: Wind speeds at the piling cluster on the southern shelf of Cayuga Lake. N/S indicates along the North/South axis, (+) traveling to the North (where here North refers to true north). E/W indicates along the East/West axis, (+) traveling to the East. Top: Deployment 1; Middle: Deployment 2; Bottom: Deployment 3.

There was no correlation between the wind speeds over the lake and $|U|$ or U_{abs} . The streamwise velocity in the inlet from the Vector measurements had no clear relation to wind speeds either. This suggests bulk flow in the inlet was dominated by other forcing mechanisms, such as tributary flows and lake seiches.

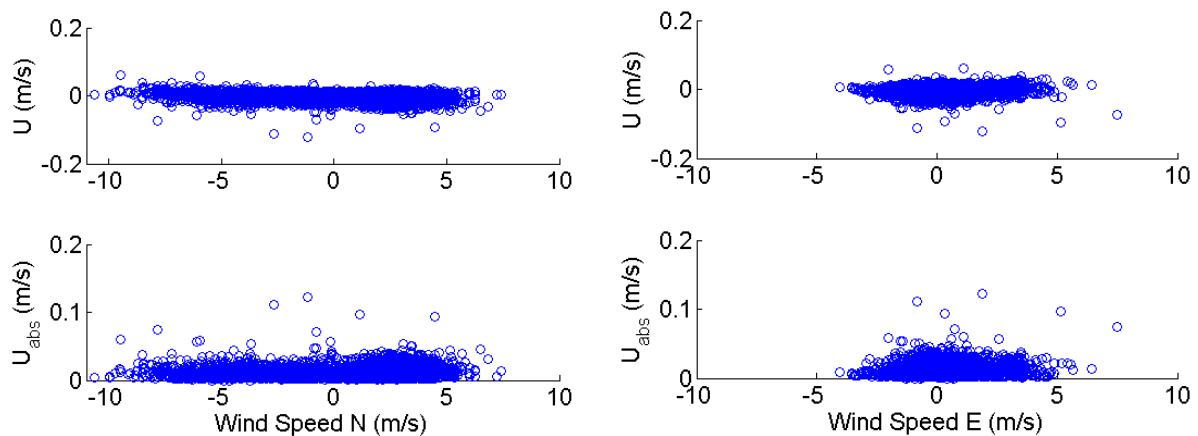


Figure 5.60.1: $|U|$ (top) and U_{abs} (bottom) compared to wind speeds to the North (left) and East (right) over Deployment 1.

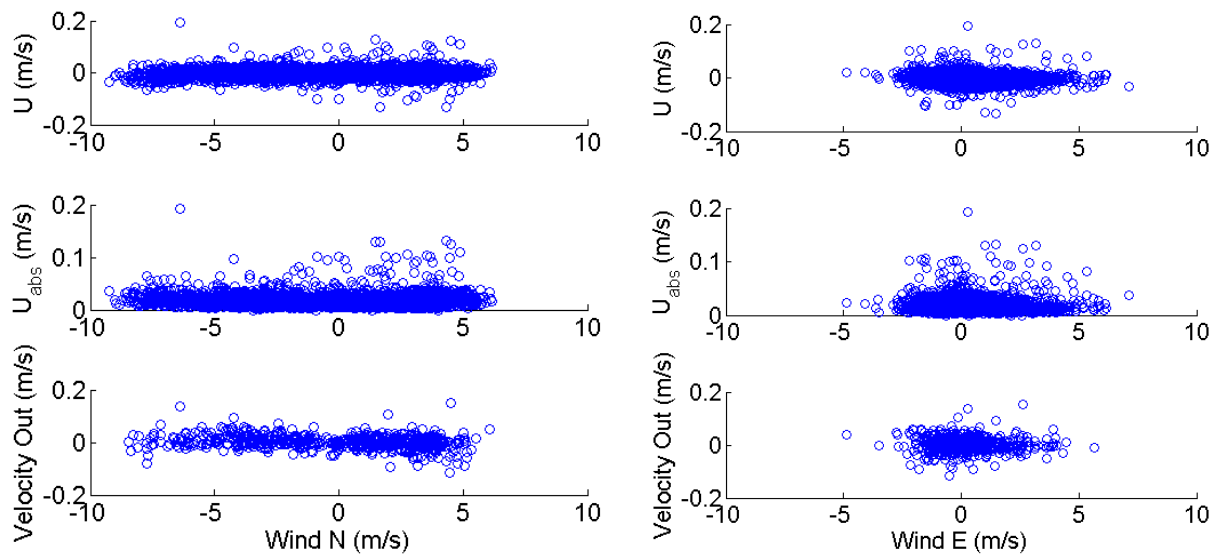


Figure 5.60.2: $|U|$ (top), U_{abs} (middle), and streamwise velocity measured by Vector (bottom) compared to wind speeds to the North (left) and East (right) over Deployment 2.

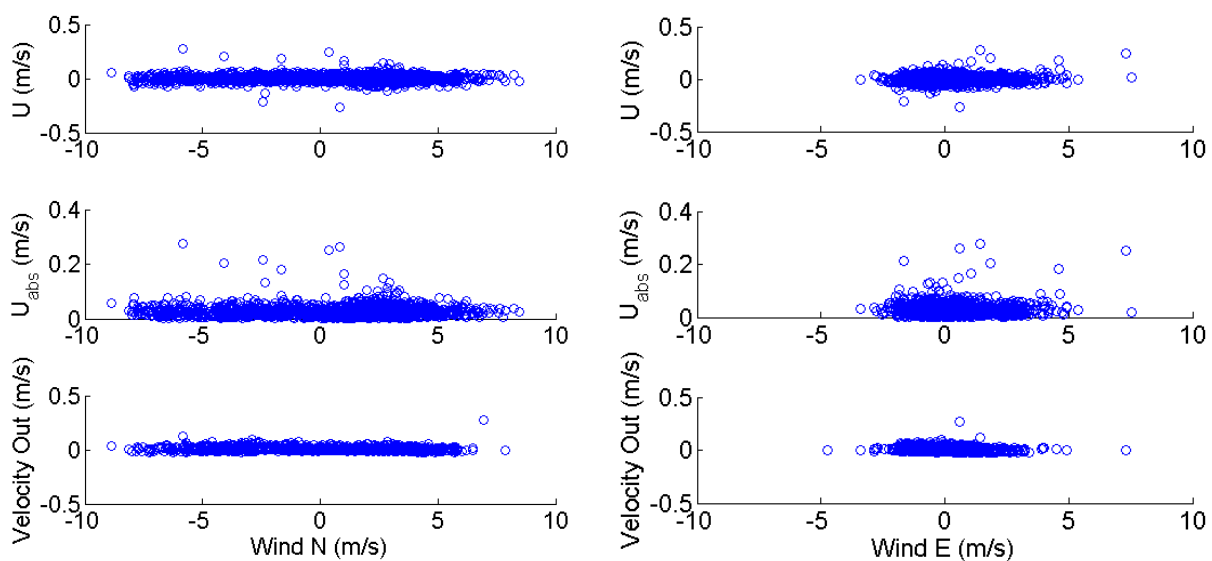


Figure 5.60.3: $|U|$ (top), U_{abs} (middle), and streamwise velocity measured by Vector (bottom) compared to wind speeds to the North (left) and East (right) over Deployment 3.

Wind stress was calculated based on the wind velocity and air temperature measured at the piling cluster on the southern shelf of Cayuga Lake (Equation 5.6). We expect strong enough winds can cause complete vertical mixing within the inlet, due to its shallow depth. Recall during Deployment 1, we captured multiple temperature profiles throughout the inlet and into the southern lake. In Figure

5.61, we show the time series of the wind stress measured at the piling cluster and N measured over the depth at two locations downstream from the primary inlet location (Tremen Marine and Inlet Lighthouse) and at the piling cluster on the southern shelf of the lake. If we focus on the largest wind stress event, in all three locations any stratification was essentially removed, as N approached 0 across the entire water column. For the other significant wind stress events, N decreased over the water column, most immediately and significantly in the surface layers.

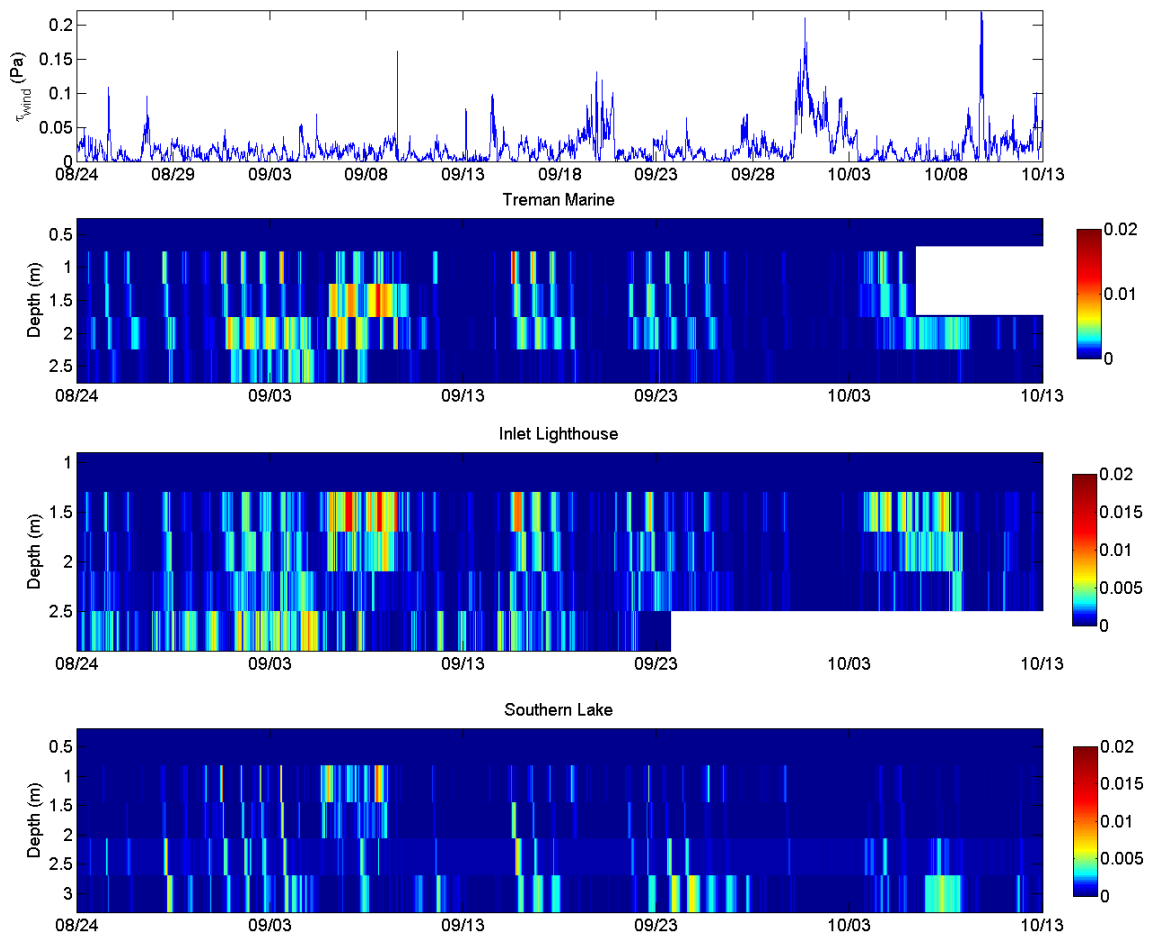
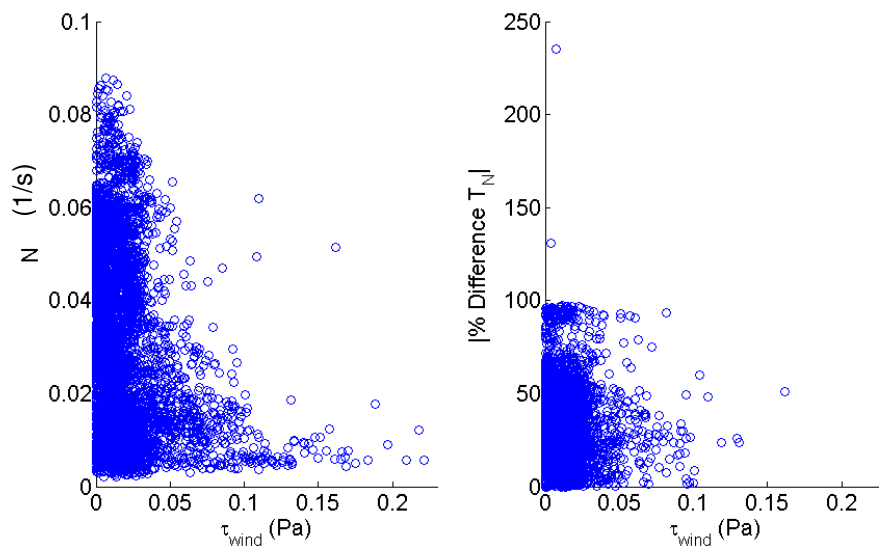


Figure 5.61: Wind stress over time (top) compared to N (1/s) over the depth based on temperature profiles at indicated locations during Deployment 1.

We were specifically interested in how the wind stress impacted vertical mixing between the top and bottom layers of the inlet at our main location. Over Deployment 1 for $\tau_{wind} > 0.1 Pa$, N

in the inlet was most frequently low and the percent difference of turbidity in the inlet was always below 60%. This agrees with what we expect for greater wind stresses to generate more vertical mixing in the inlet, thus low N and suspended sediment mixed throughout the depth. Over Deployment 2, higher percent differences in turbidity were only under a low wind stress. For the two instances the wind stress was above 0.2 Pa, the percent difference in turbidity was 26% and 20% and N was 0.10s^{-1} and 0.023s^{-1} . Recall N was relatively low throughout Deployment 2. The percent difference in turbidity remaining low under higher wind stresses suggests the inlet was vertically well mixed under such conditions. Over Deployment 3, for the wind stress above 0.12 Pa, $N < 0.03\text{s}^{-1}$, except for one outlier $N \approx 0.06\text{s}^{-1}$. Whereas for lower wind stresses, N reached up to 0.12s^{-1} . At the highest wind stress N was near the lowest recorded at 0.016s^{-1} . However, unlike for the earlier deployments, the largest wind stress was associated with a percent difference in turbidity near 100%. This suggests, just as with the shear mixing, when extreme turbidities are present as they were over Deployment 3, mixing due to a high wind stress is relatively insignificant to extreme turbidity loads that remain concentrated in the bottom layer of the inlet.



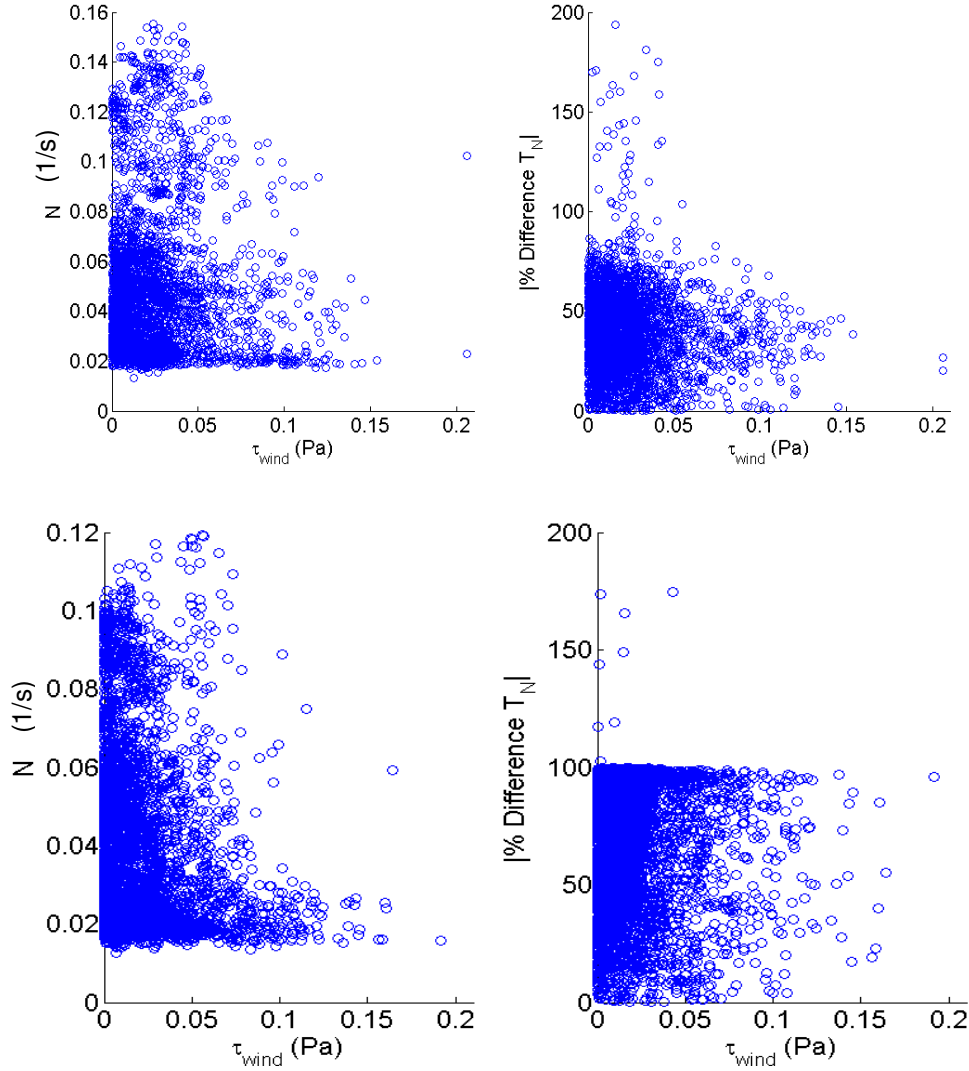


Figure 5.62: Wind stress compared to N (left) and percent difference of turbidity in the inlet (right). Top: Deployment 1; Middle: Deployment 2; Bottom: Deployment 3.

For Deployment 2 we calculated the surface water frictional velocity, $u_{*,water}$, based on the wind stress and applying stress-continuity at the air-water interface ($\tau_{wind} = \tau_{water}$).

$$\tau_{water} = \rho_{water} u_{*,water}^2 \quad (5.11)$$

No significant relationship was observed between the wind predicted $u_{*,water}$ and the measured streamwise layer velocities in the inlet. The relationship was shockingly poor, as shown by the R^2 values in Table 5.4. It is important to note the shallowest layer we have in our measurements was still

0.4m deep. Above this depth, the data exhibited interference from the water surface, thus was cut. We expect layers closest to the surface to have the strongest relationship to $u_{*,water}$. The relationship improved at shallower depths (though the highest R^2 value was only 0.125).

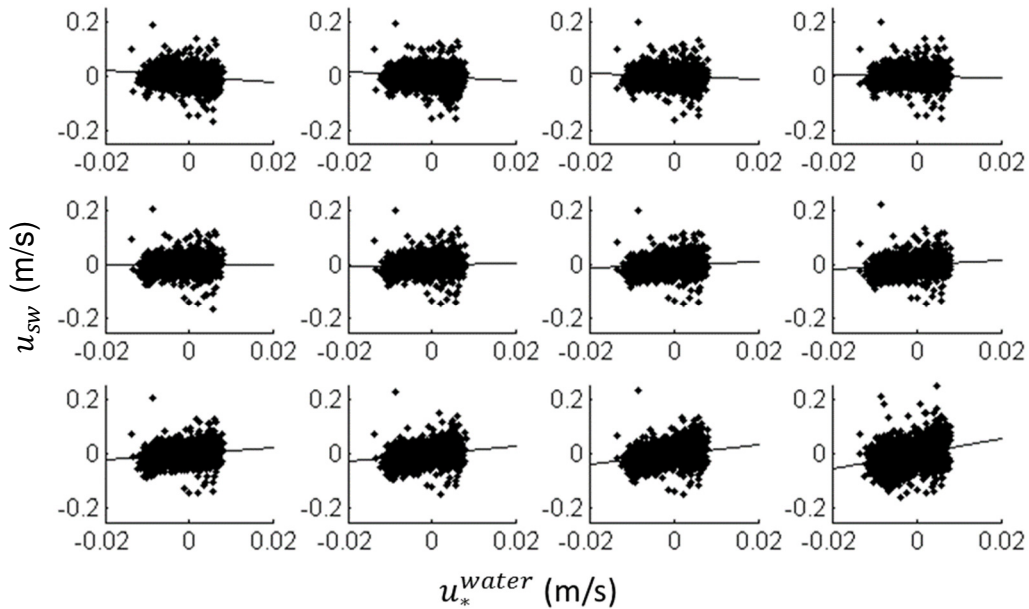


Figure 5.63: Streamwise layer velocities measured by ADCP, u_{sw} , compared to $u_{*,water}$ predicted from wind stress. Left to right and top to bottom layer depth decreases and corresponds to Table 5.4.

Table 5.4: Slopes and R^2 values for streamwise layer velocities compared to $u_{*,water}$ predicted from wind stress.

\sim Depth (m)	Slope	R^2
1.5	-1.063	0.0385
1.4	-0.938	0.0282
1.3	-0.610	0.0145
1.2	-0.305	0.00397
1.1	-0.021	0.0000205
1.0	0.248	0.00272
0.9	0.535	0.0124
0.8	0.836	0.0283
0.7	1.102	0.0454
0.6	1.381	0.0650
0.5	1.689	0.0851
0.4	2.801	0.125

Under specific assumptions, we predicted velocity profiles in the inlet based on the wind stress. First, we only consider the wind stress along the axis of the inlet, thus simplifying to a 2D problem. Second, we neglect bottom stress, assuming the bottom is far enough away that bottom stress is minimal. We also assume a constant depth, $H=2.09\text{m}$ and $\eta \ll H$, where η is the wind-induced wave height and h is the water depth (defining the water surface height as zero). Then, utilizing continuity and conservation of momentum equations under the simplifying assumptions above we calculate the velocity profile (Kinsman, 1984):

$$u(h) = \frac{u_*^2}{v_T} \left[\frac{h^2}{2H} + h + \frac{H}{3} \right] \quad (5.12)$$

To further simplify this analysis, we assumed a constant v_T of $0.002 \text{ m}^2/\text{s}$. v_T was selected assuming $v_T \sim v l_m$ where $v \sim 0.1 \bar{U} = 0.1(0.02) = 0.002 \text{ m/s}$ ($|\bar{U}|$ over Deployment 2 was approximately 0.02 m/s) and $l_m \sim kH = 0.41(2.09) = 0.84 \text{ m}$ based on the Prandtl mixing length model. The analysis was performed under different timescales ranging from 15 minutes up to 2 days. In all cases the analysis poorly predicted the velocity profile in the inlet. However, the best agreement between measured (from the ADCP) and predicted streamwise layer velocities was with a 4-hour averaging period and we show this comparison in Figure 5.64 and Table 5.5. We also compared U and U_{abs} based on the predicted velocity profiles versus observations (Figure 5.65), again with very poor results. The poor prediction from this analysis suggests other processes are dominating any direct effects of the wind on the inlet flow. We suspect flow in the inlet is primarily in response to tributary inflows and seiching behavior in the lake. Therefore, wind stresses play a more indirect role by influencing the seiching behavior in the lake.

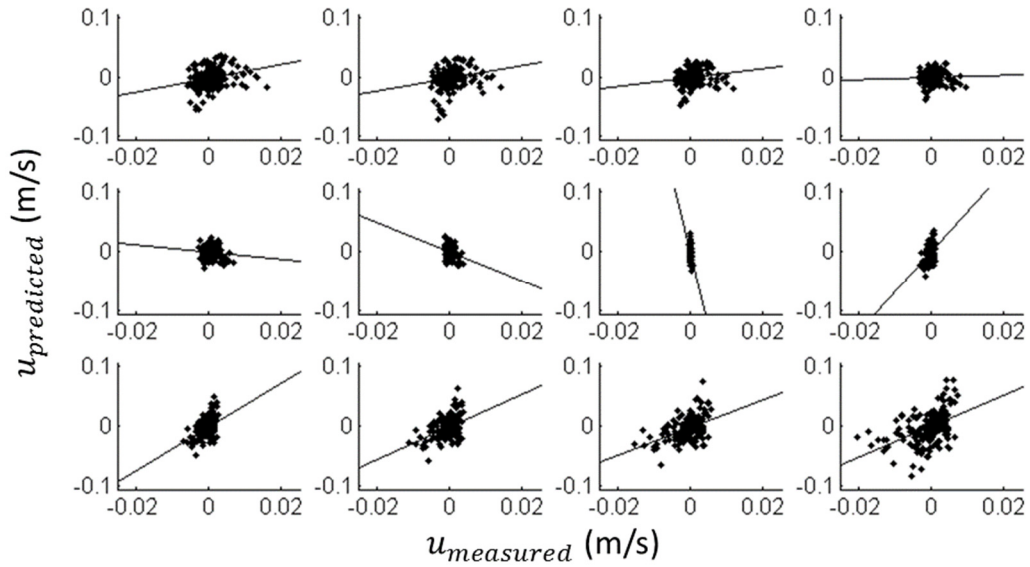


Figure 5.64: Streamwise layer velocities measured by ADCP compared predicted streamwise layer velocities from above analysis based on wind stress. Left to right and top to bottom layer depth decreases and corresponds to Table 5.5.

Table 5.5: Slopes and R^2 values for streamwise layer velocities compared to predicted streamwise layer velocities based on wind stress.

~Depth (m)	Slope	R^2
1.5	1.156	0.0727
1.4	1.083	0.0465
1.3	0.709	0.0257
1.2	0.208	0.00206
1.1	-0.592	0.0104
1.0	-2.419	0.0551
0.9	-25.778	0.110
0.8	6.702	0.147
0.7	3.669	0.175
0.6	2.744	0.193
0.5	2.323	0.212
0.4	2.581	0.226

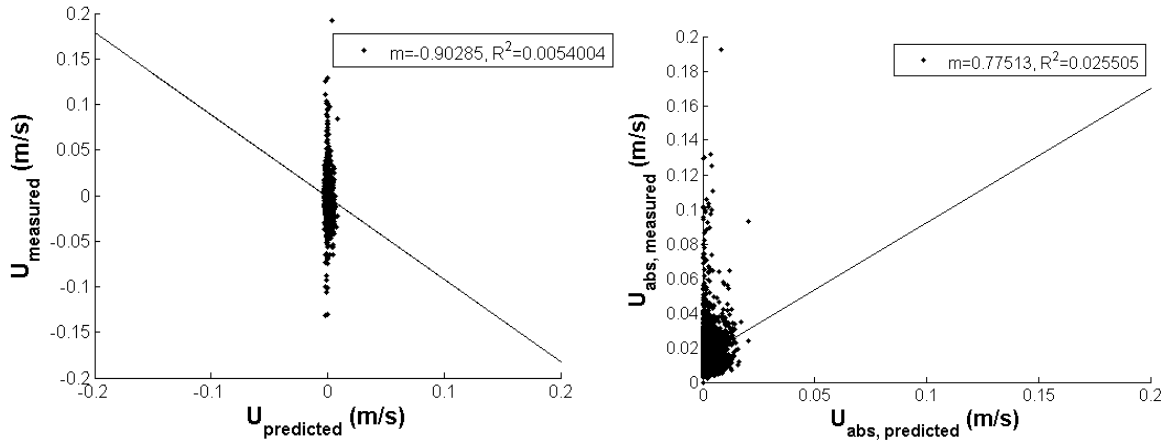
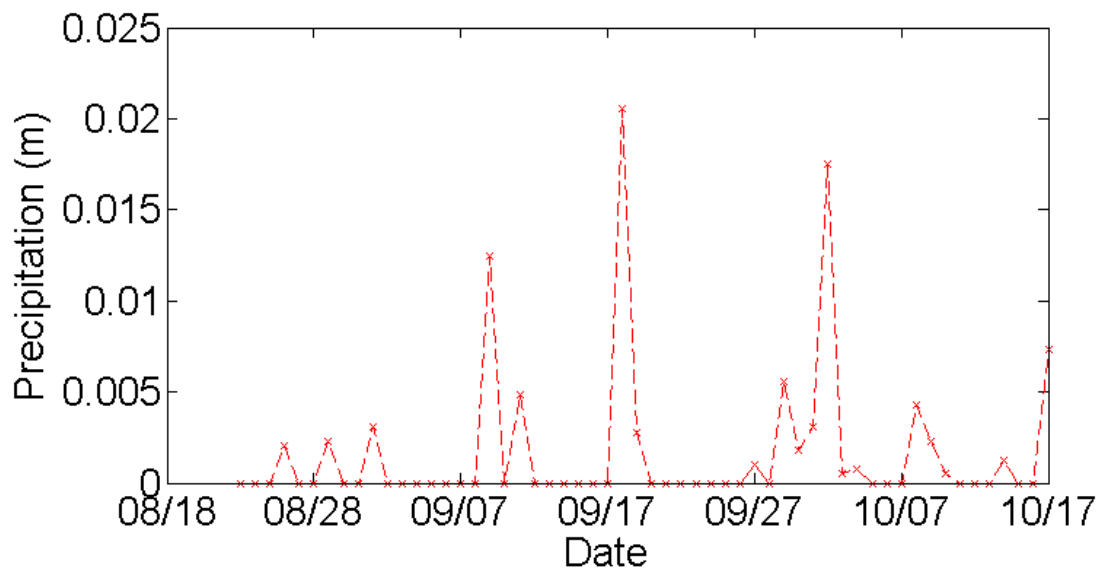


Figure 5.65: U (left) and U_{abs} (right) from ADCP measurements compared to from predicted velocity profile based on wind stress.

5.4 Specific Events

5.4.1 Maximum Tributary Flowrate

Tributary flowrates remained below $1\text{ m}^3/\text{s}$ over Deployment 1, except for one event on September 30th, 2015 where Cayuga Inlet was recorded at $6.17\text{ m}^3/\text{s}$ and Sixmile Creek was recorded at $1.61\text{ m}^3/\text{s}$. This event occurred after 4 days of significant precipitation.



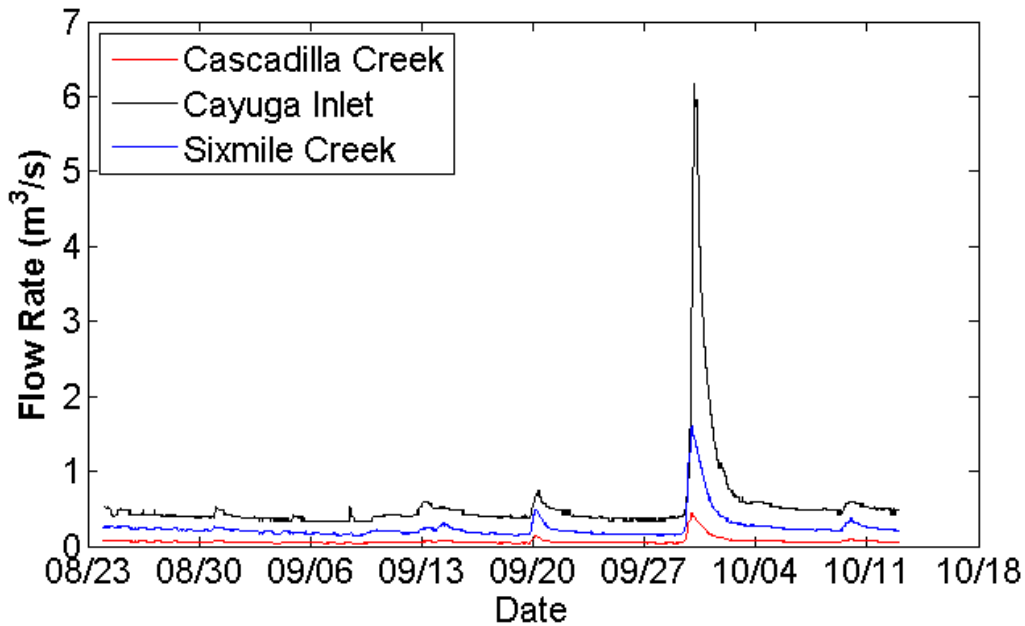


Figure 5.66: Daily precipitation (top) and flowrates from tributaries entering Cayuga Inlet (bottom).

For the period surrounding this event the bottom layer turbidity was high, however turbidity was high at times even before the increased tributary flowrates. Following the event, $|U|$ increased and the flow was dominently type 2 or 3, thus the bottom layer was always flowing out towards the lake. The stream temperature dropped much lower than the lake temperature at this time. Around the same time flowrates increased a strong northly wind was present and just following the increased flowrates the inlet water temperature in both layers significantly dropped, following the drop in stream temperatures, by approximately 6°C . Directly following the maximum flowrate was a short period of exclusively unidirectional flows through the inlet and an increase in Fr_{bulk} .

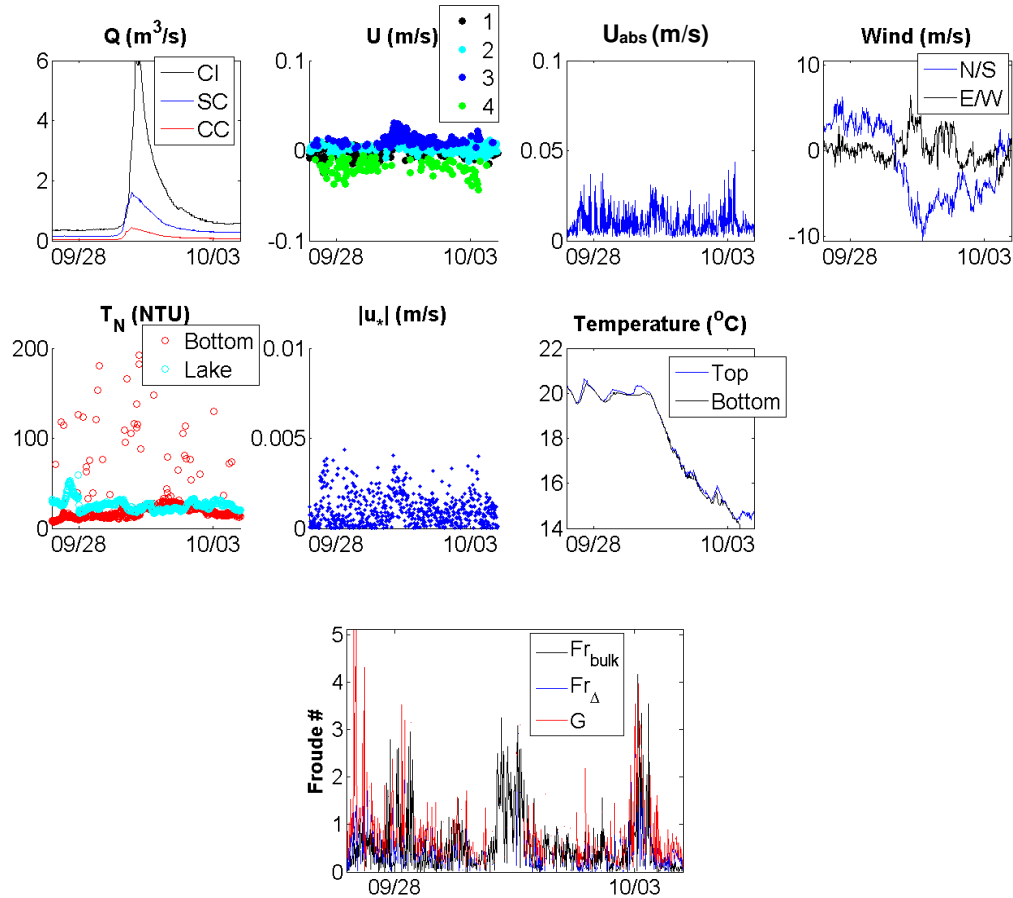


Figure 5.67: Conditions from 9/27/2015 through 10/4/2015.

5.4.2 Inlet Top Layer Turbidity > Bottom Layer Turbidity

Overall, the bottom layer turbidity was more frequently higher than the top layer turbidity. However, 8.04%, 7.62%, and 3.15% of the time over Deployment 1, 2 and 3 respectively, the top layer turbidity was higher than the bottom layer turbidity. At these times the inlet had flow condition 1 34.20%, 46.23%, and 40.48% of the time, flow condition 2 35.23%, 43.15%, and 40.48% of the time, flow condition 3 9.33%, 5.14%, and 11.90% of the time, and flow condition 4 21.24%, 5.48%, and 7.14% of the time during Deployment 1, 2 and 3, respectively. On average the top layer turbidity was slightly higher when flowing into the inlet from the lake. Comparing top layer turbidities to the daily precipitation records did not reveal any pattern. Precipitation did not appear to significantly influence turbidity in the top layer of the inlet.

Isolating the times the top layer turbidity was greater than the bottom layer turbidity in the inlet, the wind was blowing to the north more frequently than across all time (Figure 5.68). When the top layer turbidity was greater than the bottom layer turbidity N in the inlet reached higher values more frequently than across all time. Although at these times we also saw low N , more frequently $N \geq 0.1s^{-1}$. For all other times, we more frequently found $N < 0.1s^{-1}$ and rarely above this.

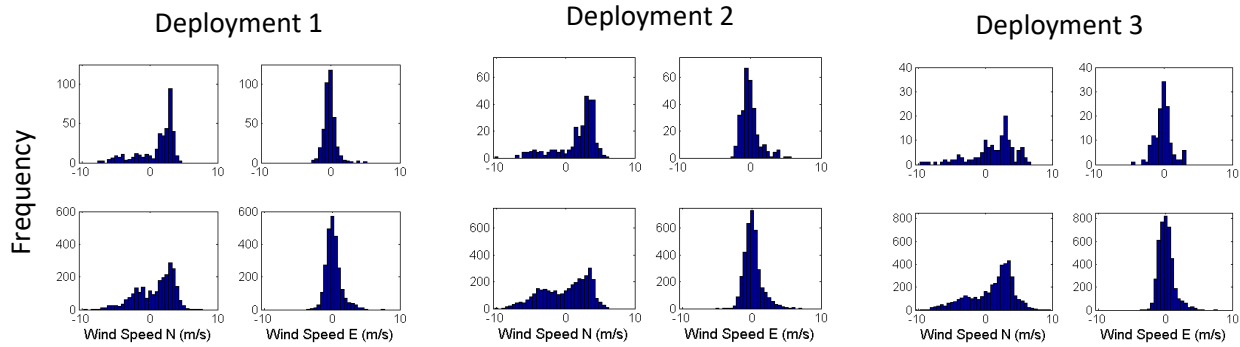


Figure 5.68: Distribution of wind speeds to the north and east when top layer turbidity was greater than bottom layer turbidity (top) and all other times (bottom).

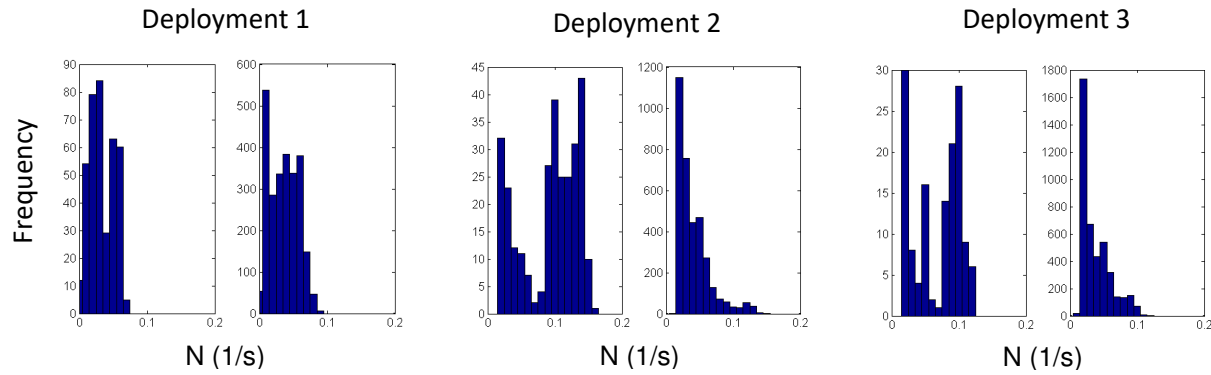


Figure 5.69: Distribution of N in the inlet when top layer turbidity was greater than bottom layer turbidity (left) and all other times (right).

5.4.3 Precipitation Events

Over Deployment 2 precipitation did not appear to significantly influence the top layer turbidity in the inlet. However, the high bottom layer turbidity event we observed towards the end of July appears to be the result of a significant increase in precipitation. It is important to note this

deployment was during a significant dry period for the area. After a long period of minimal rain, it only took a moderate rain event to see a significant increase in turbidity in the bottom layer of the inlet. We also see the effects of this rain event carrying a significant turbidity load into the southern end of the lake. First, there was a shorter turbidity increase in the inlets bottom layer then a more sustained turbidity increase in the southern lake. There was 2.73 days between the first peak in the bottom layer inlet turbidity and the first peak in southern lake turbidity. Over this period, the advective timescale, based on the depth average streamwise velocity in the inlet and the distance between the two turbidity measurements (~ 1.5 km), had a mean of 5.46 days and a median of 2.07 days. With this information, we can reason the peak in the bottom layer inlet turbidity was transported into the southern lake, contributing to the later observed increase in turbidity there. Both the bottom layer inlet and southern lake turbidities were very low throughout Deployment 2 until just after the highest rain event recorded.

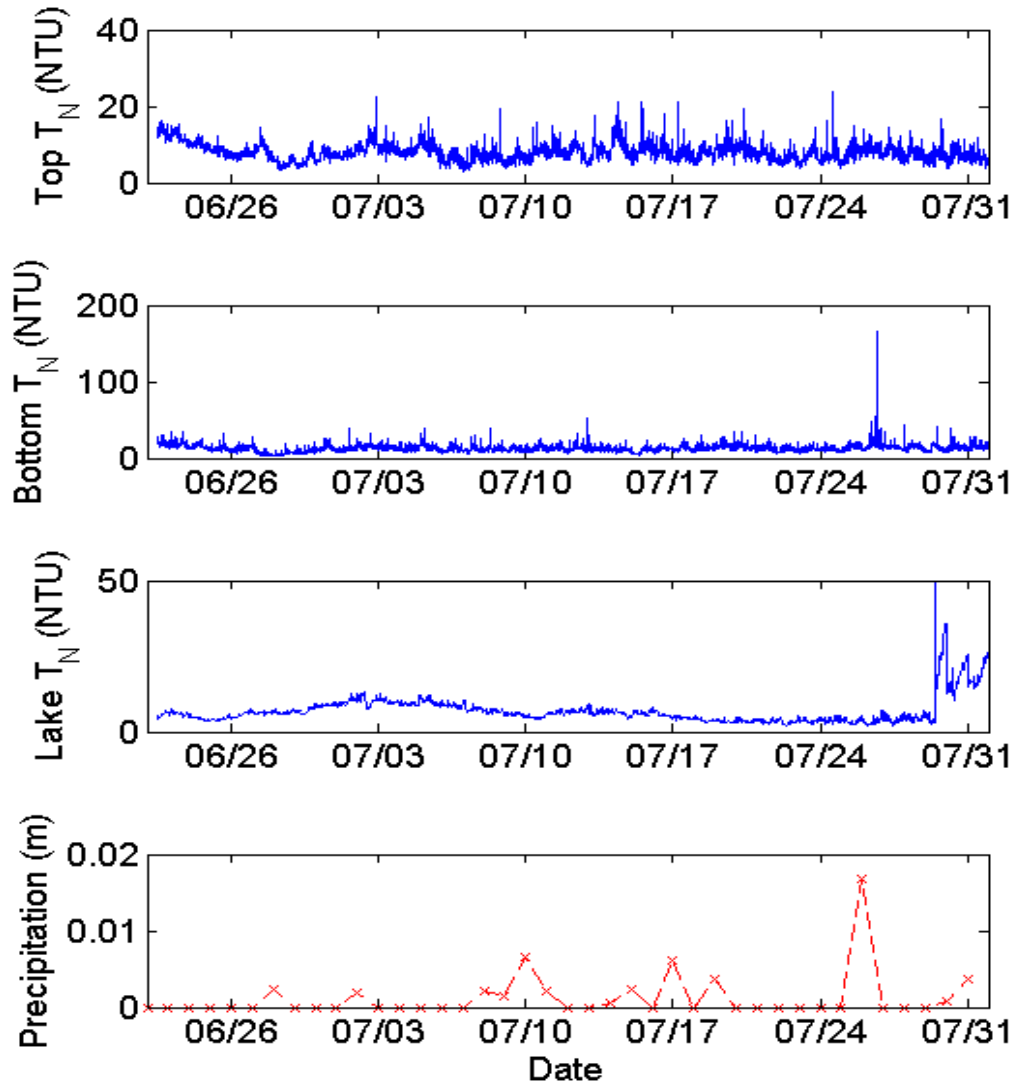


Figure 5.70: Turbidities in the inlet and southern lake and daily precipitation over Deployment 2.

During precipitation events, there was an increase in the flowrate of at least one (and typically all three) tributaries flowing into the inlet (Cayuga Inlet Creek (CI), Sixmile Creek (SC), and Cascadilla Creek (CC)). The two small precipitation events at the end of June and beginning of July in 2016 resulted in significant peaks in the Cayuga Inlet Creek flowrate. The few condensed small events in mid-July 2016 resulted in a steady increase in the Cayuga Inlet Creek flowrate and small peaks in both Sixmile Creek and Cascadilla Creek. As expected the largest precipitation event over Deployment 2, on 7/26/2016, resulted in the largest flowrate increase for all three tributaries.

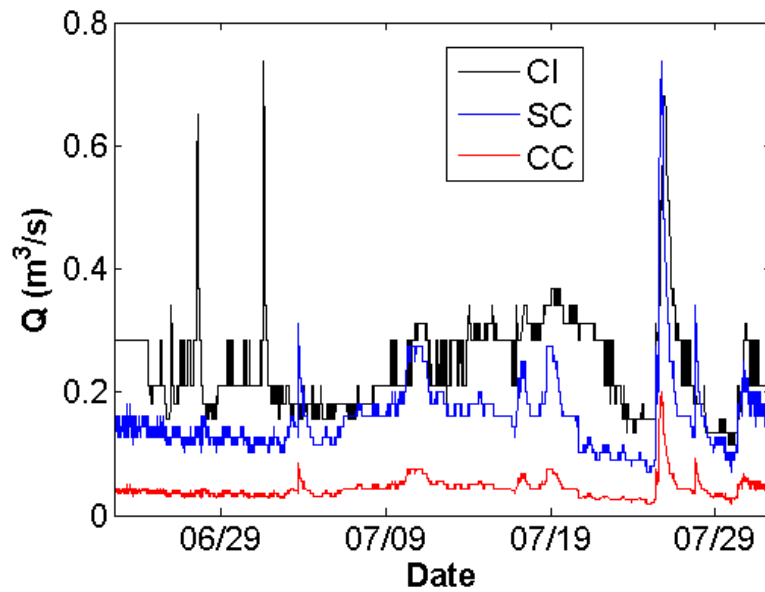


Figure 5.71: Tributary flowrates measured by USGS gage stations over Deployment 2.

We were interested in inlet conditions surrounding the three most significant precipitation events over Deployment 2 (Figure 5.72). In all three cases, U and U_{abs} increased and most significantly so for the largest precipitation event. While unidirectional flows in the inlet dominated these events, the direction of flow still fluctuated. Even with higher tributary flowrates we observed unidirectional flows from the lake into the inlet (Flow Condition 4). u_* and $\overline{u'w'}$ increased in the inlet for all these precipitation cases. As previously mentioned the largest precipitation event resulted in the greatest increase in the bottom layer turbidity. The other precipitation events however only exhibited medium-range turbidities. Two of the three precipitation events corresponded to $Fr_{bulk} > 1$, while the first event around 7/11/2016 corresponded to $G > 1$.

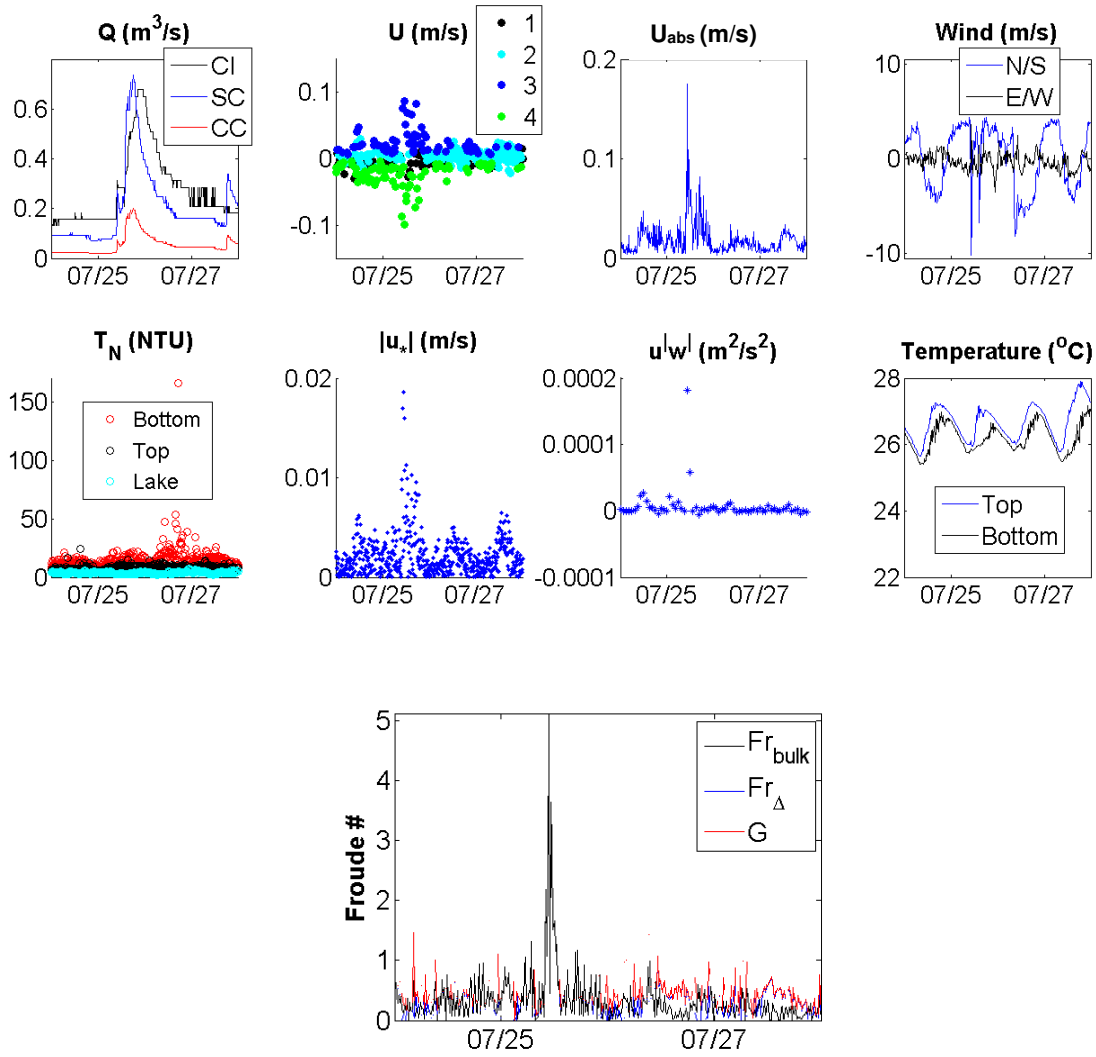


Figure 5.72.1: Conditions from 7/24/2016 through 7/28/2016.

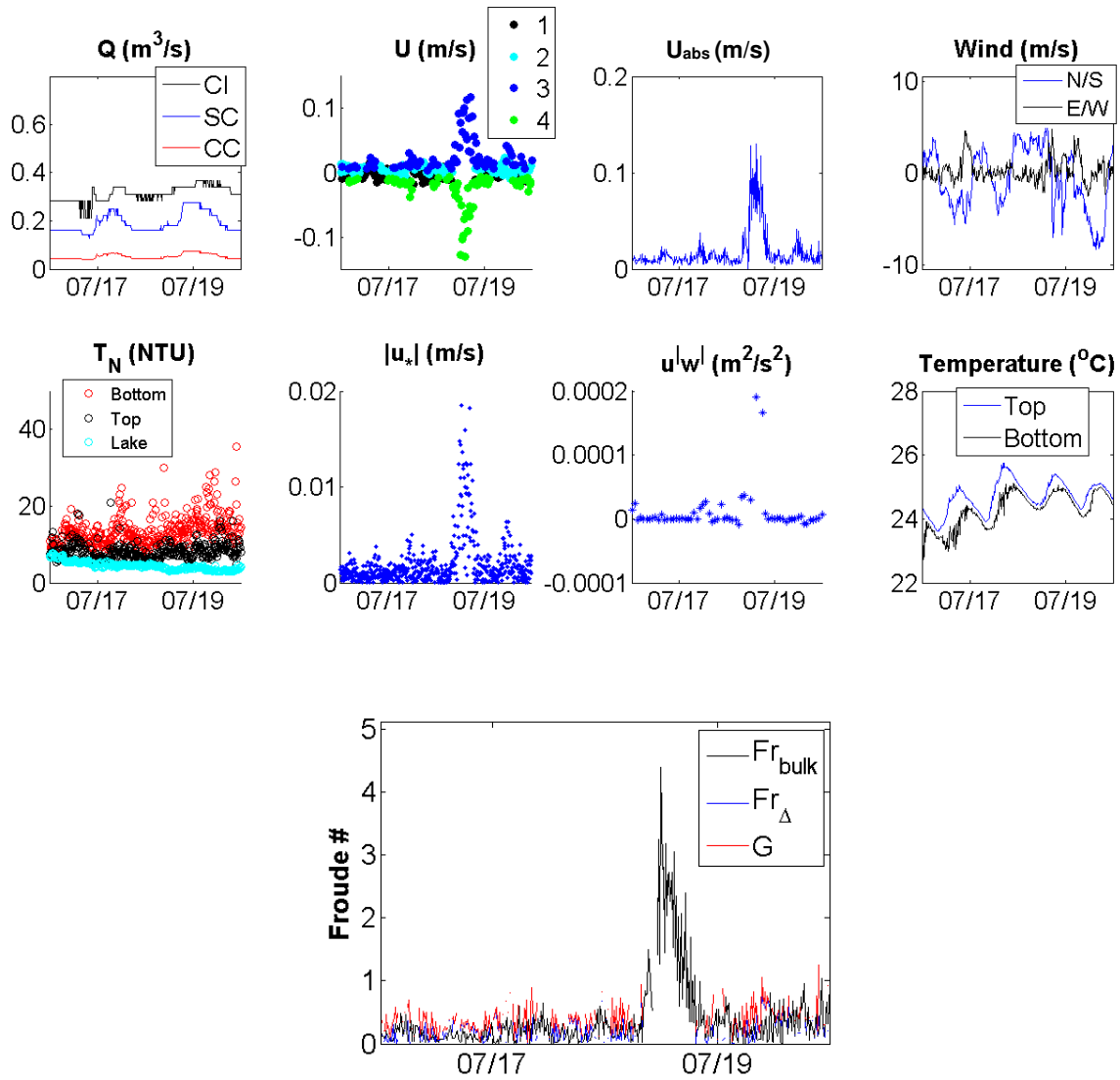


Figure 5.72.2: Conditions from 7/16/2016 through 7/20/2016.

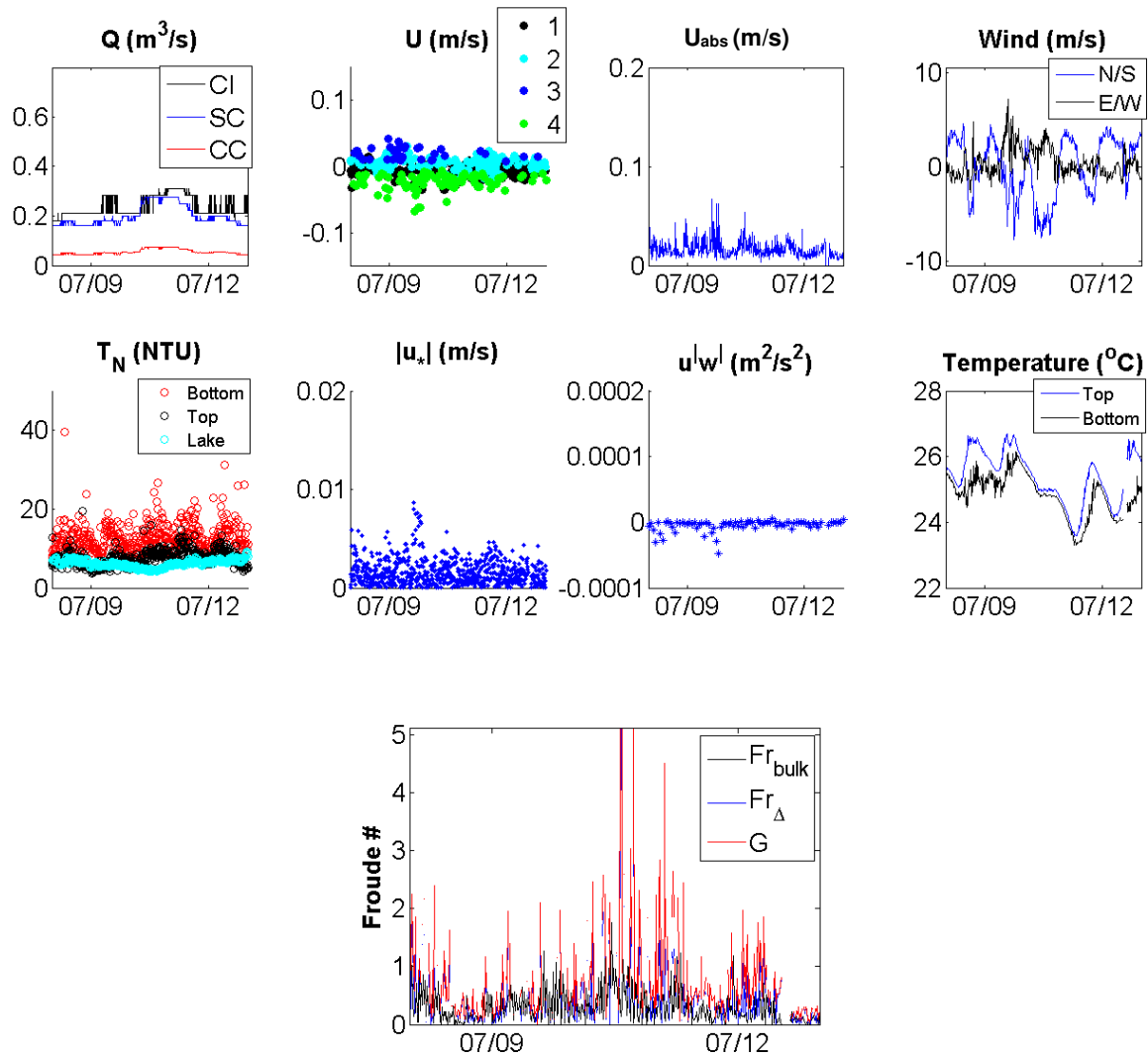


Figure 5.72.3: Conditions from 7/08/2016 through 7/13/2016.

Over Deployment 3 there were more precipitation events. At the beginning of August precipitation events were frequent and the southern lake turbidity remained up around 50 NTU. The greatest increase in the tributary flowrates was on 8/22/2016, when it rained after a few days without and precipitation events occurred at least every other day the week prior. Shortly after this, the bottom layer turbidity in the inlet quickly increased above 650 NTU, much higher than any previous values, and continued to increase to high turbidities for the rest of the deployment, with these high turbidities becoming less frequent with time. Shortly after the bottom layer turbidity in the inlet increased, the

southern lake turbidity increased above 50 NTU, after remaining below 25 NTU for the previous week. The other significant increase in tributary flowrates was on 8/10/2016 and shortly after this the bottom layer turbidity in the inlet significantly increased, above 400 NTU.

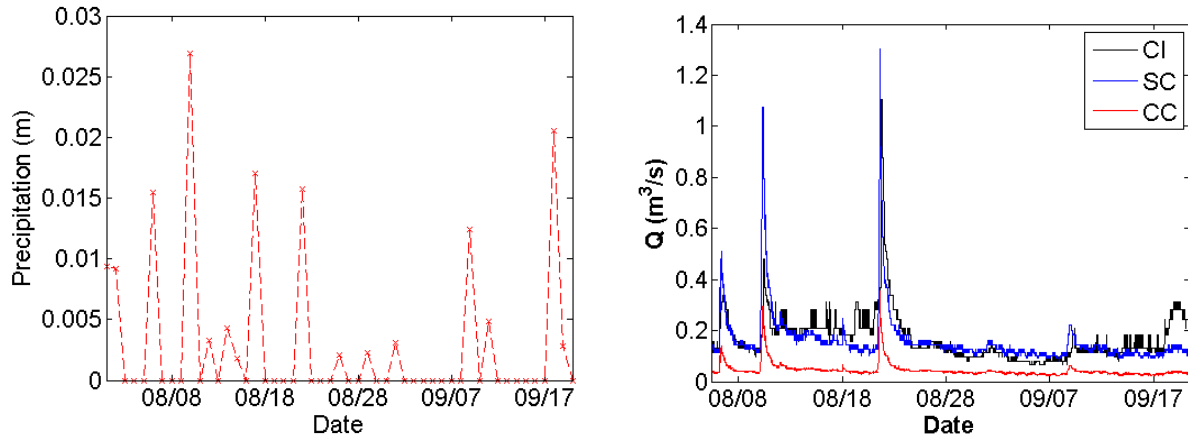


Figure 5.73: Daily precipitation (left) and Cayuga Inlet Creek (CI), Sixmile Creek (SC), and Cascadilla Creek (CC) flowrates based on USGS gage stations (right) over Deployment 3.

From 8/10/16 through 8/15/16 it rained four out of these six days and the tributary flowrates peaked on 8/10/16. On this same day, the temperature in the bottom layer of the inlet dropped while the temperature in the top layer of the inlet increased. Over this period the flow direction in the bottom layer of the inlet was predominately from the tributaries and out to the lake, whether an exchange flow or unidirectional flow. On 8/14/2016, after multiple rain events, U and U_{abs} increased, both above 0.2 m/s. On this day unidirectional flows in both directions through the inlet were present at times, with flow directed out towards the lake more typical. Leading up to this day, bottom layer inlet temperatures increased closer to top layer inlet temperatures, reducing the degree of stratification in the inlet. On 8/14/2016, $\overline{u'w'}$ increased and the bottom layer turbidity in the inlet increased above 400 NTU. We did not see any significant change in turbidities in the top layer of the inlet or in the southern lake. Over the period the stratification in the inlet was higher, due to the drop in temperature in the bottom layer, Froude numbers were low.

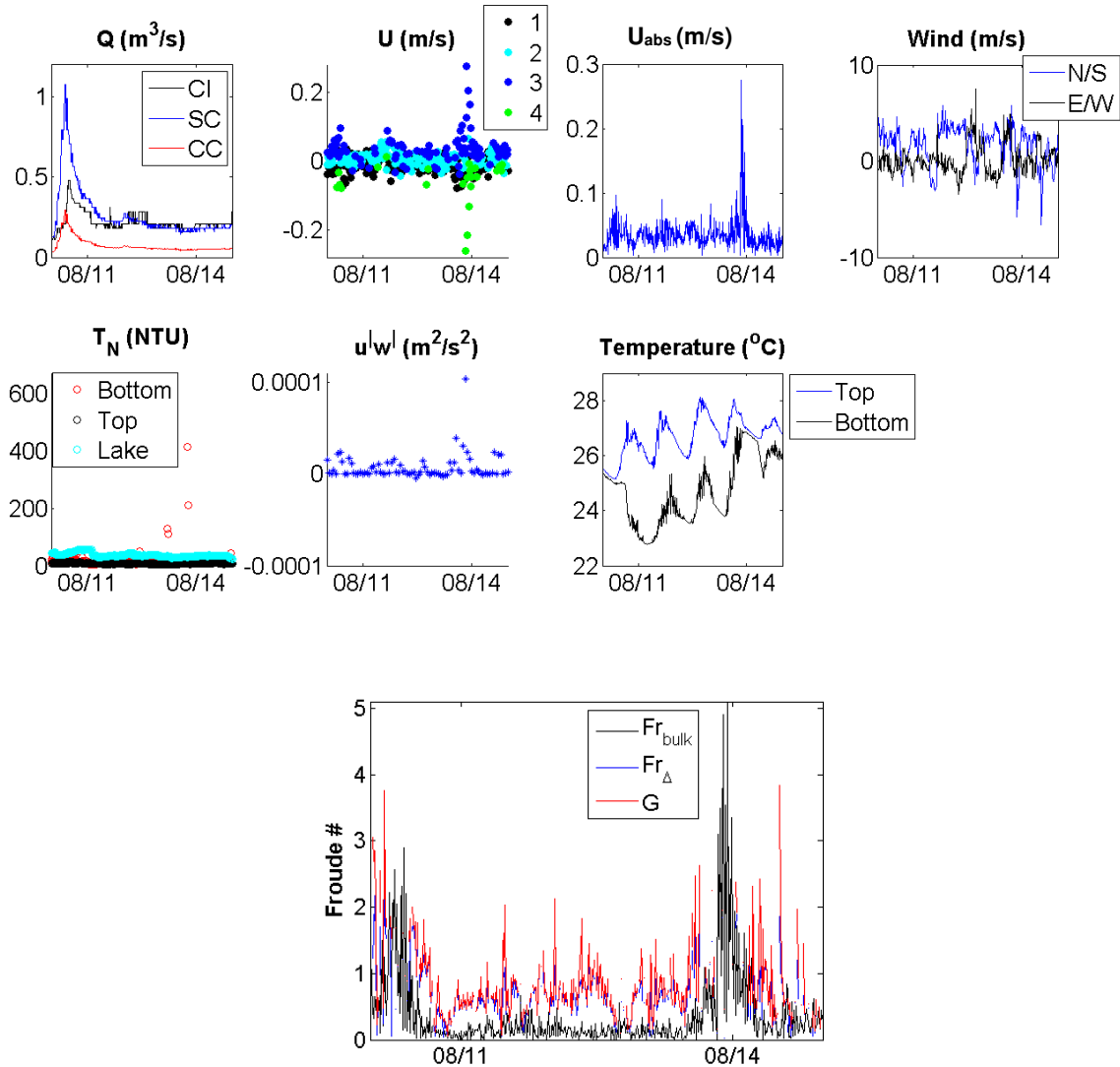


Figure 5.74: Conditions from 8/10/2016 through 8/15/2016.

5.4.4 “Upwelling” Events

Over Deployment 1 there were no clear upwelling events. However, on 9/6/2015 the southern lake and inlet temperatures rapidly dropped, while air and tributary temperatures did not. Surrounding this event, the degree of stratification in the inlet increased as the bottom layer temperature dropped. After a few days, the tributary flowrates slightly increased, but $|U|$ and U_{abs} significantly increased. u_* increased and shortly after this the bottom layer turbidities reached a

maximum for this period. Froude numbers were low and Fr_{bulk} only increased above 1 for the short period that $|U| > 0.1m/s$.

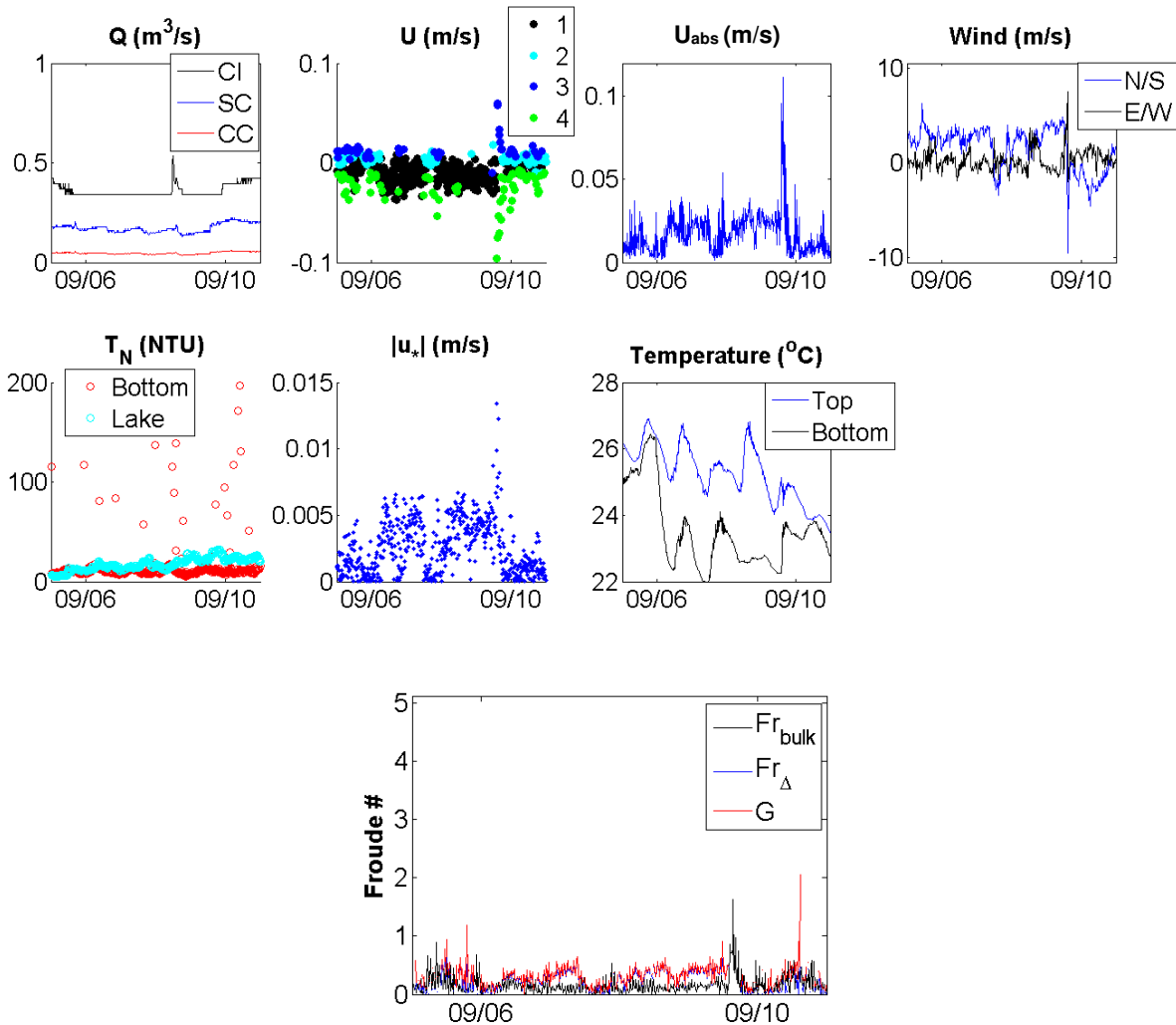


Figure 5.75: Conditions from 9/5/2015 through 9/11/2015.

There were three significant drops in the bottom layer inlet temperature over Deployment 2. We suspect this was due to upwelling events on the southern shelf of Cayuga Lake (or similar mechanisms approaching upwelling events with a tilting thermocline pushing colder water from deep layers into the southern shelf and towards the inlet). From such events the water temperature in the bottom layer of the inlet responded first and more significantly, causing an increased degree of stratification in the inlet.

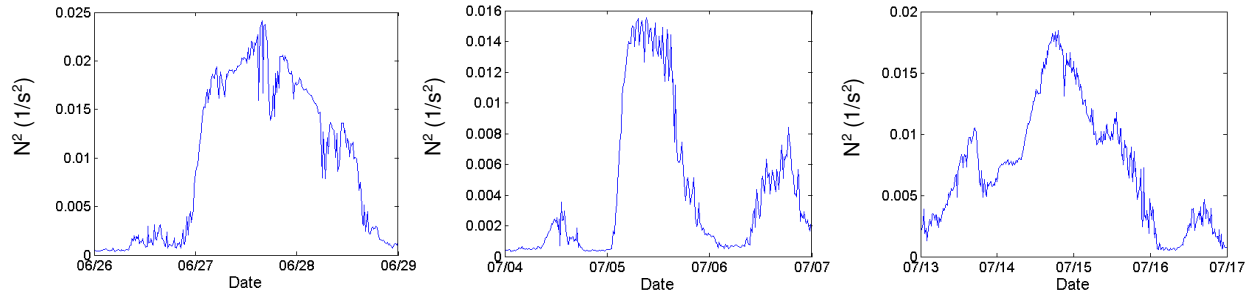


Figure 5.76: Three significant periods of increased degree of stratification in inlet starting around 6/27/2016, 7/5/2016, and 7/14/2016.

For all these events, there was a sustained southerly wind prior to the temperature dropping in the bottom layer of the inlet. Over these periods U , U_{abs} , u_* , and $\overline{u'w'}$ increased, although not as significant as that observed during the precipitation events. The one exception was the highest $\overline{u'w'}$ was recorded during the event starting around 7/14/2016. Exchange flows in the inlet dominated these upwelling events. Predominantly Flow Condition 1 in the inlet persisted during the upwelling event with the greatest drop in temperature on the southern shelf and the greatest increase in the inlet stratification. This is exactly the exchange flow in the inlet we expect resulting from upwelling events on the southern shelf of Cayuga Lake. The other two upwelling events were slightly dominated by Flow Condition 2. These two events exhibited shorter and less extreme temperature drops on the southern end of the lake. The turbidities remained in the low to medium range throughout each of these events. The strongest degree of stratification in the inlet corresponded to the lowest turbidities in the bottom layer. Each of the upwelling events corresponded to decreased Fr_{bulk} , F_{Δ} , and G following the temperature drop in the bottom layer of the inlet.

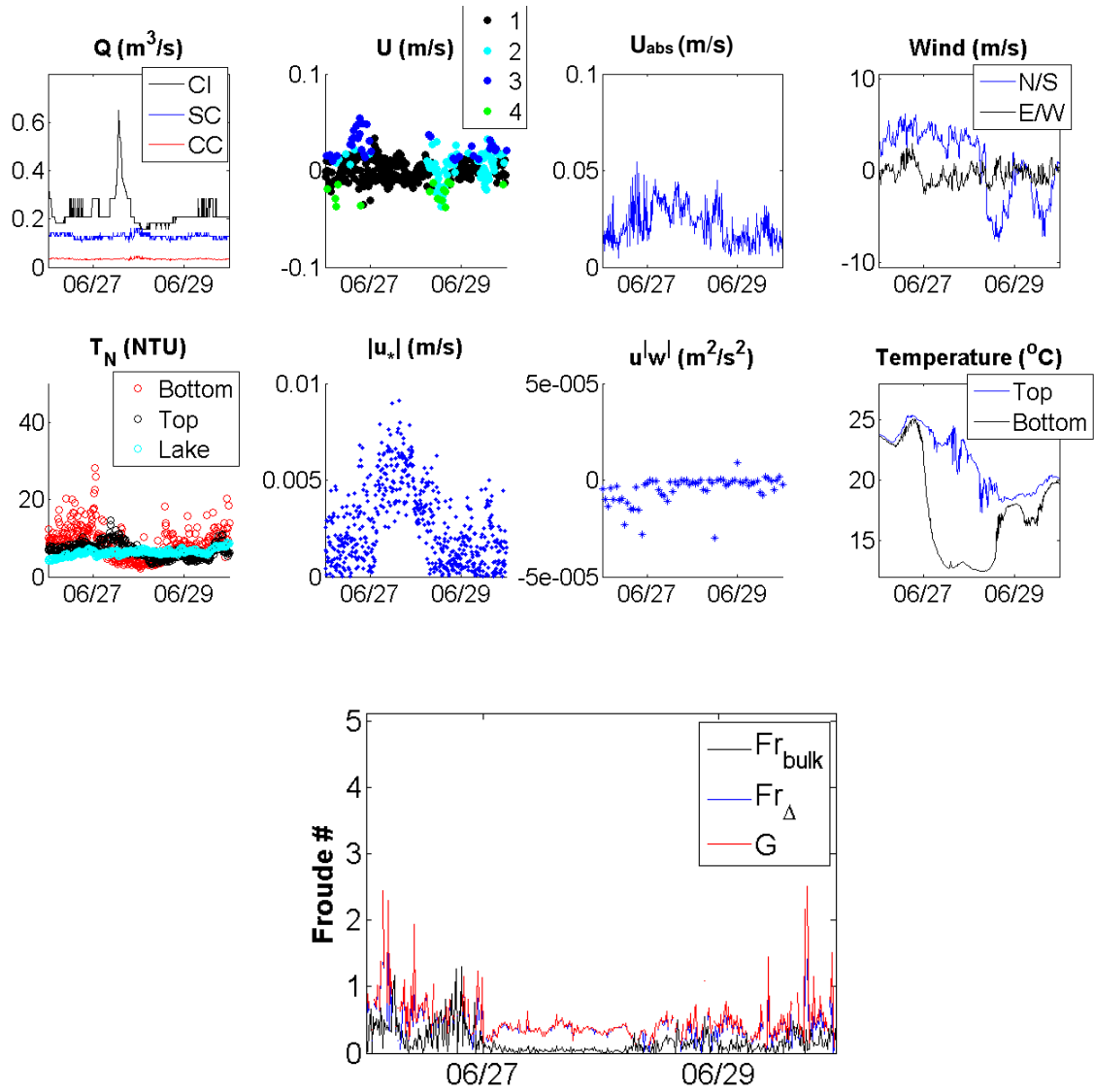


Figure 5.77.1: Conditions from 6/24/2016 through 6/30/2016.

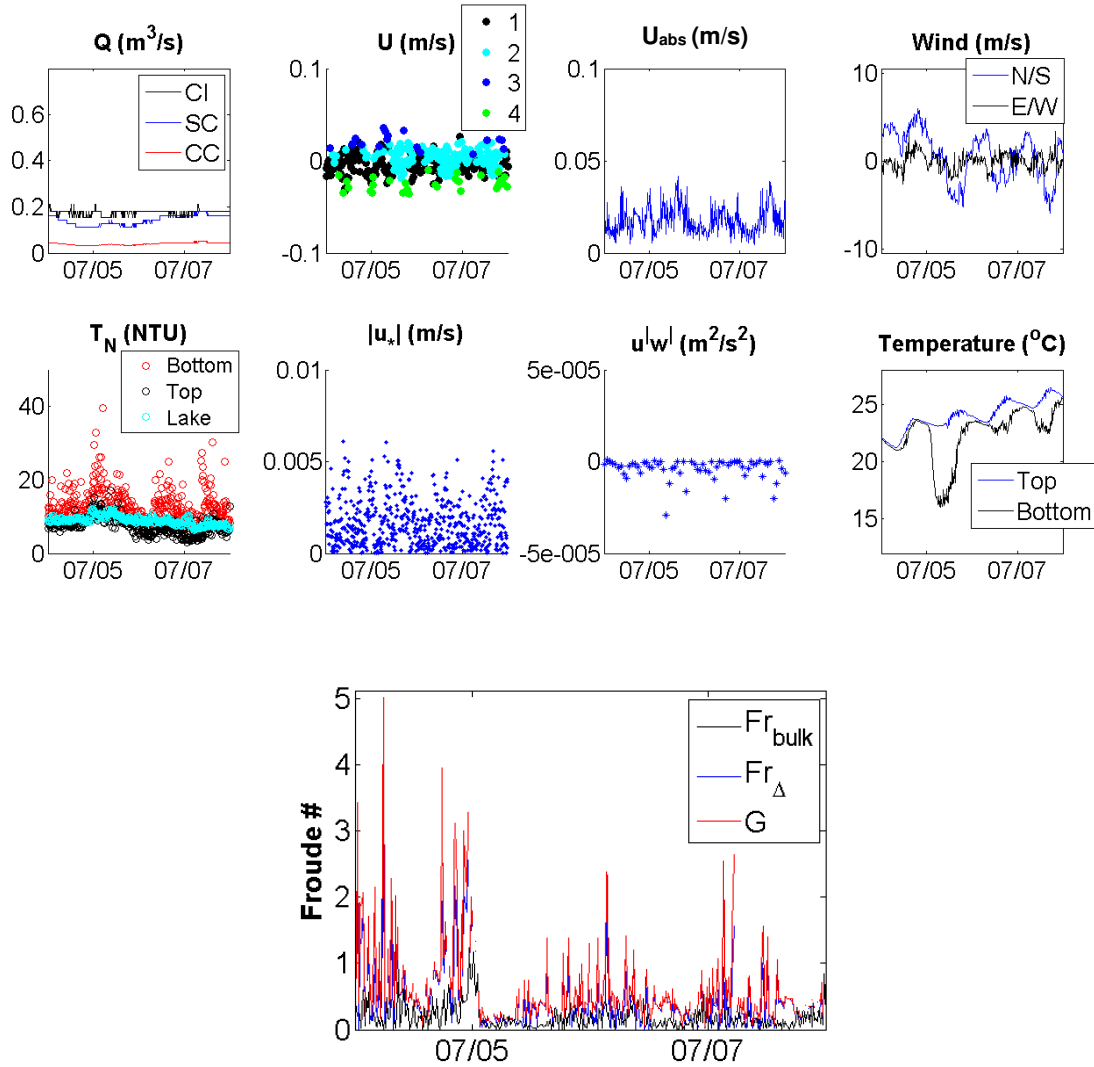


Figure 5.77.2: Conditions from 7/04/2016 through 7/08/2016.

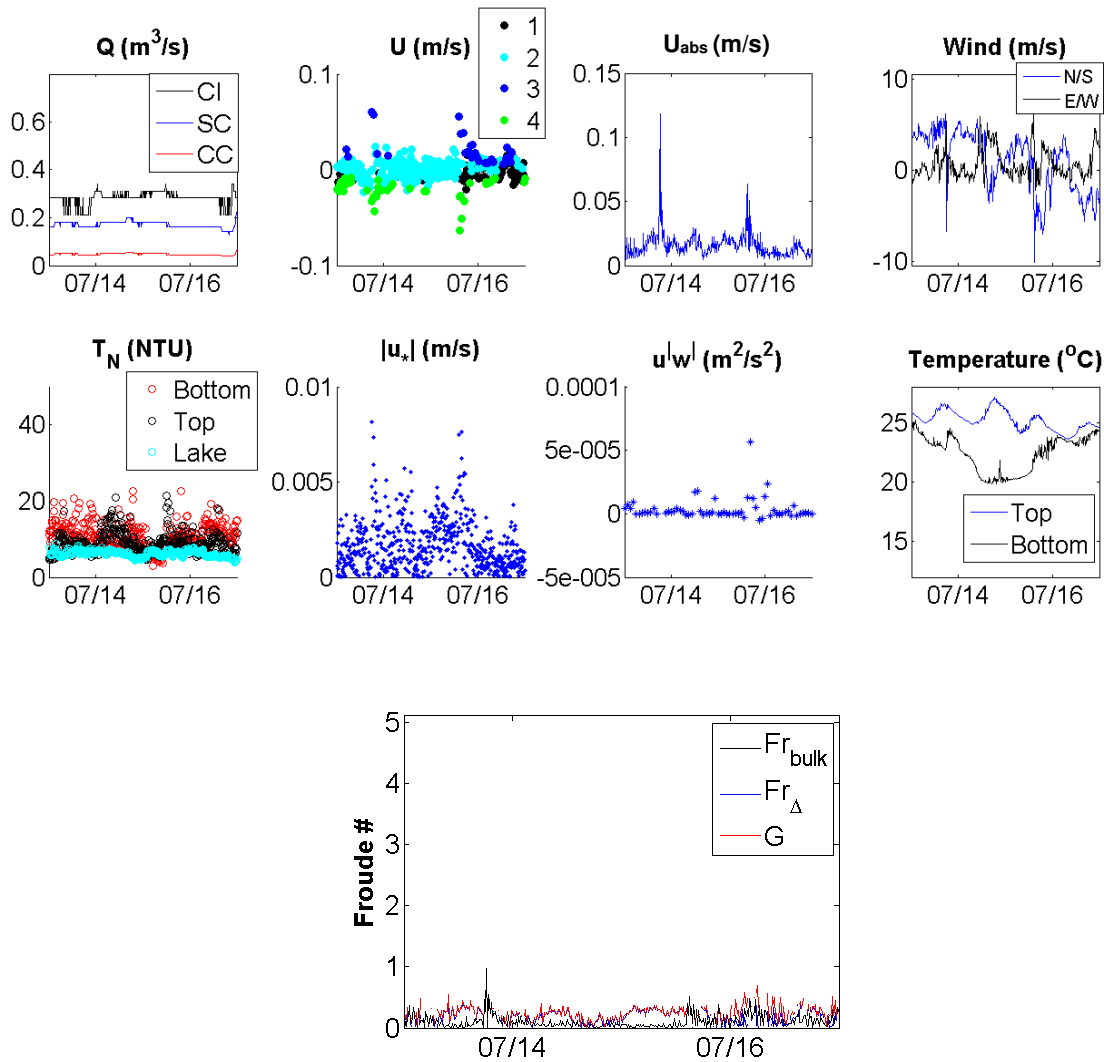


Figure 5.77.3: Conditions from 7/13/2016 through 7/17/2016.

Based on the temperature data over Deployment 3, we did not observe any clear upwelling or near-upwelling events. We focused on data from 8/19/2016 through 8/23/2016, when the southern lake temperature dropped at a quick rate for a sustained period, most closely resembling what we expect due to an upwelling event. At the same time the inlet temperature decreased and the bottom layer decreased at a faster rate than the top, thus stratification in the inlet increased. There was a sustained southerly wind over the lake prior to the temperature drops, which is expected to set up conditions for such an upwelling event. At the same time the tributary flowrates increased. There was also a significant precipitation event on 8/22/2016, when it had been dry the three previous days.

Over this period U and U_{abs} remained below 0.1 m/s and recall we do not have $\overline{u'w'}$ past 8/22/2016, as this was when the internal settings on the Vector changed. Shortly after the increased tributary flowrates and increased stratification in the inlet, the bottom layer turbidity in the inlet drastically increased above 600 NTU. We already discussed this event and how bottom layer turbidity continued to increase to such high levels after August 22, 2016.

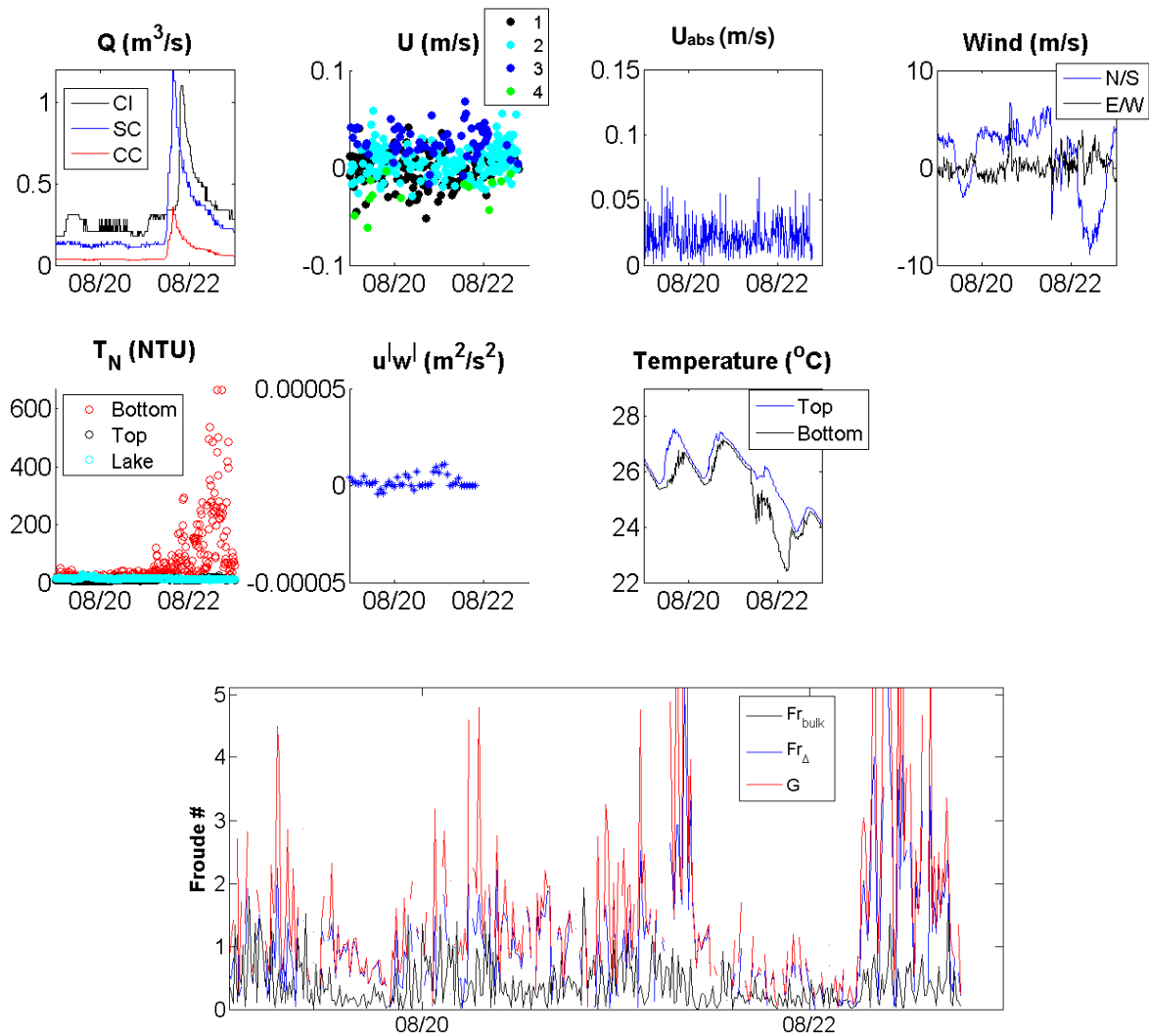


Figure 5.78: Conditions from 8/19/2016 through 8/23/2016.

5.5 Conclusion

From the end of June into mid-October, during the stratified season for Cayuga Lake, exchange flows are typical in Cayuga Inlet. Direction of bulk flow through the inlet is strongly connected to barotropic seiches in the lake, particularly when tributary flowrates are low. Stratification in the inlet is primarily dependent on the solar radiation as well as strong tributary flows or upwelling events introducing a layer of cooler (or potentially warmer in the case of tributary flows) water to the inlet. Wind stresses along the axis of the lake and inlet play an indirect role setting up flow behavior in the inlet through its influence on lake seiches. Strong enough wind stresses essentially remove any degree of stratification in the inlet and increase vertical mixing. Timescale analysis suggests over the summer months and into fall the inlet is predominantly well mixed, though we frequently found significant differences in turbidities in the top and bottom layers of the inlet.

Maximum turbidities and high percent differences in layer turbidities through the inlet are more likely when buoyancy forces dominate inertial forces. When inertial forces are significantly dominating, turbidities remain low, and during an exchange flow in the inlet the bottom layer turbidity is almost always greater than the top layer turbidity. While turbidities in the bottom layer of the inlet overall are higher than in the top layer during the investigated summer and fall months, when the degree of stratification increases due to temperature differences there is more potential for larger turbidities concentrated to the surface layer. Bed sediment resuspension has a small contribution to bottom layer turbidities, that is relatively insignificant to overall turbidity loads. There is no clear influence of flow type (unidirectional vs exchange) or flow direction on inlet turbidity loads. The inlet is a conduit through which suspended sediment is advected. Most large turbidity loads, primarily passing through the bottom layer of Cayuga Inlet and into the southern shelf of Cayuga Lake, are attributed to precipitation events. In the spring, when the southern lake is expected to be cooler than that observed over the summer and fall deployment periods analyzed here and tributary flows are

expected to warm faster, large turbidity loads may pass through the top layer of Cayuga Inlet with more frequency. The persistent exchange between the inlet and lake, along with the strong event based loading through the inlet, we suspect significantly impacts water quality on the southern shelf.

Appendix A Uncertainty Analysis

In a single-sample experimental measurement uncertainty arises due to bias and random errors. Bias, or fixed, errors are deterministic and will have a specific mean and zero variance. Random, or variable, errors will have a zero mean and non-zero variance and due to various sources of noise. For our field measurements, we first consider these two types of error separately and then combine for the total uncertainty in each measurement.

To determine bias errors we use the root-sum-square (RSS) technique as described by Kline & McClintock (1953). Where R is the measurement of interest and \bar{X}_i 's are the variables used to calculate R , the uncertainty in R , δR , is determined by:

$$\delta R = \sqrt{\sum_{i=1}^M \left(\frac{\partial R}{\partial \bar{X}_i} \delta \bar{X}_i \right)^2} \quad (\text{A.1})$$

The worst-case estimate was used to determine the bias error for each variable in a measurement. For the ADCP, manufacturers report the accuracy as $\pm 0.3\%$ of the water velocity relative to ADCP $\pm 0.3\text{cm/s}$. For the HR Profiler, manufacturers report the accuracy as $\pm 1\%$ of the measured value $\pm 0.5\text{cm/s}$. And lastly for the Vector, manufacturers report the accuracy as $\pm 0.5\%$ of the measured value $\pm 1\text{mm/s}$. The bias errors in mean streamwise velocities from all three instruments and in turbulent fluctuations from the Vector are calculated from these accuracies and the RSS technique.

To determine random errors we use the bootstrap technique as described by Efron & Tibshirani (1993). This method estimates the probability density function of statistics of a measurement by replicating a statistic from the single-sample into a multiple-sample estimate of that statistic. We estimated and report the 95% confidence interval for the random error in our measurements based on this method, with a resample number of 1000.

To determine the total error we use the RSS technique. Table A.1 summarizes the worst case 95% uncertainty intervals for our measurements in the field.

Table A.1: Worst case 95% uncertainty intervals for field experimental measurements

Deployment	Measurement	Bias	Random	Total	% of measured value
1	ADCP \bar{u} (mm/s)	± 3.2	± 0.7	± 3.3	± 22.0
	HRP \bar{u} (mm/s)	± 7.3	± 6.9	± 10.0	± 27.0
2	ADCP \bar{u} (mm/s)	± 3.9	± 0.9	± 4.0	± 20.0
	Vector \bar{u} (mm/s)	± 1.5	± 2.1	± 2.6	± 14.4
	Vector \bar{w} (mm/s)	± 0.6	± 0.2	± 0.6	± 31.6
	Vector \bar{u}' (mm/s)	± 0.5	± 0.2	± 0.5	± 14.3
	Vector \bar{w}' (mm/s)	± 0.2	± 0.1	± 0.2	± 9.5
	Vector $\bar{u}'w'$ (mm ² /s ²)	± 0.002	± 0.003	± 0.004	± 1.0
3	IAWWTP ADCP \bar{u} (mm/s)	± 4.0	± 2.0	± 4.5	± 14.0
	Vector \bar{u} (mm/s)	± 2.0	± 1.0	± 2.2	± 17.0
	Vector \bar{w} (mm/s)	± 0.7	± 0.2	± 0.7	± 27.0
	Vector \bar{u}' (mm/s)	± 0.2	± 0.1	± 0.2	± 5.7
	Vector \bar{w}' (mm/s)	± 0.1	± 0.07	± 0.1	± 4.5
	Vector $\bar{u}'w'$ (mm ² /s ²)	± 0.006	± 0.002	± 0.006	± 2.9

Bibliography

- Antenucci, J. P., Imberger, J., & Saggio, A. (2000). Seasonal evolution of the basin-scale internal wave field in a large stratified lake. *Limnology and Oceanography*, 45(7), 1621–1638.
- Armi, L., & Farmer, D. M. (1986). Maximal two-layer exchange through a contraction with barotropic net flow. *Journal of Fluid Mechanics*, 164(-1), 27.
- Armi, L. (1986). The hydraulics of two flowing layers with different densities. *Journal of Fluid Mechanics*, 163, 27–58.
- Bogucki, D., Dickey, T., & Redekopp, L. G. (1997). Sediment Resuspension and Mixing by Resonantly Generated Internal Solitary Waves. *Journal of Physical Oceanography*, 27(7), 1181–1196.
- Bricker, J. D., & Monismith, S. G. (2007). Spectral Wave–Turbulence Decomposition, 24(1970), 1479–1487. <http://doi.org/10.1175/JTECH2066.1>
- Callinan, C. W. (2001). Water Quality Study of the Finger Lakes. New York State Department of Environmental Conservation (NYSDEC).
- Cowen, E. and Monismith, S. (1997). A hybrid digital particle tracking velocimetry technique. *Experiments in Fluids* 22(3), 199-211.
- Crimaldi, J. P. (1998) Turbulence Structure of Velocity and Scalar Fields over a Bed of Model Bivalves
- Csanady, G. T. (1975). Hydrodynamics of Large Lakes. *Annual Review of Fluid Mechanics*, 7(3340), 375–386.
- Eadie, B. J., and J. A. Robbins, The role of particulate matter in the movement of contaminants in the Great Lakes, in Sources and Fates of Aquatic Pollutants, ACS Adv. Chem. Ser., vol. 216, edited by R. Hites and S. Eisenreich, pp. 319–364, Am. Chem. Soc., Washington, D. C., 1987.
- Eadie, B. J., R. L. Chambers, W. S. Gardner, and G. L. Bell, Sediment trap studies in Lake Michigan: Resuspension and chemical fluxes in the southern basin, *J. Great Lakes Res.*, 10, 307–321, 1984.
- Eaton, A. D., Clesceri, L. S., Greenberg, A. E., Franson, M. A. H., American Public Health Association., American Water Works Association., & Water Environment Federation. (1998). *Standard methods for the examination of water and wastewater*. Washington, DC: American Public Health Association.
- Effler, S. W., & Peng, F. (2014). Long-term study of minerogenic particle optics in Cayuga Lake, New York. *Limnology and Oceanography*, 59(2), 325–339.
- Fischer, Hugo B. (1979). *Mixing in Inland and Coastal Waters* (Book). New York: Academic.
- Genesee/Finger Lakes Regional Planning Council. (2000). Cayuga Lake Watershed Preliminary Watershed Characterization. New York State Department of State.

- Gordon, R. L. (1996). Acoustic Doppler Current Profiler Principles of Operation: A Practical Primer. *Teledyne RD Instruments*.
- Grant, W. D., & Madsen, O. S. (1986). The Continental-Shelf Bottom Boundary Layer, 265–305.
- Haith, D. A., Hollingshead, N., Bell, M. L., Kreszewski, S. W., Morey, S. J., & Hall, R. (2009). ESTIMATION OF NUTRIENT AND SEDIMENT LOADS TO CAYUGA LAKE USING THE GWLF WATERSHED MODEL.
- Hogg, A. M., Ivey, G. N., & Winters, K. B. (2001). Hydraulics and mixing in controlled exchange flows. *Journal of Geophysical Research*, 106(C1), 959.
- Hogg, A. M., & Killworth, P. D. (2004). Continuously stratified exchange flow through a contraction in a channel, 499, 257–276.
- Imberger, J., & Ivey, G. N. (1991). On the Nature of Turbulence in a Stratified Fluid. Part II: Applications to lakes. *Journal of Physical Oceanography*.
- Jin, K.-R., & Ji, Z.-G. (2004). Case Study: Modeling of Sediment Transport and Wind-Wave Impact in Lake Okeechobee. *Journal of Hydraulic Engineering*, 130(11), 1055–1067.
- Juday, C. (1940). The Annual Energy Budget of an Inland Lake, 21(4), 438–450.
- Kinsman, B. (1984). Wind Waves. Dover
- Kitaigorodskii, S. A., Donelan, M. A., Lumley, J. L., & Terray, E. A. (1983). Wave-turbulence interactions in the upper ocean. Part II: Statistical characteristics of wave and turbulent components of the random velocity field in the marine surface layer.
- Lampert, W., & Ulrich S. (2010). *Limnoecology*. 2nd ed. Oxford: U, 2010. Print
- Lohrmann, A., Hackett, B., & Røed, L. P. (1990). High Resolution Measurements of Turbulence, Velocity and Stress Using a Pulse-to-Pulse Coherent Sonar. *Journal of Atmospheric and Oceanic Technology*.
- Lou, J., Schwab, D. J., Beletsky, D., & Hawley, N. (2000). A model of sediment resuspension and transport dynamics in southern Lake Michigan. *Journal of Geophysical Research*:
- Ludlam, S. II. (1967). Sedimentation in Cayuga Lake, New York. *Limnology and Oceanography*, 12(4), 618–632.
- Merrick, F. (2014). The Cayuga Inlet: A History. Community Science Institute.
- Monismith, S. (1986). An experimental study of the upwelling response of stratified reservoirs to surface shear stress. *Journal of Fluid Mechanics*, 171(-1), 407.

- Moran, L. (2015). Cayuga Lake Modeling Project. Cayuga County Water Quality Management Agency meeting Jan. 8, 2015.
- Nagle, G. N., Fahey, T. J., Ritchie, J. C., Woodbury, P. B. (2007). Variations in Sediment Sources and Yields in the Finger Lakes and Catskills Regions of New York. *Hydrological Processes*, 21(1), 828-838.
- New York State Department of Environmental Conservation (NYSDEC). (2007). Cayuga Lake (0705).
- New York State Department of Environmental Conservation (NYSDEC). (2015). Cayuga Lake Watershed Management. <http://dec.ny.gov/lands/8825>.
- Nortek AS. (2005). Vector Current Meter User Manual. *Doc. No. N300-100*.
- Prestigiacomo, A. R., Effler, S. W., Gelda, R. K., Matthews, D. A., Auer, M. T., Downer, B. E., ... Walter, M. T. (2016). APPORTIONMENT OF BIOAVAILABLE PHOSPHORUS LOADS ENTERING CAYUGA LAKE, NEW YORK. *Journal of the American Water Resources Association*, 52(1). <http://doi.org/10.1111/1752-1688.12366>
- Rueda, F. J., & Cowen, E. a. (2005). Exchange between a freshwater embayment and a large lake through a long, shallow channel. *Limnology and Oceanography*, 50(1), 169–183.
- Rusello, P. J. (2009). A Practical Primer for Pulse Coherent Instruments. *Nortek Technical Note TN-027*.
- Salmaso, N. (2005). Effects of climatic fluctuations and vertical mixing on the interannual trophic variability of Lake Garda, Italy. *Limnology and Oceanography*, 50(2), 553–565.
- Schweitzer, S. (2010). THE EFFECTS OF RUNOFF AND UPWELLING EVENTS ON THE WATER QUALITY OF THE, (May).
- Shields, A. (1936). Application of similarity principles and turbulence research to bed-load movement. *Hydrodynamics Laboratory Publ. No. 167*. W. P. Ott and J. C. van Uchelen trans., U.S. Dept. of Agr., Soil Conservation Service Cooperative Laboratory, California Institute of Technology, Pasadena, Calif.
- Simpson, J. E. (1982). Gravity Currents in the Laboratory, Atmosphere, and Ocean. *Annual Review of Fluid Mechanics*, 14(1), 213–234.
- Simpson, J. H., Brown, J., Matthews, J., & Allen, G. (1990). Tidal Straining, Density Currents, and Stirring in the Control of Estuarine Stratification. *Estuaries*, 13(2), 125.
- Søndergaard, M., Jensen, J.P. & Jeppesen, E. (2003) Role of sediment and internal loading of phosphorus in shallow lakes. *Hydrobiologia* 506(1), 135-145.
- SPDES number: NY0244741. DEC number: 7-5099-00009/00001. (2013). State Pollution Discharge Elimination System (SPDES) Discharge Permit.

Stearns & Wheeler (1997) Draft environmental impact statement – Lake Source Cooling prepared for Cornell University, NY. *Tech. Rep.*. NYSDEC Application No. 7-00009/00001.

UFI & Cornell University (2014). Phase 1: Monitoring and Modeling Support for a Phosphorus/Eutrophication Model of Cayuga Lake. *Tech. Rep.*. Upstate Freshwater Institute (UFI).

United States Department of Agriculture (1987). Soil Mechanics Level 1. Soil Conservation Service.

Von Karman, T. (1931). Mechanical Similitude and Turbulence. *Tech. Mem.* NACA, no. 611. Winters, K. B., & Seim, H. E. (2000). The role of dissipation and mixing in exchange flow through a contracting channel. *Journal of Fluid Mechanics*, 407, 265–290.

Wood, I. R. (1970). A lock exchange flow. *Journal of Fluid Mechanics*, 42, 671–687.

Wüest, A., & Imboden, D. M. (1995). *Physics and Chemistry of Lakes (Book)*. *Igarss 2014* (2nd ed.). Hong Kong: Springer-Verlag.